MULTI-SCALE MODELING OF ICE CRYSTAL FORMATION IN CLOUDS

A Dissertation
Presented to
The Academic Faculty

By

Sylvia Camille Sullivan

In Partial Fulfillment
of the Requirements for the Degree
Doctor of Philosophy in the
School of Chemical and Biomolecular Engineering

Georgia Institute of Technology

August 2017

MULTI-SCALE MODELING OF ICE CRYSTAL FORMATION IN CLOUDS

Approved by:

Dr. Athanasios Nenes, Advisor
School of Chemical and Biomolecular Engineering
Georgia Institute of Technology

Dr. Corinna Hoose
Institute of Meteorology and Climate Research
Karlsruhe Institute of Technology

Dr. Mark Styczynski
School of Chemical and Biomolecular Engineering
Georgia Institute of Technology

Dr. Ronald Rousseau
School of Chemical and Biomolecular Engineering
Georgia Institute of Technology

Dr. Yi Deng
School of Earth and Atmospheric Sciences
Georgia Institute of Technology

Date Approved: May 17, 2017

À Maman et Papa qui ont tant donné pour soutenir ma curiosité et mes passions.

Acknowledgements

First and foremost to Mom, Dad, and Alan. You have always been my foundation. Then to Karen and Dick for their love and support of my crazy endeavors.

I want to thank Thanos for encouraging me to be self-confident and providing travel and development opportunities. I am grateful to Corinna, for generously given mentorship, and the rest of my Karlsruhe team for welcoming me to Germany, in particular Elke, Marco, Luisa, Alexei, and Jens. Thanks go also to Lazaros, Dongmin, and Donifan at the Goddard Space Flight Center for their support. And to Professors Agrawal and Styczynski for showing me what it means to be a good teacher.

My research group has given me both scientific and personal guidance: to Peter, career advisor, coffee-break raconteur, and in-house philosopher; to Arnaldo, for your endless optimism and patience with my thinking-aloud in the office; to Chris, for always being there to pick me up at the airport or lend an ear to my complaints; to Jameson, Matlab and Fortran King and Answerer of All Questions; and to Jackintosh, whose calm was the yin to my over-caffeinated yang.

Then I want to thank my Georgia Tech crew for your love and the good times, in particular to Weiwei, my fellow adventurer; to Queen D, I miss you so, woman; to Jojo, for tris and trips; to Andrew, we got da keys (and Amsterdam); to Tim, who rules the dance floor with me; to Kevin, my fellow runner; to Kong, for mutual love of sunshine and classical music; and to Michael and Jared, ihr seid das Beste. Also to Guillaume for time spent together, to D for the afternoon debriefing, and to Miss Ruth for keeping me blessed. It's been real, Peach State.

TABLE OF CONTENTS

LIST OF TABLES

LIST OF FIGURES

SUMMARY

Understanding human impact on climate is the foremost challenge of the 21st century. In particular, significant work remains to correctly model the liquid-ice phase partitioning in clouds. Cloud phase affects both surface temperatures, as clouds interact with terrestrial and solar radiation, and surface precipitation, as clouds are an important component of the hydrological cycle. This thesis focuses on better representing the initial formation of in-cloud ice, both via primary (thermodynamic) nucleation and secondary (mechanical) production, at various model scales.

An adjoint model of several ice nucleation codes is first constructed with automatic differentiation tools and outputs the sensitivity of ice crystal numbers to all input variables in a global climate model. The sensitivities output from this adjoint model are used to investigate nucleation efficiency and regime disparities between various formulations. Laboratory data-based formulations predict much more efficient and frequent heterogeneous ice nucleation than field data-based ones. Adjoint sensitivities are also used for large-scale attribution analysis, in which we identify the input variables that control temporal variability in output nucleated ice crystal numbers. Input vertical velocity is identified as a crucial factor, when turbulence is parameterized in global models. Its formulation should be better constrained with additional measurements to better predict in-cloud ice crystal numbers.

After development of these tools with global-scale insight, work shifts focus to a smaller scale with construction of a parcel model and mesoscale parameterizations for secondary ice production. The parcel model describes the processes of breakup upon graupel collision, rime splintering, and frozen droplet shattering within an adiabatically-rising volume of air. Hydrometeor non-sphericity increases secondarily-produced ice number significantly, but updraft stochasticity has a much smaller impact here than in the nucleation studies. Then these codes are incorporated into a more sophisticated, mesoscale meteorological model. A case study is run to understand how additional in-cloud ice from secondary production affects surface precipitation intensity.

The studies of primary nucleation and secondary production are brought together in a quantification of how many ice crystals must exist before secondary production initiates.

Simulations show that low amounts of preexisting ice are required to trigger secondary production over a wide range of thermodynamic conditions and adjustable parameter values. This result suggests that liquid droplet formation is more influential on overall phase partitioning in mixed-phase clouds. Finally, ideas are presented for future work to assess primary nucleation, secondary production, and other cloud parameterizations with satellite data and the mathematics of information theory.

ZUSAMMENFASSUNG

Das Verständnis des menschlichen Einflusses auf das Erdklima stellt eine große Herausforderung des 21. Jahrhunderts dar. Insbesondere ist noch zusätzliche Forschung erforderlich, um die Partitionierung zwischen flüssigen und festen Phasen in Wolken korrekt zu modellieren. Die Wassertröpfchen und Eiskristalle innerhalb einer Wolke modifizieren die Oberflächentemperatur der Erde, indem sie mit der Sonnen- oder Bodeneinstrahlung wechselwirken. Sie beeinflussen auch die Niederschlagsmenge, da Wolken ein wichtiger Teil des Wasserkreislaufes sind. Diese Doktorarbeit konzentriert sich auf eine bessere Parametrisierung der anfänglichen Eisbildung, sowohl durch thermodynamische Nukleation als auch durch mechanische Sekundärproduktion, auf mehrere Modellskalen.

Zuerst wird ein Adjointmodell aus diversen Eisnukleationskodes mit automatischer Differenzierung entwickelt. Dieses Modell berechnet die Sensitivität der Eiskristallanzahl bezüglich allen Eingabevariablen innerhalb eines globalen Klimamodells. Mit diesen Sensitivitätswerten können die Unterschiede in der Eisnukleationseffizienz und im Eisnukleationsregime zwischen verschiedenen Parametrisierungen erklärt werden. Auf Labordaten basierte Formulierungen sagen heterogene Eisnukleation weitaus effizienter und häufiger vor als auf in situ Daten basierte. Die Adjointsensitivitäten werden auch in einer großskaligen Attributionsanalyse angewendet. Wir identifizieren die Eingabevariablen, die die zeitlichen Schwankungen in der ausgegebenen Eiskristallanzahl kontrollieren. In Modellen, die Turbulenz parametrisieren, stellt die vertikale Windgeschwindigkeit ein äußerst wichtiges Element dar. Die Beschreibung dieser Windgeschwindigkeit sollte durch zusätzliche Messungen besser eingegrenzt werden, um die Anzahl der Wolkeneiskristalle besser vorherzusagen.

Nach der Entwicklung des Adjointmodells auf globaler Skala, konzentriert sich die Arbeit auf kleinere Skalen mit einem Luftpaketmodell und mesoskaligen Parametrisierungen von Sekundäreisproduktion. Das Luftpaketmodell beschreibt die Zersplitterung von gefrorenen Wassertröpfchen, bereiften Eishydrometeoren, und durch Graupelzusammenstöße in einer adiabatischen, aufsteigenden Luftmasse. Nichtkugelförmigkeit der Eishydrometeore führt zu einer deutlichen Zunahme des Sekundäreis, jedoch zeigt die vertikale Windgeschwindigkeit hier einen viel kleineren Einfluss auf diese Prozesse als in den Nukleationstudien. An-

schließend werden diese Kodes in ein umfassendes Wettervorhersagemodell implementiert. Eine Fallstudie wird durchgeführt, um aufzuklären, wie sich zusätzliche Wolkeneisproduktion auf die Niederschlagsintensität auswirkt.

Die Untersuchungen von Eisnukleation und Sekundärproduktion wird zusammengeführt, indem die Anzahl der nukleierten Eiskristalle, die nötig ist um Sekundärproduktion zu initiieren, berechnet wird. Die Simulationen zeigen, dass die Zersplitterungsprozesse schon bei einer geringen Menge vorhandener Eiskristallen beginnen. Dies geschieht über einen weiten Bereich von thermodynamischen Bedingungen und veränderlichen Parameterwerten. Dieses Ergebnis deutet darauf hin, dass die Bildung der flüssigen Phase einen stärkeren Einfluss als die Bildung der Eisphase auf die gesamte Partitionierung der Wolkenphasen hat. Abschließend werden Ideen für die Beurteilung von Nukleations-, Sekundärproduktions-, und anderen Wolkenparametrisierungen mit Satellitendaten und der Mathematik der Informationstheorie diskutiert.

CHAPTER 1
CLIMATE IMPACT AND MODELING OF CLOUDS

The description of cloud physics remains an important challenge in the effort to make weather predictions or climate projections. The Intergovernmental Panel on Climate Change (IPCC) states in their Fifth Assessment Report that "clouds and aerosols contribute the largest uncertainty to estimates of the Earth's changing energy budget" [1]. Mesoscale weather models or global climate models (GCMs) discretize space and time and solve mass and energy balances on this grid, but the physics of cloud formation and evolution is **subgrid**, occurring on scales smaller than this grid (Figure 1.1). To bridge this gap, **parameterizations** calculate relevant small-scale variables and pass them to the larger model framework. But a problem of scale exists even within the parameterization itself: rain drops and hail are millimeters in diameter while the particles that nucleate droplets or ice can be nanometers in diameter; vertical updrafts can extend for kilometers while turbulent eddies span only centimeters. Research is ongoing to develop physically accurate and computationally inexpensive representations of this multi-scale physics, given the radiative and hydrological impacts of clouds.

1.1 Cloud formation

Cloud formation refers to water droplet or ice crystal nucleation from atmospheric water vapor. Ice crystal nucleation is driven by **supersaturation** in the vapor phase. Saturation, $\mathcal{S}_i$, refers to the partial pressure of water vapor divided by the saturation vapor pressure over ice at ambient conditions. When saturation is greater than one, a system is said to be supersaturated.

$$s_i = \mathcal{S}_i - 1 = \frac{p}{p_{sat,i}} - 1 \tag{1.1}$$

Atmospheric supersaturation is usually generated by the adiabatic expansion of parcels of moist air. As these parcels rise to higher altitudes and lower ambient pressures, saturation

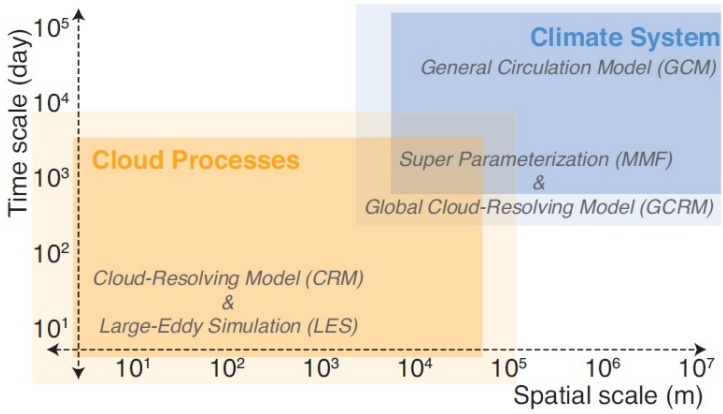

Figure 1.1: Spatial and temporal scales associated with cloud processes and climate modeling [1]

exceeds one and ice crystals begin to form. The supersaturation produced from atmospheric motions is not high enough to generate a new phase, either liquid water or ice, directly from the vapor phase. Instead, the surface of some suspended atmospheric particle, or aerosol, must be present to lower the free energy barrier for water vapor condensation or sublimation. Particles that take up liquid water to form droplets are called **cloud condensation nuclei**, or CCN, and those that facilitate ice nucleation are called **ice-nucleating particles**, or INP.

All solid or liquid forms of atmospheric water are jointly referred to as **hydrometeors** and include rain drops, graupel, and ice crystals among others. Cirrus clouds consist solely of ice hydrometeors and occur at altitudes above 5 km, while cumulus consist solely of liquid hydrometeors and generally form below 2 km. Mixed-phase clouds consist of both ice and supercooled liquid hydrometeors and form between altitudes of 2 and 5 km. The liquid portion of a mixed-phase cloud is often quantified with its **supercooled liquid fraction** (SLF), the ratio of liquid mass mixing ratio to the sum of liquid and ice mass mixing ratios [e.g., 2].

Köhler theory describes the formation of a liquid droplet of radius r_d as the balance of solute and curvature effects (or Raoult and Kelvin effects which go as r_d^{-3} and r_d^{-1} respectively):

$$\ln S_w = \frac{A}{r_d} - \frac{B}{r_d^3} \tag{1.2}$$

There is no corresponding analytical framework to describe ice nucleation, which may be either homogeneous from the supercooled liquid phase or heterogeneous on an INP surface. During **homogeneous nucleation**, random molecular fluctuations may cause an ice germ to form within the supercooled droplet; this process is strongly temperature-dependent with its speed quantified in a homogeneous nucleation rate coefficient. Classical nucleation theory approximates the critical size of this ice germ based on minimization of a Gibbs free energy which sums volumetric and surface components associated with new phase generation. Then for **heterogeneous nucleation**, there are two freezing paradigms: stochastic or singular [3, 4]. Stochastic freezing is analogous to homogeneous nucleation in that a critical germ size must be formed and time is the controlling variable. Singular freezing is determined by particle surface morphology, i.e., some surface defect or active site that "templates" the ice structure, and once a certain temperature is attained, freezing always occurs.

Atmospheric scientists have also hypothesized that secondary ice production occurs in clouds in the same manner as in industrial crystallizers [e.g., 5, 6]. Large disparities can exist between in-cloud ice crystal and INP numbers at temperatures warm enough that homogeneous nucleation does not occur [7, 8, 9, 10, 11, 12]. A variety of processes have been proposed to explain this difference [13] (Figure 1.2). **Rime splintering** has received the most attention from both measurement and modeling communities. In this process, droplets collide with a sedimenting ice hydrometeor and freeze to form rime, or fragile frozen protuberances, that later splinter off. Then some laboratory measurements have been taken of the mechanical breakup that occurs upon ice hydrometeor collision, analogous to **attrition** in industrial crystallization [14, 15]. Or larger, freezing droplets may shatter due to a latent heat realease and interal pressure build-up.

1.2 Radiative impacts of clouds

The phase and number of in-cloud hydrometeors determine the magnitude of cloud radiative forcing. This cloud radiative forcing is a balance of the reflection of solar ultraviolet (or shortwave) radiation and the absorption of terrestrial infrared (or longwave) radiation (Figure 1.3). General estimates put the cloud longwave forcing at +30 W m^{-2} and the

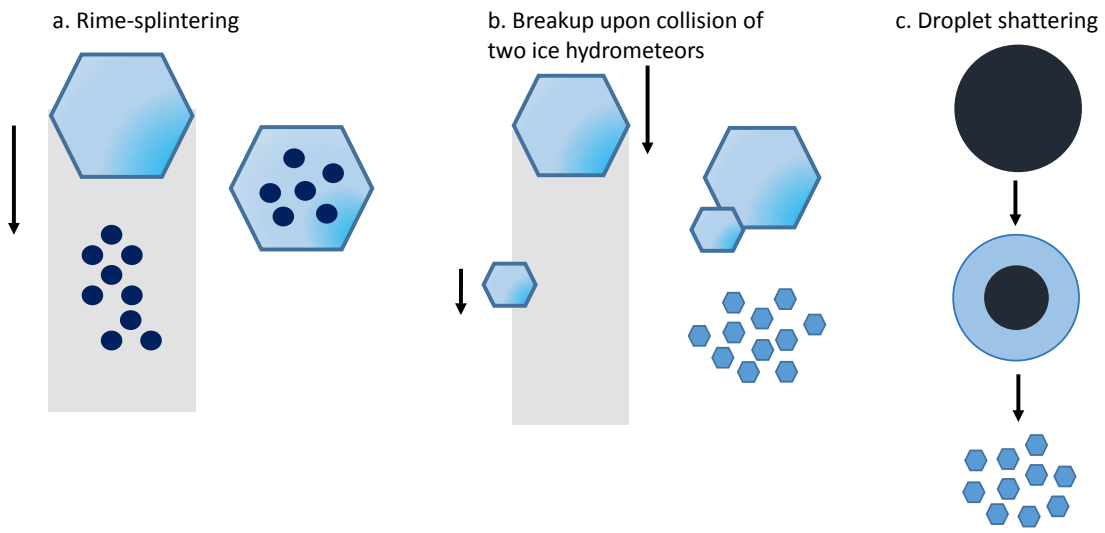

Figure 1.2: Proposed mechanisms for secondary ice production in clouds: ***(a)*** *Droplets may collide with an ice hydrometeor, freezing to rime and forming fragile protuberances that later splinter off,* ***(b)*** *Two ice hydrometeors may collide and their impact leads to shattering, or* ***(c)*** *A larger droplet may freeze from the outside in leading to internal pressure build-up and eventual shattering.*

cloud shortwave forcing at -50 W m^{-2} [16]. Many more atmospheric particles can act as CCN than as INP, so liquid droplets tend to be much smaller and more numerous than ice crystals. As a result, cirrus clouds are optically thinner than cumulus clouds and warm the planet via reduced longwave transmission. In contrast, cumulus cool the surface via shortwave reflection. Generally, any cloud with more and smaller hydrometeors reflects more incoming solar radiation in what is called the **albedo effect** (Figure 1.4). Smaller hydrometeors also stay aloft longer and extend the duration of cloud coverage in the **lifetime effect**.

Finally, more accurate predictions of Arctic stratocumulus SLF and radiative forcing are particularly important. Two-phase clouds are quite prevalent and unexpectedly long-lived at high latitudes [17, 18, 19]. Special feedbacks and extreme meteorological conditions in the Arctic also magnify climate change there [20]. Global sea level will start rising by as much as a centimeter a year if Arctic glaciers and ice sheets continue to melt at current rates [21]. Better estimates of SLF in Arctic clouds will help us to better understand the climate impact of anthropogenic activity in this sensitive region.

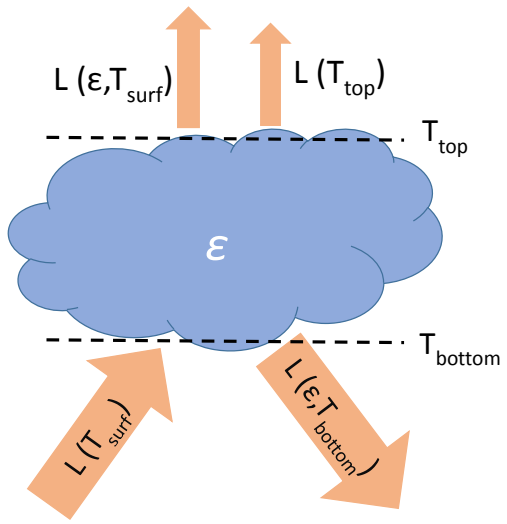

Figure 1.3: Clouds absorb and transmit terrestrial longwave radiation in proportion to their emissivity ϵ, also determined by hydrometeor number and phase. In the schematic, T_{surf} refers to the terrestrial surface temperature, whilt T_{top} and T_{bottom} are the temperatures at cloud top and bottom respectively. L indicates longwave radiation.

1.3 Hydrological impacts of clouds

Clouds also play an important role in the hydrological cycle. First, clouds and atmospheric circulation are intimately connected [22]. The phase changes described above release latent heat, which increases air temperature and buoyancy and drives convection. **Convective invigoration** refers to deeper and wider convective clouds due to the addition of particles that act as CCN or INP and the corresponding latent heat increase [23] (Figure 1.5). The interaction of clouds with solar and terrestrial radiation described above also alters the atmospheric temperature gradient and circulation.

Clouds and atmospheric turbulence are also related through factors like hydrometeor size distributions, entrainment, and hydrometeor collisional efficiency [24]. Small eddies can expose certain droplets to higher supersaturations and broaden the range of droplet sizes or create bimodal size distributions which then alter coalescence efficiencies [e.g., 25, 26]. **Entrainment** refers to the mixing of dry ambient air into the cloud, which can suppress convection, evaporate droplets, or sublime crystals [27].

Of more direct impact for humans is the control of clouds on precipitation. Precipitation may initiate in the liquid phase as droplets grow by collision-coalescence [29]. In

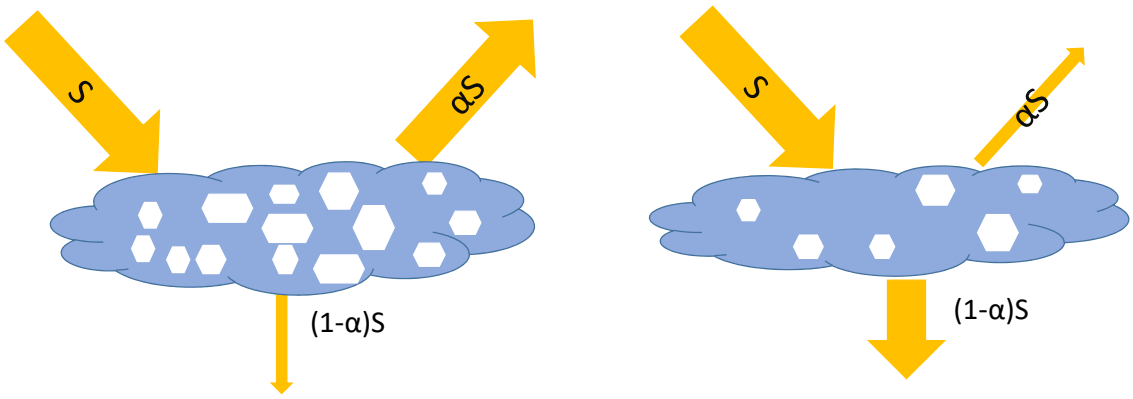

Figure 1.4: Clouds reflect solar shortwave radiation S in proportion to their albedo α, which is determined by the number and phase of hydrometeors that they contain. If there are fewer and larger hydrometeors in the cloud, it is optically thinner and reflects less incoming radiation.

polluted clouds with very many CCN and small droplets, this **warm rain process** can be suppressed, and precipitation may instead initiate in the ice phase, when ice crystals grow to sufficient sizes by the Bergeron process or collection of drops. The **Bergeron process** refers to mass transfer from liquid droplets to ice crystals when the ambient pressure is above the saturation vapor pressure with respect to ice but below that with respect to liquid. When these larger ice hydrometeors fall below the freezing level, they melt to form rain drops. These precipitating clouds tend to be convective with large vertical motions and supersaturations that allow ice crystals to grow large enough and sediment out [30]. Ice phase initiation has been associated with the top 10% of heavier rains according to the Tropical Rainfall Measuring Mission of NASA [31]. The recent study of Mülmenstädt et al. and the older one of Cantrell et al. show that the majority of continental precipitation comes from mixed-phase or ice phase clouds [32, 11]. We return to these ideas in Chapter 7.

Finally, as the atmosphere adjusts to higher concentrations of anthropogenic greenhouse gases, the distribution of precipitation intensity will change: more instances of heavy rainfall and fewer instances of light rainfall are expected [33]. This rain will also be geographically redistributed. In the trend of 'wet gets wetter, dry gets drier', the rain-limited subtropical regions are projected to become more arid in the coming years [34, 35, 36]. Other studies have instead predicted less global precipitation and more widespread aridity under global

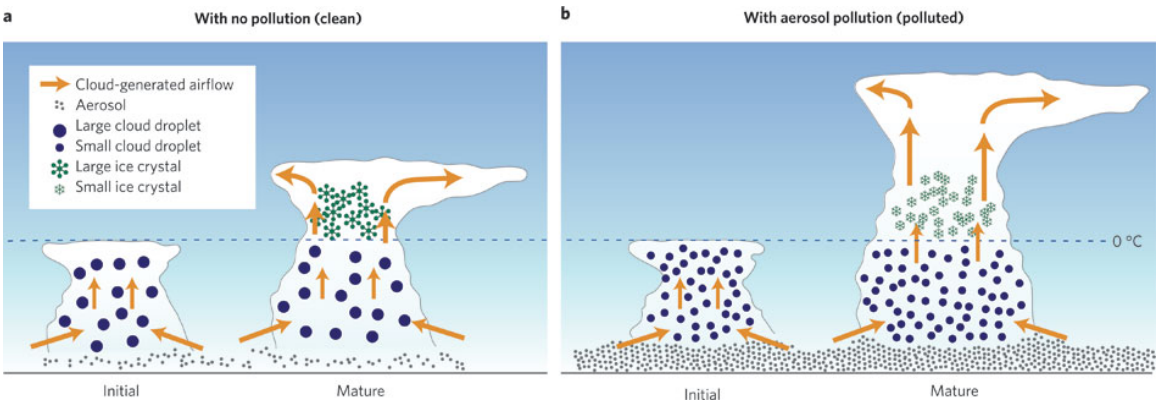

Figure 1.5: ***(a)*** *When there are few aerosol in the boundary layer, fewer droplets form, generating less latent heat and creating a lower cloud top height.* ***(b)*** *When there are many aerosol in the boundary layer, many small droplets form, generating significant latent heat and cloud buoyancy so that the cloud top reaches a much greater height. In this case, cloudy air diverges when it reaches a temperature inversion, and the ice crystals at the top of the cloud spread out into an* ***anvil cirrus*** *with large coverage and warming effect [28].*

warming [37, 38]. Either case threatens food supplies and the livelihood of farmers.

1.4 Multi-scale atmospheric modeling

Given the scale problem and highly coupled nature of the cloud system (Figure 1.6), the next question is what techniques are most appropriate to gain insight. First, development of accurate cloud parameterizations involves engineering principles through a balance of scientific accuracy and computational efficiency. Fundamentally, a cloud can be represented by the coupled set of differential equations for mass and energy within its control volume. But these are currently too computationally expensive for use in a large scale model. Indeed, to resolve the turbulence that initiates cloud formation, a spatial resolution of about 10 m is needed [39], corresponding to a 10^8-fold increase in the current number of GCM grid cells. This increase will be achievable by 2060 if computing power continues to double every 1.2 years or so. In the mean time, appropriate approximations must be made for parameterizations within large frameworks.

Along with a balance of accuracy and efficiency, this work employs multi-scale modeling. Reductionist and systemic apporoaches exist for systems with multiple, non-linear linkages [40]. The former approach isolates a few processes and seeks to understand them in detail. The latter recognizes that the system may exhibit emergence and instead seeks to clarify

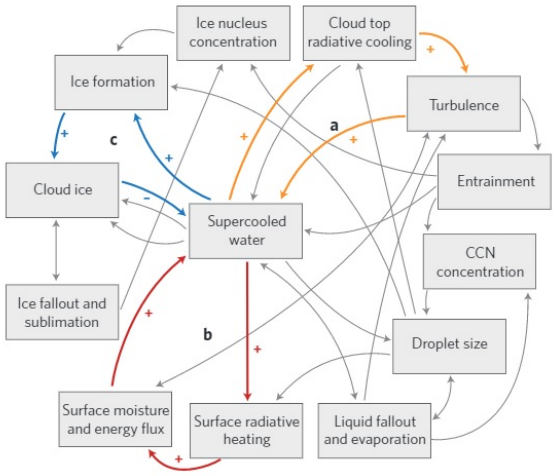

Figure 1.6: Numerous, non-linear relations exist between small-scale cloud properties, radiation, and circulation. A plus sign indicates an increase in the end quantity, and a minus sign indicates a decrease [40].

large-scale behavior. These philosophies may also be understood as bottom-up and top-down, and they are discussed again in Chapter 9. Below, the first two objectives take a systemic approach, and the last two take a reductionist approach. Some details of the frameworks used in both cases are given first.

1.4.1 Large scale models

Weather and climate models discretize space and time and solve the mass, energy, and momentum balances on this grid. The numerical solutions for atmospheric flow are called the **dynamical core**. Clouds and aerosol are components of the physics package of the model. Typically a **bulk cloud microphysics scheme** assumes some functional form for the hydrometeor size distributions [41, 42, 43]. These are computationally cheaper than spectral schemes, used in the past, that would discretize these distributions into many bins [e.g., 44]. Bulk cloud schemes may be one- or two-moment by calculating only the mixing ratio or both the number and mixing ratio from these hydrometeor size distributions. Aerosols affect the cloud through droplet or crystal number rather than mixing ratio, so two-moment schemes distribute cloud water more appropriately between liquid and ice phases and calculate radiative forcings more accurately. A typical two-moment bulk scheme includes nucleation and activation of atmospheric particles to small ice crystals and liquid

droplets; condensation, deposition, evaporation, or sublimation between ambient vapor and hydrometeors; autoconversion of droplets or crystals to rain or snow; accretion of droplets or crystals onto either rain or snow; heterogeneous or homogeneous freezing of droplets to crystals; and entrainment or detrainment of surrounding air [42].

1.4.2 Clouds in the earth system

Within these larger scale models, particularly earth system models, the dynamical core and physics package with its cloud microphysics scheme exist in the atmospheric model, along with descriptions of gas and aerosol phase chemistry and aerosol advection and deposition. But this atmospheric model is only one of several component models. As shown in Figure 1.7, land, ice, and ocean models are also part of the larger model framework, which is held together by a **coupler**. This coupler allows each component model to run at its own spatial and temporal resolution and maintains appropriate flow of data between the components. If a change is made to one component model, the others need not be recompiled. Radiative and aerosol inputs are given to the atmospheric component, which then outputs the atmospheric state, including variables like horizontal wind, carbon dioxide concentrations, and in-cloud ice crystal number, to the coupler. There are numerous ways in which these atmospheric variables interact with those of the other component models. For example, the land albedo generates differential surface heating, which drives convection and determines the strength of the vertical velocities discussed throughout this work. Sea salt concentrations from the ocean model affect concentrations in the overlying air, which alters the CCN and droplet number concentration in clouds. Or the melting of sea ice reveals more ocean surface which increases evaporative fluxes and water vapor concentrations in the atmosphere.

1.4.3 Parcel and process models

Small-scale models give insight not easily obtainable from comprehensive but complicated, large-scale frameworks. They can be used for interpretation of in-situ or remote sensing data [e.g., 45, 46], or they can be used to investigate subgrid phenomena like the effect of entrainment on the droplet size distribution mentioned above. They are also a good testbed for parameterization development [47, 48, 49].

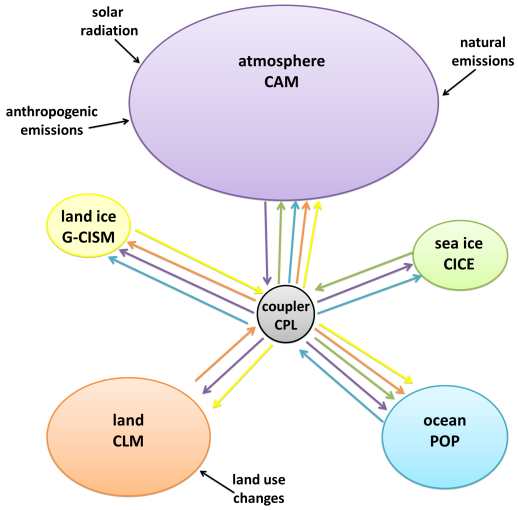

Figure 1.7: Schematic showing how the atmospheric component (e.g., the Community Atmosphere Model, CAM) of a larger earth system model. Emissions inventories, both natural and anthropogenic, and the solar spectrum are input to the atmospheric component, and the outputs are, in turn, input to a coupler

A parcel model represents an adiabatic control volume containing ice crystals, liquid droplets, or both suspended in moist air. It can take either a Lagrangian perspective in which the control volume flows along with the ambient air or an Eulerian perspective in which the control volume is fixed and the ambient air and hydrometeors flux through its boundaries. Then differential mass and energy balances are solved for the system. Process models isolate a few microphysical pathways or cloud properties and disentangle their effect on one another, also in some control volume, perhaps a single grid cell or atmospheric column of the GCM. For example, the feedbacks colored in red, blue, and gold in Figure 1.6 might be elucidated by isolating only on the involved elements of the larger system.

1.5 Particular objectives

Given the radiative and hydrological impact of clouds, and particularly of ice formation therein, this thesis considers the model representation of ice formation in several frameworks. We address the following questions:

1. Is there a novel and efficient means of comparing output ice crystal number concentration (ICNC) from various ice nucleation parameterizations in GCMs?

(a) Do different parameterizations predict different nucleation efficiencies or regimes? If so, why?

(b) Are there consistent differences between lab and field data based nucleation parameterizations?

(c) To which input variable(s) is the output ICNC most sensitive? Does this change with season or averaging?

2. Is there a novel and efficient means of attributing temporal variability of output ICNC to various inputs in GCMs?

   (a) Do dynamical or aerosol inputs induce more of the temporal variability in output ICNC?

   (b) Does this vary with GCM framework? If so, why?

   (c) If temporal variability can be attributed mostly to a single input, is it because this input has large temporal fluctuations or because the output is highly sensitive to any fluctuations in that input?

3. What could be the ICNC enhancement from secondary production within a parcel model?

   (a) Which meteorological conditions promote secondary production?

   (b) How much do ice hydrometeor non-sphericity and turbulence alter secondary production rates?

   (c) Can enhancements of the order observed in-situ be generated from breakup upon mechanical collision of ice crystals?

   (d) What is the fewest number of primarily nucleated crystals needed to initiate secondary production?

4. How does inclusion of secondary production affect ICNC and precipitation from a mesoscale model?

(a) Are enhancements of the same order as in a parcel model calculated in a mesoscale model?

(b) Does inclusion of secondary production bring modeled and measured ICNC into better agreement?

(c) Does inclusion of secondary production bring modeled and measured precipitation intensity into better agreement?

CHAPTER 2

ADJOINT MODELS FOR GLOBAL-SCALE SENSITIVITY ANALYSIS

In this chapter, the concept of climate sensitivity and techniques for sensitivity analysis are discussed. Then the construction of the adjoint of an ice nucleation parameterization is detailed. This adjoint is an efficient kind of gradient model that computes the partial derivative of nucleated ICNC with respect to all input variables. We then run this adjoint with inputs from the NCAR Community Atmosphere Model Version 5.1 (CAM5) to understand the spatial distribution in ICNC sensitivities. A key finding is that ICNC is highly sensitive to both sulfate number concentrations and vertical motions in the tropics.[1]

2.1 Climate sensitivity

The concept of sensitivity appears frequently in climate and atmospheric sciences. **Climate sensitivity** can be understood as a system gain in a process control context. Figure 2.1 shows that the atmosphere, or larger earth system, receives input solar radiation and acts upon it in a series of physical processes which yield some output radiation R. These outputs feed back on the system with some gain λ and subject to external control actions, or anthropogenic forcing, $\Delta\epsilon$ [51].

The output adjustment in radiation can be decomposed like

$$\begin{aligned} \Delta R &= \frac{\partial R}{\partial \epsilon}\Delta\epsilon + \left(\frac{\partial R}{\partial T} + \sum_{j=1}^{n} \frac{\partial R}{\partial X_j}\frac{\partial X_j}{\partial T}\right)\Delta T \\ &= \frac{\partial R}{\partial \epsilon}\Delta\epsilon + \lambda\Delta T. \end{aligned} \tag{2.1}$$

where T is temperature and X_j represent physical climate processes. Then if the system is in equilibrium, the output adjustment in radiation is zero, and climate sensitivity can be

[1] This work has been published as B. A. Sheyko, **S. C. Sullivan**, et al. (2015) Quantifying sensitivities of ice crystal number and source of ice crystal number variability in CAM 5.1 using the adjoint of a physically-based cirrus formation parameterization [50]. Figures identical to those in this publication are used here. While much of the writing and simulations were done jointly with the first author, I produced all final figures in the publication myself.

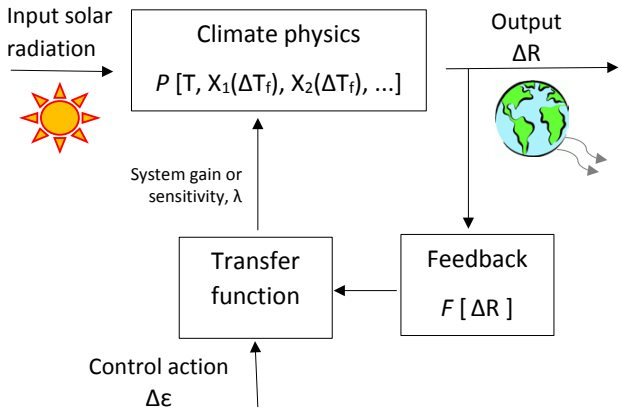

Figure 2.1: The climate system can be understood with control theory. It receives input solar radiation and acts upon it in a series of physical processes X, yielding an adjusted terrestrial radiation. This output feeds back on the system, and anthropogenic activity is a control action $\Delta\epsilon$ which modulates the output adjustment in future iterations. Figure adapted from [51].

defined as

$$\lambda_{eq}^{-1} = -\frac{\Delta T}{\partial R/\partial \epsilon \, \Delta \epsilon} \tag{2.2}$$

The IPCC uses this definition to estimate the change in equilibrium global mean surface temperature as a result of doubling atmospheric carbon dioxide concentration [1].

2.2 Sensitivity analysis in cloud schemes

More specifically, within cloud schemes, many studies calculate finite differences in a cloud property for each of a series of variables or parameter in a "one-at-a-time" (OAT) approach, [e.g., 52]. These finite differencing or OAT approaches come at a significant computational cost, since two model runs must be performed for each input. They are also subject to truncation errors, given limited machine precision, and to **approximation error** on the order of the input perturbation when model response is strongly non-linear:

$$\left(\frac{\partial Y}{\partial x}\right)_i = \frac{Y_{i+1} - Y_i}{\Delta x} - \frac{\Delta x}{2}\left(\frac{\partial^2 Y_i}{\partial x^2}\right)_i - \frac{(\Delta x)^2}{6}\left(\frac{\partial^3 Y_i}{\partial x^3}\right)_i + \ldots$$

Nevertheless this method is often used, given its ease of implementation. For example, Spracklen et al. traced greater uncertainty in cloud droplet numbers to the representation of microphysics than to the input chemical emissions [53]. Gettelman et al. used various

nucleation parameterizations to assess whether the effect of microphysical parameters on ICNC was the same for both present-day and pre-industrial emissions [54].

Sensitivity analysis may also be carried out with a "meta-model" approach, where many GCM simulations are used to constrain a simplified model or **process emulator**. For example, Lee et al. have used this method to construct a mapping of parametric uncertainty onto output CCN number uncertainty in an aerosol microphysics model [55]. Zhao et al. used a Gaussian process emulator to quantify the sensitivity of top-of-the-atmosphere radiative fluxes to 16 microphysical and aerosol parameters in CAM5 [56]. However, these emulators are labor-intensive to construct and require extensive validation.

2.2.1 Adjoint sensitivities

A different (and complementary) adjoint method is used here to provide analytically accurate, local sensitivities at minimal computational cost, [e.g., 57]. If the forward model is designated F and maps the inputs $\mathbf{x}$ onto the outputs $\mathbf{y}$, then finite differencing / OAT uses a **tangent linear model** (TLM) in which an input perturbation $\mathbf{x}'$ is mapped to an output one $\mathbf{y}'$ with the Jacobian matrix in a Taylor approximation:

$$\mathbf{y} = \mathbf{F}(\mathbf{x}) \quad \text{and} \quad \mathbf{y}' = \nabla_x \mathbf{F} \cdot \mathbf{x}' \tag{2.3}$$

Adjoints offer a more computationally efficient possibility if $\mathbf{F}$ is a functional that maps an input vector to an output scalar. If $\mathbf{F}$ is also a real-valued linear operator, its adjoint operator is simply its transpose $\mathbf{F}^T$. Then for sensitivity analysis, the adjoint is the transpose of the Jacobian that maps an output perturbation to perturbations in all inputs:

$$\mathbf{x} = \mathbf{F}^T(\mathbf{y}) \quad \text{and} \quad \mathbf{x}' = \nabla_y \mathbf{F}^T \cdot \mathbf{y}' \tag{2.4}$$

For a numerical model $\mathbf{F}$, like the ice nucleation parameterizations discussed below, operations occur in a finite sequence, and any differentiation must be done sequentially

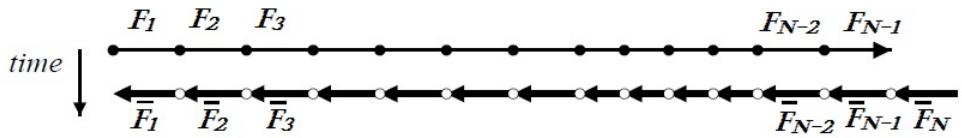

Figure 2.2: Store-all approach for reverse mode AD [58]

with the chain rule:

$$\mathbf{F}(\mathbf{x}) = F_N(F_{N-1}(\dots F_2(F_1(F_0(\mathbf{x}))))) \tag{2.5}$$

$$\mathbf{y}'^{(n)} = \begin{cases} \nabla_{\mathbf{y}^{(n-1)}}\mathbf{y}^{(n)} \cdot \mathbf{y}'^{(n-1)}, & N \geq n \geq 1 \\ \nabla_{\mathbf{x}}\mathbf{y}^{n} \cdot \mathbf{x}', & n = 0 \end{cases} \tag{2.6}$$

Automatic differentiation (AD) can be used to calculate derivatives from such a discrete sequence of operations. AD stores both normal variables $\mathbf{x}$ and their differentials d$\mathbf{x}$ as the sequence progresses. But as shown in Equation 2.6, the $(n-1)$-th differential is needed to calculate the n-th differential, the $(n-2)$-th differential is needed to calculate the $(n-1)$-th differential and so on. This issue is addressed with a Store-All approach shown in Figure 2.2: the model state is stored in a stack after each operation and then the values are popped off in reverse to evaluate differentials. This approach is fast but memory-intensive. Model non-linearity may also be a concern in some cases, but generally, the output perturbation can be sufficiently small that assuming linearity is appropriate.

Adjoints have been developed in our research group to understand liquid cloud sensitivities [59]. These models showed that uncertainty in CCN concentration translates to as much as 70% uncertainty in droplet numbers in pristine regions and only about 10% uncertainty in more polluted regions [60]. Morales and Nenes also determined that discrepancies in droplet formation parameterizations were due in large part to their treatment of water uptake by coarse mode particles [61]. Outside of sensitivity analysis, our group has used adjoints for data assimilation in chemical transport models [62, 63]; however, adjoint sensitivities have not yet been used to study the cloud ice phase. We describe construction of the adjoint model of the Barahona and Nenes ice nucleation parameterization [64, 65, 66] (BN09), its implementation in CAM5, and some sensitivity results below.

2.3 Primary ice nucleation codes

2.3.1 Barahona and Nenes ice nucleation parameterization

BN09 describes the competition for water vapor between homogeneous and heterogeneous nucleation. Homogeneous nucleation is represented by an approximate solution to the mass and energy balances of an ascending adiabatic air parcel. Several assumptions are made to obtain an analytical solution: newly-formed crystals have negligible impact on supersaturation before the maximum supersaturation $s_{i,max}$ is reached; the nucleation rate coefficient J is proportional to its value at the maximum supersaturation $J(s_{i,max})$; and the supercooled droplet size distribution is lognormally distributed.

Heterogeneous nucleation is represented by a case structure which runs various **nucleation spectra** $N_{het}(s_i)$ (Table 2.1). The most basic formulations depend solely on supersaturation, but more sophisticated ones incorporate aerosol surface area for different kinds of aerosols like dust and black carbon [67, 68, 69]. Various nucleation spectra are discussed in greater detail in Section 3.1. A bisection method is used to calculate the maximum supersaturation according to Equation 2.7, which is derived from the ice crystal growth equation and supersaturation evolution:

$$0 = N_{het}(s_{i,max}) - \frac{N^*(1 + s_{i,max})e^{2/(\lambda_i \ s_{i,max})}}{\sqrt{\Delta s_{char}}} \tag{2.7}$$

where N^* and λ_i are combinations of thermodynamic variables and Δs_{char} is the difference between ambient and threshold supersaturation for a given INP. Finally, the total ice crystal number concentration N_i is calculated as a sum of heterogeneously and homogeneously formed values:

$$N_i = \begin{cases} N_{i,hom} + N_{i,het}(s_{hom}), & s_{i,max} = s_{hom} \\ N_{i,het}(s_{i,max}), & s_{i,max} < s_{hom} \end{cases} \tag{2.8}$$

Conceptually, the active modes of ice nucleation can be understood with the **INP-N_i trace** in Figure 2.3. When the INP number exceeds a certain threshold N_{lim}, homogeneous nucleation will be suppressed because it is energetically favorable to form ice heterogeneously. In this case, or when the temperature is too warm for homogeneous nucleation,

Table 2.1: Heterogeneous nucleation spectra in BN09

Spectrum name		**Functional form** ($N_{het}(s_i)$)
Meyers et al. (1992)	Mey92 [67]	$10^3 e^{-0.639+12.69 s_i}$
Barahona and Nenes (2009)	CNT [66]	$0.05[\min(\frac{s_i}{0.2} N_{dust} e^{-0.0011\, k_{hom}(0.2-s_i)}, N_{dust}) + \min(\frac{s_i}{0.3} N_{soot} e^{-0.039\, k_{hom}(0.3-s_i)}, N_{soot})]$
Phillips et al. (2013)	PDA13 [69]	$N_{dust}[1-\exp(-\frac{2}{3} H_{dust}(s_i,T) n_{IN,*} \frac{N_{het,PDG07}}{2\times10^{-6}})] + N_{soot}[1-\exp(-\frac{82}{300} H_{soot}(s_i,T) n_{IN,*} \frac{N_{het,PDG07}}{1\times10^{-7}})] + N_{solo} \frac{18}{300} \frac{H_{solo} g_{glass}}{5.6\times10^{-6}}$

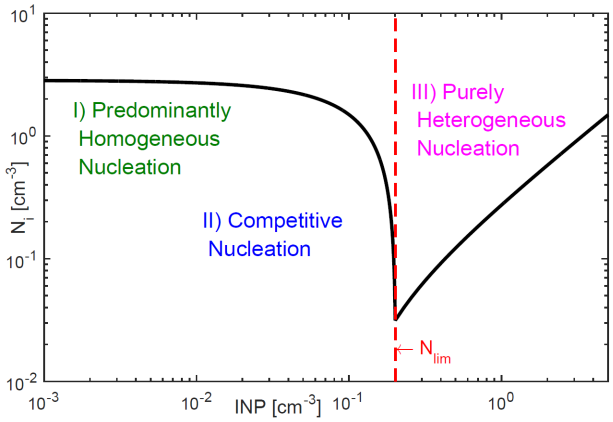

Figure 2.3: INP-N_i trace to understand when homogeneous, heterogeneous, or competitive nucleation occur within cirrus clouds.

T $\gtrapprox$ 235 K, BN09 sees only the case structure for nucleation spectra. If the INP number is instead quite low, predominantly homogeneous nucleation occurs, while at intermediate INP numbers, both homogeneous and heterogeneous nucleation occur simultaneously.

2.3.2 Adjoint of the ice nucleation parameterization

From the framework summarized in Equation 2.8, the TAPENADE automatic differentiation (AD) tool was used to construct the adjoint of BN09 (ABN09) [70, 58]. During this process, TAPENADE AD cannot handle the bisection to calculate $s_{i,max}$ mentioned above because it has no continuous functional form. To circumvent this discontinuity, a

post-convergence Newton-Raphson step is taken [71, 63]:

$$s_{i,max}^{NR} = s_{i,max}^{B} - \frac{f(s_{i,max}^{B})}{\left.\frac{\partial f(s_{i,max})}{\partial s_{i,max}}\right|_{s_{i,max}^{B}}} \tag{2.9}$$

where $s_{i,max}^{B}$ is the maximum supersaturation obtained after a bisection on Equation 2.7 converges and $s_{i,max}^{NR}$ is the maximum supersaturation resulting from the Newton-Raphson step away. $f(s_{i,max}^{B})$ is Equation 2.7 and $\partial f(s_{i,max})/\partial s_{i,max}$ is the TLM of Equation 2.7 (This TLM is also constructed using TAPENADE AD.) The forward model is run once to obtain $s_{i,max}^{B}$, and this value is then fed to the adjoint as an initial guess for the Newton-Raphson step. Although this method assumes that the system is linear over a small interval in supersaturation, the Newton-Raphson step creates an explicit functional relationship between $s_{i,max}$ and the parameterization inputs so that differentiation can occur.

The final functional form of ABN09 is

$$\begin{aligned}
\nabla N_i &= \nabla N_i(T, P, V, s_{i,max}^{B}, d_{dust}, n_{dust}, d_{org}, n_{org}, d_{sulf}, n_{sulf}, d_{bc}, n_{bc}, S_p, \alpha_d, \sigma_{sulf}, \sigma_{bc}, \sigma_{dust}) \\
\nabla N_i &= \left(N_i, N_{het}, s_{i,max}, \frac{\partial N_i}{\partial T}, \frac{\partial N_i}{\partial V}, \frac{\partial N_i}{\partial d_{dust}}, \frac{\partial N_i}{\partial n_{dust}}, \frac{\partial N_i}{\partial d_{org}}, \right. \\
&\qquad \left. \frac{\partial N_i}{\partial n_{org}}, \frac{\partial N_i}{\partial d_{sulf}}, \frac{\partial N_i}{\partial n_{sulf}}, \frac{\partial N_i}{\partial d_{bc}}, \frac{\partial N_i}{\partial n_{bc}}, \frac{\partial N_i}{\partial \alpha_d} \right)
\end{aligned} \tag{2.10}$$

where T, P, V, d_{dust}, n_{dust}, d_{org}, n_{org}, d_{sulf}, n_{sulf}, n_{bc}, and d_{bc} are the input temperature, pressure, updraft velocity, and aerosol diameters and numbers; S_p picks a nucleation spectrum from the case structure; α_d is a deposition coefficient; and σ_{sulf}, σ_{bc}, and σ_{dust} are the widths of aerosol lognormal size distributions. The **deposition coefficient** is effectively a fitting parameter to more accurately reproduce the rate of water vapor transport to ice crystals. Flow charts for the BN09 parameterization and ABN09 adjoint are shown in Figure 2.4.

Centered finite differences were computed from BN09 to validate the adjoint sensitivities from ABN09. Perturbation of $\pm$ 0.01% about the mean input state were used for all model variables. These sensitivity comparisons were performed at the 200 hPa pressure level for all grid cells globally at temperatures less than 235 K representative of only cirrus clouds.

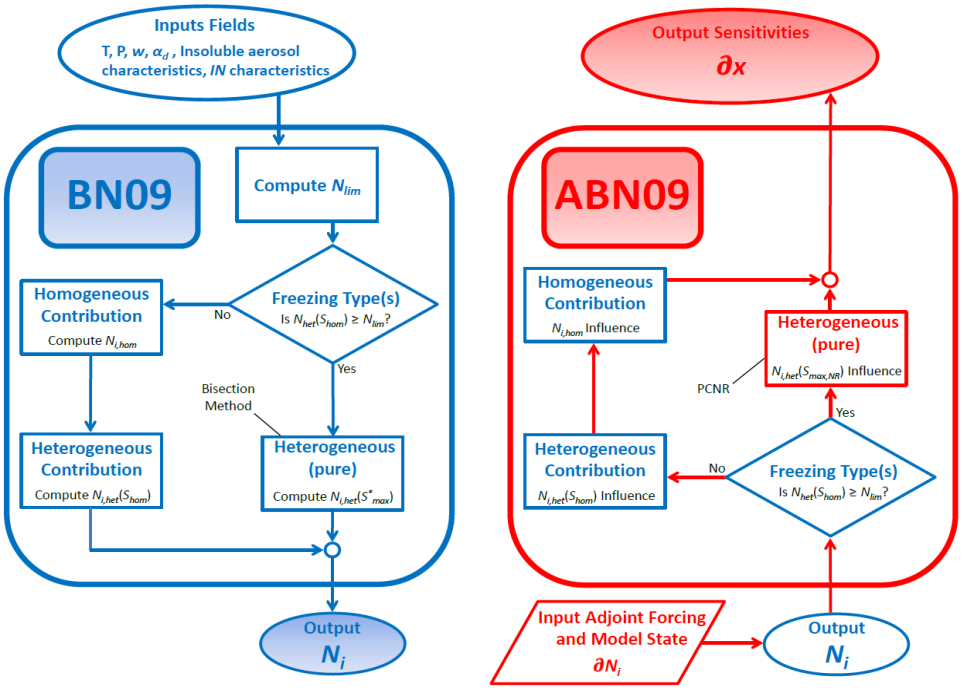

Figure 2.4: Flow chart of BN09 in blue and ABN09 in red. The parameterization takes input fields, computes N_{lim} and then determines contributions of heterogeneous and homogeneous nucleation. The adjoint takes an output perturbation (forcing) and propagates this backward through the call tree to calculate sensitivities.

The relative error between finite difference calculations and adjoint output is defined as the absolute value of their difference normalized by the finite difference sensitivity. These relative errors remain low with an average of 0.92% over all variables. Their individual values, along with a typical range in the input variables, are given in Table 2.2.

2.4 CAM5 simulation setup

Preliminary runs were performed in CAM5, using present-day sea surface temperatures and greenhouse gas mixing ratios. A one-year spin-up and one-year integration were performed with a 30-minute time step and 2.50 x 1.88 degree resolution. The two-moment bulk scheme of Morrison and Gettelman was used to calculate cloud droplet and ice crystal numbers and mixing ratios [42]. α_d was set to 0.7 [72].

In CAM5, **updraft velocity** V , or vertical motion in the cloud, is computed from

Table 2.2: Adjoint and finite difference sensitivity comparison

Input variable		**Range**	**Average Relative Error**
V	[m s^{-1}]	0 - 1	0.01
α_d		0.1 - 1.0	0.01
n_{sulf}	[cm^{-3}]	0 - 25	0
d_{sulf}	[μm]	0.02 - 0.05	1.3×10^{-6}
T	[K]	195 - 235	0.03
n_{bc}	[cm^{-3}]	0 - 0.5	0.01
d_{bc}	[μm]	0.1 - 0.2	8.9×10^{-4}
n_{org}	[cm^{-3}]	0 - 200	0.02
d_{org}	[μm]	0.1 - 0.2	0.02
n_{dust}	[cm^{-3}]	0 - 0.3	4.0×10^{-4}
d_{dust}	[μm]	1.0 - 1.5	2.8×10^{-4}

the local turbulent kinetic energy (TKE) as $V_{sub,i} = \sqrt{\frac{2}{3}\text{TKE}}$ (See Figure 2.5c for updraft magnitude. This formulation and its effects are discussed in more detail in Section 4.4.2.) For a more realistic representation of the subgrid variability of these motions, we use this value as the standard deviation $\sigma_{sub,V}$, for a Gaussian updraft velocity distribution with the mean velocity set to zero [73, 74, 75, 76]. We use this distribution to weight outputs and sensitivities:

$$\overline{f(V)} = \frac{\int_0^\infty f(V)P(V)dV}{\int_0^\infty P(V)dV} \tag{2.11}$$

where $f(V)$ is a model output, $\overline{f(V)}$ is its PDF-averaged value, and $P(V)$ is the Gaussian distribution. A 6-point Legendre-Gauss quadrature is used to numerically evaluate the integral in Equation 2.11. The quadrature weights and abscissae are chosen over the finite interval from a minimum to maximum velocity, which are four standard deviations below and above the mean updraft velocity respectively. These integral bounds are limited to the range 0.001 to 3 m s^{-1}.

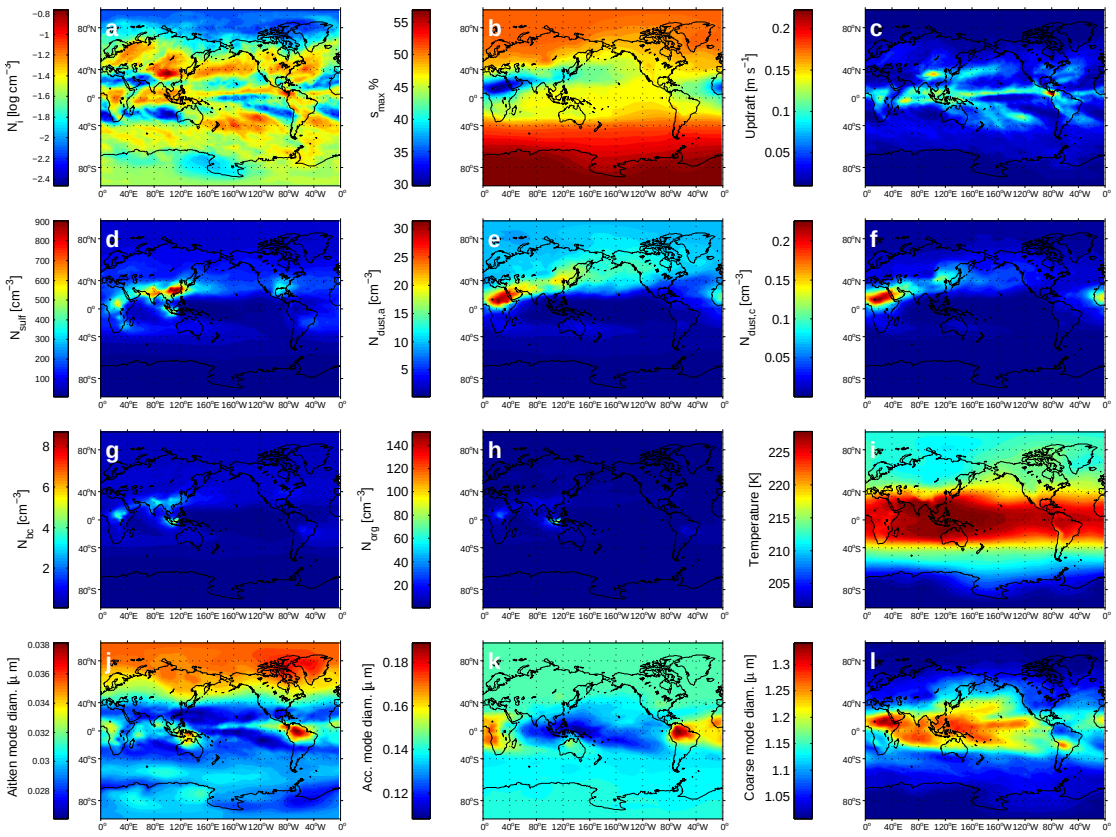

Figure 2.5: Annually-averaged CAM5 cloud formation outputs and inputs; a) Formed crystal number concentration [cm^{-3}], b) Maximum supersaturation, c) Updraft velocity [m s^{-1}], d) Sulfate number concentration [cm^{-3}], e) Accumulation mode dust number concentration [cm^{-3}], f) Coarse mode dust number concentration [cm^{-3}], g) Black carbon number concentration [cm^{-3}], h) Organic carbon number concentration [cm^{-3}], i) Temperature [K], j) Aitken mode geometric mean diameter [μm], k) Accumulation mode geometric mean diameter [μm], l) Coarse mode geometric mean diameter [μm].

Then the Lamarque et al. emissions inventory was used for input reactive gas and aerosol concentrations, and the Modal Aerosol Module version 3 (MAM3) with three, internally-mixed lognormal modes (Aitken, accumulation, and coarse) was used to treat subsequent aerosol chemistry and physics [77, 78]. Sulfate aerosol is assumed to be soluble and present in the Aitken mode. Dust is present in the accumulation and coarse modes, and black and organic carbon species in the accumulation mode only. The widths of the lognormal distributions are fixed, and the number concentration of a certain aerosol in each mode was determined by scaling the total aerosol number concentration in that mode by its mass fraction [61]. These aerosol specifications are outlined in Table 2.3.

Table 2.3: Aerosol characteristics in CAM 5.1 simulations

Species	**Size modes**	**Number conc.** [cm^{-3}]	$\mu_{\mathbf{X}}$ [μm]	$\sigma_{\mathbf{X}}$ [μm]
Sulfate	Aitken	20.0–950.0	0.02–0.04	2.3
Black carbon	Accumulation	0.0–9.0	0.1–0.2	1.8
Organic carbon	Accumulation	10.0–150.0	0.1–0.2	1.8
Dust	Accumulation	0.0–35.0	0.1–0.2	1.8
Dust	Coarse	0.0–0.23	1.0–1.5	1.6

2.5 GCM results from initial implementation

2.5.1 Primary ice nucleation in the GCM

Spatial distribution of the ice nucleation parameterization inputs and output during the CAM5 simulation are shown in Figure 2.5 at a pressure level of 232.6 hPa, the lowest altitude at which cirrus clouds formed somewhere at each integration time step. The output N_i is calculated at all grid cells and all time points and represents a maximum "cirrus potential," i.e., an $N_{i,max}$ if sufficient supersaturation with respect to ice were always generated. This $N_{i,max}$ is shown in log space in panel (a) of Figure 2.5. It reaches an overall maximum of 0.192 cm^{-3} over the tropics where deep convection produces high supersaturations and the contribution of homogeneous nucleation is largest. N_i decreases in the middle and higher latitudes but remains correlated with updraft velocity.

However, the correlation of N_i and updraft can be modulated by aerosol particles. This can be seen by comparing panels (a) and (e) in Figure 2.5 in regions of the Saharan outflow: this region is close to the tropics with strong updrafts of about 0.15 m s^{-1} but N_i remains only about 0.05 cm^{-3}. The high dust concentrations inhibit supersaturation development and reduce the homogeneously formed N_i. The modulation of the N_i-V relation is shown even more clearly in Figure 2.6. N_i is plotted against V with points colored and sized by the corresponding dust number concentration. As the dust loading gets high for the red dots, increasing updraft yields a smaller increase in N_i than when this dust loading is low for the blue dots.

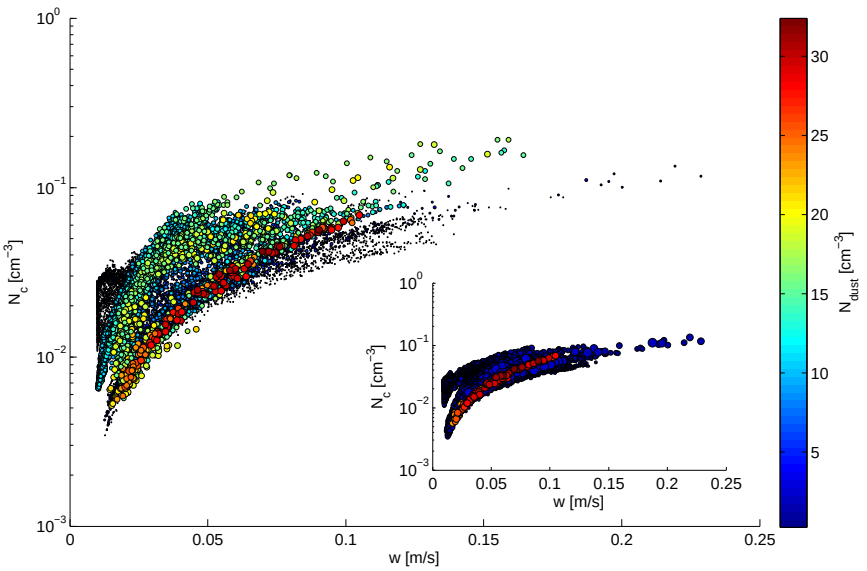

Figure 2.6: Global annually averaged CAM 5.1 formed crystal number concentration [cm^{-3}] vs. updraft velocity [$m\ s^{-1}$]. Points are colored and sized by the sum of the accumulation and coarse mode dust number concentration [cm^{-3}]. In the subplot, dust number concentrations between 5 and 22 cm^{-3} have been removed to illustrate the maximum influence of insoluble aerosol on N_i.

2.5.2 Primary ice nucleation sensitivity in the GCM

Figure 2.7 shows the spatial distribution of sensitivities produced by ABN09. These are again at the 232.6 hPa pressure level and calculated with the input fields of Figure 2.5. The sensitivities are presented as an annual mean over the daily sensitivities output during the year-long integration.

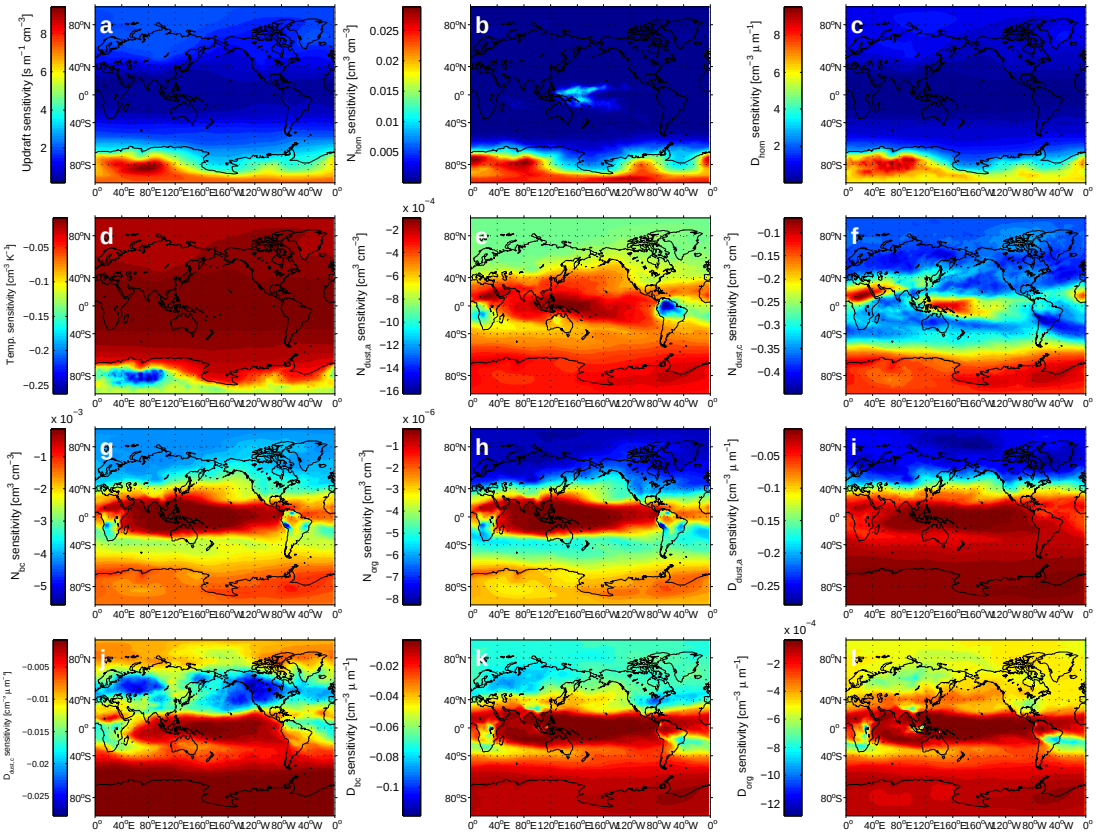

Figure 2.7: Annually averaged CAM 5.1 cloud formation sensitivities; a) Updraft velocity [cm^{-3} $m^{-1}s$], b) Sulfate number concentration [cm^3 cm^{-3}], c) Sulfate geometric mean diameter [$cm^{-3}\mu m^{-1}$], d) Temperature [cm^{-3} K^{-1}], e) Accumulation mode dust number concentration [cm^3 cm^{-3}], f) Coarse mode dust number concentration [cm^3 cm^{-3}], g) Black carbon number concentration [cm^3 cm^{-3}], h) Organic carbon number concentration [cm^3 cm^{-3}], i) Accumulation mode dust geometric mean diameter [$cm^{-3}\mu m^{-1}$, j) Coarse mode dust geometric mean diameter [$cm^{-3}\mu m^{-1}$], k) Black carbon geometric mean diameter [$cm^{-3}\mu m^{-1}$], l) Organic carbon geometric mean diameter [$cm^{-3}\mu m^{-1}$]

Panel (a) shows sensitivity to updraft velocity. If nucleation is predominantly homogeneous, additional generation of supersaturation from an increase in V yields a very large increase in N_i, e.g., over Antarctica. Here insoluble aerosol, and hence INP, concentrations are low and temperatures are coldest. $\partial N_i/\partial V$ becomes as large as 9 cm^{-3} m^{-1} s. This magnitude can be interpreted to mean that a 1 m s^{-1} increase in updraft generates 9 cm^{-3} more ice crystals in a given air parcel. In the Northern Hemisphere (NH) where insoluble aerosol concentrations are higher than the Southern Hemisphere (SH), $\partial N_i/\partial V$ drops to 3 cm^{-3} m^{-1} s: here both homogeneous and heterogeneous nucleation occur. Even when

homogeneous nucleation is completely inhibited; however, N_i and V are related through the modification of $s_{i,max}$. Strong updrafts increase $s_{i,max}$ and more of the limited insoluble aerosol number are able to act as INP. The modulation of the N_i-V relationship mentioned above can be seen again in low updraft sensitivities in the Saharan outflow where dust concentrations are high.

Sensitivities to sulfate number, n_{sulf}, and temperature, T, are shown in panels (b) and (d) respectively. Regions of high $\partial N_i/\partial n_{sulf}$ overlap with those of high $\partial N_i/\partial V$ because both are crucial to homogeneous nucleation: soluble sulfate allows formation of the supercooled liquid droplets in which an ice germ can form. $\partial N_i/\partial n_{sulf}$ values are always positive because soluble aerosol cannot depress supersaturation the way insoluble aerosol, as INP, can. Its magnitude can be as much as 0.025 cm^3 cm^{-3}, meaning that a unit increase in input sulfate number concentration will increase N_i by 0.025 cm^{-3}. Another important aspect of the $\partial N_i/\partial n_{sulf}$ field is its regional maximum in the tropics. This region is sulfate-limited: although there is adequate supersaturation provided by strong updrafts, the lack of sulfate aerosol for supercooled droplet formation inhibits ice nucleation.

Patterns in temperature sensitivities $\partial N_i/\partial T$ again mirror those in $\partial N_i/\partial n_{sulf}$ and $\partial N_i/\partial V$ with the highest magnitudes in regions of predominantly homogeneous nucleation. The similarity of these fields reflects the interdependence of these variables for homogeneous nucleation. The largest influence of T is through the per-volume homogeneous nucleation rate, which increases by orders of magnitude with decreasing temperature [79]. Another important effect will be through the diffusivity of water vapor in air which is proportional to T. At higher temperatures, water vapor is transported faster to growing crystals and supersaturation is depleted more quickly during cloud formation.

Insoluble aerosol number sensitivities are shown in panels (e), (f), (g), and (h). In general, these values are negative because when nucleation is competitive, increasing insoluble aerosol number may shut down homogeneous nucleation and decrease overall N_i. The magnitude of the values reflects the efficiency of the given aerosol species at depleting water vapor. Coarse mode dust number concentration sensitivities are largest around -0.4 cm^3 cm^{-3}, meaning that addition of 1 dust particle per cm^3 reduces N_i by 0.4 cm^{-3}. The large surface area of these coarse mode particles makes them particularly efficient at nucle-

ating ice. Especially in lower-latitude regions where updraft generates more than sufficient supersaturation, N_i can be influenced significantly by fluctuations in $N_{dust,c}$.

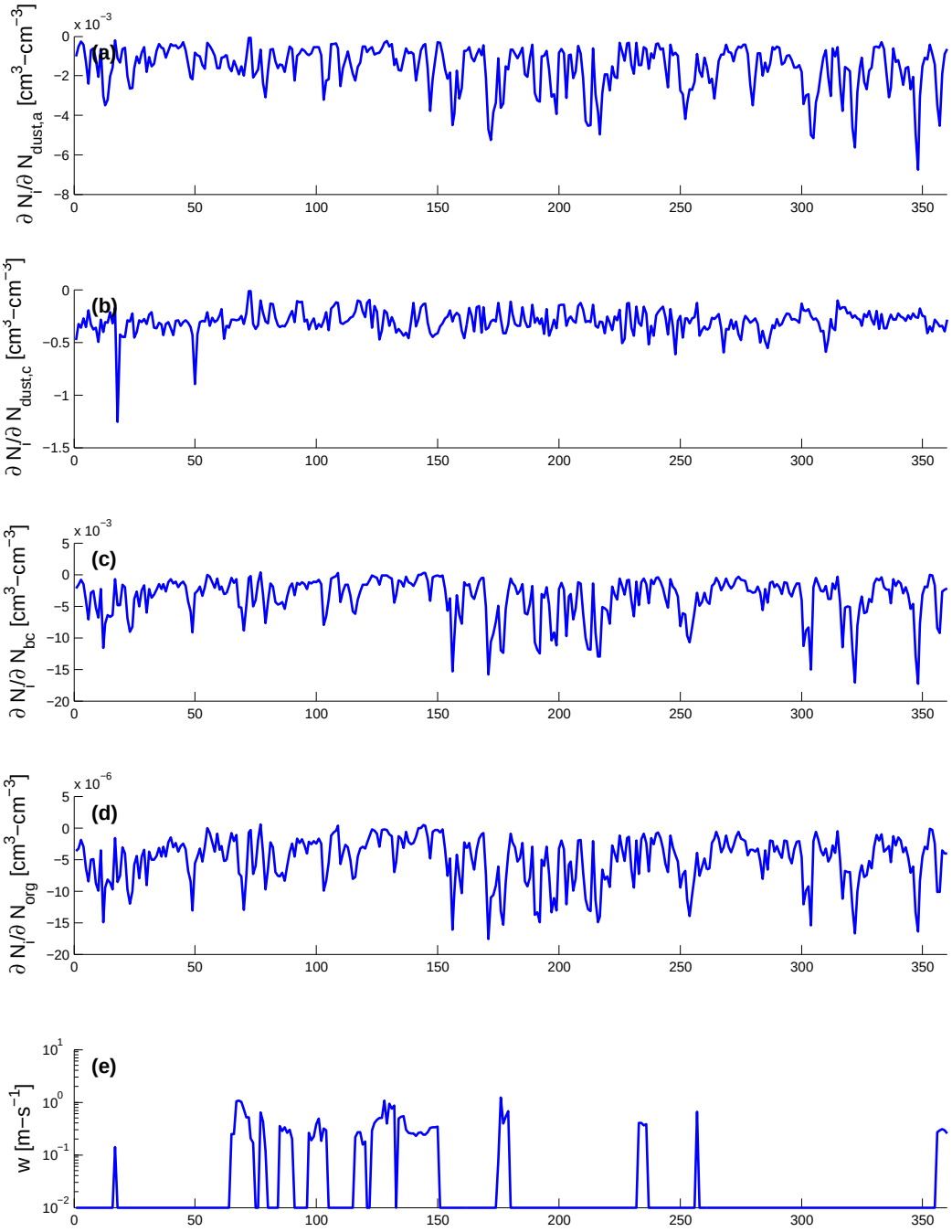

Figure 2.8: Time series of insoluble aerosol number concentration sensitivities and updraft velocity from regions of negative annually-averaged sensitivity. Sensitivities are presented in [cm^3 cm^{-3}] and updraft velocity in [$m\ s^{-1}$].

An additional important feature of the insoluble aerosol number sensitivities is their

hemispheric divide. In the NH, they have higher magnitude because the system is sitting in the competitive freezing "cusp" along the INP-N_i trace in Figure 2.3; the insoluble aerosol number in the NH is only slightly less than N_{lim}. In the SH, insoluble aerosol number concentrations are lower, and competitive nucleation less frequent, because of greater ocean coverage and reduced anthropogenic activity.

Occasionally there are localized regions around the equator of very negative insoluble aerosol number sensitivity. To understand this behavior, it is necessary to consider the time series of sensitivities from the grid cells where the anomalous behavior occurs. These are shown in Figure 2.8 and are negative of small magnitude for about 70% of the year. The other 30% of the year, however, the sensitivities are negative of quite large magnitude, reflecting competitive nucleation. The large effect of these outliers on the annually averaged sensitivities of N_i indicates that temporal averaging should be done with care. Comparing the $\partial N_i/\partial n_{\mathrm{INP}}$ series with that of input updraft velocity, we find that instances of large sensitivity correspond well to updraft maxima. This realization lead to the temporal attribution study in Chapter 4.

2.6 Chapter 2 Summary

If the earth and atmosphere system is considered in a process control context, then the concept of climate sensitivity, λ, corresponds to a system gain. Some external, anthropogenic forcing can be translated to an output adjustment in radiation, and hence surface temperature, using this factor. As clouds are a highly uncertain component of this control system, sensitivities of output cloud properties to various inputs have already been calculated with finite differences or emulation. We propose adjoint sensitivity analysis as an alternative method with greater computational efficiency and less developmental overhead.

The adjoint technique was applied to an ice nucleation parameterization using automatic differentiation tools and then implemented on the global scale in the Community Atmosphere Model. A year-long simulation was run, and the spatial and temporal patterns of output N_i and its sensitivities were analyzed. Sensitivities to updraft velocity, sulfate number, and temperature were largest over Antarctica where most nucleation is homoge-

neous. These factors are interdependent and requisite for nucleation from the supercooled liquid phase. A sulfate-limited regime in the tropics was also identified. Sensitivities to insoluble aerosol numbers reflect the efficiencies of different kinds of particles in nucleating ice heterogeneously. Their time series indicate that care must be taken in annual averaging of sensitivities, given occasional, anomalously large values associated with competitive nucleation. In the next chapter, these results are expanded upon by comparing output from four different representations of which airborne particles can nucleate ice heterogeneously.

CHAPTER 3
ASSESSING PARAMETERIZED ICE NUCLEATION REGIME AND EFFICIENCY

In this chapter, the ABN09 model developed in the last chapter is used to understand the cause of temporal and spatial variability in nucleated ice crystal number for various nucleation spectra. Along with minimizing parametric uncertainty, decomposing N_i variability is key to improving the representation of cirrus clouds in climate models. To this end, sensitivities of N_i to aerosol number and size can classify and quantify nucleation regime and efficiency respectively. Simulations are done with a theoretically derived nucleation spectrum, a lab data-based one, and two field data-based ones that differ in the supersaturation threshold for black carbon aerosol and in the active site density for dust. A key finding is that the lab data-based spectrum calculates much higher INP efficiencies than the field data-based ones.[1]

3.1 Heterogeneous nucleation spectra

As discussed in Section 1.1 and throughout Chapter 2, ice crystals in cirrus clouds may be formed by homogeneous or heterogeneous nucleation. In homogeneous nucleation, crystals form directly from an aqueous phase, typically at temperatures below about 235 K, while heterogeneous nucleation requires an INP surface [81]. Heterogeneous nucleation is actually broken down into further modes: in **deposition nucleation**, vapor deposits directly onto an aerosol; in **condensation nucleation**, the aerosol acts first as a CCN and then immediately as an INP; and in **immersion nucleation**, an aerosol submerged for some time in supercooled liquid eventually initiates ice formation. Aircraft measurements of relative

[1]This work has been published as **S. C. Sullivan**, et al. (2016) Understanding cirrus ice crystal number variability for different heterogeneous ice nucleation spectra [80]. Support came from a DOE EaSM and NESSF grants. Two anonymous reviews gave thorough and insightful feedback, in particular about measurement-model comparison. Data in Figure 3.2 below came from Andrew Heymsfield's VIPS and Paul Lawson's TDS measurements aboard the WB57 during MACPEX and from Paul Lawson's F-FSSP measurements aboard the SPEC Learjet during SPARTICUS. Heike Kalesse also provided processed vertical motion data from the SPARTICUS campaign.

humidity and ICNC indicate that heterogeneous nucleation is dominant for synoptic cirrus over North and Central America [82]. But both mechanisms can be active in cirrus clouds, and the competition for water vapor must be included in cirrus formation parameterizations [64, 65, 66, 83].

Much effort has been devoted to studying heterogeneous ice nucleation on a fundamental level [e.g., 84, 85, 86]. Ice nucleation can be understood as the formation of an ice germ in the vicinity of an active site. The nature of active sites is unknown, but current understanding suggests that they promote ordering of the water molecule layers near the particle surface. The **active site density** refers to the number of these sites per unit of aerosol surface area. A particle with more surface area will tend to have more active sites and nucleate at higher temperatures (or lower supersaturations); however, each active site varies in its efficiency, so that contact angle or site density distributions are necessary [87, 88].

Parameterizations of heterogeneous ice nucleation (referred to synonymously as nucleation spectra throughout), such as those in Table 2.1, calculate the heterogeneously formed ice crystal number, N_{het}, as a function of thermodynamic conditions and precursor aerosol properties. Empirical spectra use lab or field data to calculate an active site density. Theoretically based spectra use classical nucleation theory (CNT) and calculate a nucleation rate proportional to the aerosol surface area [e.g., 89, 90, 91, 66, 92]. Surface heterogeneity should also be considered and has recently been represented as a distribution of contact angles [93, 94]. But ice nucleation data is geographically or thermodynamically limited, taken only in localized regions or over a narrow range of temperatures and pressures. And classical nucleation theory is approximate and requires unknown or variable surface property data. As a result, the output of INP spectra has remained uncertain, with up to three orders of magnitude difference in calculated N_i [e.g., 95].

Early published INP spectra expressed active site density as a function of only temperature or supersaturation and neglected the aerosol composition and size. For example, Fletcher 1969 proposed a parameterization based solely on temperature, valid down to about 248 K [96]. The Meyers et al. INP spectrum describes deposition and condensation nucleation as a function of supersaturation only [67]. They observed a logarithmic increase in the number of ice-nucleating aerosols with supersaturation with respect to ice.

More recently published INP spectra consider the effects of size distribution and composition of ice-nucleating particles. For example, Phillips et al. 2008 (PDA08) calculates the active site density for mineral dust, black carbon, and hydrophobic organics, constrained with data from the First and Second Ice Nuclei Spectroscopy Studies (INSPECT-1 and -2) and the Cirrus Regional Study of Tropical Anvils and Cirrus Layers - Florida-Area Cirrus Experiment (CRYSTAL-FACE) [68]. Updates have been made in the Phillips et al. 2013 spectrum (PDA13) [69]. PDA08 and PDA13 are based on the singular paradigm discussed in Section 1.1. Several other studies have parameterized nucleation efficiency of mineral dusts or illite powders, using cloud chamber data or optical microscopy [e.g., 97, 98, 99, 91]. Hiranuma et al. have also developed an INP spectrum at cirrus-relevant temperatures, using data on hematite particles from the Aerosol Interaction and Dynamics in the Atmosphere (AIDA) cloud chamber at the Karlsruhe Institute of Technology [100]. This study uses the three aforementioned spectra to describe deposition nucleation. Other empirical spectra and recent heterogeneous ice nucleation experiments are further discussed in the review by Hoose and Möhler [101].

Numerous studies have examined the impact of INP spectrum on nucleated ice crystal number. Using the NCAR CAM version 3, Xie et al. evaluated how predicted cloud type, cloud properties, and radiative balance change based on the INP spectrum [102]. The study compares the Meyers et al. and DeMott et al. 2010 spectra, the latter of which links N_i with the aerosol number of diameter larger than 0.5 μm. DeMott et al. calculated a much lower N_i, and hence a higher liquid water path and lower ice water path for Arctic mixed-phase clouds. Curry and Khvorostyanov have also run the Meyers et al., DeMott et al. 1998, Phillips et al. 2008, and their own theoretical INP spectra with parcel model simulations over a range of thermodynamic conditions [103]. Barahona et al. compared the output crystal number between PDA08, Meyers et al., Murray et al. 2010, and the Barahona and Nenes CNT spectrum for both monodisperse and polydisperse aerosol [95]. They found that ice nucleation occurred more often in the competitive regime for the Meyers et al. spectrum, yielding smaller crystal numbers; however, PDA08 predicted higher crystal numbers with ice nucleation most frequently in the homogeneous regime. Similar results have also been reported for mixed-phase cloud conditions [104].

Various heterogeneous nucleation spectra are coupled with the ice nucleation adjoint described in the previous chapter. We use the output sensitivities to classify nucleation regime and quantify nucleation efficiency. This process, in turn, allows us to address how and why N_i changes with the spectrum used. The focus is on spatial and temporal output variability, distinct from output uncertainty. The development of heterogeneous ice nucleation spectra reduces parametric uncertainty; once a spectrum is chosen, the question of how input variables contribute to output variability remains. We consider the latter here.

3.2 Simulation setup and spectra

The model and setup are as detailed in Section 2.4 above. For these simulations, we compare the updraft velocity from the TKE with a Gaussian weighting to measurements with a millimeter cloud radar in Figure 3.1. The modeled and measured updraft velocities are taken at the same latitude, longitude, and altitude. Measurements are shown after Doppler velocity decomposition as described by Kalesse et al. [105].

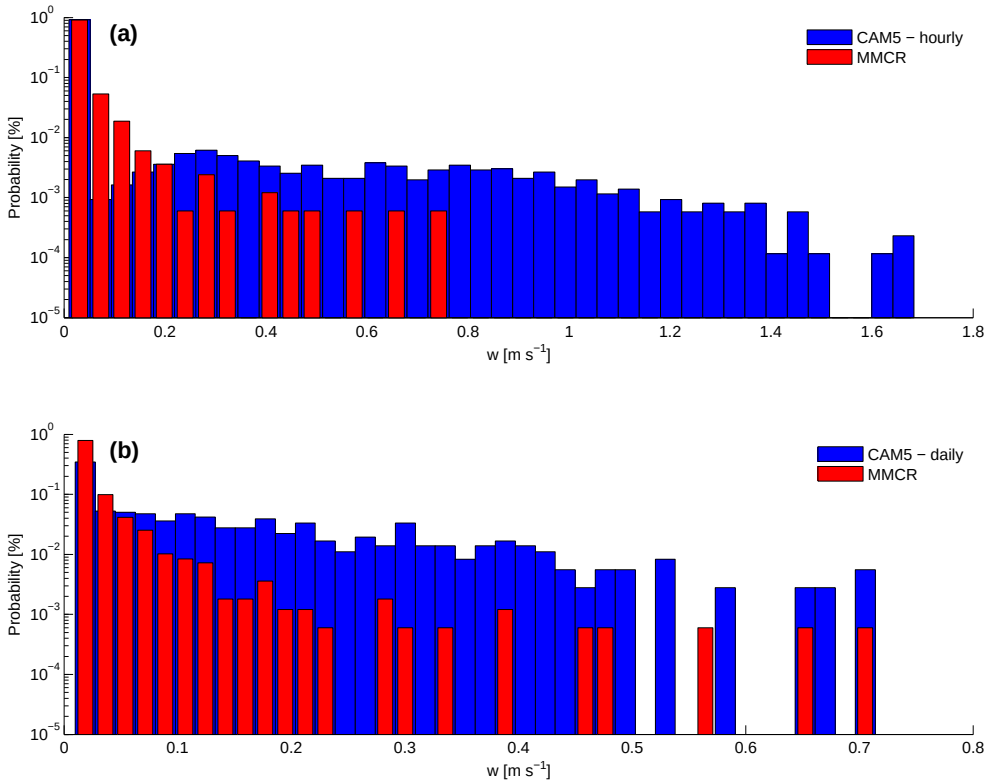

Figure 3.1: Comparison of the distribution of model input updraft velocities and of millimeter cloud radar (MMCR)-measured updraft velocities after Doppler velocity decomposition. Data include all hourly-averaged values from the ARM SGP site (36.605° N, 97.485° W) throughout 2007 around the 230 ± 20 hPa pressure levels (www.arm.gov/data/pi/76). These are compared to ***(a)*** *hourly-averaged updrafts at 232 hPa from a year-long CAM 5.1 simulation at the same latitude and longitude and* ***(b)*** *the daily-averaged updrafts over those hourly values in* ***(a)****. Daily-averaged values contain fewer instances of very large updraft and agree better with measurements. These are used to run all simulations. A strong filter for convective towers has been applied to the data and may explain its lack of higher values.*

The distribution of hourly-averaged measurements has a lower maximum and decays to smaller values than that of the hourly-averaged simulation inputs. Muhlbauer et al. noted similar behavior in which the MMCR velocities were repeatedly smaller than the in-situ ones, when comparing updraft distributions from aircraft and ground-based MMCR [106]; however, a later study of theirs also found that lower resolution models tend to decay to even smaller values than the MMCR observations because they do not resolve the gravity wave contribution [107]. This difference is probably due to the filtering of deep convective

systems within the MMCR data but no analogous filter for simulated updrafts in this case. Because the daily-averaged updraft values agree better with observations, we use these values to drive our simulations. The mean of the V distribution is set to 0.1 cm s^{-1}, but otherwise the weighting is as in Equation 2.11 of the previous chapter. Next we detail the four heterogeneous nucleation spectra used for intercomparison; their parameter values are listed in Table 3.1.

3.2.1 Phillips et al. empirical spectra

PDA08 uses the exponential correlation of crystal number and supersaturation from Meyers et al. as a reference spectrum, extending the applicable ranges of temperature and supersaturation and incorporating characteristics of the precursor aerosol. The number of ice-nucleating particles in aerosol group X, $n_{INP,X}$ (dust and metallics - DM, black carbon - BC, or organics - O) is calculated, as a function of temperature T and ice saturation ratio $\mathcal{S}_i$, with a sum over the aerosol size distribution weighted by a freezing fraction:

$$n_{INP,X} = \int_{\log 0.1\mu m}^{\infty} \{1 - \exp[-\xi_X(D, S_i, T)]\}\, n_X(\log D)\, d\log D \tag{3.1}$$

ξ_X represents the number of ice germs forming per aerosol and is the product of the active site density and aerosol surface area [108]: $\xi_X = H_X(S_i, T)\mathcal{F}_X\, n_{INP,*}\pi D^2/\Omega_{X,*}$. H_X is a threshold function that reduces INP concentrations at conditions subsaturated with respect to water and warm sub-zero temperatures; $\mathcal{F}_X$ is the portion of aerosol number belonging to group X within $n_{INP,*}$; $n_{INP,*}$ is the INP number from the reference spectrum; $\Omega_{X,*}$ is a reference aerosol surface area, which acts as a normalization factor for the size distribution; and $n_X(\log D)$ is the aerosol size distribution. H_X equals unity at water saturation and steps at certain threshold temperatures, $T_{0,X}$, and supersaturations, $s_{i,0,X}$, for the different aerosol groups.

Both PDA08 and PDA13 adopt the mathematical framework of Equation 3.1, but PDA13 employs more extensive field campaign data. The organic classification in PDA13 is also split into primary biological material and glassy organics, following recent observations of distinct ice-nucleating activity for these particle types. In this study, sensitivity of N_i to

biological INP is not considered, as CAM5 does not currently output a biological particle number.

3.2.2 Classical nucleation theory spectrum

We also use the classical nucleation spectrum developed by Barahona and Nenes in conjunction with the parameterization [66]:

$$n_{INP,X} = e_X n_X(\log D)\min\left[\frac{s_i}{s_{i,0,X}} e^{-f(\cos\theta)\, k_{hom}\, (s_{i,0,X} - s_i)}, 1\right] \tag{3.2}$$

where e_X is the nucleation efficiency of aerosol type X, $s_{i,0,X}$ is the threshold supersaturation, $n_X(\log D)$ is the aerosol size distribution, θ is the INP-ice contact angle, and k_{hom} is a parameter related to the homogeneous nucleation threshold. Dust and black carbon groups are included with parameters listed in Table 3.1; contact angles come from the laboratory data of Chen et al. [109] and e_{DM} is similar to that in Möhler et al. [110]. The stochastic component of the nucleation efficiency is assumed negligible, and the singular paradigm also underlies this spectrum.

3.2.3 Hiranuma et al. spectrum

The nucleation efficiency of hematite particles was measured at the AIDA chamber from 195 K up to 237 K, and a third-order polynomial for active site density (per m^2) was fit as a function of temperature and ice saturation ratio [100]:

$$\begin{aligned} n_s(T, \mathcal{S}_i) \;=\; & -3.777 \times 10^{13} - 7.818 \times 10^{11} T + 4.252 \times 10^{13} \mathcal{S}_i - 4.598 \times 10^{9} T^2 \\ & + 6.952 \times 10^{11} T \cdot \mathcal{S}_i - 1.111 \times 10^{13} \mathcal{S}_i^2 - 2.966 \times 10^{6} T^3 + 2.135 \times 10^{9} T^2 \cdot \mathcal{S}_i \\ & - 1.729 \times 10^{4} T \cdot \mathcal{S}_i^2 - 9.438 \times 10^{11} \mathcal{S}_i^3 \end{aligned} \tag{3.3}$$

Isolines from AIDA expansion cooling experiments are interpolated over the temperature-supersaturation space, assuming a hematite baseline surface area of 6.3×10^{-10} m^2 L^{-1}. As in Hiranuma et al., we use this active site density fit in the framework of Equation 3.1 to

Table 3.1: Adjustable parameters for ABN09 simulations with various nucleation spectra

Parameter		**Value**	**Source**
Pressure level		232 hPa	ISCCP
Deposition coefficient	α_d	0.7	[72]
Width of BC SD	σ_{BC}	1.8	[111]
Width of dust SD	σ_{DM}	1.6	[112, 113]
Width of organic SD	σ_{org}	1.8	[111]
Width of sulfate SD	σ_{sulf}	2.3	[114]
Liquid mixing ratio	q_c	1×10^{-6} kg kg^{-1}	[43]
Surface polarity	P_s	2	[115]
Organic coating	F_{oc}	10%	[115]
Threshold supersaturation for dust and metallics	$s_{i,0,DM}$	20%	[101]
Threshold supersaturation for black carbon	$s_{i,0,BC}$	35%	[101]
Maximum nucleation efficiency of dust	e_{DM}	50%	[110]
Effective contact angle for dust	θ_{DM}	16°	[109]
Maximum nucleation efficiency of black carbon	e_{BC}	2%	[81]
Effective contact angle for black carbon	θ_{BC}	40°	[109]

calculate nucleated crystal number:

$$n_{INP,X} = \int_{\log 0.1\mu m}^{\infty} \{1 - \exp[-n_s(T, S_i)\pi D^2]\}\, n_X(\log D)\, d\log D. \tag{3.4}$$

Hereafter, we refer to this formulation as the AIDA spectrum.

3.3 GCM results with various nucleation spectra

3.3.1 Model-measurement comparisons of ice crystal number

Figure 3.2 shows a comparison of the in-situ crystal number measurements, taken from the NASA MACPEX (Mid-latitude Cirrus Properties Experiment) and the DOE SPARTICUS (Small Particles In Cirrus) aircraft campaigns. Data are used from the Video Ice Particle Sampler (VIPS) and Two-Dimensional Stereo (2DS) probe during April 2011 of MACPEX and from the Forward Scattering Spectrometeor Probe (FSSP) during January 2010 of

SPARTICUS. Using simultaneous Meteorological Measurement System (MMS) pressure values, only N_i measurements taken within 20 hPa of the simulated pressure level of 232 hPa are used. Because the newly-nucleated ice crystal number concentration is simulated, we use only N_i from the smallest size bins of each instrument (see caption of Fig. 3.2). The same criterion for significant samples as in Jensen et al. is employed [116]: samples must continuously span at least 45 s. These MACPEX and SPARTICUS measurements, taken with shatter-resistant probes and analyzed with an inter-arrival time algorithm, are more reliable than older ones, especially for the smallest size bins that we consider [116].

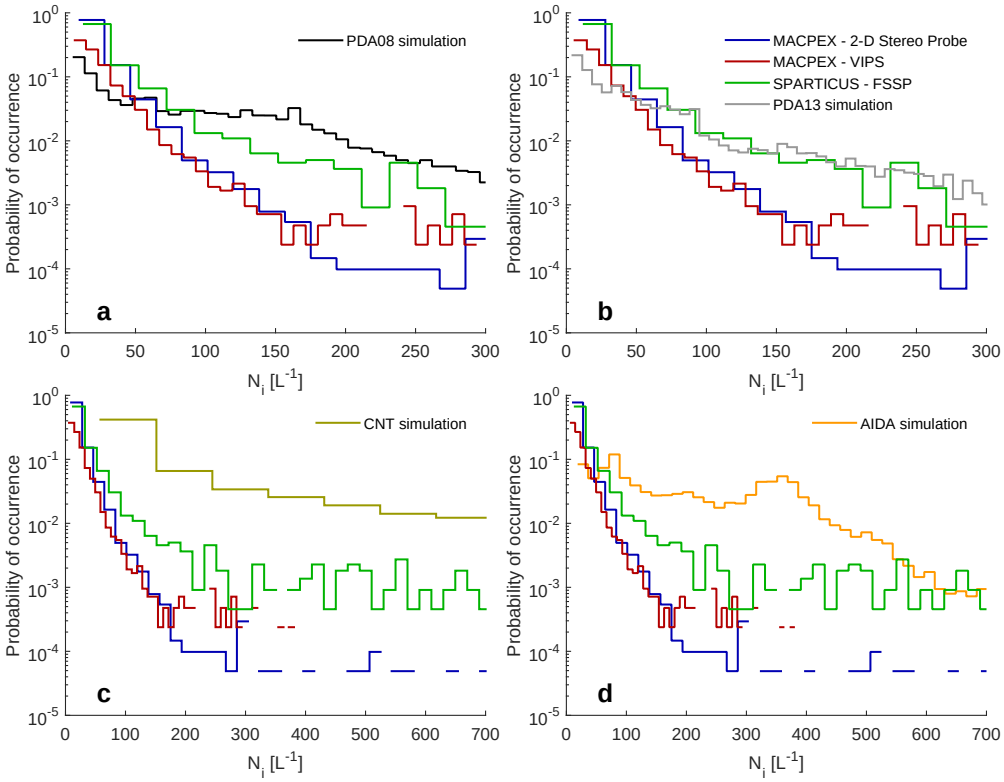

*Figure 3.2: Measurement-model comparison of probability distributions in ice crystal number concentrations. Data distributions come from the Video Ice Particle Sampler (VIPS) and the Two-Dimensional Stereo (2DS) Probe during April 2011 of the MACPEX campaign and the Foward-Scattering Spectrometer (FSSP) during January 2010 of the SPARTICUS campaigns. Only measurements from the 10-20 μm bin of the VIPS; the 5-15 μm bin of the 2DS; and the 0.89, 1.90, 3.80, 5.85, 8.30, 11.45, 14.25, 17.15, and 20.45 μm-centered bins of the 2DS are used, as approximations to the newly-nucleated ice crystal number. Measurements are also filtered for altitudes of 232 ± 20 hPa and for uniformity, lasting at least 45 s. Distributions of simulation output, i.e., of the annually averaged output nucleated ice crystal number, N_i, as in Figure 3.3, are shown using the **(a)** PDA08, **(b)** PDA13, **(c)** CNT, and **(d)** AIDA nucleation spectra. Different independent axes are used in panels **(c)** and **(d)**.*

Simulated and measured N_i agree best for the PDA13 spectrum, followed by the PDA08 and then the AIDA spectra. The CNT spectrum overestimates the frequencies of N_i greater than 10 L^{-1} by more than an order of magnitude and predicts no number concentrations less than 1 L^{-1}. Measurements show, instead, that most of the smallest crystals occur at number concentrations below 5 L^{-1}. The very high frequency of low N_i is missed by the other spectra as well, and all except PDA13 show slower decays in the frequency of high N_i than those in the measurements.

Model overestimate of high N_i at the coldest temperatures has been often noted [e.g., 117, 118, 119]. Along with this "ice nucleation puzzle" of low N_i at low temperatures [120], model-measurement discrepancy may be explained by in-cloud processes after nucleation: nucleated crystal number will tend to be higher than in-cloud crystal number, even when looking only at the smallest size bins. Preexisting ice crystals can inhibit ice nucleation [119, 121], while sedimentation can significantly reduce N_i. Spichtinger et al. have termed the latter "sedimentation induced quenching of nucleation" [122], and Jensen et al. found that omission of sedimentation resulted in higher frequency of N_i greater than 1000 L^{-1} [116].

3.3.2 Spatial patterns of ice crystal number

Figure 3.3 shows the notable spatial variability in annually averaged N_i and reflects the large variability in INP concentrations [e.g., 123, 124]. Including the microphysics after nucleation would tend to reduce this spatial variability. Some common features are still observed between fields: over the Himalayas and Rockies, N_i is higher because orographic lifting generates strong updrafts; the Saharan and Gobi desert outflows enhance N_{het}; and for INP spectra considering black carbon (all except AIDA), higher N_{het} occurs in regions of biomass burning, e.g., sub-Saharan Africa and the Amazon.

Elsewhere, N_i depends quite a bit on the nucleation spectrum. PDA08 predicts the lowest INP numbers (0.047 to 5.07 L^{-1}; Table 3.2) and is the only spectrum to calculate higher N_i in the NH than in the SH. PDA13 predicts about an order of magnitude higher INP number on average (0.57 to 28.6 L^{-1}) and more frequent inhibition of homogeneous nucleation. In localized regions of purely heterogeneous nucleation, however, PDA08 may still predict higher N_i. To understand this, we introduce the concept of an **INP abundance**, $A_{\mathrm{INP}} \equiv N_{INP}/N_{lim}$, defined as the ratio of available INP to the limiting number to inhibit homogeneous nucleation. N_{lim} increases with decreasing maximum supersaturation, $N_{lim} \propto s_{i,max}/(s_{i,max} - 1)$. An increase in N_{lim} may keep the system in the "cusp" of INP-N_i trace and outweigh an increase in N_{INP}, so that N_i actually decreases in PDA13.

INP numbers in the CNT and AIDA spectra are about tenfold higher than those in PDA13, with median values of 50.38 and 52.51 L^{-1} respectively. Such INP numbers result

in purely heterogeneous nucleation almost everywhere for these spectra. Particularly high N_i on the order of 1000 L^{-1} (larger than any of the in-situ measurements in Figure 3.2) are generated in Saharan outflows for the CNT spectrum because of the high dust nucleation efficiency and the dependence on aerosol number rather than surface area here. The overestimation of INP by CNT-based spectra has been reported elsewhere [e.g., 125].

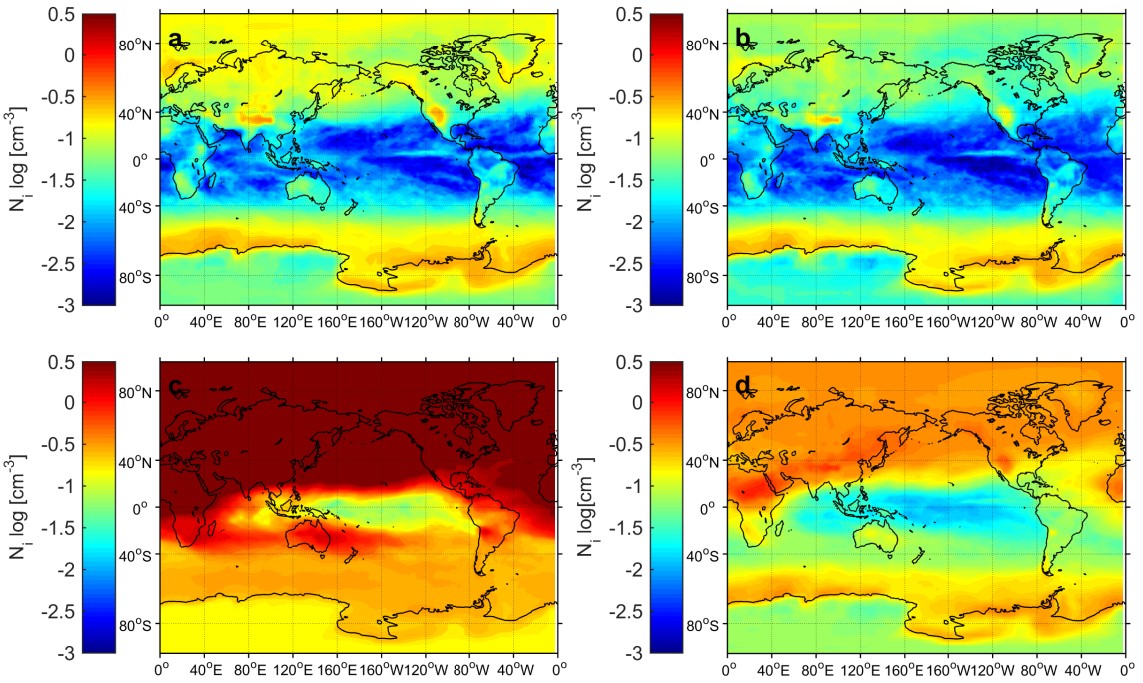

Figure 3.3: Annually averaged output nucleated ice crystal number, N_i from the cirrus formation parameterization for ***(a)*** *PDA08,* ***(b)*** *PDA13,* ***(c)*** *CNT,* ***(d)*** *AIDA nucleation spectra.*

3.3.3 Aerosol types acting as INP

Given the disparity in INP number predicted by the spectra, we investigate next which aerosol groups they predict to act as INP. Both dust and black carbon (BC) play a role for PDA08 in Figure 3.4, panels (a) and (c). Because $s_{i,0,BC}$ is a quadratic function of temperature, gradients in the BC contribution and input temperature both occur around 40°S [126]. In fact below 60°S, the BC contribution to N_{INP} is as much as 40%, an unexpected trend since BC sources tend to be continental and anthropogenic. For PDA13, on the other hand, dust is the primary contributor to N_{het} outside of a very localized region

Table 3.2: Range of predicted ice-nucleating particle numbers and abundances for different nucleation spectra. IQR = Interquartile Range

Spectrum	**PDA08**	**PDA13**	**CNT**	**AIDA**
INP Range [L^{-1}]	0.047–5.07	0.57–28.6	6.94–1270.47	3.60–855.36
Median INP number [L^{-1}]	0.48	3.60	50.38	52.51
IQR of INP number [L^{-1}]	1.05	10.56	169.82	190.49
A_{INP} range	0.0070–11.11	0.67–49.37	0.97–7220.64	4.02–4549.94
Median A_{INP}	0.34	10.25	20.80	20.47
IQR of A_{INP}	0.62	10.02	36.52	24.35

of equatorial deep convection. The correlation for $s_{i,0,DM}$ remains the same between PDA08 and PDA13 and decreases with decreasing temperature because observations show that nucleation on dust generally becomes more efficient at colder temperatures [e.g., 110, 113]. The updated correlation for $s_{i,0,BC}$ in PDA13 may play a role in these shifting contributions:

$$s_{i,0}^{BC} = \tilde{s}_{i,0} + \delta_0^1(F_{OC}, F_{OC,0}, F_{OC,1}) \times [1.2 \times \mathcal{S}_i^w(T) - \tilde{\mathcal{S}}_{i,0}] \tag{3.5}$$

where $\tilde{s}_{i,0}$ is a baseline supersaturation of 30%; δ_0^1 is a cubic interpolation over organic coating, F_{OC}, between lower and upper bounds of $F_{OC,0}$ and $F_{OC,1}$ [127, 128]; and $\mathcal{S}_i^w$ is the saturation ratio of vapor with respect to ice at exact water saturation [129]. This adjusted form is meant to account for the variety of surface features possible on BC produced from different combustion sources [115].

The shifting contributions can be understood by analyzing the expression for ξ_X. Given that the same aerosol size and number distributions have been used in both runs (Table 3.1), the difference is in the active site density parameterization, whose components were discussed above in Equation 3.1:

$$n_{S,X} = H_X(\mathcal{S}_i, T)\frac{\mathcal{F}_X n_{INP,*}}{\Omega_{X,*}} \tag{3.6}$$

Between PDA08 and PDA13, the portion of aerosol belonging to the BC group, $\mathcal{F}_{BC}$, has increased by 3%. The water-subsaturated threshold, H_X, would completely suppress BC

nucleation in PDA13 if F_{OC} were taken to be 100%; experimental evidence has shown that BC nucleation may only occur at water saturation when coating is significant [110]. But we have used F_{OC} of 10%. These factors alone actually yield a higher active site density for BC than for dust.

The difference in contributions, then, is the result of changing baseline surface area mixing ratios, $\Omega_{X,*}$. A lower active site density is needed to obtain the same freezing fraction when $\Omega_{X,*}$ is higher. Between PDA08 and PDA13, this parameter decreases fourfold for dust (2×10^{-6} m^2 kg^{-1} to 5×10^{-7} m^2 kg^{-1}) and increases about threefold for BC (1×10^{-7} m^2 kg^{-1} to 2.7×10^{-7} m^2 kg^{-1}). As a result, the freezing fraction of BC is much lower, even if $n_{S,BC}$ is somewhat higher. Dust becomes the primary INP for PDA13 because its freezing fraction has increased.

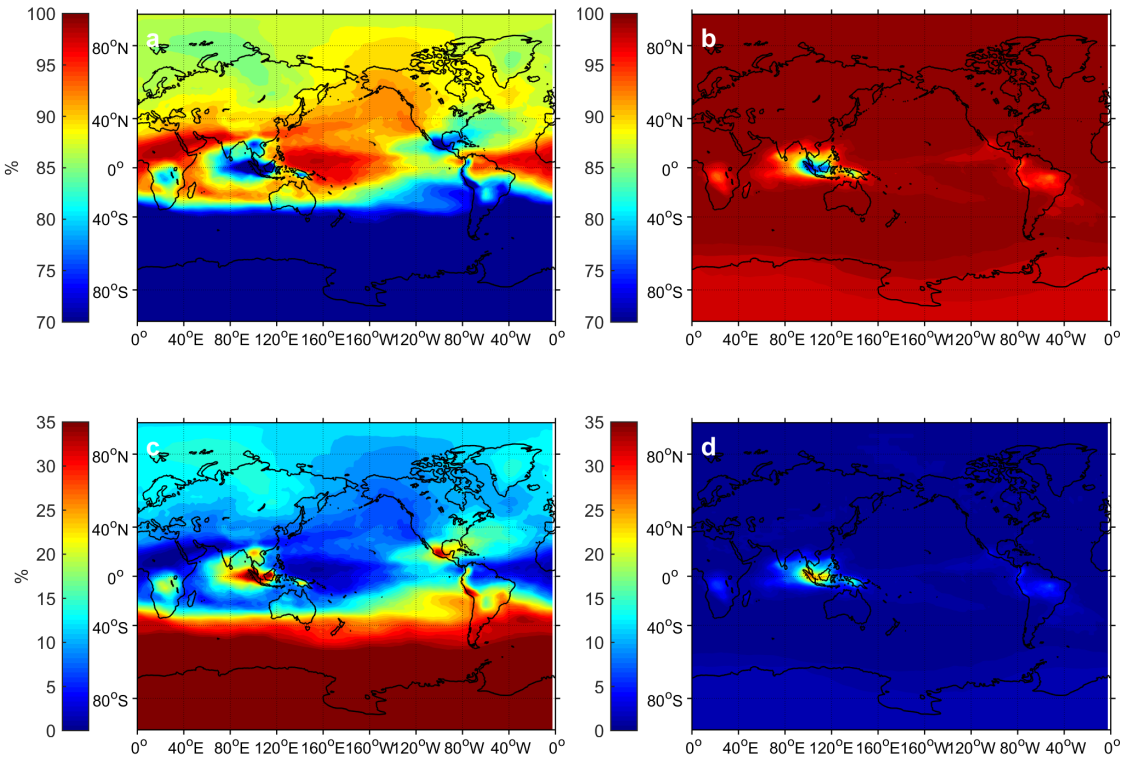

Figure 3.4: Annually averaged contributions of dust and BC to heterogeneously formed ice crystal number. ***(a)*** *Dust contribution in PDA08;* ***(b)*** *dust contribution in PDA13;* ***(c)*** *black carbon contribution in PDA08; and* ***(d)*** *black carbon contribution in PDA13.*

As a caveat, surface polarity and organic coating parameters are prescribed in these simulations and may be highly variable in the atmosphere. We have chosen a high polarity

and low organic coating, so that BC contribution calculations represent an upper bound. For simulations with higher organic coatings, any INP contribution from BC disappears completely. But polarity and coating change with morphology and porosity, which change with source [115]. A more detailed consideration of the BC emissions inventory would be needed to more accurately determine these parameters and BC contribution to crystal number. Uncertainty also exists within the BC emissions inventory itself, and this, along with the coating and polarity parameters, will translate to uncertainty in the N_i field.

3.3.4 Nucleation regime

Spatial patterns

As described above in Section 2.3.1 and with Figure 2.3, three different nucleation regimes exist along an INP-N_i trace. For low n_{INP}, nucleation is predominantly homogeneous, and the slope or sensitivity here, $\partial N_i/\partial n_{\mathrm{INP}}$, is slightly negative: addition of an insoluble particle slightly decreases N_i by competing for water vapor. Then as n_{INP} increases, the slope or sensitivity stays negative but increases in magnitude as water vapor preferentially deposits on additional INP surface and depresses N_i further. Finally when n_{INP} increases past a threshold of N_{lim} the slope or sensitivity becomes positive, as all nucleation occurs heterogeneously. The magnitude of the slope in this last regime gives an indication of the efficiency of an INP in nucleating ice.

Figure 3.5 illustrates the utility of sensitivities to classify nucleation regime with the sensitivity of N_i to accumulation mode dust number, $\partial N_i/\partial n_{dust,a}$, for the four spectra. In the SH, sensitivities for PDA08 are of small magnitude ($\mathcal{O}(10^{-4})$) and negative, as homogeneous nucleation dominates. There are localized regions of strong competitive nucleation in sub-Saharan Africa and northern South America, where sensitivities are of larger magnitude ($\mathcal{O}(10^{-3})$) and negative. Sensitivities throughout most of the NH are of moderate magnitude and negative, indicating weaker competitive nucleation.

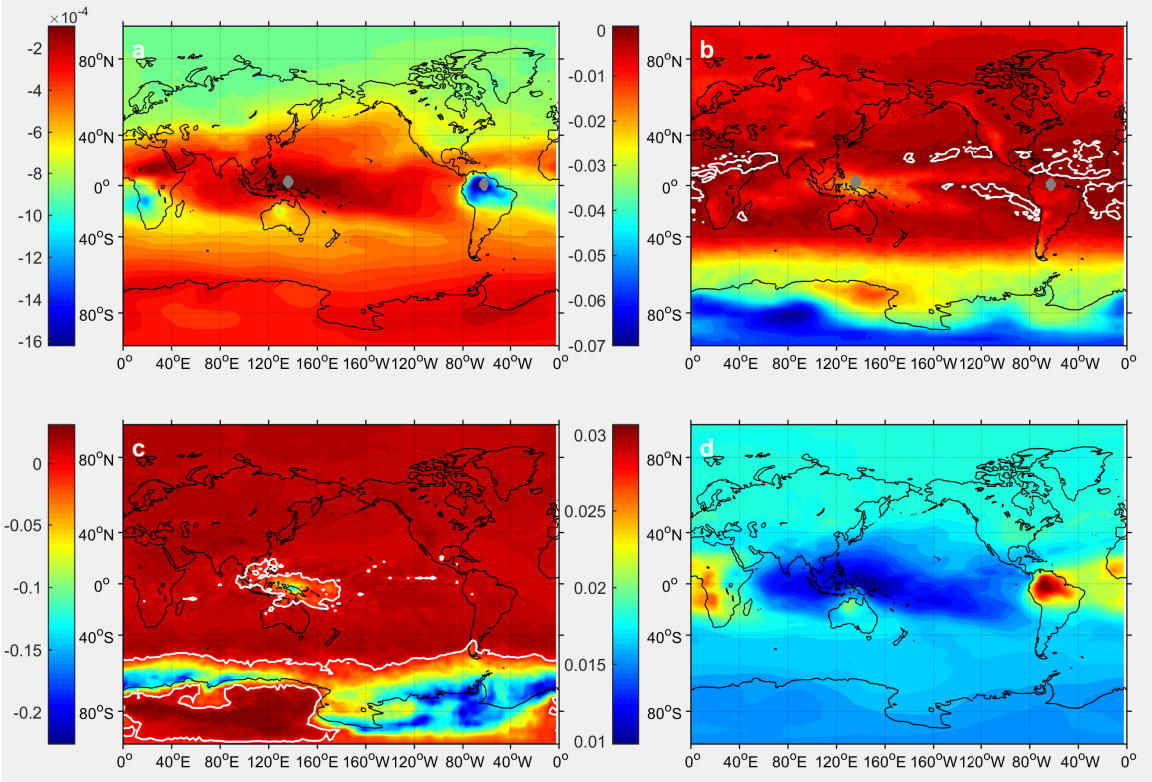

Figure 3.5: Annually averaged accumulation mode dust number sensitivities for ***(a)*** *PDA08,* ***(b)*** *PDA13,* ***(c)*** *CNT, and* ***(d)*** *AIDA.*

In contrast, the CNT field produces positive sensitivities, or purely heterogeneous nucleation, throughout most of the NH (These regions are delineated in white.) PDA13 also contains regions of purely heterogeneous nucleation but around the Equator in regions of lower updraft and higher INP. When updraft velocity increases significantly – in regions of deep convection over Indonesia or over the Himalayas or Rockies due to orographic lifting – a sufficiently high supersaturation may be generated to exceed the threshold for homogeneous nucleation and induce competitive nucleation. For both the PDA13 and AIDA spectra, regions of large and negative sensitivities, or strong competitive nucleation, appear south of 60°S. INP numbers are considerably lower than N_{lim} here, but the threshold supersaturation for homogeneous nucleation has also increased at these cold temperatures.

The magnitude of negative sensitivities during competitive nucleation reflect the threshold conditions assigned to a given aerosol group. The lower the threshold supersaturation for an aerosol group, the more readily it nucleates and the more effectively it depletes water vapor; this corresponds to larger magnitude $\partial N_i / \partial N_{dust,a}$ before N_{INP} surpasses N_{lim} and

purely heterogeneous nucleation begins. PDA13 sensitivities to BC number are of larger magnitude than PDA08 values because $S_{i,0,BC}$ is lower for the polarity and F_{OC} values used here. The cusp of the INP-N_i trace becomes steeper, and the competition for water vapor is stronger in this case.

3.3.5 Temporal patterns

Given the disproportionate effect of anomalous sensitivities on temporal averages, discussed above in Section 2.5.2, we look at time series as well for the frequency of occurrence of different nucleation regimes. Distributions of both accumulation mode dust number sensitivities and input updraft velocities are presented at (2.9°S, 135°E) over Indonesia and (0.95°N, 64°W) over northern South America in Figure 3.6. These points are denoted by diamonds in Figure 3.5. Their annually averaged sensitivities differ significantly, despite their being in the same latitudinal band with similar aerosol loadings.

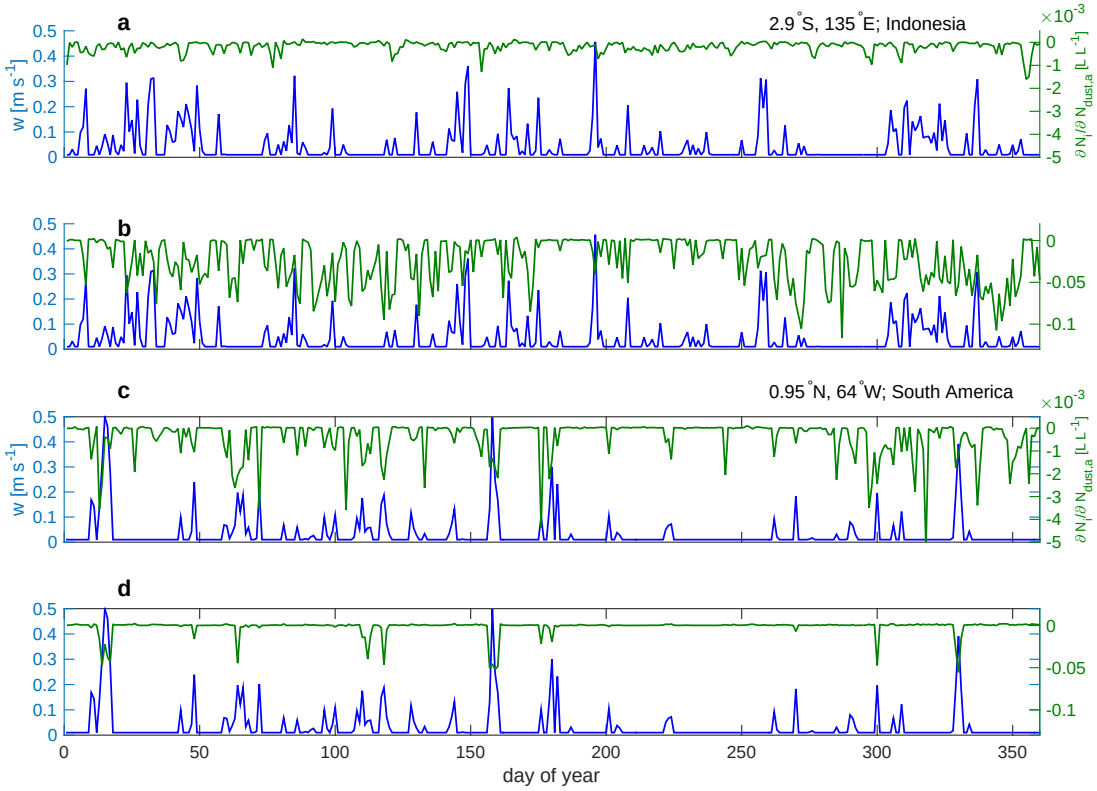

Figure 3.6: Time series of accumulation mode dust number sensitivities (green, in L L^{-1}) and input updraft velocities (blue, in m s^{-1}) over Indonesia at 2.9° S, 135° E for ***(a)*** *PDA08 and* ***(b)*** *PDA13; and over South America at 0.95° N , 64° W for* ***(c)*** *PDA08 and* ***(d)*** *PDA13.*

The location over Indonesia experiences high updraft more frequently, and the additional supersaturation generation translates to more competitive nucleation and larger magnitude sensitivities in PDA13, almost down to -0.1 L L^{-1}. In PDA08, more supersaturation generation translates to more frequent homogeneous nucleation and smaller magnitude, less variable sensitivities, on the order of 10^{-3} L L^{-1}. The location over South America has fewer instances of high updraft, so for PDA13, the system cannot always overcome the threshold supersaturation for homogeneous nucleation. Purely heterogeneous nucleation occurs more frequently: Figure 3.6d has primarily positive sensitivities of small magnitude with an occasional large spike in $\partial N_i/\partial N_{dust,a}$, which always corresponds to a large updraft. Relative to PDA13, PDA08 exhibits stronger water vapor competition: the peaks in Figure 3.6c are about four times as large as those in Figure 3.6a. This behavior can be understood in terms of a transition along the INP-N_i trace in Figure 2.3: N_i and $\partial N_i/\partial N_{INP}$ respond differently to supersaturation generation based on how many INP the nucleation spectrum predicts.

3.3.6 Nucleation efficiency

As noted above, the positive values of $\partial N_i/\partial n_{INP}$, for which nucleation is purely heterogeneous, can be understood as nucleation efficiencies: those aerosols which act as efficient INP generate a large increase in crystal number for a given increase in aerosol number. Rather than an inherent nucleation efficiency of a certain aerosol group, the sensitivity reflects an INP efficiency given the particular model state. Accumulation mode dust has a mean efficiency of 0.0012% ($\mathcal{O}(10^{-3}\%)$) in PDA08 and 0.079% ($\mathcal{O}(0.1\%)$) in PDA13, while coarse mode dust has a mean efficiency of 0.61% in PDA08 and 0.078% in PDA13. AIDA calculates considerably higher mean efficiencies of 1.4% for the accumulation mode and 52% for the coarse mode. Black carbon in PDA08 is 0.03% efficient on average, still an order of magnitude higher than the accumulation mode dust. In PDA13, on the other hand, black carbon efficiency is an order lower than accumulation mode dust and skewed toward lower values (not shown). Efficiency of organic aerosol is negligible, on the order of 10^{-5}% and skewed to values as low as 10^{-12}%.

Figure 3.7a shows these trends more concisely: we draw the distribution of a random

sample of 5000 daily-averaged dust number sensitivities, when ice nucleation is purely heterogeneous, i.e., $\partial N_i/\partial n_{INP} > 0$. The coarse mode dust number sensitivity is higher, and the accumulation mode dust sensitivity lower, for PDA08 than PDA13 because BC nucleation has been suppressed in the latter. The active site density of PDA08 BC is larger than that of dust under certain conditions, meaning that BC efficiencies are higher than the accumulation mode dust efficiencies. The coarse mode sensitivities or efficiencies are even higher because their surface area is two orders of magnitude larger, outweighing a lower active site density.

The PDA08 distributions also have many more outliers because of the greater competition for water vapor between aerosol groups. In model grid cells without BC, dust in both modes is able to nucleate much more efficiently, while in those with more BC, the dust nucleation efficiency is significantly reduced because of the competition for water vapor between the two INP groups. The narrower range of AIDA efficiencies reinforces this point: this spectrum describes nucleation by dust in idealized conditions and no other aerosol compete for water vapor. Its active site parameterization also contains no threshold functions that abruptly reduce nucleation. For application in global models, it may be more effective to use parameterizations from experiments with multiple nucleating aerosol types.

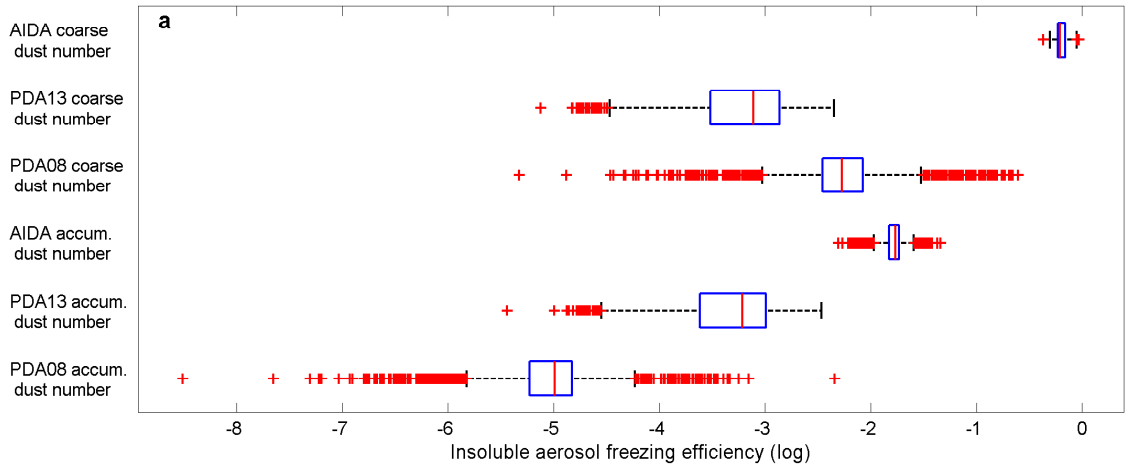

Figure 3.7: Log-space distributions of a random sampling of ***(a)*** *accumulation and coarse mode dust number and* ***(b)*** *dust diameter for PDA08, PDA13, and AIDA spectra during purely heterogeneous nucleation. The box is constructed with 25th percentile, q_1; median, q_2; and 75th percentile, q_3. Outlying points are marked with crosses if they fall outside $[q_1 - 1.5(q_3 - q_1), q_3 + 1.5(q_3 - q_1)]$*

Once an aerosol population has reached its maximum active fraction or efficiency, N_i becomes less sensitive to the number of these aerosol. In PDA13, the coarse mode dust population reaches an upper bound in its efficiency, and N_i sensitivity to coarse mode number decreases to a value comparable to the accumulation mode number. From Equation 3.1 during purely heterogeneous nucleation,

$$\frac{\partial N_i}{\partial n_X} = 1 - \exp(-n_s(\mathcal{S}_i, T)\pi D^2) \tag{3.7}$$

Then for low active fractions, this can be linearized such that $f_{INP} \sim \mathcal{O}(n_s(\mathcal{S}_i, T)D^2)$. Then with order of magnitude analysis, if $n_s \sim \mathcal{O}(10^9\ \mathrm{m}^{-2})$ and $D \sim \mathcal{O}(10^{-6}\ \mathrm{m})$ in the coarse mode, the maximum active fraction is expected to be on the order of 10^{-3}, which is indeed the value seen in Figure 3.7.

3.3.7 Temperature and sulfate number sensitivity

Finally, we shift focus to the factors influential for homogeneous nucleation. Sulfate sensitivities are generally on the order of 0.001 $\mathrm{cm}^3\ \mathrm{cm}^{-3}$ but can be as large as 0.025 $\mathrm{cm}^3\ \mathrm{cm}^{-3}$ at the coldest temperatures in the SH. This field does not change in magnitude between spectra because the treatment of homogeneous nucleation is identical in all cases. $\partial N_i/\partial n_{sulf}$ is smaller and less influential than the updraft sensitivity fields, similar to the findings of Kärcher et al. for which the aerosol size distribution did not strongly affect the number of nucleated ice crystals [89].

Temperature sensitivities, $\partial N_i/\partial T$, are generally negative because increasing temperature may exceed the threshold temperature for a certain aerosol group, deactivating it, and allowing homogeneous nucleation to generate a larger N_i. This phenomenon can be observed in both the PDA08 and PDA13 fields, in which positive sensitivities fall exclusively at the outflow of Saharan dust around the equator where input temperature is between 225 and 230 K, in the range at which the water-subsaturated threshold function for dust lowers.

The magnitude of $\partial N_i/\partial T$ is smaller than expected from classical nucleation theory due to counterbalancing effects. For example, as temperature increases so does water vapor diffusivity, which enhances crystal growth and reduces number. But latent heat of sublimation

also increases as temperature drops, which slows the crystal growth rate. The homogeneous nucleation coefficient increases by an order of magnitude with only a 30 K drop in temperature [79]. The threshold supersaturation for dust, however, also goes down, so that deposition nucleation can more easily inhibit homogeneous nucleation. These various temperature dependencies may cancel out and lead to lower temperature sensitivities within the model. Hoose and Möhler 2012 have noted an intermediate regime in nucleation experiments for which active site density isolines are independent of temperature and change primarily with supersaturation. Similar compensating effects, which cause low temperature sensitivity in the parameterization runs, might also explain this experimentally observed, temperature-independent regime.

3.4 Chapter 3 Summary

Thorough understanding of nucleated ice crystal variability in global simulations will help improve model representation of cirrus clouds and their radiative forcing. Towards this end, adjoint sensitivity analysis provides a powerful and efficient means of quantifying the ice nucleation regime and efficiency. From analysis of GCM simulations with four nucleation spectra, we have shown the following results:

- **Nucleation regime is determined by INP, but N_i is determined by INP abundance, A_{INP}.** The number of ice-nucleating particles predicted by a nucleation spectrum determines its nucleation regime. But lower ice crystal numbers can be calcualted in spite of higher INP numbers, if certain aerosols have less stringent threshold supersaturations. This threshold supersaturation affects the steepness and depth of the competitive "cusp" along the INP-N_i trace.

- **The baseline surface area mixing ratio, $\Omega_{X,*}$, strongly affects which INP contribute to N_i.** Dust contribution to heterogeneously formed number dominates on a global scale for PDA13 runs. Suppression of the BC contribution is due to a fourfold decrease in the baseline surface area mixing ratio for dust, $\Omega_{DM,*}$.

- **The sign of ice crystal number sensitivity to insoluble aerosol number or**

diameter indicates nucleation regime. When insoluble aerosol number or diameter sensitivities are small and negative, nucleation is predominantly homogeneous. When these values become large and negative, competitive nucleation has initiated, and when the values become positive, nucleation is purely heterogeneous. Spatial distributions of insoluble aerosol number sensitivity, as in Figure 3.5, can help explain those of crystal number in Figure 3.3. Temporal distributions of sensitivity can also be used to understand regime shifts along the INP-N_i trace.

- **The magnitude of positive aerosol number sensitivity reflects heterogeneous nucleation efficiency.** The range of efficiencies is limited when there is no competition for water vapor between aerosol groups. Crystal number is more sensitive to the aerosol species with higher associated surface areas, until those species reach their maximum active fractions. Nucleation spectra based upon lab data predict much higher nucleation efficiencies than those from field data.

- **Temperature sensitivities are of smaller magnitude than expected with classical nucleation theory because of compensating temperature dependencies.** Limited sensitivities to temperature reflect the empirically observed "intermediate temperature regime," where supersaturation is more influential on nucleation.

In the next chapter, we deconstruct the temporal variability of N_i is greater detail, motivated by the effect of anomalous sensitvities discussed in Chapter 1 and by the sudden shifts in nucleation regime shown here in Figure 3.6.

CHAPTER 4
ATTRIBUTION OF TEMPORAL VARIABILITY IN HYDROMETEOR NUMBER

While the direct sensitivities analyzed in the previous chapter give interesting information on nucleation regime and efficiency, even more insight can be gleaned from these values by performing attribution analyses. In this chapter, variability attribution is performed at a range of spatial and temporal resolutions with metrics derived from online adjoint sensitivies of both droplet and ice crystal number to relevant inputs. A key finding is the importance of updraft velocity fluctuations to the temporal variability in droplet and ice crystal numbers. We first restate the importance of hydrometeor formation to cloud radiative forcing.[1]

4.1 Cloud formation and radiative impacts revisited

Cloud radiative forcing remains one of the largest sources of uncertainty in the overall terrestrial radiative budget [1]. Supercooled liquid fraction can be as important as cloud cover in the calculation of this forcing [131]. Cloud long-wave emissivity depends on cloud water path and hydrometeor sizes, along with cloud height and temperature. Cloud short-wave albedo also depends on particle size, since more and smaller hydrometeors yield a higher optical depth for the same water path [1]. GCMs predict a diversity of liquid and ice water paths [2], as well as cloud hydrometeor sizes, and the treatment of initial hydrometeor formation, i.e., droplet activation or ice nucleation, contributes to this spread for all cloud types [132, 133].

The available supersaturation of a cloudy air parcel determines how many hydrometeors can form therein. Updraft velocity generates supersaturation because as an air mass ascends, it undergoes expansion cooling. Aerosol particle surfaces upon which vapor can condense (CCN) or deposit (INP) act as a sink of supersaturation. The number of newly-

[1]This work has been published as **S. C. Sullivan**, et al. (2016) Updraft velocity in temporal variability of cloud hydrometeor number [130]. Prof. Ricardo Morales-Betancourt provided CAM5.1 inputs used to run the DEF-C and DEF-Cyr simulations. I want to thank Dr. Donifan Barahona for instruction in using GEOS-5 and two anonymous reviewers for their insightful suggestions.

formed cloud hydrometeors can then be calculated from this supersaturation balance.

The model representation of new hydrometeor formation is crucial because it affects all proceeding cloud microphysics. The trend within GCMs is toward two-moment schemes which track both liquid droplet and ice crystal mass and number density [134, 135, 43, 136]. Most state-of-the-art models also incorporate sophisticated parameterizations that explicitly link hydrometeor formation to updraft velocity and aerosol properties [1].

Many studies to date have looked at the effect of various droplet activation or ice nucleation parameterizations within GCMs [e.g., 137, 138, 104, 103, 102]. The focus tends to be uncertainty analysis, or how uncertain parameters affect the cloud hydrometeor number and cloud radiative forcing. However, considerably less effort has been devoted to attributing the temporal variability of modeled hydrometeor number to various inputs, an analysis which depends both on the sensitivity to each input and the variance of those inputs. Thereafter, it is also important to understand whether the influence of an input is amplified or dampened by the inherent model sensitivity. This kind of attribution analysis can help to explain the model diversity in simulated cloud forcings and indicate when cloud evolution is particularly susceptible to anthropogenic forcing.

The rest of this chapter presents attribution analysis within two GCMs to understand which inputs contribute most to temporal variability in newly-formed droplet and ice crystal numbers. We discuss also the ability of observations to better constrain these predictions and give special focus to vertical velocity, as a poorly-constrained but crucial input for hydrometeor formation [61, 50, 80]. Previous work has shown the impact of spatial scales and aggregation on the cloud albedo effect [139]. Here we consider the impact of temporal scales on hydrometeor formation, by performing attribution analysis at different model time steps and output resolutions.

4.2 Attribution metrics

Two attribution metrics are defined here with adjoint sensitivities and input variances. First, the temporal attribution, $\xi_{x_j}^{(Y)}$, is given in Equation 4.1 and represents the fraction of temporal variability in either droplet or ice crystal number, Y, which is explained by the

variability in an input, x_j. For droplets, the temporal attribution includes vertical velocity and organic, sulfate, sea salt, and black carbon aerosol numbers and hygroscopicities. For ice crystals, it includes vertical velocity and dust, sulfate, and black carbon aerosol numbers.

> The **temporal attribution**, $\xi_{x_j}^{(Y)}$, of the input variable x_j, i.e., updraft velocity or aerosol number, for output scalar Y, i.e., N_d or N_i, is defined as
>
> $$\xi_{x_j}^{(Y)} = \frac{(\overline{\partial Y/\partial x_j})^2 \sigma_{x_j}^2}{\sum_{j=1}^{J} (\overline{\partial Y/\partial x_j})^2 \sigma_{x_j}^2} \tag{4.1}$$
>
> where $\overline{\partial Y/\partial x_j}$ is the mean adjoint sensitivity to input x_j, $\sigma_{x_j}^2$ is the variance of input x_j and J the number of input variables considered.

The second metric, temporal attribution fraction, $\zeta_{x_j}^{(Y)}$, is given in Equation 4.2 and expresses whether model sensitivity amplifies, i.e., $\zeta_{x_j}^{(Y)} > 1$, or dampens, i.e., $\zeta_{x_j}^{(Y)} < 1$, the temporal variability of x_j in that of hydrometeor number Y. Robustness of these metrics to temporal averaging and integration time step make them particularly useful.

> The **temporal attribution fraction**, $\zeta_{x_j}^{(Y)}$, of input x_j to output Y for a given grid cell is defined as
>
> $$\zeta_{x_j}^{(Y)} = \frac{(\overline{\partial Y/\partial x_j})^2}{\sigma_{x_j}^2} \frac{\overline{x_j}^4}{\overline{Y}^2} \tag{4.2}$$
>
> where $\overline{x_j}$ is the mean of input x_j, and $\overline{Y}$ is the mean output value at each grid cell.

Sensitivities used for both metrics are calculated at each model state, varying for each grid point between time steps. The construction of the GEOS-5 ice adjoint was based on the Barahona and Nenes cirrus ice nucleation parameterization as detailed in Chapter 2 [66, 50, 80]. The droplet adjoint was constructed from the set of Nenes droplet activation parameterizations [140]. These sensitivities, along with the input and output values, are filtered for cases in which new hydrometeor formation is non-negligible, i.e., $dN_d > 1$ cm^{-3} and $dN_i > 1$ L^{-1}, and then averaged.

4.3 GEOS-5 and CAM5 simulation setups

Attribution metrics are calculated from four simulations with the NASA Global Modeling and Assimilation Office Goddard Earth Observing Model, Version 5 (GEOS-5): two month-long runs with daily output and different integration time steps (DEF-G and DEF-G2) and two month-long runs with hourly output, one in NH winter (HITEMP-1) and the other in NH summer (HITEMP-2). The HITEMP versus DEF simulations consider the effect of temporal averaging on each attribution metric, and HITEMP-1 versus HITEMP-2 considers their seasonality. A simulation (DEF-C) with the National Center for Atmospheric Research Community Atmosphere Model, Version 5.1 (CAM5.1) is used to compare the results between GCMs. Droplet number variability within this framework has also been considered by Morales-Betancourt and Nenes 2014 [140]. Simulations with both models are extended to a full year (DEF-Gyr and DEF-Cyr) to see how metrics change with simulation length.

The Ganymed 4.0 subversion of GEOS-5 is run, along with the Microphysics of clouds with Relaxed Arakawa-Schubert and Aerosol-Cloud interaction (McRAS-AC) and the Rapid Radiative Transfer Model for GCMs (RRTMG) schemes [141, 142]. Sea surface temperatures are prescribed using monthly SST datasets from which daily SST are linearly interpolated. The GOCART aerosol module [143, 144], 2° spatial resolution, and a 30-minute time step were also used, except in DEF-G2 for which the time step is 15 minutes. Aerosol mass from GOCART is converted to number, assuming volume mean radii and species densities. The monthly simulations (DEF-G, DEF-G2, and HITEMP-1) were run for January 2010 with the exception of HITEMP-2 run for July 2010. The yearly simulation (DEF-Gyr) was run from January through December 2010.

The DEF-C and DEF-Cyr simulations are done with inputs from CAM 5.1 at 2.5 x 1.88° resolution, a 30-minute time step, emissions from Lamarque et al., and the MAM3 model [78]. A given aerosol number concentration in a given mode is calculated by scaling the total aerosol number concentration in that mode by the mass fraction of the given aerosol in the given mode (as in Section 2.4 and Table 2.3) [61]. The geometric standard deviation for the Aitken mode is set to 2.3, for the accumulation mode to 1.8, and for the coarse mode

to 1.6. The Morrison and Gettelman microphysics scheme is used, replacing the default Liu and Penner ice nucleation scheme with that of Barahona and Nenes. The deposition coefficient is set to 0.7.

Analysis of attribution metrics is centered at the 875 hPa (277.5 ± 10.9 K) pressure level for cloud droplets and the 350 hPa (236.7 ± 11.9 K) pressure level for ice crystals, based on where median cloud fraction for warm stratiform and cirrus clouds is highest. Analysis is also carried out for adjacent pressure levels (at 825 and 925 hPa for stratiform and at 250 and 450 hPa for cirrus clouds), as limits that bound 75% of the altitudinal distribution in median droplet or ice crystal number. The metrics are calculated only for instances in which new hydrometeor formation is non-negligible, i.e., $dN_d > 1$ cm^{-3} and $dN_i > 1$ L^{-1}.

4.4 Attribution grids

Figure 4.1 shows the *primary* and *secondary* attribution grids for cloud droplet number, N_d, and ice crystal number, N_i, in the DEF-G simulation at the central pressure level. In the **attribution grids**, each grid cell is colored by the input variable with the highest (primary) or second highest (secondary) temporal attribution, $\xi_{x_j}^{(Y)}$, averaged monthly. A given aerosol number may appear for a grid cell in both the primary and secondary grids, but these represent that aerosol number in different modes; updraft, as a single variable, may only appear in one grid or the other. Similar grids from the longer DEF-Gyr simulation are shown in Figure 4.2.

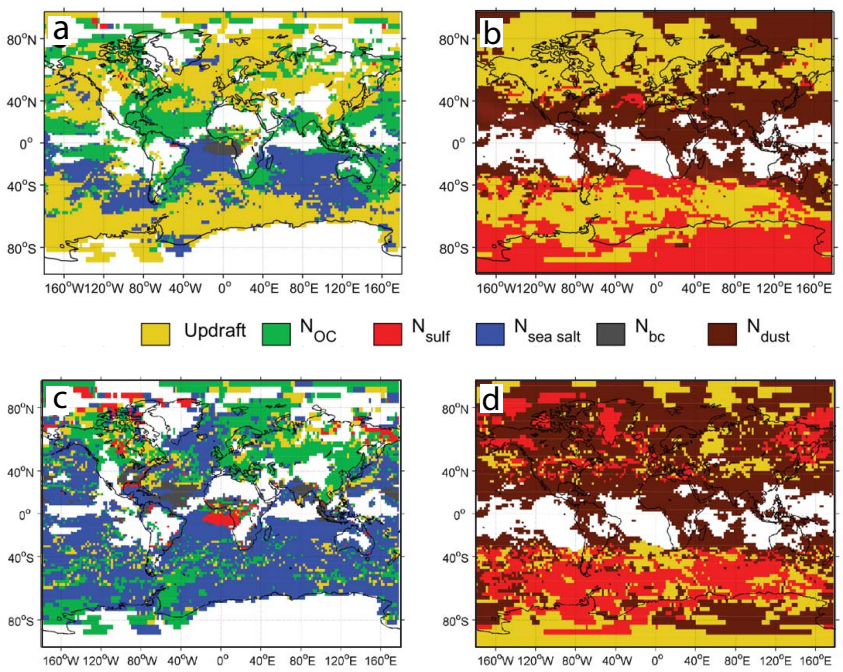

Figure 4.1: Primary attribution grids, i.e., grid cells colored according to the input variable whose temporal attribution is largest, for ***(a)*** *liquid droplets at 875 hPa ($\bar{T}$ = 277.5 ± 10.9 K) and* ***(b)*** *for ice crystals at 350 hPa ($\bar{T}$ = 236.7 ± 11.9 K). Secondary attribution grids, i.e., grid cells colored according to the input variable whose temporal attribution is second largest, for* ***(c)*** *liquid droplets at 875 hPa and* ***(d)*** *ice crystals at 350 hPa. Values are taken from the DEF-G simulation using the Phillips et al. 2008 heterogeneous nucleation spectrum. Grid cells and time points for which new hydrometeor formation is negligible, i.e., $dN_d < 1\ cm^{-3}$ and $dN_i < 1\ L^{-1}$, are filtered out; regions of negligible cloud hydrometeor formation over the month are shown in white.*

Updraft velocity is the primary driver of N_d variability for 45.5% of the grid, as shown in Figure 4.1a. The importance of vertical velocity increases with altitude, covering 24.5% of the grid at 925 hPa and 61.4% at 825 hPa. The global grid-averaged value of $\xi_w^{(N_d)}$ value goes from 21.0% at 925 hPa to 39.5% at 875 hPa to 53.9% at 825 hPa (Figure 4.3). As temperature drops, the water vapor availability for generating supersaturation decreases. Increased competition for water vapor by CCN promotes the sensitivity to updraft fluctuations.

For ice crystals, updraft velocity is the primary driver of variability for 38.0% of the global grid at 350 hPa, as shown in Figure 4.1b. The importance of vertical velocity for N_i decreases with altitude, as the grid coverage changes from 48.4% at 450 hPa to 21.6% at 250 hPa. The global grid-averaged $\xi_w^{(N_i)}$ varies from 39.5% at 450 hPa to 34.6% at 350 hPa

to 21.0% at 250 hPa (Figure 4.3). These trends can be explained by the strong decrease in magnitude of updraft velocity and its fluctuations with altitude.

Sea salt and organic aerosol number are the most important aerosol drivers of N_d variability, especially closest to the surface, where aerosol number covers 73.9% of the grid with a mean $\xi_{N_{aer}}^{(N_d)}$ value of 59.2%. Over most marine environments, temporal variability in droplet activation is influenced by sea salt numbers, while organic-rich aerosol dominates over land (Figure 4.1c and Figure 4.2), often due to its large input variance. Sulfate and accumulation mode dust numbers are the important aerosol drivers of N_i variability, especially farthest from the surface, where aerosol number covers 77.5% of the grid with a mean $\xi_{N_{aer}}^{(N_i)}$ of 71.9%. The dominance of sulfate versus accumulation mode dust number depends on the ice nucleation regime, either homogeneous or heterogeneous respectively.

The seasonal dependence of temporal attributions can be seen by comparing the HITEMP-1 grids during NH winter (Figure 4.10) and the HITEMP-2 grids during NH summer (Figure 4.11); these are shown further below under a discussion of the effect of output frequency. The seasonality is most prominent for the ice crystal attributions, as $\xi_{N_{dust}}^{N_i}$ coverage is 10 to 20% greater in the NH summer than in the winter at all pressure levels. $\xi_{N_{sulf}}^{N_i}$ coverage is comparable in both seasons. These trends are a result of nucleation regime: in the SH where aerosol is limited and temperatures remain low, most nucleation is homogeneous, while in the NH where aerosol is abundant and temperatures are warmer, most nucleation is heterogeneous. This regime split is less apparent, when NH temperatures become colder during winter there.

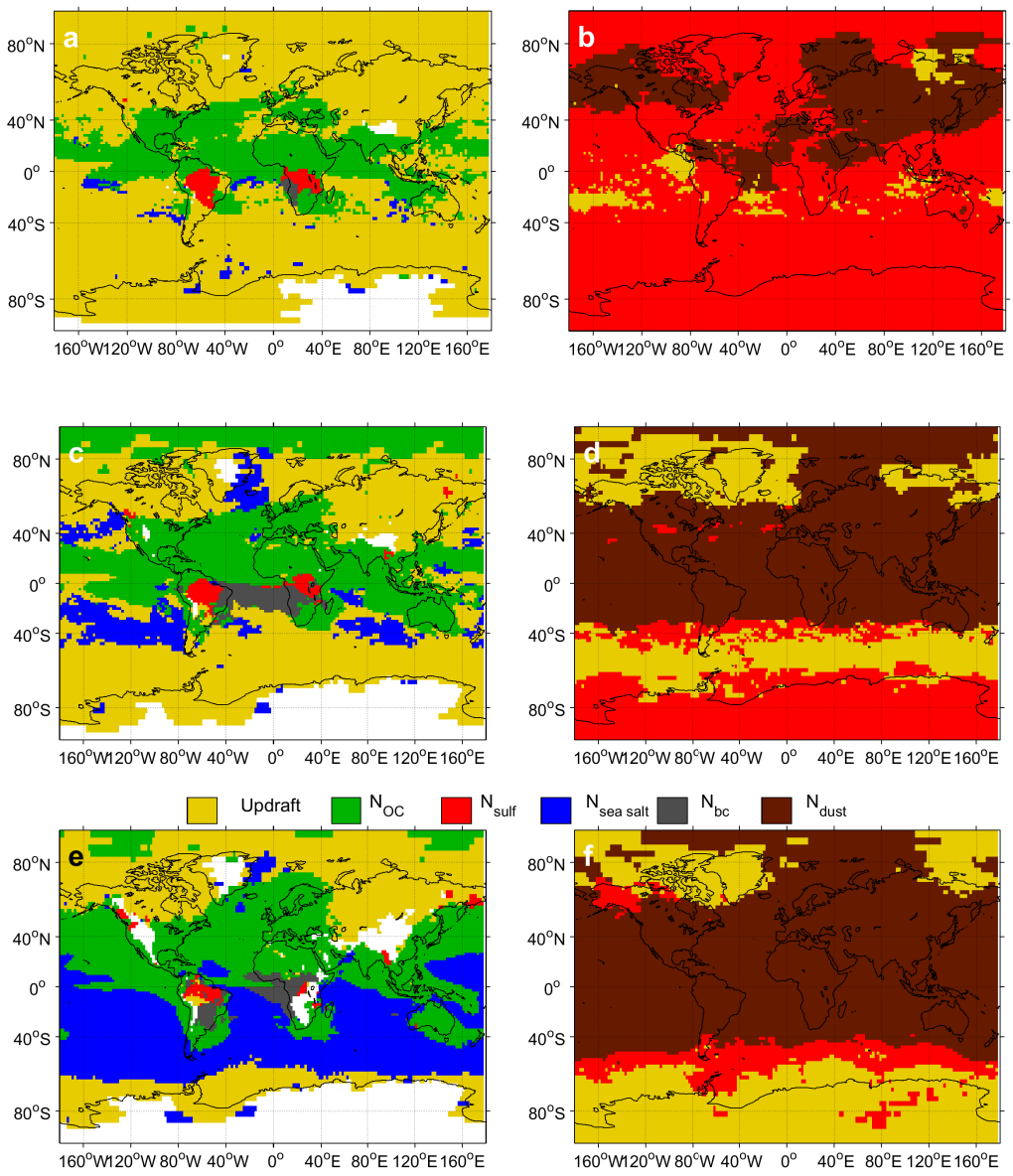

Figure 4.2: Primary attribution grids as in Figure 4.1 at (a) 825 hPa, (c) 875 hPa, and (e) 925 hPa for liquid droplets; at (b) 250 hPa, (d) 350 hPa, and (f) 450 hPa for ice crystals but with values from the DEF-Gyr simulation, a year-long GEOS-5 simulation at 2° spatial resolution, using PDA08. One daily-averaged set of inputs and sensitivities is recorded per day. Then the annual variance of these inputs and mean of these sensitivities are used in the calculation of Equation 4.1.

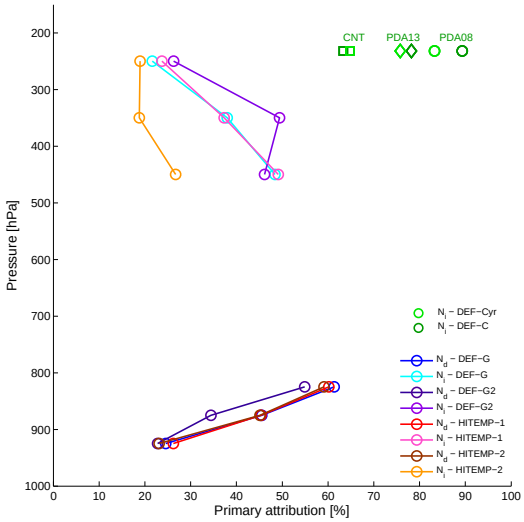

Figure 4.3: Coverage of $\xi_w^{(N_X)}$ in the primary attribution grids, i.e. the percentage of all grid cells where non-negligible hydrometeor formation occurs for which updraft velocity has the largest temporal attribution. Values are shown for all simulations, at 825, 875, and 925 hPa for droplets in the GEOS-5 simulations (N_d in the legend); at 250, 350, and 450 hPa for ice crystals in the GEOS-5 simulation; and at 232 hPa for ice crystals in the CAM simulation (N_i in the legend).

4.4.1 Effects of aerosol representation

For ice crystal formation, different representations of INP concentrations may influence the attribution calculation. Figure 4.4 show attribution grids using three of the INP spectra from Chapter 3 (PDA08 [68], PDA13 [69], and CNT [66]) for the DEF-C simulation. Updraft velocity is the dominant driver of variability in all simulations, covering 89.3%, 78.2%, and 63.4% of the primary attribution grids with mean values of 84.6%, 71.4%, and 52.9% for PDA08, PDA13 and BN09, respectively. Coverage values are shown in green in Figure 4.3; the simulation length, considered between DEF-C and DEF-Cyr does not have a strong impact on the temporal attribution. In regions where updraft appears for these primary attribution grids, the magnitude of $\xi_V^{(N_i)}$ is often greater than 80%, so that its attribution dominates over dust concentrations by a large margin.

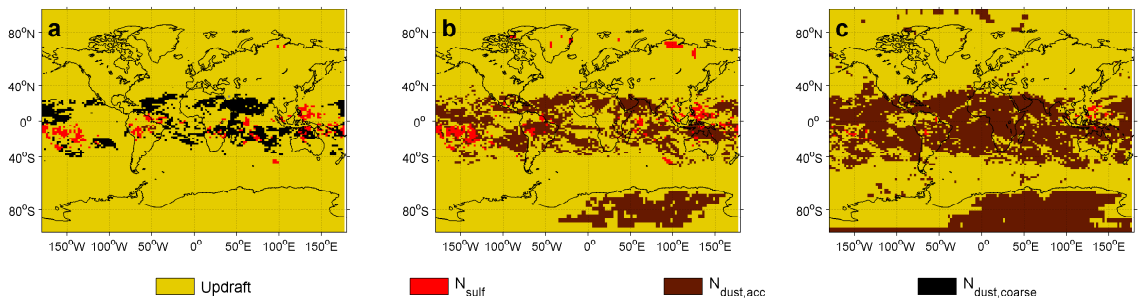

Figure 4.4: Primary attribution grids for ice crystals at 232 hPa from the DEF-C simulation using (a) PDA08, (b) PDA13, and (c) CNT.

Like the INP spectrum, the aerosol module can influence the attribution calculations through the size, number and hygroscopicity of the aerosol that can act as CCN. Large differences in the accumulation mode dust and Aitken mode sulfate numbers between the GEOS-5 and CAM5 simulations are shown in Figure 4.5. GEOS-5 uses the GOCART bulk aerosol scheme, which tracks aerosol mass; although the model reproduces satellite aerosol optical thickness well, volume mean radii and species densities are assumed to convert mass to the input aerosol numbers for the ice crystal number calculation. CAM5 uses the MAM3 modal scheme, where both aerosol mass and number are explicitly simulated and input to the ice nucleation parameterization. Despite these large differences in aerosol representation and resulting concentrations, the treatment of subgrid updraft variability impacts output temporal variability more than the different aerosol modules. As a follow-up to this conclusion, it would be of interest to switch aerosol treatments within these model frameworks and understand how the attribution grids shift. The GOCART assumed radii and densities could be applied to the MAM3 aerosol mass fractions, or an updated version of GEOS-5 linked with MAM3 could be run.

4.4.2 Updraft representation

Given such high updraft temporal attributions, it is important to understand the differences in model representation of updraft between the GEOS-5 and CAM5. Both the magnitude and structure of updraft sensitivity fields, $\partial N_i/\partial V$, for the two models are similar, as long as a version of the Phillips heterogeneous nucleation spectrum is used (Figure 4.6); however,

the updraft variance, σ_V^2, can be drastically different, as shown in Figure 4.7.

In GEOS-5, the subgrid updraft velocity, $V_{sub,i}$, is the summation of the grid-scale vertical velocity from the omega equation plus a term calculated from latent heating and the dry environmental lapse rate. The droplet activation parameterization uses only this value, with a minimum of 1 cm s^{-1} enforced. The BN ice nucleation parameterization uses this value, with the same minimum, as the mean of a Gaussian updraft distribution; the standard deviation is set to 0.25 m s^{-1}. Outputs are then weighted by a six-point Gauss Legendre quadrature over the range $V \pm 4\sigma_V$. For the lower bound of this quadrature, another minimum of 0.1 cm s^{-1} is enforced. As shown by the very low updraft variances in Figure 4.7c, the model state is often at the lower bound for V of 1 cm s^{-1}.

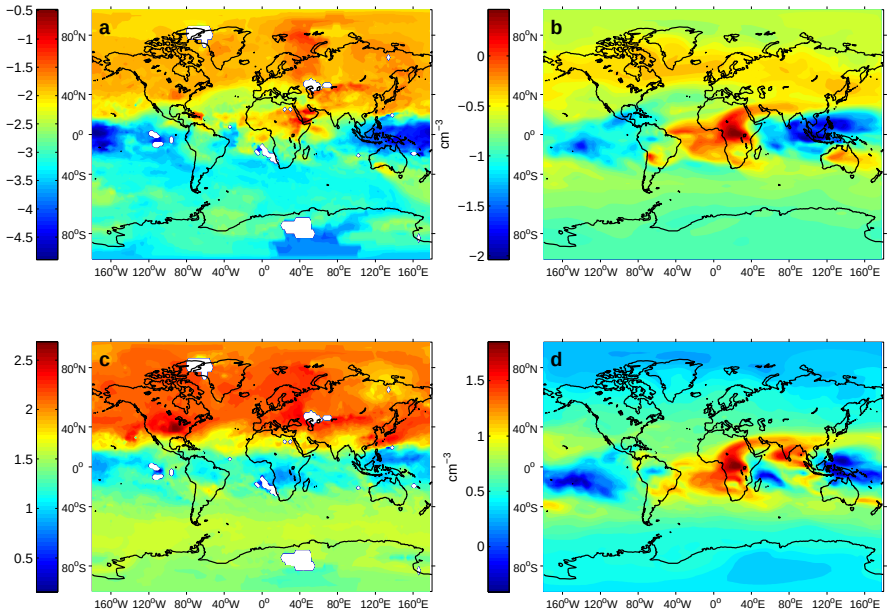

Figure 4.5: Comparison of the input dust and sulfate aerosol number concentrations, N_{dust} and N_{sulf}, between GEOS-5 at 250 hPa for DEF-G (left) and CAM5 at 232 hPa for DEF-C (right) simulations in log space: ***(a)*** *N_{dust} from the second bin of the GOCART aerosol module;* ***(b)*** *N_{dust} from the accumulation mode of the MAM3 aerosol module;* ***(c)*** *N_{sulf} from GOCART; and* ***(d)*** *N_{sulf} from MAM3. GOCART aerosol mass is converted to number, assuming a volume mean radius for dust of 1.4 μm and for sulfate of 0.0566 μm (r_g = 0.02 μ m, σ_g = 2.3). Dust density, ρ_{dust}, is taken to be 2.5 g m^{-3}, and sulfate density, ρ_{sul}, is taken to be 1.841 g m^{-3}. For DEF-C, both aerosol mass and number are tracked within MAM3. Lognormal size distributions are assumed for the Aitken, accumulation, and coarse modes, with fixed σ_g of 2.3, 1.8, and 1.6 respectively.*

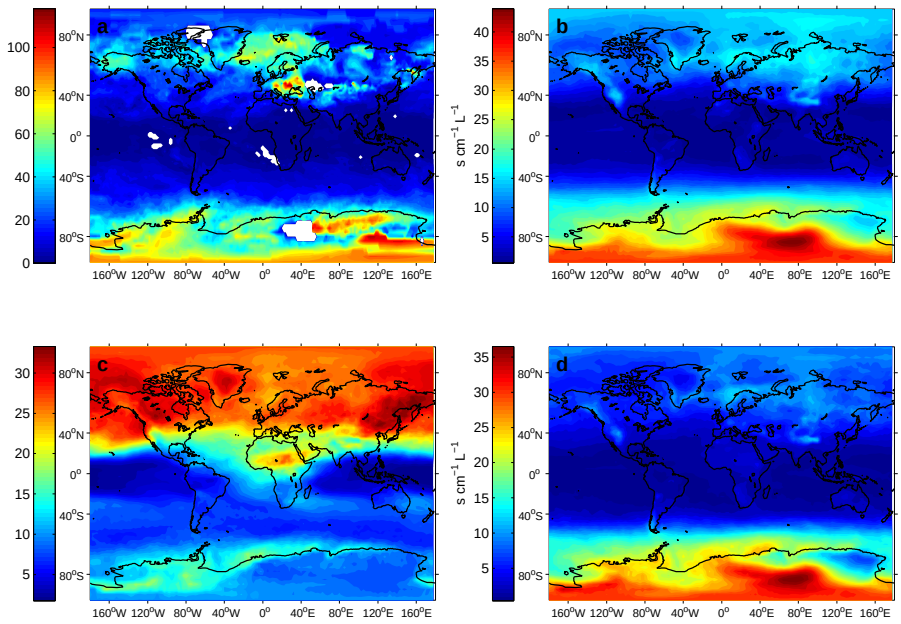

Figure 4.6: Comparison of the ice crystal number sensitivity to updraft velocity, $\partial N_i/\partial V$ [s cm^{-1} L^{-1}], between GEOS-5 and CAM5 simulations: ***(a)*** *$\partial N_i/\partial V$ from the DEF-G simulation with the Phillips et al. 2008 nucleation spectrum at 250 hPa and after filtering out grid cells and time points where $dN_i < 1$ L^{-1};* ***(b)*** *DEF-C simulation at 232 hPa with the Phillips et al. 2008,* ***(c)*** *Barahona and Nenes 2009 CNT, and* ***(d)*** *Phillips et al. 2013 nucleation spectra.*

In CAM, the subgrid updraft velocity does not involve the grid-scale velocity, only a subgrid value calculated from the square root of the turbulent kinetic energy from the moist turbulence scheme, which uses a first order, small-eddy closure [145]. Both parameterizations use this value, with a minimum of 0.2 m s^{-1} enforced for droplet activation and of 0.1 cm s^{-1} for ice nucleation. The default maxima are 10 m s^{-1} and 2 m s^{-1} respectively, but we eliminate this ice nucleation maximum and use the same quadrature approach described above. Although CAM input updrafts tend to be smaller, parameterizing turbulence increases its updraft variance by orders of magnitude (Figure 4.7d) and makes these vertical motions the dominant driver of temporal variability in N_i. Using an updraft velocity threshold which is too large may mute the variability in N_d or N_i and shift the temporal attribution from dynamical to aerosol parameters.

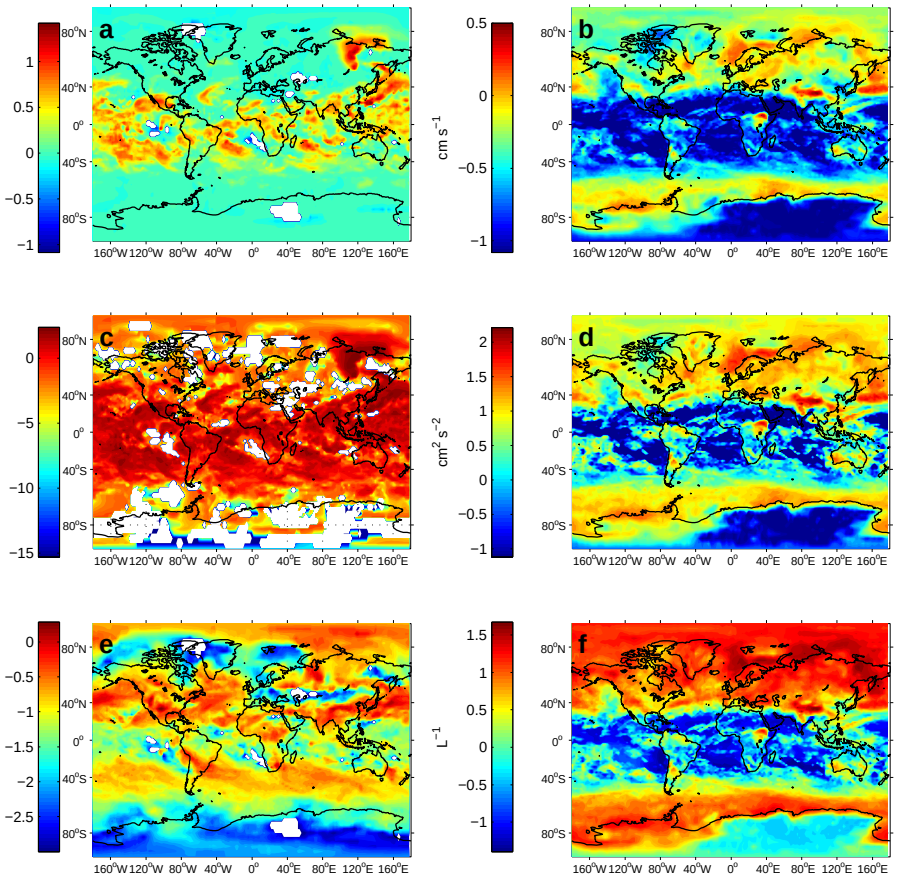

Figure 4.7: Comparison of the input updraft velocity, V, its variance, σ_V^2, and output newly-formed ice crystal number concentration, N_i, between GEOS-5 (left) and CAM5 (right) simulations, all shown in log space: V from (a) DEF-G and (b) DEF-C [cm s^{-1}]; σ_V^2 from (c) DEF-G and (d) DEF-C [cm^2 s^{-2}]; and N_i from (e) DEF-G and (f) DEF-C [L^{-1}]. GEOS-5 maps are shown at 250 hPa, after filtering out grid cells and time points where $dN_i < 1$ L^{-1}, i.e. only when non-negligible hydrometeor formation occurs. CAM maps are shown at 232 hPa. Additional regions of panel (c) are omitted when $\sigma_V^2 < 10^{-15}$ cm^2 s^{-2}.

The importance of input updraft variance versus inherent sensitivity to updraft can also be assessed with the temporal attribution fraction, $\zeta_V^{(N_X)}$. If $\zeta_V^{(N_X)} << 1$ the hydrometeor number is relatively insensitive to updraft fluctuations; the input updraft variance has to be large to dominate the temporal attribution. Conversely, when $\zeta_V^{(N_X)} >> 1$, the hydrometeor number is quite sensitive to updraft fluctuations; the input variance can be small and still dominate the temporal attribution. In the latter case, any uncertainty in V translates to large uncertainty in hydrometeor concentration.

Figure 4.8 shows the updraft temporal attribution fraction, $\zeta_V^{(N_X)}$, in log space for liquid

droplets and ice crystals in the DEF-G simulation at 875 and 350 hPa respectively. $\zeta_V^{(N_X)}$ is generally small, on the order of 10^{-2}, with input updraft variability contributing more to output variability than $\partial N_X/\partial V$. At high latitudes, where V often encounters its lower bound and σ_V^2 drops off, $\zeta_V^{(N_X)}$ can increase dramatically (Figures 4.8c and d). Updraft sensitivity is also highest at these extreme latitudes (Fig. 4.6a), and the increase in $\zeta_V^{(N_X)}$ with latitude is even more pronounced at higher altitudes. At lower altitudes, the attribution fraction is more likely to remain small at all latitudes because fluctuations in input updraft velocity will be large. At times, for example, 925 hPa will still be within the boundary layer and subject to strong vertical mixing.

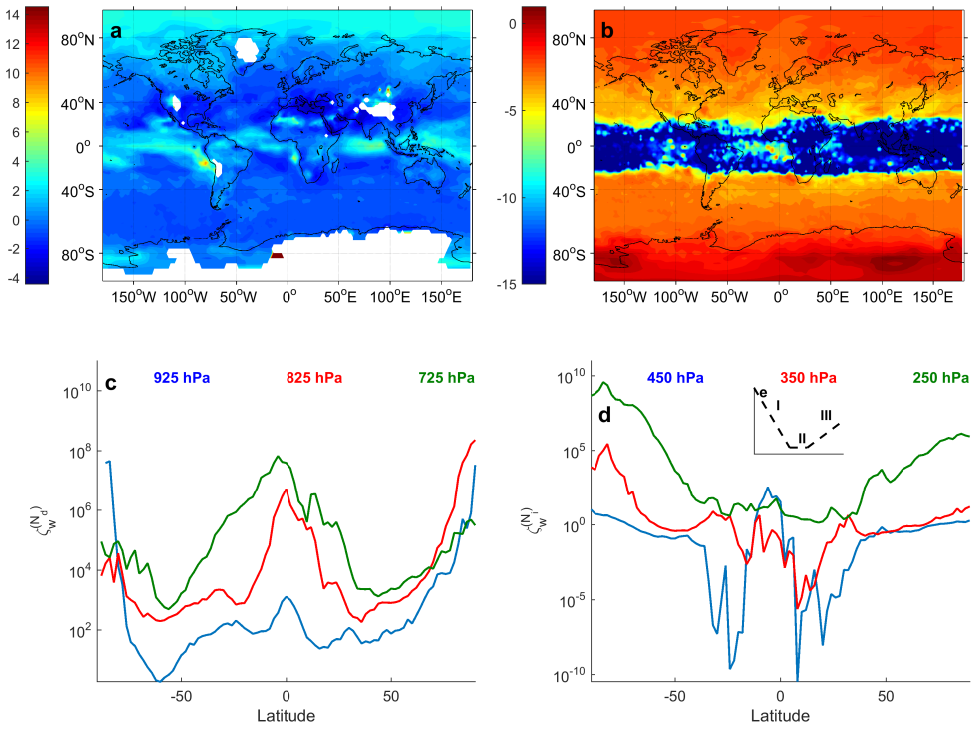

Figure 4.8: Temporal attribution fractions of updraft velocity, $\zeta_V^{(N_X)}$ for ***(a)*** *liquid droplets at 875 hPa and* ***(b)*** *ice crystals at 350 hPa, plotted in log space for the DEF-Gyr simulation. Annually-averaged sensitivities and annual variances are used in the calculation of Equation 4.2. Zonally-averaged traces are also shown of* ***(c)*** $\zeta_V^{(N_d)}$ *and* ***(d)*** $\zeta_V^{(N_i)}$ *for all three pressure levels from DEF-Gyr. The three latitudinal "regimes" for $\zeta_V^{(N_i)}$ traces are schematized in inset* ***(e)****.*

Hemispherical asymmetry in $\zeta_V^{(N_i)}$, can be explained by nucleation regime. Nucleation

is primarily homogeneous in the SH due to colder temperatures and less aerosol. Ice crystal number also increases more rapidly with updraft during homogeneous nucleation, so $\zeta_V^{(N_i)}$ becomes larger in the SH; this is denoted Regime I in the inset (e) of Figure 4.8. In the NH, heterogeneous nucleation is promoted because additional aerosol increase the likelihood of available INP and warmer temperatures suppress homogeneous nucleation. Because ice crystal number increases less rapidly with updraft during heterogeneous nucleation, $\zeta_V^{(N_i)}$ does not increase so rapidly with latitude, denoted Regime III in Figure 4.8e. Almost no crystal formation is seen at tropical latitudes, except at the highest altitude, and $\zeta_V^{(N_i)}$ remains flat in this Regime II.

The latitudinal profile of $\zeta_V^{(N_d)}$ also has asymmetry because $\partial N_d/\partial V$ increases for higher aerosol loadings. As a result, $\zeta_V^{(N_d)}$ tends to be higher in the NH than in the SH where aerosol loading is higher, or equivalently active fraction is lower. $\zeta_V^{(N_d)}$ also increases toward more extreme latitudes because the updraft magnitude is lower and an incremental increase in supersaturation is more influential.

4.5 Sensitivity attribution[2]

Here we define a third and final metric, the **sensitivity attribution**, as the cross correlation of sensitivity anomalies and input anomalies. Its magnitude quantifies which inputs drive temporal variability in hydrometeor number sensitivity to aerosol number.

> The x_j, x_k sensitivity attribution, or attribution of input x_j to the x_k sensitivity of Y, is defined as
>
> $$\eta_{x_j,x_k}^{(Y)} = \frac{\sum_t x_j'^2 (\partial Y/\partial x_k)'^2}{\sigma_{x_j}^2 \sigma_{(\partial Y/\partial x_k)}^2} \tag{4.3}$$
>
> x_j' is the anomaly in input x_j and $(\partial Y/\partial x_k)'$ is the anomaly in output sensitivity to input x_k. $\sigma_{x_j}^2$ and $\sigma_{\partial Y/\partial x_k}^2$ are the variances of these two fields respectively.

Sensitivity attributions are tested for statistical significance using the Student's t-distribution. In the DEF-G run, the number of observations, n, is 31 for the month-long run with daily

[2]Work in this section is unreviewed and unpublished.

output, while in the HITEMP-2 run, n is 744 for the July run with hourly output. The alternative hypothesis is taken to be non-zero correlation.

Given the importance of $\xi_V^{(N_X)}$ and $\zeta_V^{(N_X)}$ above, we take x_j to be updraft and investigate the extent to which it can affect the other variables which appear in the attribution grids. Sulfate and accumulation mode dust numbers also appear prominently in the primary attribution grids (Figs. 4.1 and 4.11) and are the aerosol of primary importance for homogeneous and heterogeneous ice nucleation respectively. So we calculate distributions of updraft-sulfate number sensitivity attribution, $\eta_{V,N_{sulf}}^{(N_i)}$, and updraft-accumulation mode dust number sensitivity attribution $\eta_{V,N_{dust,3}}^{(N_i)}$ for the DEF-G and HITEMP-2 simulations at all pressure levels. Their distributions are shown in Figure 4.9. Updraft and sulfate number sensitivity are positively correlated because, given sufficient supersaturation, the ice crystal number increases rapidly with any increase in aqueous sulfate droplets. At 250 hPa, the updraft-sulfate number sensitivity attribution has a median of 0.453 in the DEF-G simulation, significant at the 99% level for 78.7% of the grid, and 0.635 in the HITEMP-2 simulation, significant at the 99% level for 85.7% of the grid. The correlation strength drops with altitude because any temperature fluctuations strongly influence sulfate number sensitivity at colder temperatures.

$\eta_{V,N_{dust,3}}^{(N_i)}$ values are negative at 350 and 250 hPa because nucleation occurs competitively between homogeneous and heterogeneous nucleation. When nucleation is competitive, higher updrafts generate more supersaturation and facilitate homogeneous nucleation relative to heterogeneous nucleation, causing sensitivity to ice-nucleating particles to drop, i.e. a negative anomaly. At the lowest altitude, however, nucleation tends to be purely heterogeneous and increasing updraft will increase the efficiency of certain particles to nucleate ice. Tails of the $\eta_{V,N_{dust,3}}^{(N_i)}$ distribution contain positive values. The updraft-accumulation mode dust number sensitivity attribution is somewhat less than $\eta_{V,N_{sulf}}^{(N_i)}$, with a median of -0.256 for DEF-G and -0.222 for HITEMP-2 at 350 hPa and -0.290 and -0.229 for the two at 250 hPa. These sensitivity attributions are statistically significant at the 99% level for 91.2, 83.9, 93.8, and 84.5% of the grid respectively.

Distributions of sulfate number-updraft sensitivity attribution and dust number-updraft sensitivity attribution are also constructed to see if, instead, perturbations in aerosol are

linked to higher model sensitivity to updraft. $\eta^{(N_i)}_{N_{sulf},V}$ has a median value of 0.035 in the DEF-G simulation and 0.073 in the HITEMP-2 simulation. $\eta^{(N_i)}_{N_{dust,3},V}$ has median values of -0.062 and -0.098 for the two simulations. Updraft fluctuations, then, are far better correlated with anomalous aerosol sensitivities than aerosol fluctuations are with anomalous updraft sensitivities.

At the highest altitude, a similar effect of updraft perturbations on droplet number sensitivity to organic aerosol number can be seen. We have also visualized distributions of $\eta^{(N_d)}_{V,N_{org}}$ (not shown), and the median value at 725 hPa is 0.336 in the DEF-G simulation, 99% significant for 50.3% of the grid, and 0.443 in the HITEMP-2 simulation, 99% significant for 23.1% of the grid. This sensitivity attribution appears only at the highest and cleanest altitude; when conditions are polluted, the droplet activation fraction remains low and additional supersaturation activates larger sea salt or biomass burning particles, as shown in Figures 4.2e and 4.10e.

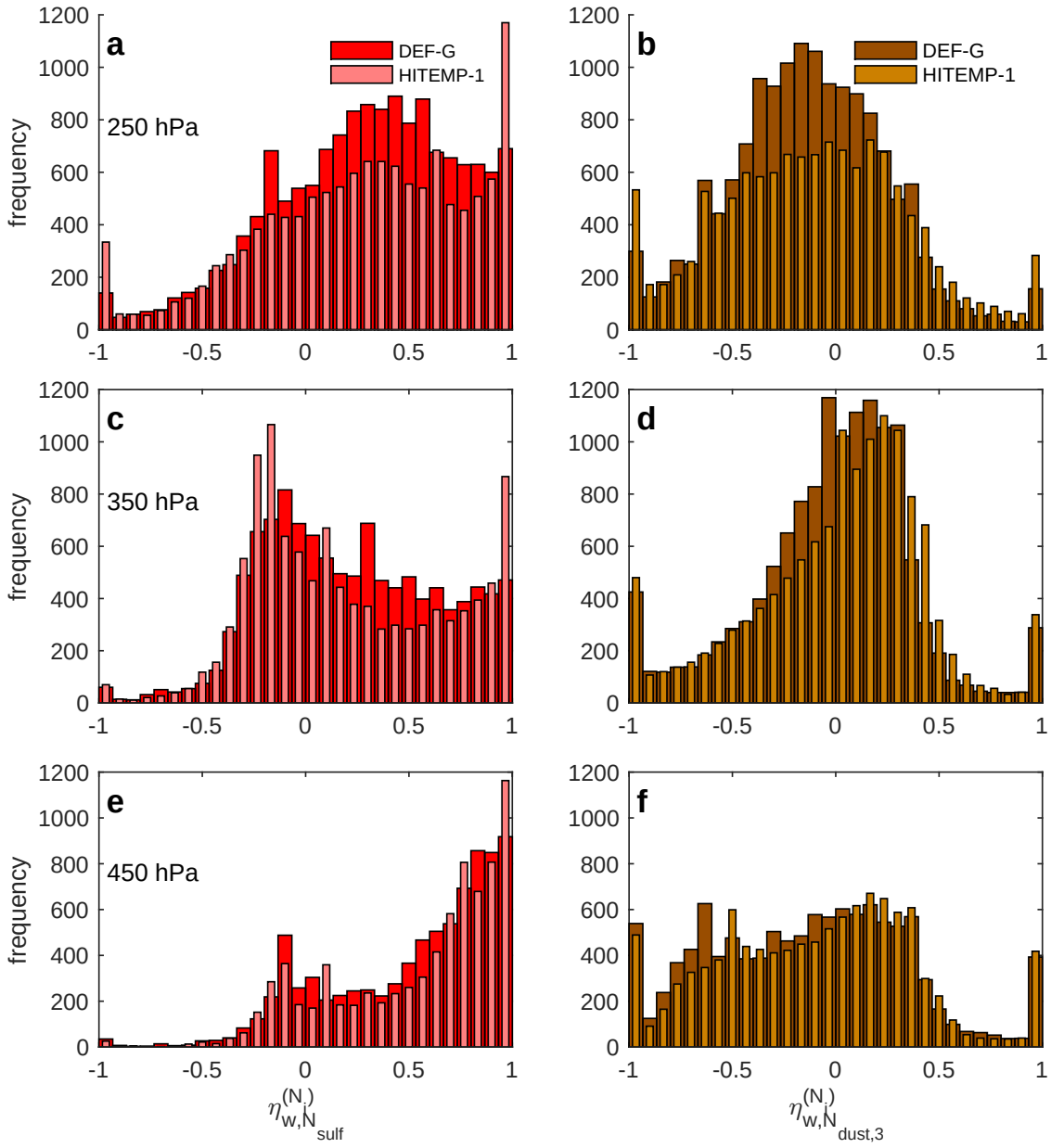

Figure 4.9: Distributions of the updraft-sulfate number sensitivity attribution, $\eta^{(N_i)}_{V,N_{sulf}}$, on the left and the updraft-accumulation mode dust number sensitivity attribution, $\eta^{(N_i)}_{V,N_{dust,3}}$ on the right. Values from both the DEF-G and HITEMP-1 simulations at ***(a), (b)*** *250 hPa;* ***(c), (d)*** *350 hPa; and* ***(e), (f)*** *450 hPa. 16380 η values are calculated for each simulation at each pressure level. Anomalies are calculated from each simulation's monthly average, e.g., the updraft anomaly at grid point x_i is $V'(x_i, t_i) = V(x_i, t_i)$ - $\overline{V(x_i)}$, where $\overline{V(x_i)}$ is the monthly-averaged input updraft after filtering out time points with negligible hydrometeor formation.*

Interestingly, while altitudinal dependence remains for this last metric, there is limited dependence on resolution. On average, the ice crystal sensitivity attributions increase in magnitude by only 0.031 between the lower-resolution DEF-G and higher-resolution HITEMP-2 simulation. $\eta^{(Y)}_{x_j,x_k}$ is calculated from instantaneous sensitivities and input values within anomaly series, rather than temporally averaged sensitivities or variances. When attribution metrics use averaged output values, rather than instantaneous ones, they become resolution dependent.

4.6 Temporal averaging and integration time step effects on attribution metrics

An important consideration in the attribution analysis is the effect of temporal averaging and time step. Figure 4.10 shows primary attribution grids from the HITEMP-1 simulation, during which temporal attributions are calculated using means and variances for hourly output. In this case, updraft velocity is the primary contributor for between 26.4% (925 hPa) and 60.2% (825 hPa) of the N_d grid and between 23.7% (250hPa) and 49.2% (450 hPa) of the N_i grid. These values closely resemble the DEF-G attributions. DEF-G2 simulation attributions, for which the GCM integration time step is half of the DEF-G time step, yield $\xi^{(N_X)}_w$ coverage and mean values within 10% of the DEF-G values. Robustness across temporal averaging and integration time step make the adjoint sensitivity attribution metrics particularly useful. The results of these simulations are shown also in Figure 4.3.

4.7 Implications

The GEOS-5 and CAM5 simulations demonstrate the importance of updraft velocity for hydrometeor concentrations. When subgrid-scale variability from turbulence is parameterized, vertical velocity is a dominant contributor to hydrometeor number variability over most of the globe. Although previous work has shown the existence of aerosol- and updraft-dominated hydrometeor formation regimes [e.g., 146], these have not necessarily considered the input variance. Recent work has shown the importance of dynamics for the liquid phase and aerosol for the ice phase. Simmel et al. showed with a small-scale model that changes

in INP number have a larger effect on simulated ice water content or path than changes in dynamic parameters [147]. In contrast, liquid water content or path was more sensitive to adjustments in cloud base or updraft velocity. Collocated Raman and Doppler lidar measurements also confirm that turbulence and entrainment convolute the aerosol-droplet number correlation above the cloud base within altocumulus [148]. Along with studies like these, the attribution metrics presented here are useful in determining if models capture the correct source of N_d and N_i variability.

Future work should focus on eliminating vertical velocity thresholds and include more physical updraft distributions to better predict hydrometeor number and its temporal evolution. Additional updraft measurements will be critically important to this end. Simulated vertical velocity distributions are rarely evaluated against sparse observations, in contrast to relatively frequent evaluation of aerosol properties against relatively abundant data. Updraft measurements must be made, however, at appropriate temporal and spatial resolution and with low enough uncertainty for meaningful evaluations. The temporal attribution fractions here indicate that the most accurate updraft measurements must be made at high latitudes and altitudes. If such accurate measurements are not possible or the approximations in turbulence parameterizations are too great, then irreducible uncertainties in modeled hydrometeor number may remain.

4.8 Chapter 4 Summary

Understanding how dynamical and aerosol inputs affect the temporal variability of hydrometeor formation in climate models will help to explain sources of model diversity in cloud forcing. To better understand the sources of this variability, we have defined metrics for temporal attribution, temporal attribution fraction, and sensitivity attribution here. These are defined from input variances and adjoint sensitivities and calculated for several simulations both with the GEOS-5 and CAM frameworks for a variety of time steps, output resolutions, and durations.

Analysis shows that sensitivity to updraft is fairly high for both droplet and ice crystal numbers in GEOS-5. The former increases with altitude, as the surface sources of aerosol

become less influential, and the latter decreases with altitude, as vertical motions become smaller in the upper troposphere. The nucleation regimes discussed throughout Chapters 2 and 3 are reflected here as seasonality and latitudinal changes in the ice crystal attributions: aerosol is more influential on N_i in the NH and during summer, when heterogeneous nucleation is more frequent.

When the same analysis is performed in CAM, the sensitivities to updraft are much higher. We trace this shift in attribution back to the effects of aerosol module (a formulation which tracks airborne number versus mass) and updraft representation (whether turbulence is parameterized).

A few other notable results are that

- artificial thresholding of the updraft velocity significantly dampens variability in hydrometeor number;
- additional measurements could best constrain model updraft formulations in the tropics because updraft sensitivity is lowest, and variability highest, there, and;
- anomalously large sensitivities to aerosol number are strongly correlated with anomalously large updrafts.

Simulated updraft velocity distributions are rarely evaluated against observations due to the sparsity of relevant data. Our results suggest that coordinated effort by the atmospheric community to develop more consistent, observationally based updraft treatments will help simulate cloud hydrometeor formation more accurately.

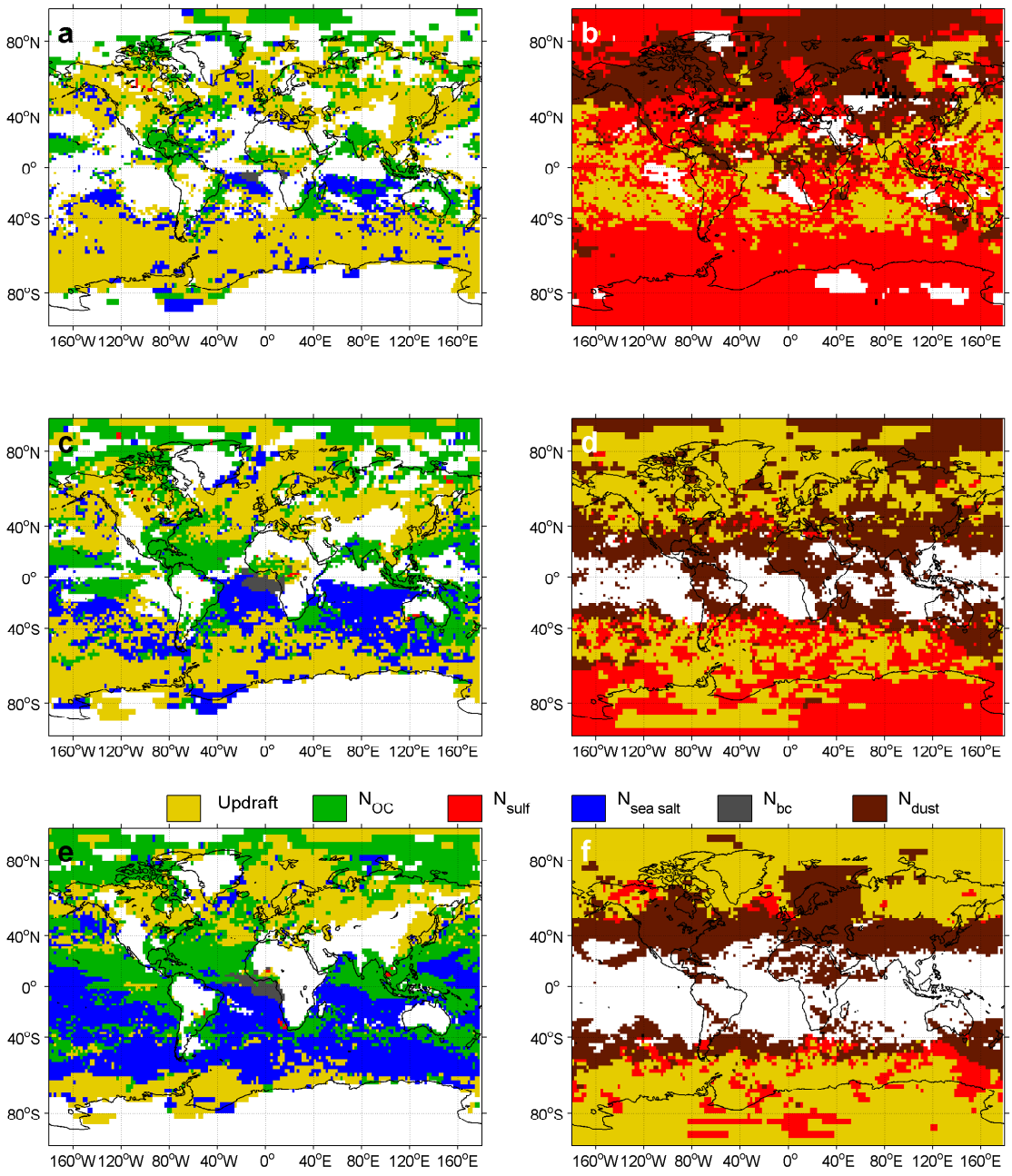

Figure 4.10: As in Figure 4.2 but primary attribution grids with values taken from the HITEMP-1 simulation.

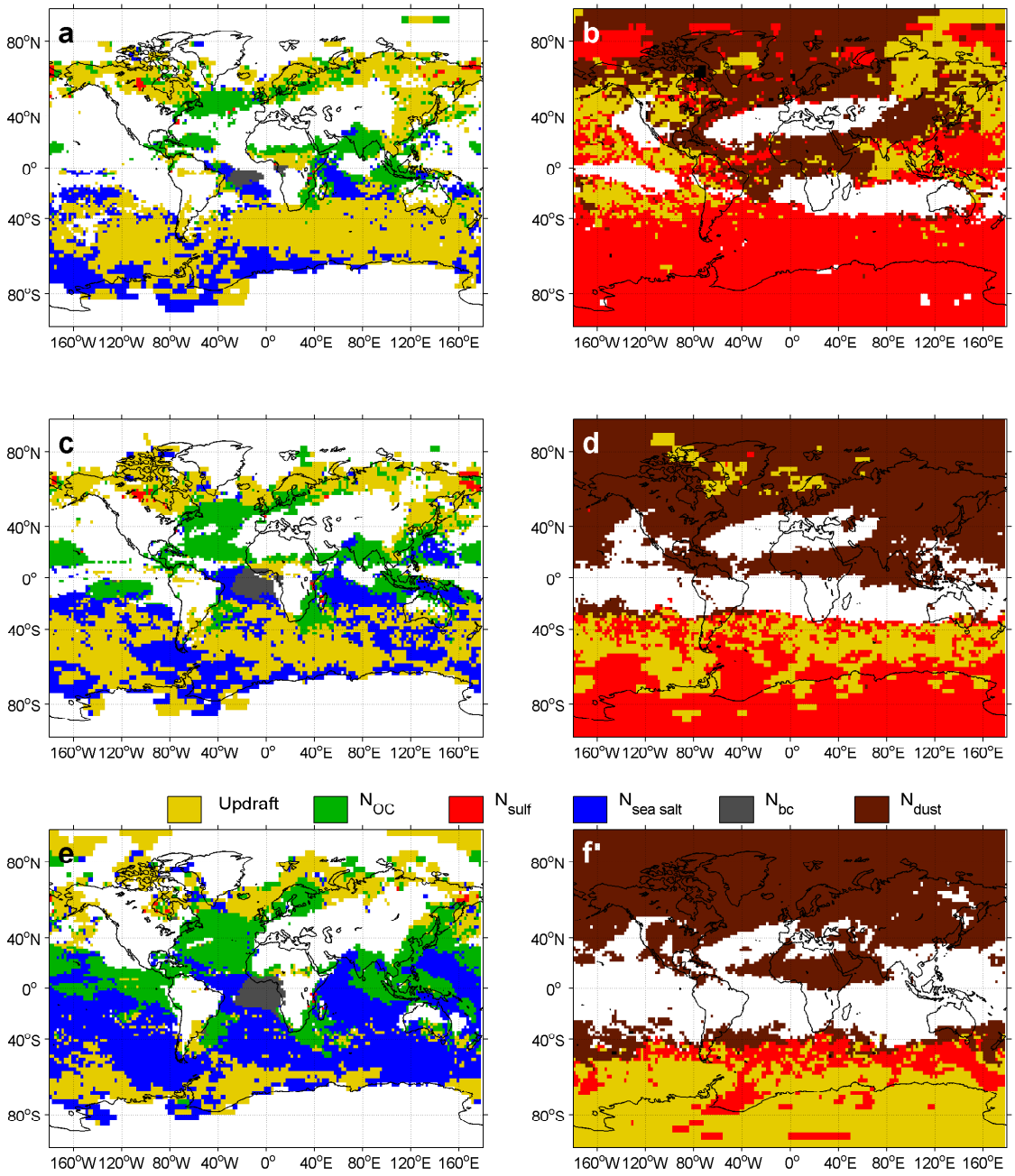

Figure 4.11: As in Figure 4.2 but primary attribution grids with values taken from the HITEMP-2 simulation.

CHAPTER 5
PARCEL MODEL FOR PROCESS-SCALE ANALYSIS

The past three chapters have focused on primary ice nucleation and large-scale modeling frameworks. This chapter shifts gears and considers secondary ice production with a small-scale parcel model. A history of measurements has shown that ICNC can be orders of magnitude higher than INP numbers and that some other process must generate atmospheric ice crystals. Various mechanisms have been proposed, including breakup upon ice hydrometeor collision (analogous to attrition in industrial crystallizers) and rime splintering in which fragile protuberances splinter off as a hydrometeor falls out of the cloud. But the relative importance and even the exact physics of these proposed processes are not well-known. In this chapter, we develop a parcel model with six 'hydrometeor classes' to estimate the potential enhancement in ICNC from these secondary mechanisms.[1]

5.1 In-situ ice crystal measurements

Secondary ice production was discussed in Section 1.1, but a more thorough overview is given here. Ice crystal number concentrations significantly higher than the pre-cloud INP number concentrations have been observed in field studies over the past 40 years [e.g., 150, 7, 8, 151, 10, 152, 153]. ICNC measurements can be made with an imaging probe (like the 2DS that took the measurements plotted in Figure 3.2), which visualizes a particle with a set of photodiodes. Airborne optical particle size spectrometers also measure ice crystal size by shining a laser beam on a particle within a sample volume and measuring the intensity distribution of forward scattered light to determine an equivalent optical diameter (EOD) [154]. Measurements with either of these techniques are difficult: delayed response

[1]Parts of the background section in this chapter are adapted from a review by P. Field, [28 co-authors], and **S. C. Sullivan** (2017) Secondary ice production: Current state of the science and recommendations for the future [13]. The remainder on model development has been resubmitted after revision as **S. C. Sullivan** et al. (2017) Investigating the contribution of secondary ice production to ice crystal number concentrations [149]. Support for the latter came from DOE EaSM and NESSF grants, as well as the President's Initiative and Networking Fund (VH-NG-620). Thanks go in particular to Alexei Kiselev and Thomas Leisner for helpful discussion regarding laboratory experiments on secondary ice production.

of photodiodes causes limited depth-of-field in imaging probes, while EOD changes based on crystal orientation in particle spectrometers [e.g., 155].

Of particular concern in understanding the discrepancy between ICNC and INP numbers is the potential for ice crystal shattering at the probe inlet (Figure 5.1a). This shattering artificially enhances the number of ice crystals with diameter less than 100 μm [156, 157, 158]. In an effort to mitigate these artifacts, probe tips (called K-tips below and shown in Figure 5.1b) have been developed to minimize inlet surface area, airflow disturbances around the inlet, and any inefficient heating that leads to ice build-up on the probe exterior [159, 160]. Overcounting can also be filtered from data with interarrival time (IAT) algorithms, which assume that shattering artifacts arrive in the probe sampling volume in much quicker succession than natural ice crystals do [161, 162, 163]. But even in data sets that use K-tips and IAT filtering, an **"enhancement"** of ice crystal number beyond the INP number has persisted. A list of recent measurements, employing corrective measures and relevant to Chapters 5 to 8, is given in Table 5.1.

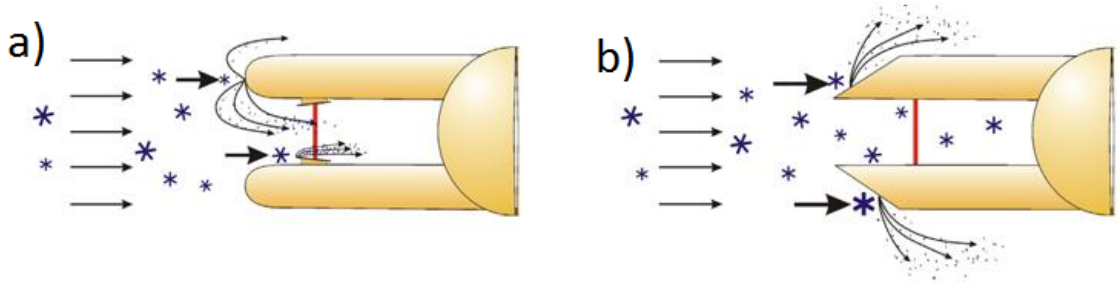

Figure 5.1: (a) Cylindrical tips on an older cloud imaging probe and (b) Korolev tips on an updated, shatter-resistant cloud imaging probe. Images adjusted from www.dropletmeasurement.com and Korolev et al. [164].

5.2 Secondary production mechanisms in this study

A variety of microphysical processes, jointly called **secondary ice production**, has been proposed to explain the ICNC enhancement. For example, the Hallett-Mossop rime splintering (RS) process refers to the production of ice splinters after supercooled droplets rime onto small graupel [165]. It occurs principally for cloud temperatures between 265 and 270 K [165, 7], cold enough that impacting drops freeze on an ice surface, forming **rime**, but

warm enough that they spread out beforehand and form a fragile ice shell that splinters upon internal pressure build-up [166, 167]. A broad droplet size distribution, with large droplets of diameter greater than 24 μm and small ones of less than 13 μm, also facilitates this process [165, 150]. Mossop has hypothesized that small droplets form fragile rime that can then be shattered by impact with larger droplets [168]. In addition, the graupel which undergoes riming must have an appreciable terminal velocity, of about 0.7 m s^{-1} or greater [165, 7]. This process is self-sustaining, as these ice splinters can depositionally grow to a rimable size in a matter of minutes.

Table 5.1: ***ICNC enhancements from observations relevant to this work***
Campaigns: APPRAISE = Aerosol Properties, PRocesses And InfluenceS on the Earth's climate; NAMMA = NASA African Monsoon Multidisciplinary Analyses; ICE-T = Ice in Clouds Experiment-Tropical; COPE = COnvective Precipitation Experiment; HAIC-HIWC = High Altitude Ice Crystals - High Ice Water Content project
Instrumentation: CDP = Cloud Droplet Probe; CIP = CCD Imaging Probe; 2D-S = Two-dimensional Stereo Probe; 2D-C = Two-dimensional Cloud Probe; FSSP = Forward Scattering Spectrometeor Probe; CAS = Cloud Aerosol Spectrometer; IATF = Interarrival time filtering; OAP = Optical Array Probe; CPI = Cloud Particle Imager; K-tips = shatter-resistant cloud probe tips [164]; SID-2H = Small Ice Detector-2 High-Performance Instrumented Airborned Platform for Enviromental Research

Source	***Technique***	***Enhancement***	***Conditions***
1. Crawford et al. [153] APPRAISE	CDP, CIP-100, 2DS	$N_i \sim \mathcal{O}$ (100 L^{-1}) for $N_{INP} \sim \mathcal{O}$ (0.01 L^{-1})	Shallow convection $T_{top} \approx -7.5°C$ $\overline{w}$ = 1-2 m s^{-1}
2. Crosier et al. [169] APPRAISE	CDP, CIP-100 (with IATF) 2D-S	N_i (2 km, -8°C) = 10-100 L^{-1} while $N_i(< 2$ km$) \sim \mathcal{O}$ (1 L^{-1})	Cold frontal rainband T_{top} = -10 to -50°C $(w_{max}, \overline{w})$ = (6.9, 2) m s^{-1}
3. Heymsfield & Willis [170]; NAMMA	CAS (0.5-50 μm with IATF) 2D-S (> 25-50 μm)	$\overline{N_i}\,(D_i > 125\mu$m) = 108.5 L^{-1} for $N_{INP} \approx$ 1-2 L^{-1}	Mesoscale convection $0 < T <$ -15°C w = 0-5 m s^{-1}
4. Lasher-Trapp et al. [171]; ICE-T	FSSP (2-47 μm), 2D-C (both with IATF); SID-2H	$N_i^{(max)}\,(D_i > 100\,\mu$m) = 126 L^{-1} for N_{INP} = 0.001-0.05 L^{-1}	Maritime cumuli $T_{top} \approx$ 14°C, T = -6 to -10°C $w(N_i^{(max)})$ = 1.5 m s^{-1}
5. Taylor et al. 2016 COPE	CDP, 2D-S, CIP-100 (all with IATF and K-tips)	$\overline{N_i}$ = 137 L^{-1} (mature turret) with $N_{INP,top}$ = 1.2 L^{-1}	Line of convective cells (T, T_{top}) = (-12, -16)°C $w(N_i^{(max)} \approx$ 1-2 m s^{-1}
6. Ladino et al. 2017 HAIC-HIWC	FSSP-100, OAP, 2DC, 2D-S (all with IATF and K-tips)	$\overline{N_i} \approx 200$ L^{-1} N_{INP} (−5°C) $\approx 10^{-3}$ L^{-1} N_{INP} (−14°C) $\approx 10^{-1}$ L^{-1} as in DeMott et al. [123]	Mesoscale convection T = -5 to -15°C

Rime splintering parameterizations generally depend on the mass of rimed droplets, enhanced by a fixed fragment number and weighted by a temperature efficiency. Others depend instead on the number of rimed droplets that are larger than a threshold size. Blyth et al. ran a multi-trajectory cloud model with such a parameterization and introduced nucleated ice crystals at the top of a thermal, assuming that 50 ice splinters were produced per milligram of rime [172]. They found that ice crystal number enhancement was most sensitive to the liquid water content. Cardwell et al. implemented a new microphysics scheme with explicit hydrometeor size distributions, an RS parameterization, and embedded convection in the Hadley Centre climate model [173]. Their RS parameterization assumed 200 ice splinters produced per milligram of rime, and its influence was greatest for thermals ascending fast enough to facilitate riming. Many other studies have also examined the effect of rime splintering within three-dimensional frameworks [e.g., 174, 175, 176, 177, 178].

In some cases, however, the rime splintering process alone cannot explain observed ice crystal number enhancements [e.g., 179, 7, 180]. Laboratory experiments show that about one splinter is produced per milligram of rime [e.g., 181, 182], while a value on the order of 100 is needed to reproduce some observations [179]. Temperature and droplet size distributions do not always favor the RS process [183], and a second peak in ice crystal number enhancement around 258 K has been observed [184, 185]. Finally, such large number concentrations appear quite quickly: hundreds of ice crystals per liter can form within 10 to 15 minutes [e.g., 9, 151, 180], a time frame too rapid to be explained by rime splintering alone. Although estimates depend on factors like updraft and liquid water content, a calculation by Mason shows that the cloud should exist for about an hour to generate observed enhancements solely from rime splintering [167].

Breakup upon mechanical collision of two ice hydrometeors (**breakup** hereafter) has been suggested as an additional mechanism in the development of such large ice number concentrations [e.g., 186, 14, 15]. In particular, Takahashi et al. performed laboratory experiments in which they saw a maximum in the number of ejected ice crystals around 257 K [15]. Few breakup parameterizations have been developed, and they have not been incorporated into models. Vardiman calculated a fragment generation rate as the product of collision frequency and a fragment number, dependent on the change in momentum be-

tween the two colliding hydrometeors [14]. Simulations showed that the mechanism could be important under quite limited conditions, but particularly for embedded convective clouds. More recently, Yano and Phillips developed a zero-dimensional, time-lag model and identified an atmospherically relevant regime of explosive ice crystal generation by breakup based on two non-dimensional parameters [187].

In calculating potential ice crystal number enhancements, other counteracting microphysics should be considered. In particular, ice-ice aggregation is most efficient around 258 K [188, 189], the same temperature for which breakup seems to be most active. This aggregation may occur through interlocking of dendritic branches, electrostatic forces, or regelation [190, 191]. Appropriate collection kernels or sticking efficiencies have been recently developed. For example, Field et al. used sweep-out, sum, and modified-Golovin collection kernels to reproduce ice crystal size distributions that were affected by aggregation during the Cirrus Regional Study of Tropical Anvils and Cirrus Layers - Florida Area Cirrus Experiment (CRYSTAL-FACE) campaign [113]. They obtained the most accurate reproductions using a modified-Golovin kernel. Phillips et al. parameterized sticking efficiency of ice crystals on snow or graupel as an exponential function of collisional kinetic energy and a thermal smoothness coefficient to describe surface texture effects [192].

5.2.1 Mechanisms not considered here

Contact nucleation refers to the impact of an INP with a liquid droplet that leads to its freezing. This nucleation process may be enhanced by phoretic forces [8, 193, 10], which refer to the movement of the INP through the surrounding gas toward the droplet due to local temperature or concentration gradients or radiation pressure. These three forces are called thermophoresis, diffusiphoresis, and photophoresis respectively. For large particles, the description becomes more complicated as a gradient can be established within the particle itself. Heymsfield and Willis have commented that these gradients are likely too weak and the INP-droplet collisions too slow to have a meaningful contribution to ice formation [170].

It has also been suggested that pre-activated INP may enhance ICNC [10, 46]. **Pre-activation** refers to the observation that certain particles after having once nucleated ice,

nucleate subsequent times at a warmer temperature or lower supersaturation [194, 195]. The exact mechanism is uncertain, but it has been suggested that remnants of the crystalline ice structure remain in hydrophilic pores or surface features, templating ice during future exposure to supersaturation. INP may also be recycled in and out of a cloud: ice crystals fall below the cloudy air, sublime, and are later carried back into the cloudy air to re-nucleate. Coupling of preactivation and INP recycling may dramatically increase ICNC.

5.3 Parcel model

Given the large parametric and even process uncertainties for secondary ice production, the work in the next few chapters takes a reductionist approach. A parcel model with a minimal number of hydrometeor classifications is constructed to estimate relative contributions, favorable conditions, and the minimum INP number necessary for initiation. The rest of this chapter focuses on model development.

5.3.1 Hydrometeor number tendencies

The model tracks six interacting hydrometeor classes for small ice crystals and droplets, small and large graupel, and medium and large droplets. The simulations are generally initialized with no hydrometeors present; once these begin to form, the sizes in each class are initialized with values in Table 5.2 and evolved according to growth equations. For small ice crystals, a generation function, G_{ice}, is defined as the summation of primary nucleation and secondary production by breakup and rime splintering:

$$G_{ice}(t) = c_0\big(T(t)\big)H(t)+\eta_{br}K_{br}\aleph_{br}N_g(t)N_G(t)+\eta_{RS}\Big[K_{RS,g}\aleph_{RS}N_g(t)+K_{RS,G}\aleph_{RS}N_G(t)\Big]N_R(t) \tag{5.1}$$

where c_0 is the nucleation rate; H is the Heaviside function; K are the collection kernels defined below in Equation 5.9; η are process weightings from 0 to 100%; and N_i, N_g, and N_G are ice crystal, small graupel, and large graupel numbers respectively. All variables are also included in the Notation appendix at the end. c_0 is calculated as the product of updraft, V; an assumed lapse rate Γ of 6 K km^{-1}; and the derivative of the temperature-dependent fit to INP data from DeMott et al. 2010 [123]: $c_0 = V\Gamma d/dT\,[a_1 \exp(a_2(T-a_3))]/f_{red}$. The final

f_{red} factor is introduced to account for limited INP at the warmer subzero temperatures where the simulation is initiated. $\aleph_{br}$ is the number of fragments generated upon breakup as a four-parameter distribution of temperature based on data from Takahashi et al. [15]: $\aleph_{br} = F_{br}(T - T_{min})^{1.2}\exp[-(T - T_{min})/\gamma_{br}]$, where F_{br} is a leading coefficient, T_{min} is a lower temperature bound beyond which no breakup occurs, and γ_{br} controls the decay rate of fragment numbers at warmer subzero temperatures. Below -20°C, $\aleph_{br}$ is set to 10 (see Figure 5.3a). $\aleph_{RS}$ is the number of splinters produced per number of large droplets, given the large droplet radius and assuming 300 splinters per milligram of rime [165].

For the liquid phase, the droplet number generation function, G_{drop}, consists simply of the product of droplet activation rate and a Heaviside function:

$$G_{drop}(t) = V\Gamma ds_w/dT \cdot N_{CCN}k_{CCN}s_w(t)^{k_{CCN}-1}H(t) \tag{5.2}$$

where V is updraft velocity, Γ is the lapse rate, ds_w/dT is the temperature derivative of the supersaturation correlation, N_{CCN} and k_{CCN} are the coefficient and exponent of a Twomey power-law CCN spectrum [196], and s_w is liquid supersaturation. Default values for V, N_{CCN}, and k_{CCN} are given in Table 5.2.

The number balance in each class is then the generation function at the current time as a source and the generation function at a time delay as the sink, along with aggregation, rime splintering, and coalescence losses [187]:

$$\frac{dN_i}{dt} = G_{ice}(t) - G_{ice}(t - \tau_i) - \eta_{agg}K_{agg}N_iN_g \tag{5.3}$$

$$\frac{dN_g}{dt} = G_{ice}(t - \tau_i) - G_{ice}(t - \tau_i - \tau_g) - \eta_{agg}K_{agg}N_iN_g \tag{5.4}$$

$$\frac{dN_G}{dt} = G_{ice}(t - \tau_i - \tau_g) - G_{ice}(t - \tau_i - \tau_g - \tau_G) + \eta_{agg}K_{agg}N_iN_g \tag{5.5}$$

$$\frac{dN_d}{dt} = G_{drop}(t) - G_{drop}(t - \tau_d) - \eta_{coal}K_{coal}N_dN_r \tag{5.6}$$

$$\frac{dN_r}{dt} = G_{drop}(t - \tau_d) - G_{drop}(t - \tau_d - \tau_r) - \eta_{coal}K_{coal}N_dN_r \tag{5.7}$$

$$\frac{dN_R}{dt} = G_{drop}(t - \tau_d - \tau_r) - G_{drop}(t - \tau_d - \tau_r - \tau_R) + \eta_{coal}K_{coal}N_dN_r - \eta_{RS}\Big[K_{RS,g}N_g + K_{RS,G}N_G\Big]N_R \tag{5.8}$$

where τ_i is the time for growth of ice crystals to small graupel, τ_g for growth of small to large graupel, τ_G for large graupel to fall out, τ_d for growth of small to medium droplets, τ_r for growth of medium to large droplets, and τ_R for large droplets to fall out. The generation function at time delay represents depositional, riming, or condensational growth of hydrometeors to the next largest size class. Time delays are solved for approximately using growth equations, evolving temperature and material properties but assuming a constant supersaturation and a constant radius for the riming droplets. This set of hydrometeor number tendencies is solved with an explicit Runge-Kutta (2,3) pair extended for delay-differential equations [197].

In the generation functions and number balances above, gravitational collection kernels are used to describe all processes:

$$
\begin{aligned}
K_{br}(t) &= \pi(\xi_G a_G(t)^2 + \xi_g a_g(t)^2)(v_{t,G} - v_{t,g}) \\
K_{RS,g}(t) &= \pi(r_R(t)^2 + \xi_g a_g(t)^2)(v_{t,g} - v_{t,R}) RS_T \\
K_{RS,G}(t) &= \pi(r_R(t)^2 + \xi_G a_G(t)^2)(v_{t,G} - v_{t,R}) RS_T \\
K_{agg}(t) &= \pi(\xi_g a_g(t)^2 + r_i^2)(v_{t,g} - v_{t,i}) \\
K_{coal}(t) &= \pi(r_r^2 + r_d^2) v_{t,r}
\end{aligned}
\tag{5.9}
$$

where ξ is the ratio of actual cross section to that of a circumscribed circle as in Jensen and Harrington [198], a is a spheroidal major axis, r is a radius, and v_t is the hydrometeor terminal velocity as in Mitchell and Heymsfield [199]. Within the coalescence kernel, we assume a coalescence efficiency of 1 and that the terminal velocity of small droplets is negligible relative to that of medium droplets. RS_T is a temperature weighting for the rime splintering process, equal to 50% from 269 to 271 K and from 265 to 267 K, 100% from 267 to 269 K, and 5% from 243 to 265 K [200].

5.3.2 Microphysical assumptions

Figure 5.2 shows a schematic of the model microphysics. In the calculation of the hydrometeor number tendencies, the following simplifying assumptions are made:

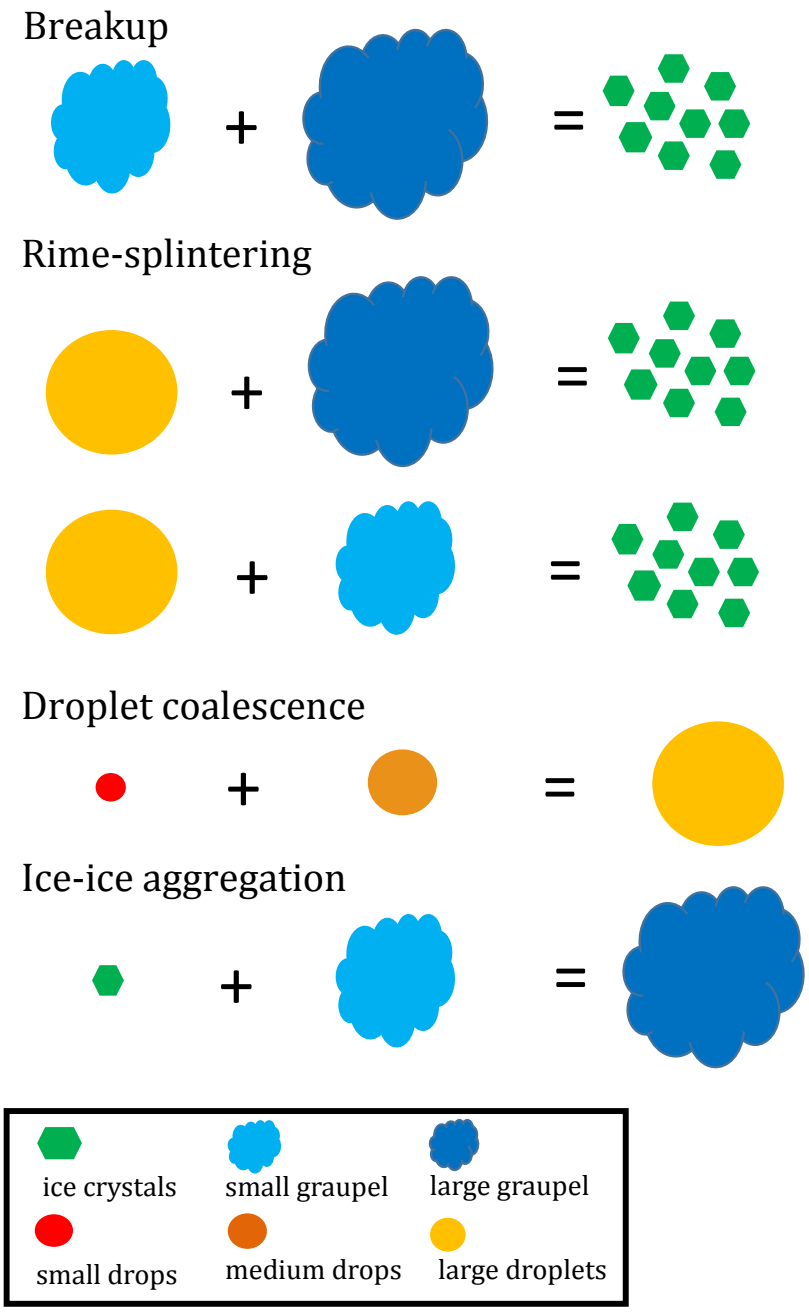

Figure 5.2: Schematic of the simplified, six-bin microphysics. Small and large graupel may break up upon collision to form ice crystals; small and large graupel may rime-splinter to form ice crystals; small and medium droplets may coalesce to form large droplets; and ice crystals and small graupel may aggregate to form large graupel.

1. *Breakup and rime splintering generate ice crystals in the smallest class.*

   All fragments from breakup are assumed to be small ice crystals because there are no laboratory measurements of the fragment size distribution. For rime splintering, experimental evidence indicates that fragments have a size on the order of 10 μm [e.g., 165] (their Figure 1b) and [170] (their Figure 2c), or even smaller [e.g., 182].

2. *Only small and large graupel undergo breakup upon collision.*

   We assume that riming protuberances and sufficient momentum are required for a fragment-generating collision. Small ice crystals do not have elaborate enough geometry or large enough terminal velocity to shatter upon collision. Precedence for these assumptions comes from Vardiman [14]: only for large degrees of riming and relative velocities between hydrometeors did fragments actually form upon breakup during experiments. The results of Takahashi et al. are also relevant only for collisions of larger ice hydrometeors [15]: the apparatus diameter used to simulate breakup was 1.8 cm, orders of magnitude larger than any ice crystal.

3. *Rime splintering occurs on both small and large graupel.*

   The initial major axis of small graupel, a_{g0}, is 50 μm and that of large graupel, a_{G0}, is 200 μm. Ono has shown that riming is rare on columnar ice hydrometeors with a major axis less than 50 μm or on planar ones with a major axis of less than 150 to 200 μm [201].

4. *Aggregation generates graupel in the largest class.*

   Laboratory and field studies have shown that aggregates have a maximum dimension on the order of a few hundred microns. For example, the pristine ice hydrometeors in the cloud chamber study of Connolly et al. have a maximum dimension of about 100 μm (their Figure 6) [189], while aggregates have a maximum dimension of a few hundred microns (their Figure 7). In-situ CPI imagery of Field et al. shows almost no aggregation for hydrometeors collected with diameter 100 μm or less but large numbers of aggregates for those of a few 100 μm diameter [161].

5. *Aggregation occurs between ice crystals and smaller graupel. Coalescence occurs be-*

tween small and medium droplets

Because the initial diameter of the ice crystals, $2r_{i,0}$, is an order of magnitude smaller than the initial major axis of small graupel, we assume that collisions between two ice crystals will be relatively less efficient than collisions between an ice crystal and a small graupel particle, even when N_i is about an order of magnitude larger than N_g. A larger relative terminal velocity between ice crystals and small graupel will also enhance this collection kernel relative to that between two ice crystals. We also do not consider aggregation between large graupel and ice crystals. Hosler et al. performed aggregation measurements for ice crystals of diameter 7 to 13μm and noted that additional contact area beyond a critical overlap does not increase sticking efficiency [188] . And while aggregation may be possible over a large range of sizes, collisions of similarly-sized hydrometeors is most important to initial aggregate formation [189]. Finally the coalescence of small droplets with one another is assumed negligible, given an efficiency around 5% or less according to Klett et al.[202].

5.3.3 Moist thermodynamic tendencies

The hydrometeor number tendencies, Equations 5.3 to 5.8, are coupled to the following moist thermodynamic equations to account for the changing system supersaturation:

$$\frac{dp}{dt} = -\frac{gpu_z}{R_aT} \tag{5.10}$$

$$\frac{dT}{dt} = -\frac{gu_z}{c_p} + \frac{\Delta H_v}{(1+q_v)c_p}\frac{dq_w}{dt} + \frac{\Delta H_s}{(1+q_v)c_p}\frac{dq_i}{dt} \tag{5.11}$$

$$\begin{aligned}\frac{ds_w}{dt} = (1+s_w)\Bigg[&\left(\frac{g\Delta H_v}{c_pR_vT^2} - \frac{g}{R_aT}\right)V - \left(\frac{1}{q_v} + \frac{\Delta H_v^2}{c_pR_vT^2}\right)\frac{dq_w}{dt} \\ &- \left(\frac{1}{q_v} + \frac{\Delta H_v\Delta H_s}{c_pR_vT^2}\right)\frac{dq_i}{dt}\Bigg]\end{aligned} \tag{5.12}$$

$$\frac{dq_w}{dt} = 4\pi\frac{\rho_w}{\rho_a}\left[N_w r_w^2\frac{dr_w}{dt} + N_r r_r^2\frac{dr_r}{dt} + N_R r_R^2\frac{dr_R}{dt}\right] \tag{5.13}$$

$$\frac{dq_i}{dt} = 4\pi\frac{1}{\rho_a}\left[\rho_i N_i r_i^2\frac{dr_i}{dt} + \rho_\Delta\left(N_g\frac{(2+\Gamma_{IG})^2 a_g^{2\Gamma_{IG}+2}}{9c_g}\frac{da_g}{dt} + N_G\frac{(2+\Gamma_{IG})^2 a_G^{2\Gamma_{IG}+2}}{9c_G}\frac{da_G}{dt}\right)\right] \tag{5.14}$$

$$\frac{dq_v}{dt} = -\frac{dq_w}{dt} - \frac{dq_i}{dt} \tag{5.15}$$

$$\frac{dr_d}{dt} = \frac{s_w}{r_d}\left[\frac{\rho_w\Delta H_v^2}{k_aR_vT^2} + \frac{\rho_wR_vT}{e_w(T)\mathcal{D}_v}\right]^{-1} \tag{5.16}$$

$$\frac{dr_r}{dt} = \frac{s_w}{r_r}\left[\frac{\rho_w\Delta H_v^2}{k_aR_vT^2} + \frac{\rho_wR_vT}{e_w(T)\mathcal{D}_v}\right]^{-1} \tag{5.17}$$

$$\frac{dr_R}{dt} = \frac{s_w}{r_R}\left[\frac{\rho_w\Delta H_v^2}{k_aR_vT^2} + \frac{\rho_wR_vT}{e_w(T)\mathcal{D}_v}\right]^{-1} \tag{5.18}$$

$$\frac{dr_i}{dt} = \frac{(\xi s_w + \xi - 1)}{r_i}\left[\frac{\rho_i\Delta H_s^2}{k_aR_vT^2} + \frac{\rho_iR_vT}{e_i(T)\mathcal{D}_v}\right]^{-1} \tag{5.19}$$

$$\frac{da_g}{dt} = \frac{3(\xi s_w + \xi - 1)c_g}{(2+\Gamma_{IG}(T))a_g^{\Gamma_{IG}(T)+1}}\left[\frac{\rho_\Delta\Delta H_s^2}{k_aR_vT^2} + \frac{\rho_\Delta R_vT}{e_i(T)\mathcal{D}_v}\right]^{-1} \tag{5.20}$$

$$\frac{da_G}{dt} = \frac{3(\xi s_w + \xi - 1)c_G}{(2+\Gamma_{IG}(T))a_G^{\Gamma_{IG}(T)+1}}\left[\frac{\rho_\Delta\Delta H_s^2}{k_aR_vT} + \frac{\rho_{\Delta G}R_vT}{e_i(T)\mathcal{D}_v}\right]^{-1} \tag{5.21}$$

The hydrostatic approximation is made for pressure evolution in Equation 5.10, and Equation 5.11 is the adiabatic energy conservation equation. Equation 5.12 is the supersaturation balance, derived for a mixed-phase parcel in Korolev et al. [208] (their Appendix A). Equations 5.13 to 5.15 are liquid, ice, and vapor mixing ratio evolutions, and Equations 5.16 to 5.21 are the growth equation for droplet and crystal radii and graupel axes. Calculation of

thermodynamic values like heat of sublimation and vaporization is detailed next.

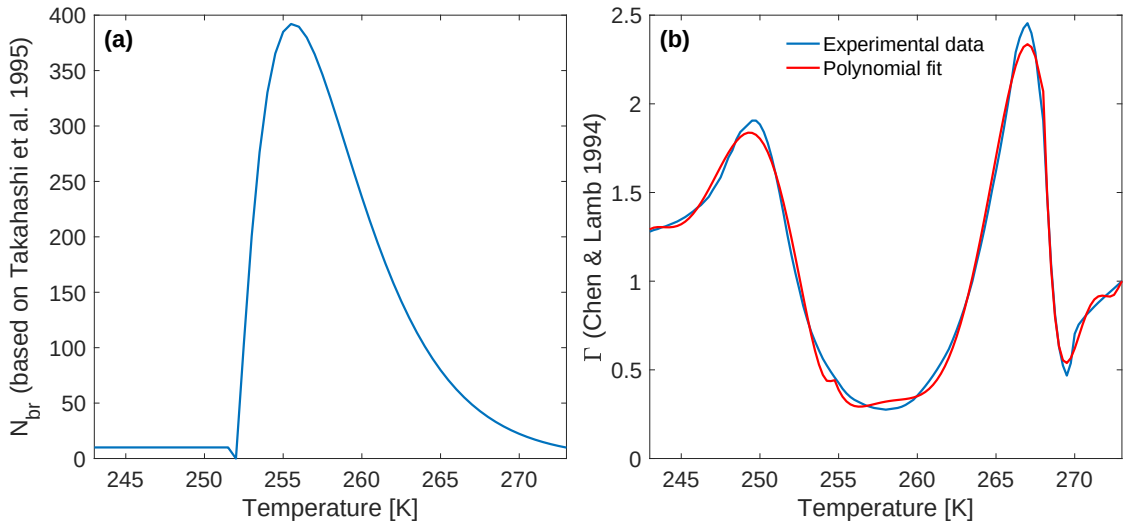

Figure 5.3: ***(a)*** *Fragment generation function as a function of temperature, $\aleph_{br}(T)$, based upon laboratory data of Takahashi et al. 1995;* ***(b)*** *Inherent growth factor as a function of temperature $\Gamma_{IG}(T)$ from Chen and Lamb 1994, as in their Figure 3.*

Recently-nucleated ice crystals are assumed to be spherical with a radius, r_i; bulk ice density, ρ_i; and unit capacitance. Graupel is assumed to be spheroidal with a horizontal axis, a_g or a_G; deposition density, ρ_Δ; and capacitance according to McDonald [209]. The model uses the mass distribution hypothesis of Chen and Lamb [210] to describe the relative depositional growth of spheroidal axes. A temperature-dependent polynomial, $\Gamma_{IG}(T)$, is fit to the inherent growth factor data in Figure 5.3b. In general, a single updraft velocity is prescribed, but one simulation performs a Monte Carlo sampling of a Gaussian updraft distribution to mimic the effects of turbulent velocity fluctuations. This set of thermodynamic tendencies is solved with a modified Rosenbrock formula of order 2 [211].

5.3.4 Thermodynamic correlations and parameters

For heat of sublimation, ΔH_s, a temperature-dependent correlation of Rogers and Yau [212] is used. The correlation for the latent heat of vaporization of supercooled liquid is used

from Murphy and Koop [213].

$$\Delta H_s \approx 10^3 \Big[2834.1 - 0.29(T - 273.15) - 0.004(T - 273.15)\Big] \tag{5.22}$$

$$\Delta H_v \approx 56579 - 42.212T + \exp[0.1149(281.6 - T)] \tag{5.23}$$

Capacitances of small and large graupel are calculated via an electrostatic analogy, according to McDonald [209]:

$$c = \begin{cases} \frac{a\Omega}{\arcsin\Omega} & \Gamma_{IG} > 1 \ \text{(oblate hydrometeor)} \\ \frac{\Psi}{\ln(a^{\Gamma_{IG}-1} + a^{-1}\Psi)} & \Gamma_{IG} < 1 \ \text{(prolate hydrometeor)} \end{cases} \tag{5.24}$$

where

$$\Omega = \sqrt{1 - a^{2(\Gamma_{IG}-1)}} \ \text{ and}$$
$$\Psi = \sqrt{a^{2(\Gamma_{IG}-1)} - a^2}$$

The temperature-dependent correlation of thermal conductivity and saturation vapor pressure over water and ice are used from Kannuluik and Murphy and Koop respectively [214, 213]:

$$k_a = 0.024\Big[1 + 0.00317(T - 273.15) - 2.1 \times 10^6 (T - 273.15)^2\Big] \tag{5.25}$$

$$\begin{aligned} e_w = \exp\Big[&54.842 - 6763.22/T - 4.210 \ln T + 0.000367\, T + \\ &\tanh[0.0415(T - 218.8)](53.878 - 1331.22/T - \\ &9.44523 \ln T + 0.01402T\Big] \end{aligned} \tag{5.26}$$

$$e_i = \exp\Big[9.550 - 5723.265/T + 3.5306 \ln T - 0.00732833\, T\Big] \tag{5.27}$$

Viscosity comes from the Sutherland model, and diffusivity from the temperature- and pressure-dependent correlation given in Seinfeld and Pandis [215]:

$$\mu = 18.27 \times 10^{-6} \frac{411.15}{T + 120} \left(\frac{T}{291.15} \right)^{3/2} \tag{5.28}$$

$$\mathcal{D}_v = \frac{0.211}{p} \left(\frac{T}{273} \right)^{1.94} \tag{5.29}$$

Hydrometeor terminal velocities are calculated according to Mitchell and Heymsfield [199]:

$$Re = \frac{\rho v_t L_c}{\mu} = \frac{\delta^2}{4} \left[\left(1 + \frac{4X^{1/2}}{\delta^2 B_0^{1/2}} \right) - 1 \right]^2 \tag{5.30}$$

where the characteristic length L_c in the Reynolds number is taken to be the hydrometeor radius or axis; δ and B_0 are parameters accounting approximately for surface roughness; and X is the Davies number. Finally the temperature dependence of densities and heat capacities is neglected: ρ_a is taken as 1.395 kg m^{-3}, ρ_i as 919 kg m^{-3}, ρ_w as 998 kg m^{-3}, and c_p as 1850 J kg^{-1} K^{-1}. The inherent growth factor and fragment generation function upon breakup versus temperature are shown in Figure 5.3.

5.4 Chapter 5 Summary

Since the 1960s, certain field measurements have shown ICNC to be orders of magnitude larger than the INP number, meaning that processes other than primary nucleation must generate atmospheric ice. These measurements, generally taken with imaging probes or particle spectrometers, may be subject to shattering at an inlet. But even after use of shatter-resistant probe tips or artifact-removal algorithms, large discrepancies have remained, supporting various hypothesized secondary ice production mechanisms. In particular, rime splintering refers to the splintering off of fragile protuberances as an ice hydrometeor falls out of a cloud. Shatter due to the impact of a mechanical collision, called breakup here, has also been proposed.

It is not yet appropriate to describe these processes at a global scale, given large parametric and process uncertainties and only localized field measurements (Table 5.1). Instead a minimalistic parcel model is constructed here to estimate the upper bound of an en-

hancement from this secondary production. It includes classes for small ice crystals and droplets, small and large graupel, and medium and large droplets. The depositional, condensational, or riming growth of these hydrometeors is described with a set of time-delay equations. These hydrometeor number tendencies are coupled to a set of moist thermodynamic tendencies and solved iteratively. A novel feature of the model is the inclusion of ice hydrometeor non-sphericity through an empirical 'inherent growth factor'.

Table 5.2: Default model values for all parameters

Parameter		**Value**	**Source**
Process weightings	η_{coal}	100%	
	η_{agg}	100%	
	η_{br}	100%	
	η_{RS}	100%	
Initial conditions	N_{X0}	0 cm^{-3}	
	r_{d0}	1 μm	Mossop 1978 [168, 7]
	r_{r0}	12 μm	Mossop 1978 [168, 7]
	r_{R0}	25 μm	Mossop 1978 [168, 7]
	r_{i0}	5 μm	Zhang et al. 2014 [203]
	a_{g0}	50 μm	Reinking 1975 [204]
	a_{G0}	200 μm	Reinking 1975 [204]
	T_0	272 K	
	P_0	680 hPa	
	$s_{w,0}$	10^{-6}%	
Time scales	τ_d	5 min	Approximate solution of Eq. 5.16
	τ_r	15 min	Approximate solution of Eq. 5.17
	τ_R	25 min	Approximate solution of Eq. 5.18
	τ_i	7.5 min	Approximate solution of Eq. 5.19
	τ_g	20 min	Approximate solution of Eq. 5.20
	τ_G	17.5 min	Approximate solution of Eq. 5.21
Time step	Δt	6 sec	
Droplet spectrum	k_{CCN}	0.308	Hegg 1992 [205]
	N_{CCN}	100 cm^{-3}	Hegg 1992 [205]
Updraft	V	2 m s^{-1}	Korolev et al. 2008[206]
			Bühl 2015 [207]
Terminal velocity	B_0	0.6	Mitchell and Heymsfield 2005 [199]
	δ	5.83	Mitchell and Heysmfield [199]
Nucleation reduction	f_{red}	10^2	

CHAPTER 6
ASSESSING THE CONTRIBUTION OF SECONDARY PRODUCTION TO ICE CRYSTAL NUMBER

Here the parcel model from the previous chapter is used to estimate the maximum possible ICNC enhancement in the parameter space and to identify atmospherically relevant conditions for which a maximal enhancement occurs. We also consider the relative contributions of rime splintering and breakup to ICNC and the effect of including graupel non-sphericity or turbulence.[1]

6.1 Simulation setup for enhancement estimates

Twelve simulations are run with the parcel model from the previous chapter, as detailed in Table 6.1. The first set - Cases 1, 2, and 3 - use process weightings before the breakup and rime-splintering tendencies in G_{ice} and before the aggregation and coalescence tendencies in Equations 5.3 to 5.8. These process weightings are denoted respectively η_{br}, η_{RS}, η_{agg}, and η_{coal}. The processes are turned off ($\eta_X = 0\%$) or set at moderate ($\eta_X = 50\%$) or high ($\eta_X = 100\%$) values to estimate a range of values for N_{ice}, the total number of ice phase hydrometeors. The weightings act as a mathematical tool to investigate how hydrometeor numbers evolve when conditions favor different processes.

In Case 1, secondary production via rime-splintering and breakup is turned off, while Case 3 promotes secondary production with high weightings. Case 2 is intermediate with moderate weightings for all processes. These first three cases are run with the default values listed in Table 5.2. They are initiated for an unsaturated parcel just below the freezing temperature at a mixed-phase pressure level, ascending at a modest convective updraft.

Cases 1 to 3 are then rerun, assuming sphericity for all ice hydrometeors, and denoted

[1]This work has been resubmitted after revision as **S. C. Sullivan** et al. Investigating the contribution of secondary ice production to ice crystal number concentrations [149]. Support came from DOE EaSM and NESSF grants, as well as the President's Initiative and Networking Fund (VH-NG-620). Thanks go to Alexei Kiselev and Thomas Leisner for helpful discussion.

Case 1S, 2S, and 3S respectively. The description of non-sphericity is removed by replacing deposition density with bulk ice density and graupel major axes by radii. The inherent growth factor and graupel capacitances are set to unity, and the graupel terminal velocities and collection kernels are calculated as for the other spherical hydrometeors. All other parameters and weightings remain the same as in Cases 1, 2, and 3. Another variant of these cases is run as Case 2T and 3T, in which a small ensemble of simulations is run with updrafts set at each time step by Monte-Carlo sampling from a normal distribution.

Case 4A and 4B investigate the maximum contribution of breakup to secondary production. Case 4A adjusts process weightings and parameters to favor breakup: rime-splintering and coalescence are turned off, the updraft is decreased, the nucleation rate is increased, and the simulation is run with some small and large graupel initially. Case 4B adjusts growth times to favor breakup: rime-splintering is allowed to occur again with low weighting, and the initial temperature is lowered to 265 K, elongating the characteristic times for the liquid phase. Case 4AT and 4BT use the same setup as Cases 4A and 4B but with an ensemble of Monte-Carlo sampled updrafts as in Case 2T and 3T.

Finally, three points are defined in the parameter space with conditions similar to particular cloud states. A continental convective (CC) case has a stronger updraft and steeper CCN spectrum [81]. Continental aerosol loading can be quite high, so the initial droplet radius is smaller than the default value, and the characteristic times for all hydrometeors are shorter because a stronger updraft yields faster growth rates. For an Arctic stratocumulus (AS) case, updraft is lowered and a more gradual CCN spectrum is chosen. Aerosol loading is generally lower, so the run is initialized with larger droplet and ice crystal radii. Characteristic times are adjusted to account for the different initial sizes, lower updraft, and colder initial temperature. Finally, a maritime convective (MC) case lies between the CC and AS cases, as Case 2 did above: updraft, CCN spectrum, and initial hydrometeor size are all intermediate. Characteristic times are adjusted for the updraft and initial sizes.

Table 6.1: All simulations with process weightings or parameters adjusted from the default values in Table 5.2. All τ values are given in minutes.

Case 1	***Case 2***	***Case 3***
Suppress secondary production	All processes equally weighted	Promote secondary production
$\eta_{RS}, \eta_{br} = 0\%$	$\eta_{coal}, \eta_{agg}, \eta_{RS}, \eta_{br} = 50\%$	$\eta_{agg}, \eta_{coal} = 0\%$
Case 1S	***Case 2S***	***Case 3S***
Suppress secondary production	All processes equally weighted	Promote secondary production
Assume sphericity	Assume sphericity	Assume sphericity
$\rho_\Delta = \rho_i$	$\Gamma_{IG}(T) = 1$ $a_{g,G} = r_{g,G}$	$c_{g,G} = 1$
	Case 2T	***Case 3T***
	All processes equally weighted	Promote secondary production
	Include turbulence	Include turbulence
	$V = \mathcal{N}(\mu = 2 \text{ m s}^{-1}, \sigma = 0.4 \text{ m s}^{-1})$	
Case 4A	***Case 4B***	
Promote breakup	Promote breakup	
Adjust process weightings	Adjust characteristic times	
$\eta_{coal}, \eta_{RS} = 0\%$	$\eta_{coal} = 0\%$ $\eta_{RS} = 1\%$	$(\tau_d, \tau_r, \tau_R) = (7.5, 15, 35)$
$V = 0.75 \text{ m s}^{-1}$	$V = 0.75 \text{ m s}^{-1}$	$(\tau_i, \tau_g, \tau_G) = (7.5, 20, 17.5)$
$N_{g0} = N_{G0} = 10 \text{ m}^{-3}$	$N_{g0} = N_{G0} = 10 \text{ m}^{-3}$	
$f_{red} = 10$	$f_{red} = 10$ $T_0 = 265 \text{ K}$	
Case 4AT	***Case 4BT***	
Promote breakup	Promote breakup	
Include pseudo-turbulence	Include pseudo-turbulence	
$V = f(\mu = 0.75 \text{ m s}^{-1}, \sigma = 0.25 \text{ m s}^{-1})$		
Case CC	***Case MC***	***Case AS***
Continental convective	Maritime convective	Arctic stratocumulus
$r_{d0} = 0.5 \ \mu\text{m}$	$r_{i0} = 7.5 \ \mu\text{m}$	$r_{d0} = 5 \ \mu\text{m}$ $r_{i0} = 10 \ \mu\text{m}$
$N_{CCN} = 300 \text{ cm}^{-3}$	$N_{CCN} = 125 \text{ cm}^{-3}$	$N_{CCN} = 10 \text{ cm}^{-3}$
$k_{CCN} = 0.9$	$k_{CCN} = 0.3$	$k_{CCN} = 0.5$
$V = 3 \text{ m s}^{-1}$	$V = 2 \text{ m s}^{-1}$	$V = 1 \text{ m s}^{-1}$ $T_0 = 268 \text{ K}$
$(\tau_d, \tau_r, \tau_R) = (1.5, 4.5, 9)$	$(\tau_d, \tau_r, \tau_R) = (2, 6, 12)$	$(\tau_d, \tau_r, \tau_R) = (4.5, 18, 25)$
$(\tau_i, \tau_g, \tau_G) = (7.5, 12.5, 12.5)$	$(\tau_i, \tau_g, \tau_G) = (7.5, 22.5, 12.5)$	$(\tau_i, \tau_g, \tau_G) = (9, 22.5, 12.5)$

6.2 Parcel model results

6.2.1 Process Weightings

The ice hydrometeor number evolution for Cases 1, 2, and 3 is shown below in Figure 6.1. The simulations run until the parcel becomes subsaturated with respect to liquid, a duration that is longest for Case 1 when secondary ice production is turned off. Only when a large number of small ice crystals are formed is depositional growth rapid enough to deplete supersaturation. When the secondary production is turned on, formation of large hydrometeors also plays a role in the simulation duration: once large droplets or graupel form, they feed into the rime-splintering or breakup tendencies respectively and form the supersaturation-consuming ice crystals. When aggregation is suppressed in Case 3, small graupel are not efficiently consumed, and their growth speeds up the subsaturation in Case 3 relative to Case 2. The formation of large droplets and graupel around 20 and 28 minutes respectively is also reflected in the timing of the large and sudden enhancements in N_{ice}.

Of greater interest is the total ice hydrometeor number, N_{ice}, before subsaturation. The fewest ice hydrometeors form in Case 1: N_{ice} reaches a maximum of only 0.113 L^{-1} over 56.9 minutes. In Case 2, the maximum N_{ice} is two orders of magnitude higher at 31.9 L^{-1} over about half that time. If the Case 1 and 2 N_{ice} values at the same time point around 30 minutes are compared, the ice crystal number enhancement is instead four orders of magnitude (0.0062 L^{-1} relative to 31.9 L^{-1}). Finally N_{ice} reaches a maximum of 24.6 L^{-1} in Case 3. Although secondary ice production weightings are high, these tendencies require large droplets or graupel. When droplet coalescence and aggregation are suppressed, these large hydrometeors are only slowly formed by growth from smaller hydrometeor classes.

Along with the static metrics of simulation duration and maximum N_{ice}, the overall simulation structure indicates which processes are most influential when. Droplets activate rapidly early on up to an N_d of a couple hundred per cm^3 for all cases, until supersaturation peaks and begins to drop off. After about 5 minutes, the small droplets have had enough time to grow by condensation to medium droplets. Large droplets form thereafter, most quickly in Case 1 when droplet coalescence is promoted.

In the ice phase, new ice crystals nucleate throughout the simulation, and small graupel

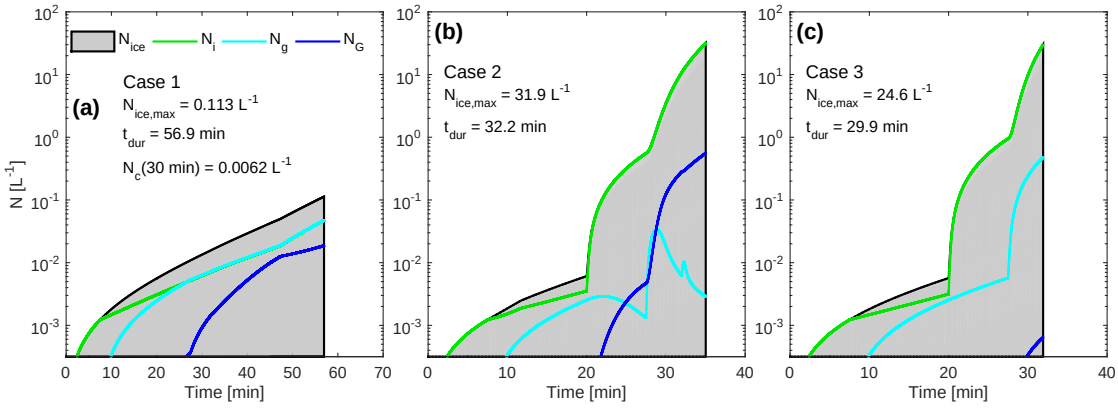

Figure 6.1: Ice hydrometeor number evolution for Case 1 in panel ***(a)****, 2 in panel* ***(b)****, and 3 in panel* ***(c)****. N_i denotes the number of ice crystals, N_g small graupel, and N_G large graupel. The total ice hydrometeor number, N_{ice}, is shaded in gray, and the maximum ice number, $N_{ice}^{(max)}$, and simulation duration, t_{dur}, are given for each case.*

begin to form after 7.5 minutes. Formation of small graupel stunts the increase in N_i: their growth consumes supersaturation and the aggregation sink activates. Formation of large graupel, on the other hand, boosts the increase in N_i because generation from rime-splintering and breakup initiates. Part of the reason that $N_{ice}^{(max)}$ is lower in Case 3 than in Case 2 is that the large graupel number stays very low in the former. In Case 2, N_G can reach higher values due to active aggregation. A final point is that small graupel act as 'limiting hydrometeor class', when ice crystal number enhancement is largest in Case 2. Small graupel feed the breakup tendency both directly through the collision itself and indirectly through aggregation to generate large graupel. Small graupel also rime-splinter, and these numerous sinks mean they are quickly consumed and can limit secondary production.

Referring to the measurements in Table 5.1, these values and evolution are comparable to those from Crawford et al., Heymsfield and Willis, and Lasher-Trapp et al. [153, 170, 171] with modest updraft, warmer in-cloud temperatures, and $(N_{INP}, N_i^{(max)}) \sim \mathcal{O}$ (0.01 or lower L^{-1}, 100 L^{-1}). These studies explained the observed enhancement solely with rime splintering, and indeed for our simulations, the contribution of rime splintering is greater than 90% for both Case 2 and 3. Given the large cloud depth in Lasher-Trapp et al. [171], these cases replicate some aspects of the "microphysical progression" in that study as well: N_R greater than 100s L^{-1} that feeds into coalescence, N_g on the order of 0.1 L^{-1} around -5°C, and highest N_i and continued presence of N_g as the parcel decayed.

6.2.2 Impact of ice hydrometeor sphericity

The next set of simulations is run to investigate the contribution of graupel non-sphericity to ice crystal number enhancement. The parcel model is particularly insightful in this case because larger-scale weather and climate models cannot generally afford the computational expense of evaluating temperature-dependent inherent growth factors, deposition densities, and capacitances. Non-sphericity will affect the ice hydrometeor fall velocity and collisional cross-section if low-density, elongated protuberances or dendrites form. In particular, the effect of including this geometry should be important at -6 and -15°C, where more extreme needle and plate geometries form respectively. These deviations from sphericity are captured in Γ_{IG} in Case 1, 2, and 3. But when these are rerun as Case 1S, 2S, and 3S, Γ_{IG} and graupel capacitances are set to unity, and the deposition density is set to the bulk ice density. Swept-out volumes, including terminal velocities, are calculated with graupel radius rather than spheroidal major axis. Parameters outside of the collection kernel, like N_{br} and N_{RS}, are assumed to be independent of habit and remain unchanged.

The ice phase hydrometeor number evolution for these cases is shown in Figure 6.2. All simulations in this set remain supersaturated longer than the corresponding ones in the first set. Especially in Cases 2 and 3, the sphericity assumption extends the simulation duration by a factor of about 2.1 or half an hour. Evolution of the liquid phase numbers (not shown) is almost identical to that in the first set; the only modification is to the rate of consumption of N_R due to changes in the rime-splintering collection kernel. A lower number of ice crystals and slower graupel growth rate allow the parcel to remain supersaturated for longer, elongating the simulation duration.

Despite their longer durations, Case 1S, 2S, and 3S produce much lower values of $N_{ice}^{(max)}$ than the first three cases.$N_{ice}^{(max)}$ decreases by a factor of 3 between Case 2 and Case 2S from 31.9 L^{-1} down to 10.8 L^{-1}. Between Case 3 and 3S, it decreases by a factor of 2.6 from 24.6 L^{-1} down to 9.4 L^{-1}. These decreases can be attributed to smaller collisional cross sections in the rime-splintering and breakup collection kernels. The graupel develop less extreme dimensions when we assume sphericity. Non-sphericity causes preferential deposition in regions of small radius of curvature, according to Fick's law of diffusion, which in turn

generates more extreme dimensions [210, 216]. As a sidenote, the trend is reversed between Case 1 and 1S: $N_{ice}^{(max)}$ is slightly larger in Case 1S because a smaller collisional cross section lowers the aggregation sink rather the secondary production sources.

We can also estimate that the difference in graupel dimension between the spherical and non-spherical case will be more pronounced, just as secondary production begins: simulations are initiated from 272 K with an updraft of 2 m s^{-1}, and assuming an adiabatic lapse rate of 6 K km^{-1}, the parcel temperature reaches -15°C when large graupel begin to form around 20 minutes. At this temperature, Γ_{IG} is particularly low because more dendritic shapes are favored. And at this time in Case 2, the most dramatic increase in N_i begins.

Hydrometeor terminal velocity should also be considered, along with collisional cross section. In cases with sphericity, the less extreme dimension and higher density increase hydrometeor terminal velocity. Faster terminal velocities increase the rime-splintering and breakup collection kernels. This effect, however, depends linearly on dimension, and that of collisional cross section is second-order, so that the latter dominates.

Returning to the observations in Table 5.1, Heymsfield and Willis note that N_i was highest, on the order of 100 L^{-1} when the concentrations of needle and columnar ice from the CIP were highest [170]. Indeed, they specifically categorize secondary ice particles as those with these highly non-spherical geometries. Sample images from the 2D-S probe in Crosier et al. show dendritic and capped column geometries (their Figure 9) [169]. They understand the latter to be the product of rime splintering that is then transported to higher altitudes and colder temperatures that favor plate-like geometry. And CIP-100 images from Taylor et al. show the most non-spherical geometries in mixed-phase regions (Region II and V in their Figure 5) [217].

We can also consider the effect of sphericity on simulated ice production rates relative to those in the studies from Table 5.1. For example, if we assume the ice production rate from Taylor et al. [217], calculated according to Harris-Hobbs and Cooper [218], of 0.14 L^{-1} s^{-1}, the parcel should produce N_{ice} of about 120 L^{-1} over 15 minutes. This generation is faster by a factor of 4 than that occurring from 20 to 32 minutes of Case 2 and 3, but a factor of 35 faster than the generation from 20 to 65 minutes in Case 2S and 3S. Or if we use the ice production rate of 50 s^{-1} at 1.8 m s^{-1} and about -4°C from Mossop et al. [219]

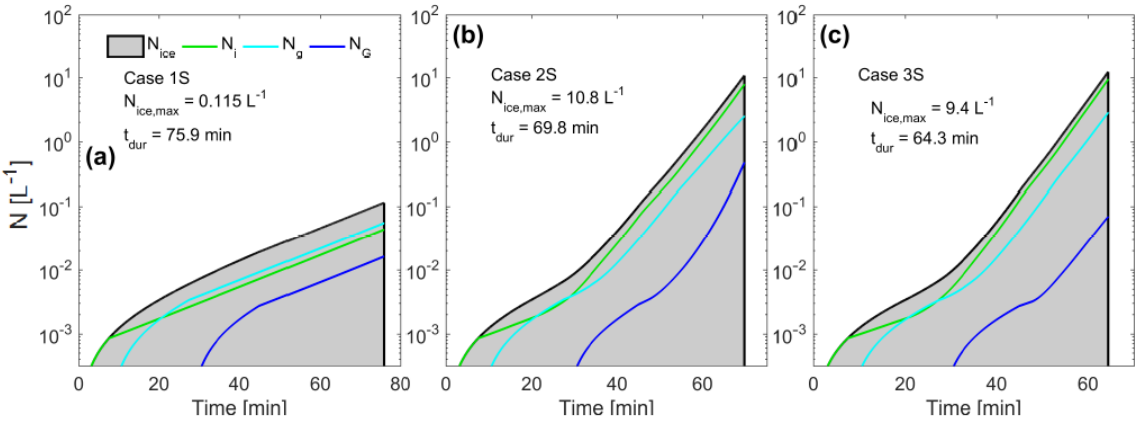

Figure 6.2: Ice hydrometeor number evolution for Case 1S in panel ***(a)****, 2S in panel* ***(b)****, and 3S in panel* ***(c)****. N_i denotes ice crystals, N_g small graupel, and N_G large graupel. The overall hydrometeor number in the ice phase, N_{ice}, is shaded in gray, and the maximum ice number, $N_{ice}^{(max)}$, and simulation duration, t_{dur}, are given for each case.*

and presented in Heymsfield and Willis [170], the parcel should produce an N_{ice} of about 45 L^{-1} over 15 minutes. Case 2 and 3 produce about this concentration in this time frame, while Case 2S and 3S require 3 times as long to produce 3 times less ice.

To bring simulated and measured production rates into even better agreement, the description of ice hydrometeor non-sphericity could be made even more sophisticated. Ventilation effects on depositional growth of falling hydrometeors could be incorporated [210], accelerating growth rates and yielding even more extreme graupel geometries (see Discussion below). Ice hydrometeors also do not necessarily maintain a fixed orientation as they fall through turbulent air [220, 221]. Including hydrometeor oscillations or tumbling would tend to decrease the effective hydrometeor dimension and collection kernels.

6.2.3 Breakup contribution

The simulated N_{ice} values can be broken down into process contributions to indicate which microphysical processes X are contributing most to the generation of new ice crystals. A process contribution, p_X, is defined as the percentage of small ice crystals generated by

process X:

$$p_X = \frac{\left(\frac{dN_i}{dt}\right)_X}{\sum\limits_{i \in X} \left(\frac{dN_i}{dt}\right)_i} \tag{6.1}$$

Nucleation, rime-splintering, and breakup tendencies go into this calculation; as a sink, aggregation is not included. p_{br} for Cases 1, 1S, 2, 2S, 3, and 3S is around 5% or less. This low contribution of breakup is due in part to the consideration of water saturated conditions only. To investigate whether p_{br} could be more significant, Cases 4A and 4B are run with conditions favorable to breakup. In Case 4A, no rime splintering or coalescence occurs and the updraft is smaller. The parcel is initiated with N_g and N_G of 10 m^{-3} each, and a higher nucleation rate is assumed. These conditions could represent the larger stratiform deck adjacent to or surrounding convective cores. These regions are generally characterized by modest ascent and cold temperatures. Lofting or formation of large droplets is unlikely, but graupel may be present due to advection or detrainment from the core. Taylor et al. note that both the preexisting ice and millimeter-sized graupel requisite for breakup were present in their observations of cumulus clouds off the South West Peninsula [217]. They measured N_{ice} on the order of hundreds per liter at temperatures below -8°C and recorded the highest N_{ice} of 350 L^{-1} in a mature, mostly quiescent stratiform region (Table 5.1).

The ice hydrometeor numbers are shown for all classes in Figure 6.3a. A limited number of small hydrometeors and modest updraft lead to much longer-lived liquid supersaturation than in the first six cases: the simulation lasts 113.9 minutes, 50% longer than any of the previous cases. $N_{ice}^{(max)}$ reaches 0.93 L^{-1} in this time, about an order of magnitude less than Case 2, but still an eight-fold ice crystal number enhancement from Case 1. The slower growth in N_i can be explained via an order of magnitude analysis. $N_R \sim \mathcal{O}(10^2$ $\text{cm}^{-3})$, $N_G \sim N_g \sim \mathcal{O}(10^{-5}$ $\text{cm}^{-3})$, $N_{br} \sim \mathcal{O}(10^2)$, and $N_{RS} \sim \mathcal{O}(10^{-2})$, so that the breakup tendency is 10^2 to 10^3 times weaker than the rime-spintering one. If even larger initial graupel numbers are feasible, $N_{G0} \sim N_{g0} \sim \mathcal{O}(10^{-3}$ cm^{-3} or 1 $\text{L}^{-1})$, then the rime-splintering and breakup tendencies approach the same order, and a larger ice crystal number enhancement may be generated by breakup over a shorter time frame.

We also look at the contribution of nucleation versus breakup for this case in Figure

6.3c. p_{nuc} is reduced from 100% initially by the presence of pre-existing graupel. Both N_{br} and c_0 increase as the parcel temperature gets colder, but the N_{br} temperature dependence is stronger and p_{br} steadily grows at the expense of p_{nuc} until it reaches a maximum of 38.2% after 27.9 minutes. Thereafter, N_{br} decreases with decreasing temperature, while c_0 continues to increase, and p_{nuc} dominates the remaining ice production.

In Case 4B, we adjust characteristic times rather than microphysical properties to favor breakup. The simulation is initiated from a colder temperature of 265 K, and the liquid phase growth times are elongated due to decreased water vapor diffusivity and slower condensational growth. The ice phase growth times are held constant, assuming that growth by riming dominates. In line with this assumption, rime-splintering is allowed to occur again with a low weighting. These conditions represent a cloud close to glaciation with minimal supercooled liquid fraction.

The ice phase number evolution is shown in Figure 6.3b. As in Case 4A, an initial tradeoff occurs between increasing N_{br} and c_0, but the N_{br} temperature dependence dominates and p_{br} reaches a maximum of 54.9% after 25.5 minutes. Subsaturation occurs after 91.6 minutes with $N_{ice}^{(max)}$ having reached 0.997 L^{-1}. With a reduced weighting for rime-splintering, p_{RS} does not rise much about 5%.

From Cases 4A and 4B, the promotion of purely ice-phase microphysics (i.e., aggregation and breakup) relative to mixed- or liquid-phase microphysics (i.e. rime-splintering or droplet coalescence) can increase p_{br} to significant values. But the more influential factor is when large hydrometeors in either phase first form. If large droplets form well in advance of large graupel, rime-splintering will be favored as in Cases 1, 2, and 3. If large graupel are able to form simultaneously or even earlier than large droplets, breakup contributes to secondary production. Early formation of large ice hydrometeors is feasible for colder in-cloud temperatures at which condensational growth rates, but not necessarily riming rates, have slowed. Graupel could also form outside of the cloud and be advected or detrained in. Independent of how graupel reaches the parcel, a modest nucleation rate is favorable so that large N_i does not deplete supersaturation too quickly: the time to produce a meaningful ice crystal number enhancement from breakup is relatively long.

As a final point, the necessary impact for two hydrometeors to shatter upon impact is

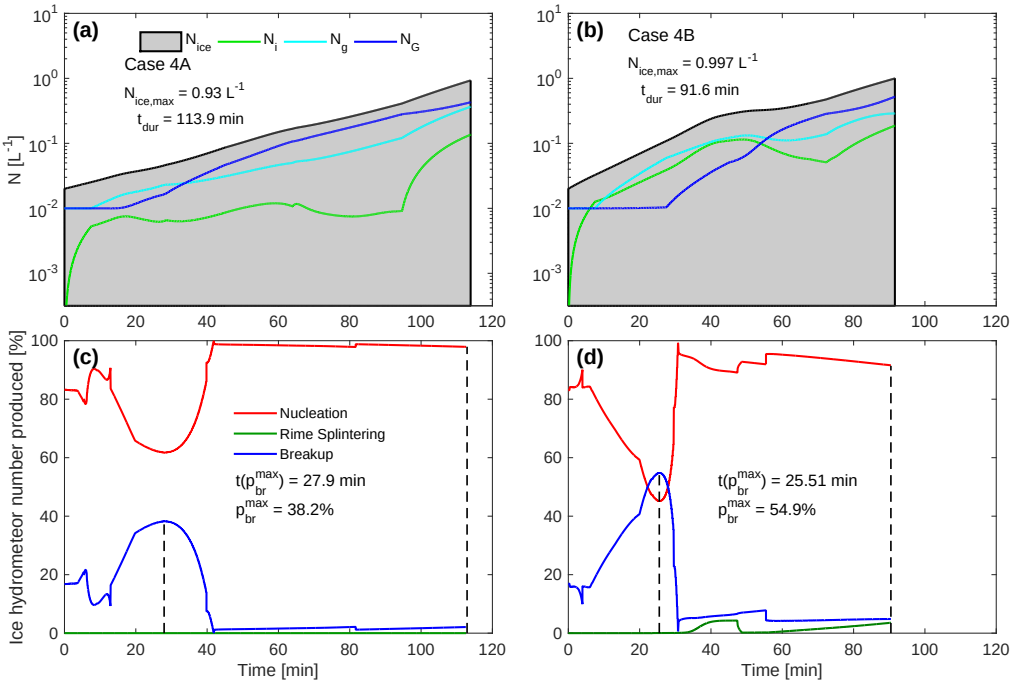

Figure 6.3: Ice hydrometeor number evolution for Case 4A in panel ***(a)*** *and 4B in panel* ***(b)*** *with maximum ice number, $N_{ice}^{(max)}$, and simulation duration, t_{dur}, given for both cases. Contributions of nucleation, breakup, and rime-splintering to N_i are shown over the simulation duration for Case 4A in panel* ***(c)*** *and 4B in panel* ***(d)*** *with maximum breakup contribution, $p_{br}^{(max)}$, and its time of occurrence, $t(p_{br}^{(max)})$, given for both cases.*

still highly uncertain. N_{br} is probably a function of relative terminal velocity, along with temperature. Understanding this dependence will be important in order to identify the actual cloud states for which p_{br} may be important.

6.2.4 Updraft velocity for secondary production

Having considered how microphysical parameters affect secondary production, a set of simulations is run to understand the effect of dynamical parameters. The constant updraft from the first eight simulations is replaced by a Gaussian updraft distribution with mean, as in the corresponding non-turbulent case, and standard deviation as in Table 6.1. At each time point, a new updraft is Monte-Carlo sampled from the distribution. A ten-run ensemble is done for each of these cases to investigate variability in $N_{ice}^{(max)}$ and t_{dur}.

Figure 6.4 shows N_{ice} and p_X for this ensemble of Case 2, 3, 4A, and 4B reruns, denoted 2T, 3T, 4AT, and 4BT respectively. The inclusion of the updraft distribution in Case 2T and 3T does not drastically affect the N_{ice} structure: primary nucleation dominates initially, followed by an exponential growth in N_{ice} after large droplet formation around 20 minutes. In Case 4AT and 4BT, both nucleation and breakup contribute initially with average updraft strength modulating the slope of the increase in N_{ice} and the simulation duration significantly. This modulation is due to the temperature dependences of c_0 and N_{br}, noted above. When updraft is lower, it limits the nucleation rate or fragment number upon breakup through temperature. Fewer ice crystals yield fewer graupel, less secondary production, and later water subsaturation. We call this cycle a "dynamically-limited case".

The structure and duration vary between the simulations with fixed and variable updraft, but also between the ensemble runs themselves. Figure 6.4 displays the standard deviation in maximum ice hydrometeor number, $\sigma_{N_{ice}}$, for each simulation: 5.59, 4.995, 0.297, and 0.338 L^{-1} for Case 2T, 3T, 4AT, and 4BT respectively. If $\sigma_{N_{ice}}$ is normalized by the $N_{ice}^{(max)}$ value, however, these values become 0.17, 0.20, 0.32, and 0.34. The cases favoring breakup have larger normalized variability than the cases with different weightings due to the dynamic modulation described above.

We also consider the maximum contribution of breakup for Case 4AT and 4BT in Figure 6.4e and f. Runs with the highest $N_{ice}^{(max)}$ and shortest duration have lower p_{br} relative to the ensemble mean. Here again, there is a cycle of "dynamically-limited cases": lower updraft decreases nucleation rate and increases and delays $p_{br}^{(max)}$. Slower ascent increases and delays $p_{br}^{(max)}$ because fewer small crystals are nucleated and the parcel attains colder temperatures where N_{br} is large before p_{nuc} outweighs p_{br}.

More generally, for models which include droplet evaporation, a mixed-phase cloud state may be sustained by a fluctuating updraft under which droplets evaporate and reactivate periodically [222]. Theoretically this 'steady state' is not attainable for a uniformly ascending parcel, and glaciation will occur more quickly. Case 4AT and 4BT exhibit similar behavior, as they can be lengthened by 20% relative to their uniformly ascending equivalents. These simulations are halted with water subsaturation not glaciation, but water subsaturation is a prerequisite for the Bergeron process and often a predecessor to glaciation [e.g., 223].

Looking back at Table 5.1, Heymsfield and Willis found that the highest N_{ice} was formed at modest updrafts for which hydrometeors could "loiter within the secondary production zone" [170]. This behavior is replicated in our simulations; however, the ensembles in Figure 6.4 (particularly panels a and b) do not replicate the large observed variability in ice counts or production rate with updraft fluctuations $\sim \mathcal{O}$ (0.5 m s^{-1}) (their Figures 1 and 12d; [168]).

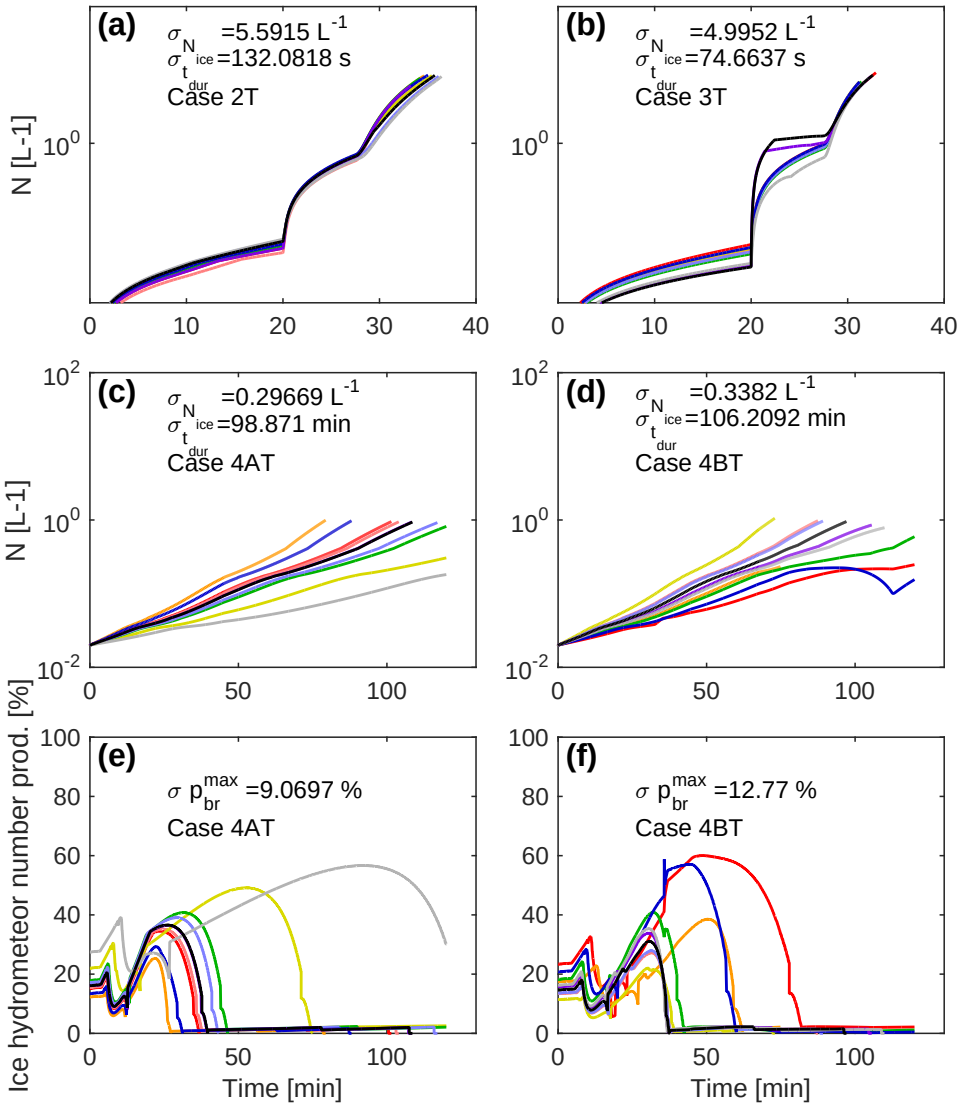

*Figure 6.4: Total ice hydrometeor number, N_{ice}, evolution for Case 2T in panel **(a)**, Case 3T in panel **(b)**, Case 4AT in panel **(c)**, and Case 4BT in panel **(d)**. For each case, an ensemble of ten runs is done with each run shown in a different color. Panels **(e)** and **(f)** show the contribution of nucleation, rime-splintering, and breakup to N_i for Case 4AT and 4BT.*

6.2.5 Representative cloud states

The process weightings of Case 1, 2, and 3 are intended as a mathematical tool to test the parameter space. To ensure atmospheric relevance, a final three simulations are run to characterize different cloud states with parameters in Table 6.1. A continental convective case is characterized by stronger updrafts, a steeper droplet spectrum, more and smaller droplets initially, and longer characteristic growth times for the liquid phase. The latter three conditions are proxies for higher continental aerosol loading. N_{ice} in this case is the smallest of all cloud states, reaching only 0.069 L^{-1} in 30.3 minutes. Although the updraft is strong, rapid growth of many, small droplets depletes supersaturation before large hydrometeors in either phase can form and feed into secondary ice production.

The maritime convective case, characterized by intermediate updrafts, is shown in Figure 6.5b. The initial droplet number, droplet spectrum, and ice crystal radius are all intermediate between that of the continental convective and Arctic stratocumulus cases. $N_{ice}^{(max)}$ is largest in this case with a value of 7.29 L^{-1} in 42.1 minutes. Here supersaturation generation and consumption balance to allow the greatest ice crystal number enhancement. The initial hydrometeor number and size are large enough that the rime-splintering tendency becomes significant, while updraft is strong enough to sustain this secondary production over a matter of minutes.

Finally, the Arctic stratocumulus case is shown in Figure 6.5c. Here, the updraft and initial droplet number are set to much lower values to represent stratiform clouds with limited aerosol loading. The initial droplet and ice crystal radii are assumed to be larger and the characteristic times for the ice phase are shorter. Here N_{ice} has a maximum of 0.079 L^{-1} over 56.0 minutes. Because the initial number of hydrometeors is lower, the parcel remains saturated for a longer period of time, allowing larger hydrometeors and secondary ice production, in particular breakup, to occur. But once these microphysics begin to enhance ice crystal number, the weaker updraft is insufficient to maintain supersaturation.

Many of the enhancements included in Table 5.1 have been observed in maritime convective systems. The NAMMA campaign took place in the Pacific from the Cape Verde archipelago off the coast of West Africa, while the ICE-T campaign focused on the cumuli

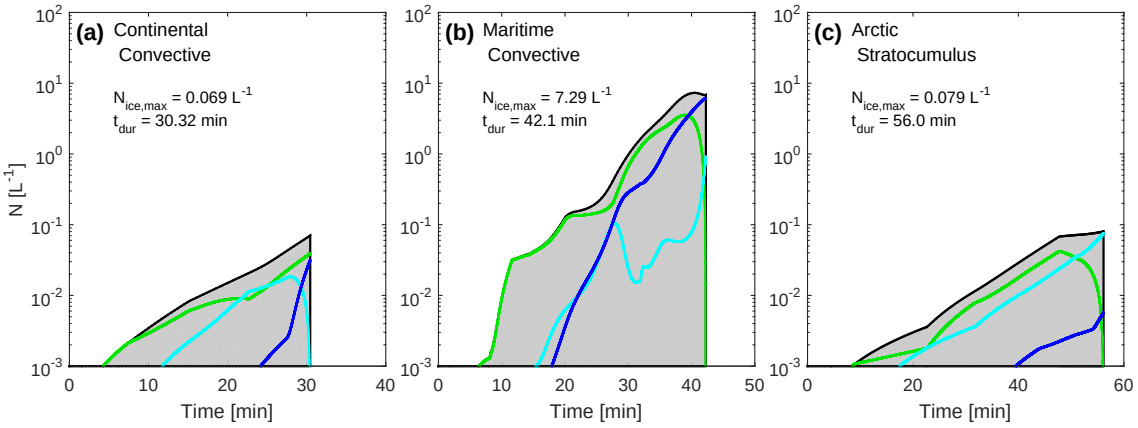

Figure 6.5: Ice phase hydrometeor number evolution for the continental convective in panel ***(a)****, maritime convective in panel* ***(b)****, and Arctic stratocumulus in panel* ***(c)*** *cloud states. N_i denotes ice crystals, N_g small graupel, and N_G large graupel. The overall hydrometeor number in the ice phase, N_{ice}, is shaded in gray, and the maximum ice number, $N_{ice}^{(max)}$, and simulation duration, t_{dur}, are given for each case.*

in the Caribbean around St. Croix and HAIC-HIWC occurred over the tropical Atlantic off the coast of French Guiana. And while Lawson et al. have found that strong updrafts may favor frozen droplet shattering, many other studies report only modest updrafts of 1 to 2 m s^{-1} [224].

6.3 Discussion of model limitations

The model microphysics is intentionally limited to facilitate analysis. With a limited number of linkages between the liquid and ice phase hydrometeor number tendencies, we can better elucidate how increases in one tendency affect another. Nonetheless, it is worthwhile to consider how the inclusion of additional microphysics would affect the results. One important limitation is the lack of sedimentation. Including sedimentation will reduce the large hydrometeor number concentrations and the magnitude of the secondary production tendencies in general. Simulations will also be shorter due to the exclusion of sedimentation. Without the loss of large hydrometeors, the depositional growth sink of supersaturation is overestimated.

Then simulations are stopped when the parcel becomes subsaturated with respect to water. If this limit were removed and the Bergeron process was included, N_{ice} should increase

at the expense of N_{liq}, and the larger hydrometeor numbers, N_g and N_G, should increase as the depositional growth time delays shorten. Larger N_g and N_G and smaller N_{liq} would then shift contributions towards breakup as it depends only on the ice phase. The parcel has also been assumed spatially homogeneous. If 'pockets' of one phase or another were to form, then mixed-phase secondary production through a process like rime-splintering would decrease. The contribution of breakup, as a single-phase secondary production process, would again become more significant. Other studies suggest that frozen droplet shattering could be another influential mixed-phase secondary production process [224, 217]. A follow-up study incorporates this process as well.

We could also consider the effect of entrainment of subsaturated air by small-scale eddies. This can have three effects. If the air is subsaturated with respect to both water and ice, and the motions are strong enough to induce homogeneous mixing, supersaturation will drop and may ultimately lead to liquid droplet evaporation and ice crystal sublimation, affecting primarily hydrometeor size not number [e.g., 27]. The secondary production collection kernels would be reduced. If the motions are not strong enough to induce homogeneous mixing, only those droplets or ice crystals near the entrained air will evaporate or sublimate, affecting primarily hydrometeor number not size. Although this may lead to shorter-lived parcel, it will also strengthen secondary ice production. Finally, if the entrained air is subsaturated only with respect to water, the Bergeron process will generate larger ice hydrometeors more quickly, at the expense of the liquid phase. The breakup contribution in this case could be large, assuming the larger-scale motion is strong enough to keep these large hydrometeors aloft.

A final consideration is the ventilation effect mentioned above. Estimates of a ventilation coefficient from the Froessling equation ($\mathrm{Sh}/2 = 1{+}0.276(\mathrm{Re})^{1/2}(\mathrm{Sc})^{1/3} = \bar{f}_v$) indicate that it may be on the order of 10 for the graupel classes. Convectively-enhanced mass transfer will generate the large hydrometeors more quickly, fueling secondary production if the updraft is sufficient to keep them aloft and maintain supersaturation. But including this effect does not seem to counterbalance the diminished secondary production from spherical ice hydrometeors in Section 6.2.2. While coefficients are larger for spherical hydrometeors than nonspherical ones due to a larger characteristic velocity and density in the Reynolds

number, these effects are somewhat offset by a smaller characteristic length, and our estimates indicate that the two values would be within 1% of one another for the default simulations.

6.4 Chapter 6 Summary

Fifteen simulations were run with a minimal, six-hydrometeor-class parcel model. These simulations consider the effect of microphysical process weightings, graupel non-sphericity, and turbulence on the total ice hydrometeor number, N_{ice}, and process contributions, p_X, in the air parcel. In particular, we have shown the following:

- **The largest ice crystal number enhancement occurs for intermediate conditions, when all microphysical processes are moderately active.**

  Intermediate process weightings (Case 2) and the maritime cumulus 'cloud state' (Case MC) produce the largest $N_{ice}^{(max)}$. In these cases, neither the process weightings nor the dynamic-aerosol proxy conditions are too extreme. The large $N_{ice}^{(max)}$ in Case 2 indicates that secondary ice production is promoted when the microphysics which produce larger hydrometeors are also active. For Case MC, secondary ice production is promoted by a balance of moderate updraft and moderate aerosol loading. V is strong enough and N_{d0} is low enough to maintain supersaturation throughout secondary ice production.

- **The relative contribution of rime splintering versus breakup is determined primarily by when large hydrometeors form in the liquid versus ice phase.**

  Secondary ice production occurs after the formation of larger hydrometeors, which can rime or break up. If conditions favor large droplet formation, the rime splintering contribution will dominate. If conditions favor large graupel formation, the breakup contribution will dominate. This finding extends the first: intermediate conditions favor secondary ice production because they allow the development of larger hydrometeors in one phase or the other. For example, large droplets form quickly when coalescence is efficient. Broad droplet size distributions accelerate coalescence and

result from an intermediate aerosol loading, with enough CCN for sufficient initial activation but also few enough for growth of some droplets to large sizes.

- **Including graupel non-sphericity significantly increases secondarily-produced N_i.**

  Representing graupel growth with spheroidal, rather than spherical, geometry leads to the development of larger maximum dimensions and to an increase in the aggregation, breakup, and rime-splintering collection kernels, predominantly through the collisional cross section. The contribution of rime splintering versus breakup remains relatively independent of graupel geometry.

- **Lower updraft velocity may cause a "dynamically-limited case" with diminished secondary production.**

  When the average updraft is lower, nucleation rate and the fragments generated upon breakup are decreased because of the temperature dependence of these factors. Fewer ice crystals are then formed, decreasing graupel numbers and the secondary production tendencies. In this case, the parcel remains supersaturated for a long time and has lower $N_{ice}^{(max)}$ and later $p_{br}^{(max)}$. The impact of updraft in these secondary production simulations seems to be much less than that shown for primary nucleation in Chapter 4.

CHAPTER 7

EFFECT OF SECONDARY ICE PRODUCTION IN A RAIN BAND

The parcel model of the previous two chapters provides estimates of enhancement from and favorable conditions for secondary ice production. But as discussed in Section 6.3, certain results may change as additional processes, like hydrometeor sedimentation or entrainment, are incorporated in a less minimalistic framework. To begin a kind of 'scaling-up' for the secondary production parameterizations, we incorporate them into a mesoscale meteorological model in this chapter. A cold frontal rain band from the APPRAISE field campaign is simulated to investigate any effect of additional cloud ice on surface precipitation.[1]

7.1 Cloud formation and hydrological impacts revisited

Precipitation from clouds may begin in either the liquid or ice phase. In either phase, solely condensational or depositional growth does not form hydrometeors large enough to fall out of the cloud in a fast enough time frame. Instead, **accretional growth** is required. Accretional growth encompasses the collision-coalescence of liquid droplets, the riming of liquid droplets on ice hydrometeors, and aggregation of ice crystals. The efficiency of these processes is controlled by hydrometeor size [e.g., 29, 225], as shown for the liquid phase in Figure 7.1. When the size of a collected drop is much smaller than the size of the collector drop, $r_d/r_R < 0.1$ in panel (a), the small drops follow the streamlines around the larger one because they have little inertia. Over an intermediate range of r_d/r_R, the collection efficiency plateaus, as the inertia of the collected drops increases and they collide with the collector drop more readily.

If many CCN are present in a polluted cloud, then the droplets will be quite small, and the collision efficiency will be quite low as in Figure 7.1(a). In this case, precipitation

[1]This work was completed during a visit in the group of Corinna Hoose at the Karlsruhe Institute of Technology funded by the Helmholtz Association through the President's Initiative and Networking Fund (VH-NG-620). Thanks go to Christian Barthlott for helping me to port the COSMO model to a local cluster. Also to Jonny Crosier and Andrew Barrett for providing APPRAISE data and to Alexei Kiselev for helpful discussion during my KIT visit.

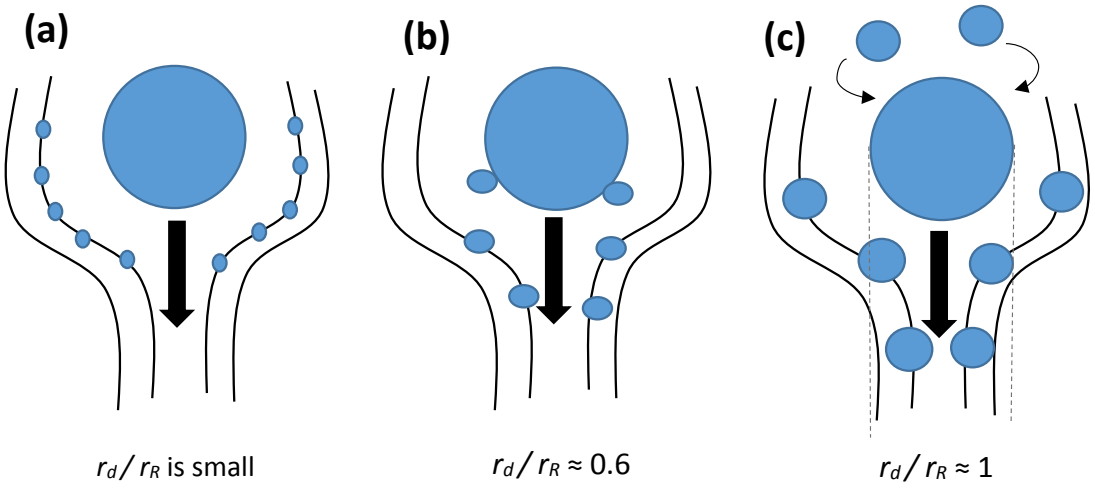

*Figure 7.1: The efficiency of droplet collisions depends on the relative sizes of small, collected droplets and a large collector droplet, i.e., r_d/r_R: **(a)** When this ratio is quite small, the collected droplets do not have enough inertia for successful collision. **(b)** As the collected droplets become larger, collision efficiency increases to a plateau. **(c)** Eventually the collision efficiency can surpass unity, as droplets outside the swept-out volume of the collected droplet are pulled into its wake.*

generation may begin via the Bergeron process, as water vapor is transferred from evaporating droplets to growing ice hydrometeors. These ice hydrometeors eventually fall out of the cloud and reach an altitude at which they melt to form rain drops. The majority of precipitation initiates as ice over the continents in the middle latitudes, given the higher levels of pollution, and hence CCN, in these regions [32, 30]. Cold phase initiation also tends to occur in convective clouds for which the vertical motions are strong enough to carry droplets above the freezing level (see Figure 1.5).

Inclusion of secondary ice production in meteorological models may yield more accurate forecasts of ice-initiated precipitation. On the one hand, an additional source of many small ice crystals could extend cloud duration and delay precipitation in a kind of lifetime effect (Section 1.2). On the other hand, the depositional growth of these small ice crystals could deplete supersaturation to the level at which the Bergeron process initiates. Then ice hydrometeors quickly become large, shortening cloud duration and accelerating precipitation. A final linkage of secondary ice and precipitation has been proposed via a 'cascade effect' in which small ice crystals collide with large droplets, freezing and then shattering them and

ultimately generating more small ice crystals [224] (This process is explained and modeled in Sections 8.1 and 8.4.2.)

Several existing studies have considered these linkages, both with measurements and models, but no consensus has been reached on their importance. For example, Connolly et al. did not see a large change in surface precipitation from a tropical thunderstorm when they altered the rime splintering rate in the Weather Research and Forecasting model [226]. Dearden et al. also found that depositional growth of ice crystals was much more influential than inclusion of rime splintering for the spatial distribution of precipitation [227]. On the other hand, Clark et al. found that the latent heating from additional ice generation could modify the vertical temperature profile, and hence precipitation rates [176]. And Taylor et al. (whose measurements were discussed in Table 5.1 and throughout Chapter 6) concluded that the combination of droplet coalescence and secondary ice production often determined precipitation timing and intensity in the maritime cumuli they observed [217].

7.2 Case study from the APPRAISE campaign

To weigh in on the debated importance of precipitation-secondary ice linkages, a case study was performed both with and without secondary production parameterizations in the COnsortium for Small-scale MOdeling (COSMO) framework of the German Weather Service. We chose to simulate a narrow cold frontal rainband, which passed over the United Kingdom on 3 March 2009 during the Aerosol Properties, PRocesses And InfluenceS on the Earth's climate programme, Clouds project (APPRAISE-Clouds). A **narrow cold-frontal rain band**, or NCFR, refers to a region of heavy precipitation formed by strong convection along a cold front. Often the strong precipitation associated with passage of an NCFR is localized in precipitation cores that are separated by stable 'gap regions' [228]. The precipitation generation in the cores can lead to a positive feedback, schematicized in Figure 7.2: as precipitation evaporates or melts along the leading edge of the cold front, it cools the cold sector further, strengthening the temperature gradient for a fixed pressure (baroclinicity), cold air advection, and ultimately atmospheric convection [229, 230]. Increased convection generates stronger precipitation. The leading edge of the cold front that we consider can be

seen in the sharp gradient in equivalent potential temperature θ_e from about (50°N, 8°W) up to (62°N, 1°E) in Figure 7.2b. θ_e is the hypothetical temperature that a volume of air would have if the water vapor within it were to condense and release its latent heat. A decrease in θ_e with height indicates atmospheric instability, as less buoyant air lies above more buoyant air.

Crosier et al. published a thorough analysis of the in-situ cloud microphysical and ground-based meteorological measurements taken of the NCFR during APPRAISE-Clouds [169]. Some of these data were presented in Table 5.1 as an empirical reference for the parcel model results. In-situ measurements with a cloud droplet probe, 2-D stereo probe, and cloud imaging probes were taken with the UK Facility for Airborne Atmospheric Measurement BAe-146 aircraft. The interarrival time algorithms and K-tips discussed in Section 5.1 were used for these measurements. The Chilbolton Advanced Meteorological Radar took remote sensing measurements of precipitation, while vertical velocity was inferred from Doppler radar measurements. Ground-based measurements were taken at the Chilbolton Facility for Atmospheric and Radio Research (CFARR) in Southern England (51.14°N, 1.44°W and marked with an **X** in Figure 7.3b). Precipitation intensities up to 50 mm hr^{-1} were associated with the NCFR. This precipitation first passed over the western coast of England around 1800 UTC (Figure 7.3b below) and then over the CFARR at 2035 UTC on 3 March 2009.

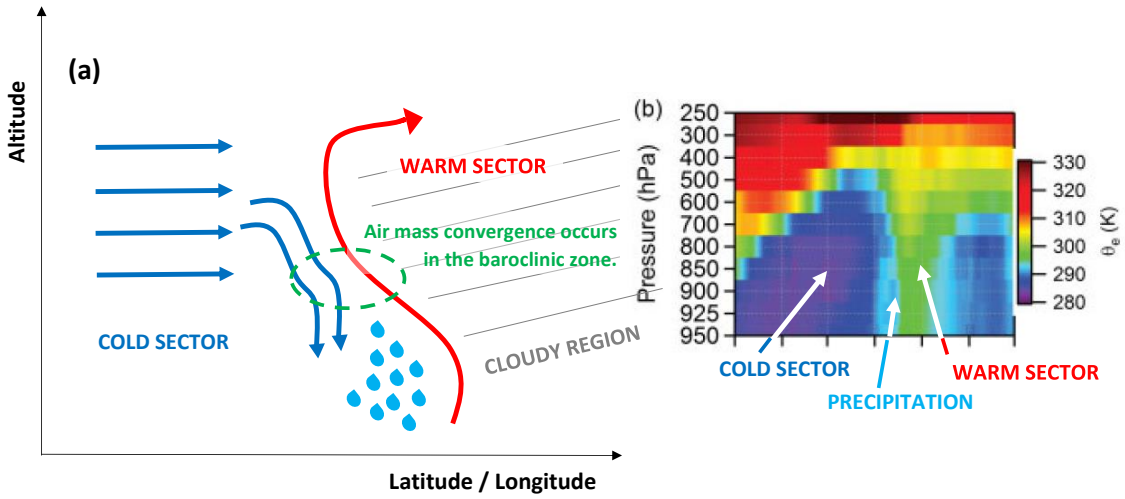

Figure 7.2: ***(a)*** *Schematization of an ana-type cold front. The red arrow represents the cold front, along which the advancing air of the* ***cold sector*** *meets the air of the warm sector. Convergence occurs in the* ***baroclinic zone****, i.e., region where a temperature gradient exists along a fixed atmospheric pressure level, and beneath this zone, precipitation forms. The warm sector has a higher relative humidity, so it is also the cloudy region.* ***(b)*** *Profile of calculated equivalent potential temperature θ_e from meteorological data for the the case study cold front along 51.24°N latitude. Panel (b) is taken from Crosier et al. [169] (their Figure 1b).*

An important result from the parcel model simulations in the previous chapter was that intermediate conditions favor secondary ice production, and the NCFR is chosen as a case study because its meteorological and microphysical properties span this intermediate regime. A peak updraft of 6.9 m s^{-1} was measured within the leading edge of the cold front; this strong vertical motion generates the larger droplets necessary for efficient coalescence (Figure 7.1) and eventual frozen droplet shattering (Figure 1.2c; [224]). But this strong vertical motion was surrounded by stratiform regions with updrafts of only 1 to 2 m s^{-1}, where hydrometeors may "loiter within the secondary production zone" (Section 6.2.4, [170]). In the stratiform regions, low liquid water contents $\sim \mathcal{O}$ (0.1 g m^{-3}) were observed, while in the strong convective region, high concentrations of supercooled droplets were formed. The former, more glaciated conditions should favor breakup, while greater presence of liquid should favor rime splintering or frozen droplet shattering. Then cloud top temperatures were recorded from -50 down to -10°C, a range wide enough that the underlying cloud temperatures should encompass the optimal rime splintering temperature

zone as well as the observed peak probability for breakup and droplet shattering.

7.3 COSMO simulation setup

All simulations are run with the COSMO model [231, 232] and the 2-moment bulk microphysics scheme of Seifert and Beheng [41] (called SB06 hereafter). SB06 has six hydrometeor classes for cloud droplets ($r_d < 40$ μm), rain drops ($r_R \geq 40$ μm), ice crystals, snow, graupel, and hail. The last four ice phase classes are categorized by specific power law coefficients and exponents (a_1, a_2, b_1, b_2 below) that relate their mass to an equivalent radius and terminal velocity:

$$r_X = a_1 \, m_X^{b_1} \qquad v_{t,X} = a_2 \, m_X^{b_2} \tag{7.1}$$

Then for each of these six classes, a budget is constructed, as the summation of accumulation and advection equal to sedimentation losses and parameterized sources and sinks, $\mathcal{P}_X$:

$$\frac{\partial N_X}{\partial t} + \nabla \cdot [\mathbf{v} N_X] = \frac{\partial}{\partial z}[v_{t,X} N_X] + \mathcal{P}_X \tag{7.2}$$

SB06 also assumes a generalized gamma distribution for the mass of each hydrometeor type, m_X:

$$f(m_X) = A m_X^{\nu} \exp(-\tilde{\lambda} m_X^{\tilde{\mu}}) = \frac{\tilde{\mu} N}{\Gamma(\frac{\nu+1}{\tilde{\mu}})} \left[\frac{\Gamma(\frac{\nu+1}{\tilde{\mu}})}{\Gamma(\frac{\nu+2}{\tilde{\mu}})} \overline{m_X} \right]^{-(\nu+1)} m_X^{\nu} \exp\left[- \frac{\Gamma(\frac{\nu+2}{\tilde{\mu}})}{\Gamma(\frac{\nu+1}{\tilde{\mu}})} \frac{m_X}{\overline{m_X}} \right]^{\tilde{\mu}} \tag{7.3}$$

where $(\nu + 1)/\tilde{\mu}$ is the shape parameter and $\tilde{\lambda}$ the rate parameter of the distribution. $\overline{m_X}$ is the mean mass of hydrometeor type X, equal to the liquid or ice water content over the number concentration of type X, e.g., IWC / N_{ice}. Addition of a hydrometeor size distribution overcomes the limitation of monodispersity, and continuous hydrometeor sedimentation or growth the threshold behavior from time delays, in the parcel model simulations.

Fifty vertical levels are used with a time step of 25 seconds and a 2.8 km horizontal

resolution. The parameterization of Phillips et al. 2008 is used for primary ice nucleation (see Table 2.1 and Section 3.2.1) [68]. A shallow convection parameterization is included in these simulations, but the aerosol physics component (ART) is not. The int2lm application is used to **int**erpolate the initial and boundary conditions from existing coarse-grid model output or data of the European Center for Medium-Range Weather Forecasts to the **l**ocal **m**odel grid. The simulation domain is centered at 53°N, 5°W, with longitudes ranging from 65°N down to 46°N and latitudes ranging from 18°W to 10°E, shown in Figure 7.3a.

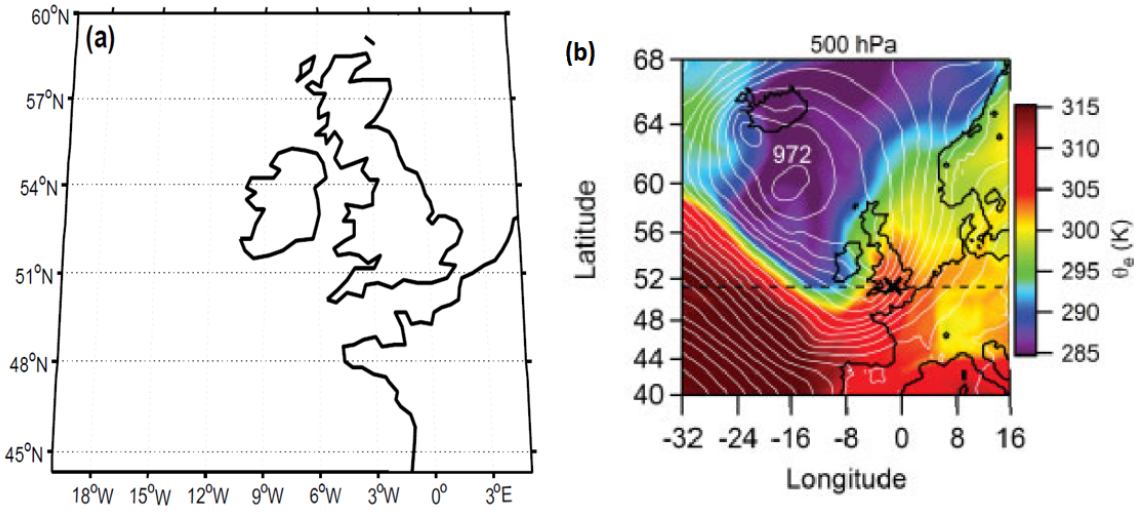

Figure 7.3: ***(a)*** *The COSMO simulation domain for the APPRAISE NCFR and* ***(b) equivalent potential temperature*** θ_e *at 1800 UTC 3 March 2009 over the simulation domain. The contours show mean sea level pressure at 3 hPa intervals and a minimum at 972 hPa. The CFARR is marked with an* ***X*** *at (51.14°N, 1.44° W). Panel b is taken from Crosier et al. [169] (their Figure 1a).*

7.3.1 Secondary ice production parameterizations

Rime splintering, breakup upon ice hydrometeor collision, and frozen droplet shattering parameterizations are incorporated into SB06 within the COSMO model. These processes are chosen, first because the parcel model has been used to refine formulations and make estimates for the first two in Chapter 6 and for all three in Chapter 8. Then, as a set, they indicate the extent to which additional cloud ice is generated from pre-existing ice versus liquid. Rime splintering involves both the liquid and ice phases, while breakup involves only ice, and droplet shattering involves only the liquid phase. When generation from frozen droplet shattering is large, the liquid phase controls ice formation in mixed-phase

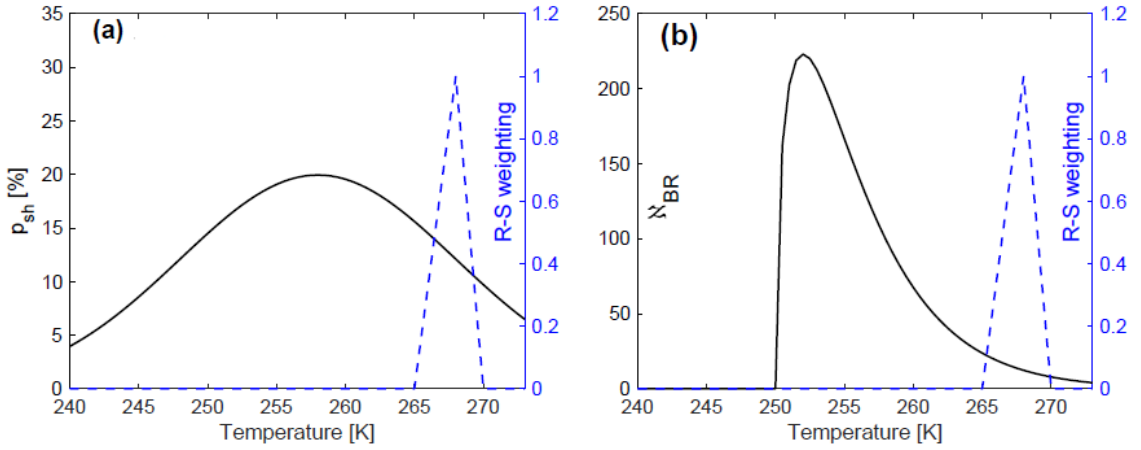

Figure 7.4: ***(a)*** *Shattering probability, p_{sh}, as a function of temperature, within the fragments generated from droplet shattering $\aleph_{DS}$ and* ***(b)*** *fragments generated from breakup $\aleph_{BR}$. The rime splintering weighting versus temperature is overlaid in blue.*

clouds, and exactly parameterizing ice nucleation is less important under these conditions. When generation from breakup is large, on the other hand, accurate calculations of primarily nucleated ICNC will be quite influential on the cloud phase partitioning.

To model frozen droplet shattering, a shattering probability is calculated from a Gaussian temperature distribution, with a maximum of 20% at 258 K and a standard deviation of 10 K as shown in Figure 7.4a (and as given later in Table 8.2 for the parcel model). These values are based upon droplet levitation experiments of Kiselev and Leisner [184]. Then the droplet shattering tendency is calculated as the product of this shattering probability, a fixed number of fragments per shattering event, $N_{frag}^{(DS)}$, and the number of frozen raindrops for a given time step as in Bigg [233].

$$p_{sh} = \frac{p_{sh}^{(max)}}{\sigma\sqrt{2\pi}} \exp\left[\frac{-(T-\overline{T})^2}{2\sigma^2}\right] = 0.2\,\mathcal{N}(258\text{K}, 10\text{K}) \tag{7.4}$$

$$\frac{\partial N_{freez}}{\partial t} = p_{fr}(t, T, D_R) N_R = \left[1 - \exp\left[-\frac{\pi}{6} D_R^3\, t\, K \exp(A(273-T)-1)\right]\right] N_R \tag{7.5}$$

$$\left.\frac{\partial N_{ice}}{\partial t}\right|_{DS} = p_{sh}(T)\; N_{frag}^{(DS)}\; \frac{\partial N_{freez}}{\partial t} \tag{7.6}$$

For breakup upon ice hydrometeor collision, the number of fragments generated is also calculated as a function of temperature based upon Takahashi et al. shown in Figure 7.4b

[15]:

$$\aleph_{BR} = F_{BR}(T - T_{min})^{1.2} \exp\big[-(T - T_{min})/\gamma_{br}\big]. \tag{7.7}$$

Collision frequency is far more difficult to formulate given the gamma size distributions. The number of particles of type j collected by those of type k is given by the following equation:

$$\left.\frac{\partial N_j}{\partial t}\right|_{coll,jk} = -\int_0^\infty \int_0^\infty f_j(m_j) f_k(m_k) K_{jk}(m_j, m_k) dm_j dm_k \tag{7.8}$$

where K_{jk} is a collection kernel given as the product of the collisional cross section, a collection efficiency, and the terminal velocity difference:

$$K_{jk}(m_j, m_k) = \frac{\pi}{4}[r_j(m_j) + r_k(m_k)]^2 E_{jk}(m_j, m_k)|v_{t,j}(m_j) - v_{t,k}(m_k)| \tag{7.9}$$

To avoid look-up tables, the efficiencies in Equation 7.8 are assumed to be independent of particle sizes, $E_{jk}(m_j, m_k) \approx \overline{E_{jk}}$, as are the terminal velocity differences, $|v_j(m_j) - v_k(m_k)| \approx \overline{\Delta v_{jk}}$. Then, for example, the loss of graupel to collision with hail is given by

$$\begin{aligned}\left.\frac{\partial N_g}{\partial t}\right|_{coll,gh} &= -\frac{\pi}{4}\overline{E_{gh}} N_g N_h \big[\delta_g^0 D_g^2(\overline{m_g}) + \delta_{gh}^0 D_g(\overline{m_g}) D_h(\overline{m_h}) + \delta_h^0 D_h^2(\overline{m_h})\big] \\ &\quad \times [\theta_g^0 v_g^2(\overline{m_g}) - \theta_{gh}^0 v_{t,g}(\overline{m_g}) v_{t,h}(\overline{m_h}) + \theta_h^0 v_h^2(\overline{m_h})]^{1/2}\end{aligned} \tag{7.10}$$

where δ_x^0 and θ_x^0 are dimensionless constants that depend upon the power law coefficients and exponents in Equation 7.1 and the shape and rate parameters of the mass distribution in Equation 7.3. Then the final breakup tendency is the product of the fragment number and the collision frequency:

$$\left.\frac{\partial N_{ice}}{\partial t}\right|_{BR,gh} = -\aleph_{BR} \left.\frac{\partial N_g}{\partial t}\right|_{coll,gh}. \tag{7.11}$$

The various hydrometeor classes that are allowed to breakup upon collision are listed in Table 7.1.

Finally, rime splintering parameterizations exist already in SB06:

$$\left.\frac{\partial N_{ice}}{\partial t}\right|_{RS} = C_{mult}\, w_{RS}(T)\, q_{rime} = 3 \times 10^8 \max\left[1, (T-265)^{-1}\right] \cdot \max\left[1, (270-T)^{-1}\right] q_{rime} \tag{7.12}$$

where the prefactor C_{mult} is set to $3{\times}10^8$ fragments per milligram of rime as a default value from the experiments of Hallett and Mossop [165]. The various hydrometeor classes that are allowed to rime splinter are shown in Table 7.1. The default, triangular temperature weighting $w_{RS}(T)$ is shown in both panels of Figure 7.4 and is adjusted in the sensitivity tests described next.

Table 7.1: Secondary ice nucleation interactions between various hydrometeor classes

	cloud droplets	***raindrops***	***ice crystals***	***snow***	***graupel***	***hail***
cloud droplets					RS	RS
raindrops		DS	RS		RS	RS
ice crystals		RS			BR	BR
snow					BR	
graupel	RS	RS	BR	BR		BR
hail	RS	RS	BR		BR	

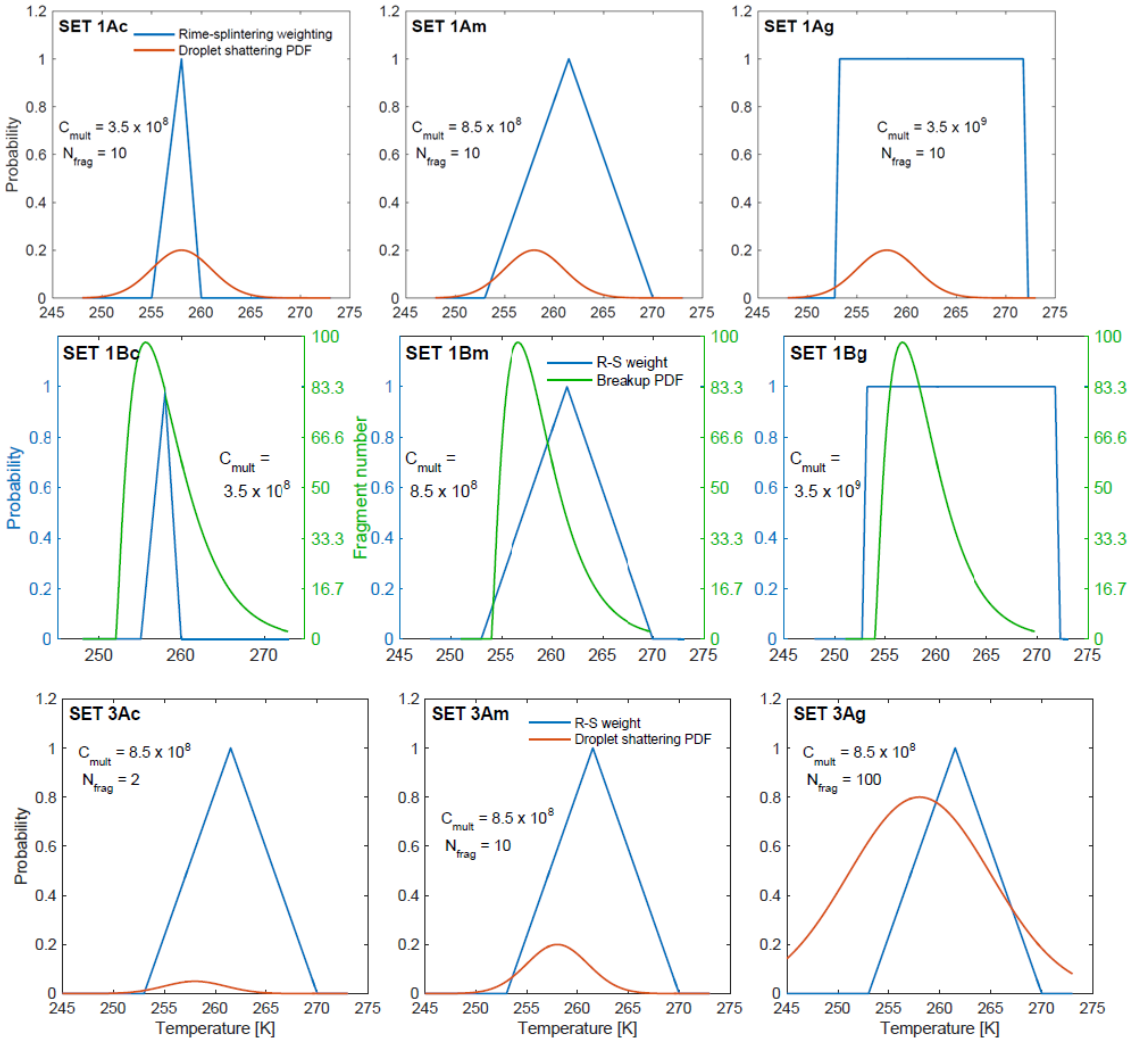

Figure 7.5: COSMO simulations performed with frozen droplet shattering, breakup upon collision, and rime splintering. The top panels show Set 1A in which the temperature weighting for rime splintering $w_{RS}(T)$ is adjusted. The middle panels show Set 1B in which the fragment number for breakup $\aleph_{BR}$ is adjusted. And the bottom panels show Set 3A in which the shattering probability distribution $p_{sh}(T)$ is adjusted.

7.3.2 Sensitivity tests

Figure 7.5 illustrates the nine simulations that were run. The first set, denoted **Set 1A** in the top row, includes frozen droplet shattering and rime splintering. The temperature weighting and prefactor for rime splintering are adjusted from **c**onservative values (1Ac) to **m**oderate ones to **g**enerous ones. The second set, denoted **Set 1B** in the middle row, includes breakup upon collision and rime splintering, and the same conservative, moderate, and generous values for $w_{RS}(T)$ and C_{mult} are used in 1Bc, 1Bm, and 1Bg. Finally the third set, denoted **Set 3A** in the bottom row, again includes frozen droplet shattering and rime splintering. Here the maximum and standard deviation of the shattering probability are adjusted from conservative (3Ac) to moderate (3Am) to generous (3Ag) values.

7.4 Mesoscale results from initial implementation

Replication and analysis of these simulations is still underway, but preliminary results are presented below. First, the secondarily produced N_{ice} is shown in the top panels Figure 7.6 from 2000 to 2030 UTC during rain band passage over the CFARR. The rain band feature can be clearly seen in the top two panels from about (48°N, 9°W) up to (51°N, 4°W) around the Southwest Peninsula. A comma shape characteristic of mid-latitude cyclones is also clear in these secondarily produced N_{ice} fields. Panel (a) shows results from Set 1Ac with the more conservative RS formulation, while panel (b) shows the results from Set 1Ag with the more generous one. As expected, large values of secondarily produced N_{ice} are more extensive in 1Ag. For 1Ac, the highest values stay quite localized around the rain band feature.

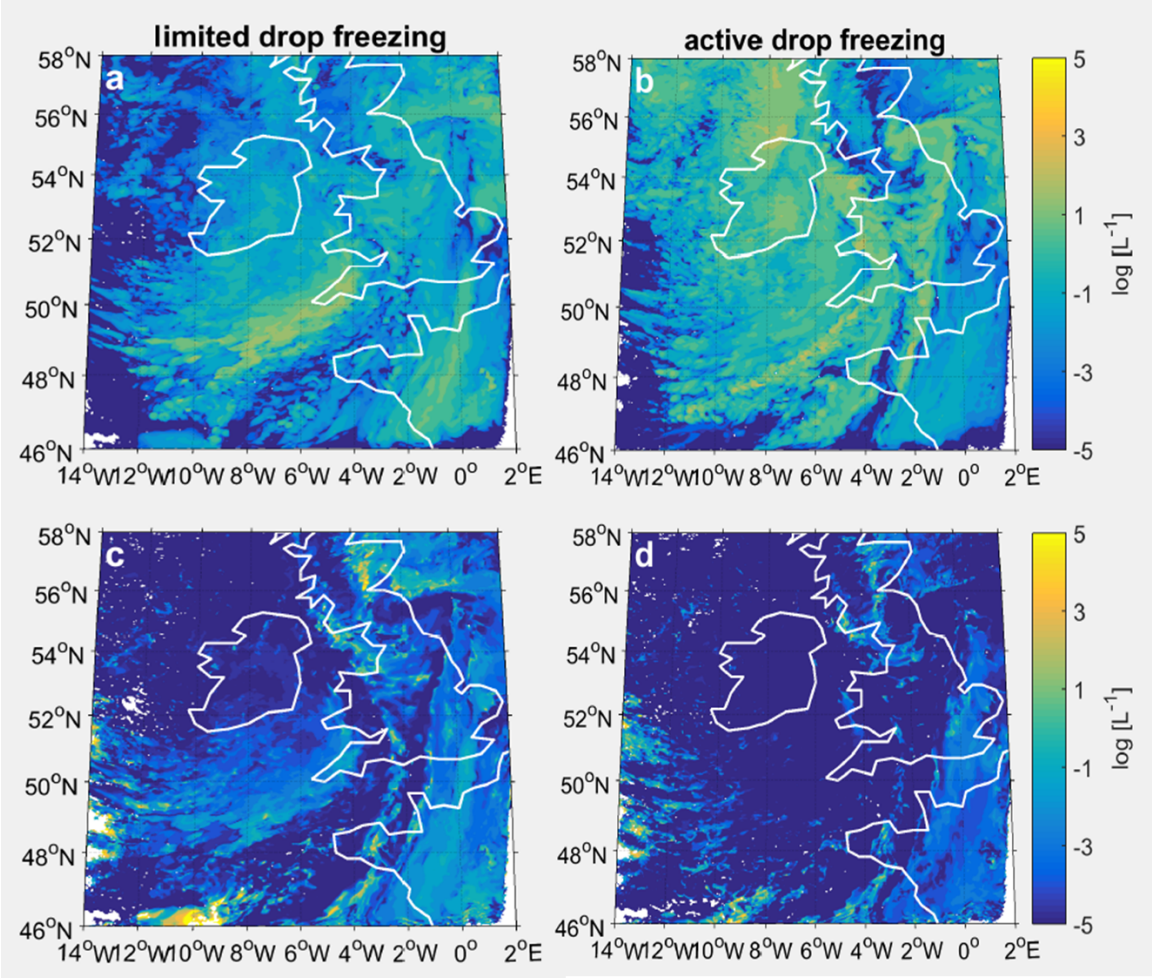

Figure 7.6: Secondarily produced N_{ice} from ***(a)*** *Set 1Ac and* ***(b)*** *Set 1Ag and ratio of secondarily produced to primarily nucleated N_{ice} from* ***(c)*** *Set 1Ac and* ***(d)*** *Set1Ag between 2000 UTC to 2030 UTC during rain band passage over the CFARR ground site. The scale is logarithmic and the domain is shown at an altitude of 7.5 km which has a $\overline{T}$ of 258 ± 7 K, where the droplet shattering and breakup probability distributions peak.*

Panels (c) and (d) show the ratio of secondarily produced to primarily nucleated N_{ice} to determine whether the contribution of secondary production is non-negligible relative to primary nucleation. Although large regions of the ratio field remain small, the secondarily produced N_{ice} can be 10 to 100 times as large as the primarily nucleated numbers in regions around the rain band. These large ratios are more prevalent in the 1Ac simulation (panel c) than the 1Ag one (panel d) because Figure 7.6 shows results from a single altitude of 7.5 km for which the mean temperature coincides with the narrow peak of the 1Ac RS temperature weighting.

Only spatial fields from Set 1A are shown here. The same fields have been plotted for Set 3A, but there the adjustment of the shattering probability parameters between 3Ac and 3Ag does not make a meaningful difference in either the secondarily produced N_{ice} or ratio fields. Temperature weighting for rime splintering seems to be more influential than the droplet shattering probability, most likely because rime splintering can occur for many more hydrometeor classes than droplet shattering can (Table 7.1).

Given the extensive in-situ data for the NCFR, the simulated N_{ice} from Sets 3A and 1B is next compared to that measured with the CIP, and their histograms are plotted in Figure 7.7. The CIP measurements are filtered for the altitude of 7.5 km shown also in the spatial fields, while the simulated N_{ice} are filtered for the latitudes and longitudes in which the BAe-146 aircraft sampled. The vast majority of simulated N_{ice} values fall in the lowest bin of 0 to 10 L^{-1}, and values of 50 L^{-1} or more appear in the measurements about 10 times as often as in the simulations. This underestimation occurs for all secondary production parameterizations, even 3Ag (denoted active drop freezing) and 1Bg (denoted active hydrometeor breakup). Different primary nucleation parameterizations could be run to see if this 'fills the gap'. As discussed in Chapter 3, dust is a much more efficient INP in the PDA13 parameterization, and additional heterogeneous nucleation could bring the simulated and measured N_{ice} into better agreement. Or comparisons of the altitudinal profiles of N_{ice} could be made. It is possible that the ice formation is simply distributed incorrectly within the modeled atmospheric column.

Finally we compare the time series of precipitation intensity from simulations with and without the secondary production parameterizations in Figure 7.8. These values are shown for all of 3 March 2009 at the CFARR location. Particularly for the simulations with active hydrometeor breakup (1Bg) and active droplet shattering (3Ag), a more accurate peak precipitation intensity is output than in the control simulation. These peaks also occur with correct timing at 2000 UTC. Those with the more limited formulation (1Bc and 3Ac) also have a higher peak precipitation intensity than the control run; however, it occurs about an hour too early. Given the large variability in these series, ensembles will be run next to determine the statistical significance of these differences.

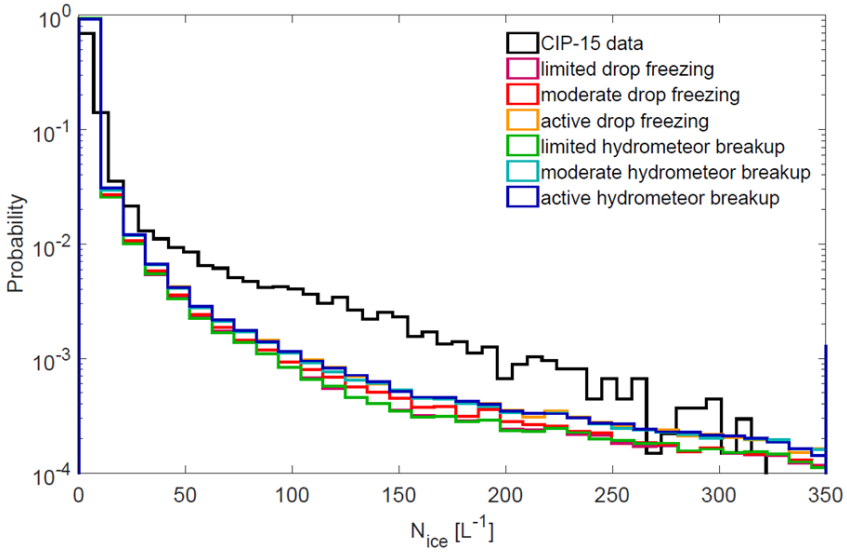

Figure 7.7: Comparison of simulated N_{ice} with various secondary production parameterizations and observed N_{ice} from the Cloud Imaging Probe during Flight B434 of the BAe-146 aircraft during APPRAISE. Values are filtered for an altitude of 7.5 km with $\overline{T}$ of 258 ± 7 K as in Figure 7.6. CIP-15 values from J. Crosier. Limited drop freezing = 3Ac; Moderate = 3Am; Active = 3Ag; Limited hydrometeor breakup = 1Bc; Moderate = 1Bm; Active = 1Bg.

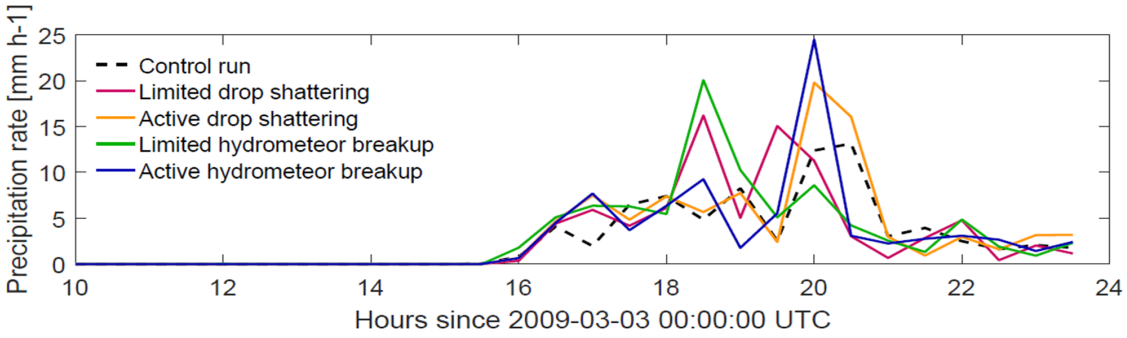

Figure 7.8: Simulated precipitation rate time series at the ground site (CFARR, 51.14° N, 1.44° W) for a control run and with various secondary production parameterizations.

7.5 Chapter 7 Summary

In this chapter, parameterizations of frozen droplet shattering and breakup upon collision were implemented in the COSMO mesoscale meteorological model of the German Weather Service. The parcel model in Chapters 5, 6, and 8 was used to make estimates and develop formulations for these processes, but COSMO includes hydrometeor size distributions and continuous sedimentation and growth processes, where the parcel model assumed monodis-

persity and characteristic time delays. From sensitivity runs in this more comprehensive framework, the following preliminary conclusions are made:

- **Secondarily produced N_{ice} can be about 1000 times as large as primarily nucleated N_{ice} in localized regions and altitudes.**
- **Simulations still underestimate the frequency of larger $N_{ice} \sim \mathcal{O}$ (100 $\mathbf{L}^{-1}$) at an altitude with $\overline{T}$ of 258 K.**
- **Including secondary ice production seems to increase the peak in simulated precipitation intensity.**
- **The temperature weighting for rime splintering is more influential than the droplet shattering probability on secondarily produced N_{ice}.**

CHAPTER 8
INITIATION OF SECONDARY ICE PRODUCTION BY PRIMARY NUCLEATION

In this chapter, we link the primary ice nucleation work from Chapters 2 to 4 to the secondary production work from Chapters 5 to 7. We quantify how many primarily nucleated ice crystals must exist before secondary production initiates, $N_{INP}^{(lim)}$, with the parcel model of Chapter 5. The framework is extended to include frozen droplet shattering, and three sets of simulations are performed to understand the impact of thermodynamic conditions and parametric uncertainty on $N_{INP}^{(lim)}$, as well as the ICNC enhancement from secondary production and the timing of a 100-fold enhancement.[1]

8.1 INP limitation to secondary production

INP numbers in the atmosphere span orders of magnitude from a few per cubic meter up to 100s per liter [e.g., 123]. At temperatures greater than about -15°C, these concentrations remain low: only one particle in every 10^3 or 10^4 will nucleate an ice crystal [235, 236, 237]. But even at these warmer subzero temperatures, ICNC can be orders of magnitude higher [e.g., 165, 170, 171, 217, 238]. Even as instrumentation and algorithms have been developed to minimize shattering artifacts [159, 163], the disparity has remained, supporting secondary ice production.

The parcel model includes the processes of rime splintering and breakup, which have already been described. In this chapter, the framework is extended to include shattering of frozen droplets with a diameter of 50 to 100s of μm upon freezing [239, 184, 224]. At sufficiently cold temperatures, latent heat release leads to the formation of a liquid core-ice shell structure that eventually shatters upon internal pressure build-up. Given the uncertainty in the number of fragments generated and the temperature dependence of these processes, small-scale models provide a good tool to gain insight on secondary production

[1]This work has been submitted as **S. C. Sullivan** et al. (2017) Initiation of secondary ice nucleation in clouds [234]. Support came from DOE EaSM, NESSF, and NASA MAP grants.

processes [13]. In particular, we use the model here to estimate the minimum number of INP necessary to initiate secondary production, called $N_{INP}^{(lim)}$ hereafter.

Some previous studies have estimated $N_{INP}^{(lim)}$ on the basis of in-situ data. For example in a study of ice initiation in cumulus, Beard found that a nucleated ICNC of 0.001 L^{-1} could trigger raindrop freezing around -5°C [10]. More recently, Crawford et al., with Aerosol Properties, PRocesses And InFluenceS (APPRAISE) campaign data, and Huang et al., with Ice and Precipitation Initiation in Cumulus (ICEPIC) campaign data, identified a primarily nucleated ICNC of 0.01 L^{-1} as sufficient to initiate rime splintering [153, 240]. Connolly et al. found that the rime splintering tendency increased with increasing primarily-nucleated ICNC, but this result was based upon adjusting the primary nucleation rate rather than the absolute N_{INP} [226]. Clark et al. also adjusted the primary nucleation rate relative to the rime splintering one, but gave no approximate $N_{INP}^{(lim)}$ values or thermodynamic constraints [176]. These studies have also considered only rime splintering, despite evidence that multiple processes occur simultaneously [152]. We provide more comprehensive estimates of $N_{INP}^{(lim)}$ over a range of fragment numbers and thermodynamic conditions.

8.2 Extended parcel model framework

To estimate ICNC enhancements and $N_{INP}^{(lim)}$, we run the parcel model from Chapter 5 [149]. The number in the six hydrometeors classes is again denoted N_i, N_d, N_g, N_G, N_r, and N_R for small ice crystals, small liquid droplets, small and large graupel, and medium and large droplets. Primary nucleation and secondary production by breakup upon collision, rime splintering, and now frozen droplet shattering are included:

$$G_{ice} = c_0 H(t) + \eta_{BR} K_{BR} \aleph_{BR} N_g N_G + \eta_{RS} \aleph_{RS} \Big[K_{RS,g} N_g + K_{RS,G} N_G \Big] N_R + \eta_{DS} \aleph_{DS} N_R. \tag{8.1}$$

c_0 is the primary nucleation rate [123]; H is a Heaviside function; η_X is the weighting for process X; K_X is a gravitational collection kernel for process X; and $\aleph_X$ is the fragment number generated by process X. The specific forms of $\aleph_X$ are given in Table 8.2. BR stands for breakup upon collision, DS for droplet shattering, and RS for rime splintering. In particular, $\aleph_{DS}$ contains a product of droplet freezing and shattering probabilities, p_{fr} and p_{sh} (as in Equation 7.6), and the number of fragments is not fixed as in Chapter 7, but dependent on droplet size. Later, the droplet shattering tendency is modified to represent a collisional process (denoted $DScoll$) with a product of large droplet and ice crystal numbers. The droplet generation function consists of activation from a Twomey power-law (Equation 5.2), and the number balance in each class is again the generation function at the current time as a source and the generation function at a time delay as the sink, along with aggregation and coalescence losses (Equations 5.3 to 5.8 with the droplet shattering tendency added in). The moist thermodynamic equations and non-sphericity formulations are as in Chapter 5. The updated microphysics is shown schematically in Figure 8.1, and parameter values and sources are given in Table 8.2.

8.3 Parcel model simulation setup for limiting INP

The three rows of Table 8.1 show three sets of simulations with the parcel model. First we investigate the evolution of the total ice hydrometeor number, N_{ice}, i.e. the summation of N_i, N_g, and N_G, in default simulations with fixed fragment numbers and thermodynamic conditions. Simulation acronyms include BR for breakup upon collision, DS for droplet shattering, RS for rime splintering, or ALL if all processes are active (see also Table 8.1 caption). These runs address how the value of $N_{INP}^{(lim)}$ and enhancement magnitude or timing vary when different processes are active. We quantify enhancement from secondary production as the ratio of the total ICNC to the number generated by primary nucleation when the simulation ends, i.e., when the parcel becomes water subsaturated or reaches a temperature of 237 K where homogeneous nucleation may occur: $N_{ice}^{(max)}/N_{INP}(t_{end})$. An enhancement of 10 can be understood as *at least* a 10-fold increase in ICNC due to secondary production, as an aggregation sink is also active in the simulations. In the

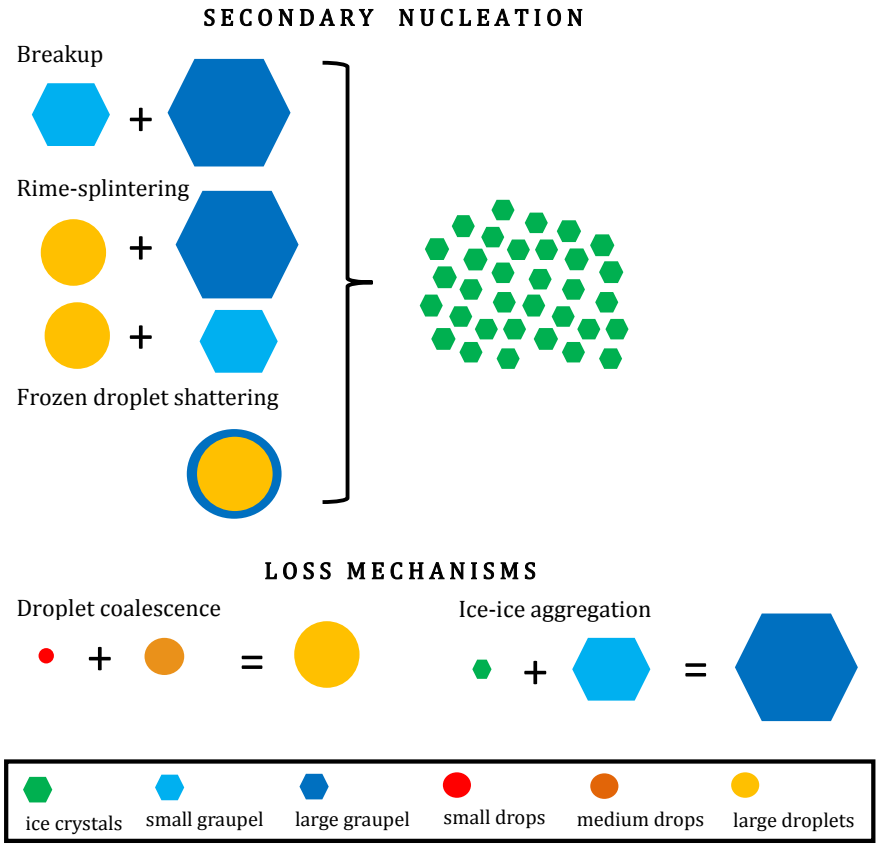

Figure 8.1: Schematic of the simplified six-bin microphysics model. The secondary nucleation processes included are the breakup of small and large graupel upon collision; the rime-splintering of either small or large graupel; or the shattering of large droplets upon freezing. Loss of hydrometeor number occurs through coalescence of small and medium droplets and aggregation of ice crystals and small graupel.

absence of secondary production, ICNC enhancement does not exceed one.

The second set of simulations considers the effect of updraft velocity and initial temperature in the parcel; this set is denoted 'th' for thermodynamics. The updraft is varied from 0.1 up to 4 m s^{-1} to simulate both stratiform and convective conditions, while the initial parcel temperature is adjusted from just below freezing (272 K) down below the peak of the droplet shattering probability distribution (256 K). These conditions also ensure numerical stability, given the stiffness of the coupled equations. The final set, denoted 'pp', performs parameter perturbations. In particular, we vary the leading coefficient of the fragment number generated per collision, F_{BR}; the minimum temperature for which breakup occurs, T_{min}; the functional form of the fragment number generated per shattering droplet; and the

Table 8.1: All simulations with parameters adjusted from the default values in Table 8.2. A control run with no secondary production, i.e., $\eta_{DS} = \eta_{BR} = \eta_{RS} = 0\%$ is denoted INP below. Thermodynamic simulations are run with combinations (BRDSth, BRRSth, and DSRSth) or all (ALLth) of the processes and shown solely in the Supplement.

Run BR	***Run DS*** ***(Run DScoll)***	***Run RS***
Breakup upon collision only	Droplet shattering only (Collisional shattering only)	Rime splintering only
$\eta_{DS} = \eta_{RS} = 0\%$	$\eta_{BR} = \eta_{RS} = 0\%$	$\eta_{BR} = \eta_{DS} = 0\%$
Run BRth	***Run DSth***	***Run RSth***
Thermodynamic variations for breakup	Thermodynamic variations for droplet shattering	Thermodynamic variations for rime splintering
V = { 0.1, 0.5, 1, 1.5, 2, 2.5, 3, 3.5, 4 m s^{-1}}	T_0 = { 256, 258, 260, 262, 264, 268, 270, 272 K}	
Run BRpp	***Run DSpp***	***Run RSpp***
Parameter perturbations for breakup	Parameter perturbations for droplet shattering	Parameter perturbations for rime splintering
F_{BR} = {0, 90, 140, 200, 280}	F_{DS} = {25, 75}x $10^{-12} D^{-4 \text{ or } -3}$	F_{RS} = {9, 15, 30, 45, 80} x 10^7 (kg rime)$^{-1}$
	(β, γ) = { (-0.016, 500), (-0.015, 400)}	
T_{min} = {246, 249, 252, 255, 258 K}	$p_{sh}^{(max)}$ = {1, 5, 10, 20, 30%}	

maximum of the temperature-dependent droplet shattering probability distribution, $p_{sh}^{(max)}$. The effect of these parameters on the generated fragment numbers is shown in Figure 8.2, and the alternate sigmoid functional forms for $\aleph_{DS}$ are shown in Figure 8.3.

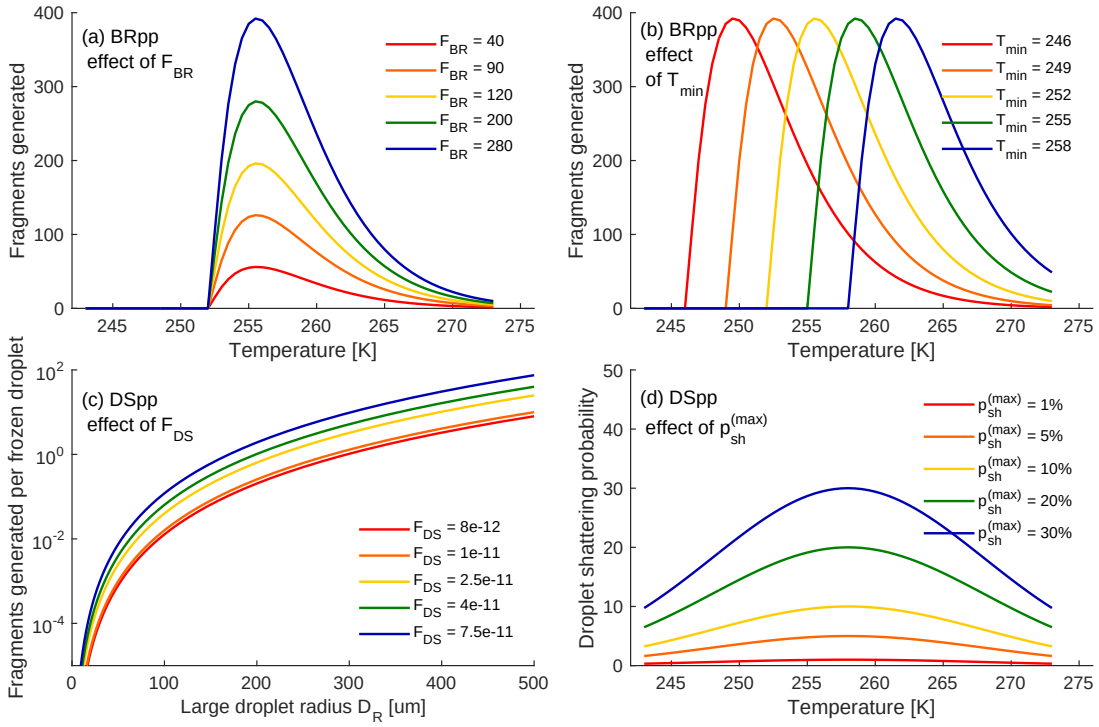

Figure 8.2: Effect of adjustments during the parameter perturbation simulations. Panel ***(a)*** *shows the effect of the leading coefficient F_{BR}, and panel* ***(b)*** *the minimum temperature of occurrence, within the breakup fragmentation generation function. Panel* ***(c)*** *shows the effect of the fragments generated by shattering per frozen droplet F_{DS}, while panel* ***(d)*** *shows various temperature-dependent freezing probability distributions. Parameter values increase from red to blue.*

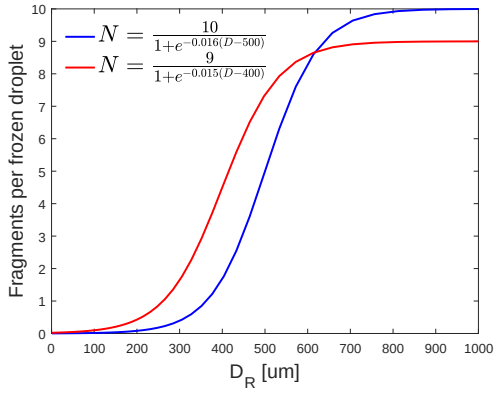

Figure 8.3: Alternate sigmoidal functions for the fragments generated per frozen droplet. $\aleph_{DS}^{(sig)}$ in Table 8.2 below.

Table 8.2: Default parameter values from simulations and their sources

Parameter	Value	Source
Fragment number		
$\aleph_{RS} = F_{RS}\rho_w \frac{\pi}{6} D_R^3$	F_{RS} = 300 frag (mg rime)$^{-1}$	Hallett & Mossop [165]
$\aleph_{BR} = F_{BR}(T - T_{min})^{1.2} \mathrm{e}^{-(T-T_{min})/5}$	F_{BR} = 280 T_{min} = 252 K	Takahashi et al. [15]
$\aleph_{DS} = F_{DS} D_R^4 p_{fr}(t, T, D_R) p_{sh}(T)$	$p_{sh} = 0.2\mathcal{N}$(258 K, 10 K) (see also Equation 7.4) p_{fr} = 1 - exp $\left[-\frac{\pi}{6} D_R^3 \, t \, K \exp(A(273 - T) - 1)\right]$	Droplet levitation experiments Bigg [233]
$\aleph_{DS}^{(coll)} = F_{DS} D_R^4 p_{sh}(T)$	p_{sh} as above	Droplet levitation experiments
	F_{DS} = 2.5 x 10^{-11} frag (drop diam [μm])$^{-4}$	Lawson et al. [224]
$\aleph_{DS}^{(sig)} = \frac{\alpha \, p_{fr}(t, T, D_R) p_{sh}(T)}{1 + \exp[-\beta(D_R - \gamma)]}$	α = 10; β = -0.016 γ = 500	Droplet levitation experiments
Initial conditions		
N_{X0}	0 cm^{-3}	
T_0, P_0, $s_{w,0}$	272 K, 680 hPa, 10^{-6}%	
r_{d0}, r_{r0}, r_{R0}	1, 12, 25 μm	Mossop [168, 7]
r_{i0}, a_{g0}, a_{G0}	5, 50, 200 μm	Zhang et al. [203]
Time scales		
τ_d, τ_r, τ_R	5, 15, 25 min	Approximate solution
τ_i, τ_g, τ_G	7.5, 20, 17.5 min	of growth equations
Droplet spectrum		
k_{CCN}, N_{CCN}	0.308, 100 cm^{-3}	Hegg et al. [205]
Updraft V	2 m s^{-1}	Korolev et al. [206]
Time step Δt	3 sec	

8.4 Parcel model results for limiting INP

8.4.1 Hydrometeor number evolution

The temporal evolution of N_{ice} in the default simulations is shown in Figure 8.4. Each simulation is done for a range of total INP number within the parcel, $N_{INP}^{(tot)}$. The structure in the number evolution can be understood by considering whether the process is collisional and whether it involves hydrometeors in one or both phases (liquid or ice).

N_{ice} from breakup and rime splintering evolves non-linearly, as these processes involve

a product of hydrometeor numbers. Independent of $N_{INP}^{(tot)}$, N_{ice} grows steadily throughout the simulation for these collisional secondary production processes. Even as graupel or large droplets are consumed, those hydrometeors still in the parcel continue to grow by deposition or condensation respectively. This ongoing hydrometeor growth increases the secondary production tendencies via their collection kernels, and this link itself is non-linear because both hydrometeor terminal velocity and collisional cross section increase with growth.

Droplet shattering is not modeled as a collisional process here, and its tendency is only proportional to a single hydrometeor number, N_R. As a result, N_{ice} does not grow steadily throughout the DS simulation, but rather exhibits threshold behavior when the temperature becomes cold enough for a non-negligible freezing probability according to Bigg [233]. A decrease in N_{ice} occurs right before the sudden increase for the DS simulation because large graupel begin to fall out of the parcel around 45 minutes. Below in Section 8.4.2, when we model collisional droplet shattering ($DScoll$), a steady increase appears again.

The ice phase is also influential for the enhancement timing from rime splintering or breakup. Because their tendencies involve graupel numbers, increasing $N_{INP}^{(tot)}$ boosts their rates of generation. For breakup, a parcel with 0.0129 L^{-1} INP reaches 10 $L^{-1} N_{ice}$ in 23 minutes, while that with 0.167 L^{-1} INP reaches the same value in 17 minutes. For rime splintering, the same increase in INP shifts the time to reach 10 L^{-1} N_{ice} from 30 minutes back to 25. While these differences in enhancement timing sound small, they can help infer which secondary production processes are active from in-situ N_{INP} and ICNC data. For example, ICNC on the order of hundreds per liter can form within 10 to 15 minutes [9, 151, 180]. This timing is too rapid to be explained by rime splintering alone [167], in agreement with our RS simulation. Simulations with breakup and rime splintering in combination, on the other hand, *are* sufficiently rapid.

As with enhancement timing, its magnitude can be explained in terms of non-linearity and hydrometeor phases involved. The breakup tendency is proportional to the product of two ice hydrometeor numbers, N_g and N_G, so the impact of varying $N_{INP}^{(tot)}$ is most pronounced for the BR simulations. Increasing $N_{INP}^{(tot)}$ by two orders of magnitude (0.001 to 0.167 L^{-1}) increases $N_{ice}^{(max)}$ by four order of magnitude (0.0023 to 37.6 L^{-1}). The rime splintering and droplet shattering tendencies are proportional to N_R which is around 10^6

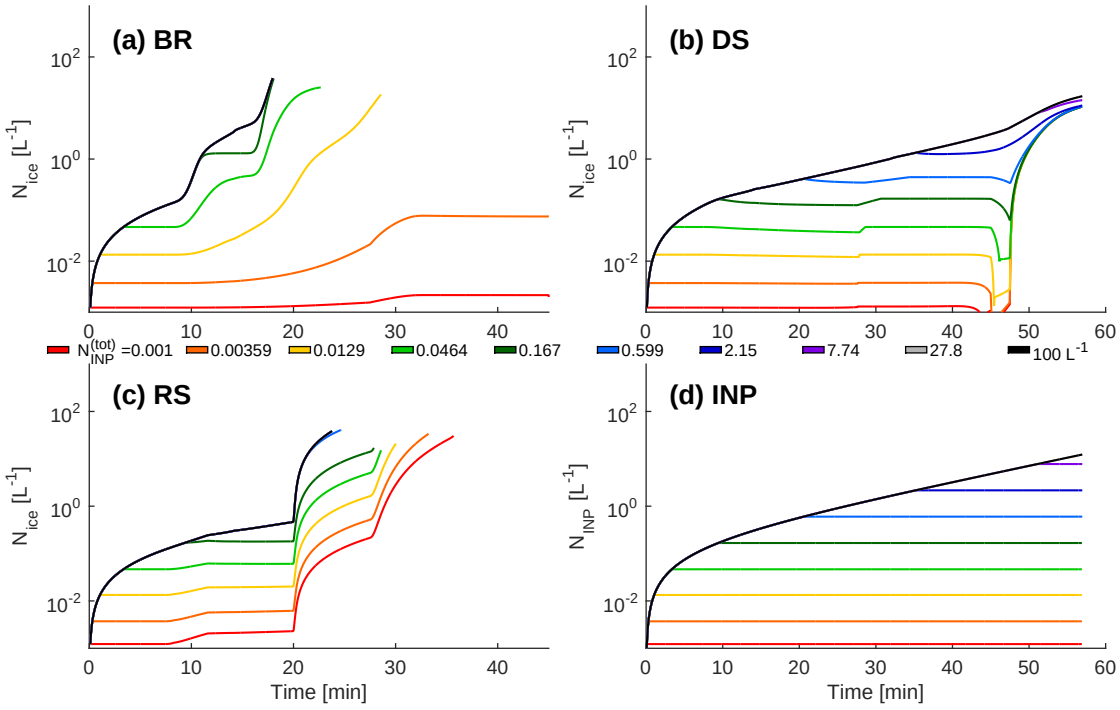

*Figure 8.4: Evolution of the total ice hydrometeor (summation of ice crystal, small and large graupel numbers) number for default simulations with a range of $N_{INP}^{(tot)}$ from 0.001 L^{-1} up to 100 L^{-1}: **(a)** breakup upon collision only, **(b)** droplet shattering only, **(c)** rime splintering only, and **(d)** a control run when only primary nucleation is active. These default simulations are run for V of 2 m s^{-1} and T_0 of 272 K.*

times as large as N_g or N_G, so the impact of $N_{INP}^{(tot)}$ for these processes is diluted. For the purely liquid-phase droplet shattering, the two-order-of-magnitude increase in $N_{INP}^{(tot)}$ has no significant impact on $N_{INP}^{(max)}$. For rime splintering, it actually translates to a two-fold decrease in $N_{ice}^{(max)}$ (30.58 to 16.67 L^{-1}). This decrease is the result of an increasing denominator in the $N_{ice}^{(max)}/N_{INP}(t_{end})$ expression (see also the RS panels of Figures 8.6 and 8.7 below). The rime splintering tendency is strong enough that it always generates additional ice crystals, so increasing $N_{INP}^{(tot)}$ actually decreases enhancement. The total INP number does, however, affect which rimers contribute to enhancement: when $N_{INP}^{(tot)}$ exceeds 0.167 L^{-1}, only rime splintering of small graupel can occur before subsaturation of the parcel.

Finally, increasing $N_{INP}^{(tot)}$ increases the ice generation rates from breakup and rime splintering only up to a certain point. Beyond an $N_{INP}^{(tot)}$ around 0.599 L^{-1}, additional INP do not

increase $N_{ice}^{(max)}$. The parcel is in a supersaturation-limited regime, for which it becomes subsaturated before the effect of additional primary nucleation can be felt by secondary production.

8.4.2 Collisional droplet shattering

As an extension of the default simulations only, we consider N_{ice} evolution and enhancement from droplet shattering as a collisional process; no parameter perturbations or varying thermodynamics are run for this collisional formulation. In this case, the tendency is proportional to both N_R and N_i, rather than just N_R as in Equation 8.1:

$$\left.\frac{dN_i}{dt}\right|_{DS} = \eta_{DS} K_{DS} \aleph_{DS}^{(coll)} N_R N_i \tag{8.2}$$

The fragment number from [224] ($F_{DS} D_R^4$) and p_{sh} are retained as in the DS simulation, but p_{fr} is removed with the understanding that the ice crystal-droplet collision initiates the freezing.

In Figure 8.5a, the threshold behavior of the enhancement from pure liquid droplet shattering is replaced by a steady increase similar to that from rime splintering or breakup. In fact, the growth in N_{ice} is now more gradual than that from RS or BR because N_i is also consumed by collisions now; there is effectively a linear increase in log space as $dN_i/dt \propto N_i$. This combined source and sink of N_i from droplet shattering also yields a smaller $N_{ice}^{(max)}$ of only 3.47 L^{-1} when 2 fragments are generated per collision and 7.87 L^{-1} when 10 are generated. The enhancement timing, on the other hand, has been much accelerated to about 14 (n = 10) or 15 (n = 2) minutes. $N_{INP}^{(tot)}$ still has no meaningful effect on either enhancement magnitude or timing.

As an uppermost bound for the enhancement from droplet shattering, we rerun the DS simulation with p_{fr} set to 1. In this case, an $N_{ice}^{(max)}$ of 17.67 L^{-1} is obtained over 27.8 minutes, not as fast as the collisional droplet shattering but about twice as fast as DS with non-unity p_{fr}. The temperature-dependent freezing probability above delays the DS enhancement, and in cases where p_{fr} is higher, droplet shattering may occur much more rapidly. Future work should also incorporate a dependence of p_{fr} on the number of

submerged INP [241], rather than just on time and temperature. Temperature and updraft dependencies are investigated in more detail next.

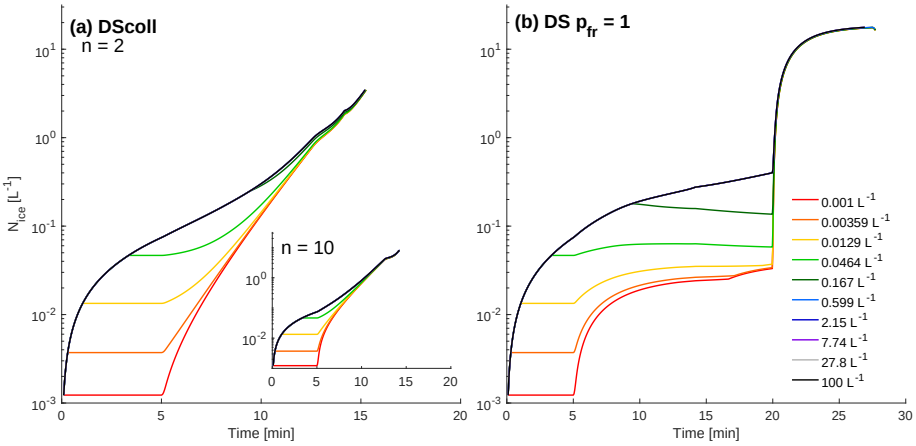

Figure 8.5: Evolution of N_{ice} for ***(a)*** *collisional droplet shattering and* ***(b)*** *droplet shattering with p_{fr} of 1 over the same range of $N_{INP}^{(tot)}$ as in Figure 8.4. p_{sh} is set to the default value of 20%. For the main panel* ***(a)****, droplet shattering generates 2 fragments per collision, and for the inset, 10 fragments per collision. These extensions to the default simulations are run for V of 2 m s^{-1} and T_0 of 272 K.*

8.4.3 Varying thermodynamics

Secondary enhancements from the simulations with varying thermodynamics are shown in Figures 8.6 and 8.7. Runs are performed for a range of updraft velocities and initial temperatures given in Table 8.1, but we focus on the extremes, as behavior in between is intermediate.

The top panels of Figure 8.6 show enhancements for stratiform conditions, i.e. V of 0.5 or 1 m s^{-1}, and a range of cloud base temperatures T_0. $N_{INP}^{(lim)}$ values for breakup upon collision can be seen in panel **(a)**. As T_0 decreases from 272 to 270 to 268 K, $N_{INP}^{(lim)}$ drops from 32.8 to 21.5 to 2.1 m^{-3}. At 266 K, $N_{INP}^{(lim)}$ increases again, reaching an $\mathcal{O}(10^2)$ enhancement only for an INP concentration of 0.143 L^{-1}. Larger ICNC occur only at these warmer T_0 because the parcel remains in the mixed-phase temperature range long enough that large graupel can form. For droplet shattering and rime splintering, there is no $N_{INP}^{(lim)}$ value greater than 1 m^{-3}.

Then when V is increased to 4 m s^{-1} in the bottom panels, the T_0 range over which droplet shattering and rime splintering occur expands, while the enhancement magnitude

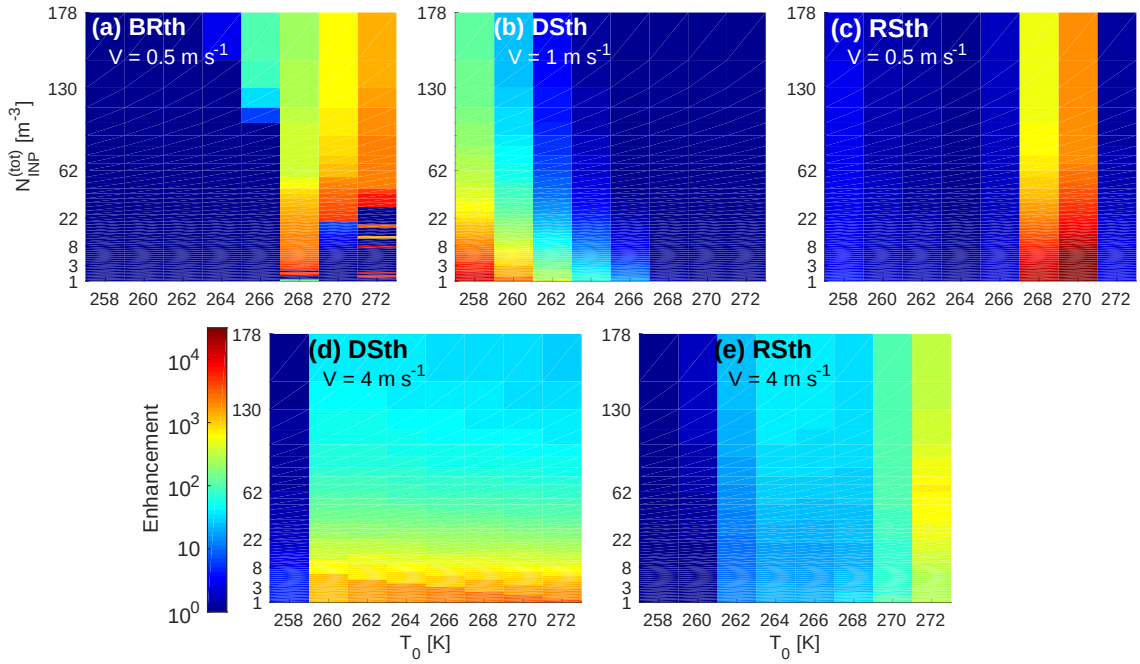

Figure 8.6: Ice crystal number concentration enhancement, i.e., $N_{ice}(t_{end})/N_{INP}(t_{end})$, for the thermodynamics simulations at various values of $N_{INP}^{(tot)}$, the total INP number in the parcel, and T_0, the initial temperature. Red indicates a larger enhancement per INP. Panels ***(a)****,* ***(b)****, and* ***(c)*** *show the enhancement for breakup and rime splintering at a low, stratiform-like updraft of 0.5 m s^{-1}. Droplet shattering is shown at 1 m s^{-1} because only very small enhancements occur at lower V. Panels* ***(d)*** *and* ***(e)*** *show the enhancement for droplet shattering and rime splintering at a higher, convective-like updraft of 3.5 m s^{-1}. No meaningful enhancements are generated by breakup at this larger updraft.*

shrinks. If T_0 is too cold and V is too strong, or conversely T_0 is too warm and V is too weak, the parcel does not remain in the appropriate temperature range for a long enough time to generate large hydrometeors that can shatter or collide. In particular, enhancement from breakup disappears for all T_0 values at a larger V because the parcel is too short-lived for graupel to form again. As the parcel moves faster, it is more likely to pass through the 'RS temperature zone' of 267 to 269 K or obtain higher p_{sh} or p_{fr}, but it also spends less time in these optimal zones.

If instead, we fix T_0 and look at a range of V as in Figure 8.7, breakup remains the only process with a defined $N_{INP}^{(lim)}$. This value decreases from 32.8 m^{-3} at 0.5 m s^{-1} down to 1.52 m^{-3} at 1.5 m s^{-1}. At 2.5 m s^{-1}, it increases back up to 50 m^{-3}, and at the fastest updraft velocities, no enhancement from breakup occurs.

For colder T_0, the idea of a 'sweet spot' in V appears again. The updraft must be

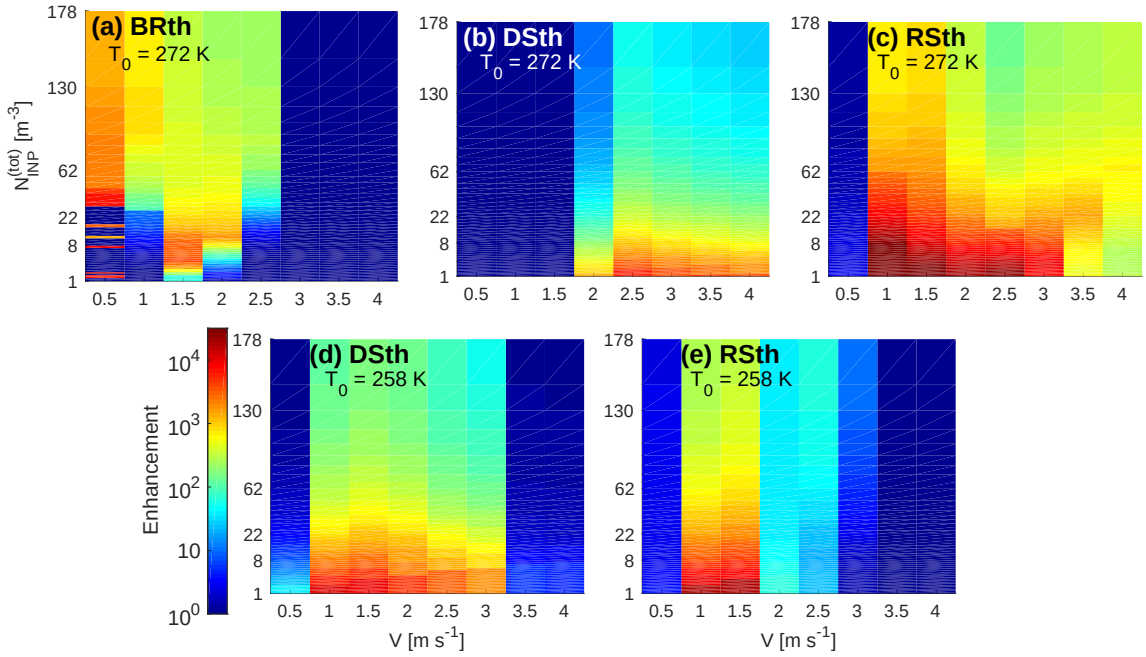

*Figure 8.7: Ice crystal number concentration enhancement, i.e., $N_{ice}(t_{end})/N_{INP}(t_{end})$, for the thermodynamics simulations at various values of $N_{INP}^{(tot)}$, the total INP number in the parcel, and V, the updraft velocity. Red indicates a larger enhancement per INP. Panels **(a)**, **(b)**, and **(c)** show the enhancement for breakup, droplet shattering, and rime splintering only at a warmer cloud base temperature of 272 K. Panels **(d)** and **(e)** show the enhancement for droplet shattering and rime splintering at a colder cloud base temperature of 258 K. No meaningful enhancements are generated by breakup at this colder T_0.*

strong enough that large droplets form by condensational growth but modest enough that these droplets remain in an appropriate temperature range for long enough. These trends are summarized in the first panel of Figure 8.12 and agree generally with [7] in which enhancement was possible down to 0.55 m s^{-1} but highest around 1.8 to 2 m s^{-1}. Mossop used a shell-fracture hypothesis to explain this optimum: too high a velocity and the riming drop spreads across the ice surface, rather than forming a fragile protuberance, and too small a velocity and an incomplete ice shell may form around the riming drop. Although not a validation of this hypothesis, the simplified model is, interestingly, able to reproduce this V behavior without such detailed rime physics.

Although there is no meaningful $N_{INP}^{(lim)}$ for droplet shattering or rime splintering, N_{INP} still affects enhancement from these processes. In fact, increasing $N_{INP}^{(tot)}$ generally decreases enhancement for all $V - T_0$ conditions. This can be understood in terms of a sort of INP

efficiency: the highest ICNC per INP is produced when $N_{INP}^{(tot)}$ is lowest. Mathematically, increasing $N_{INP}^{(tot)}$ increases the denominator of the enhancement ratio without a corresponding increase in the numerator. Physically, a higher $N_{INP}^{(tot)}$ depletes supersaturation more rapidly, as many small ice crystals grow by deposition, or it may keep the parcel warmer with latent heating. Fragment numbers, $\aleph_{DS}$ and $\aleph_{RS}$, also depend on the large droplet radius or rimed mass, which are reduced at lower supersaturation. Previous work corroborates this understanding: [226] found that increasing primary nucleation led to a decrease in the freezing of rain in cloud resolving simulations, while many studies have shown the importance of liquid phase properties to the rime splintering tendency [168, 7, 8, 170, 224].

Finally, Figures 8.6 and 8.7 show enhancement from a single process, but enhancement from multiple secondary production processes simultaneously can generally be understood as the linear combination of that from these single processes. For example, the pattern of enhancement from ALLth in Figure 8.8 looks like the addition of the patterns from RSth, DSth, and BRth in Figure 8.6.

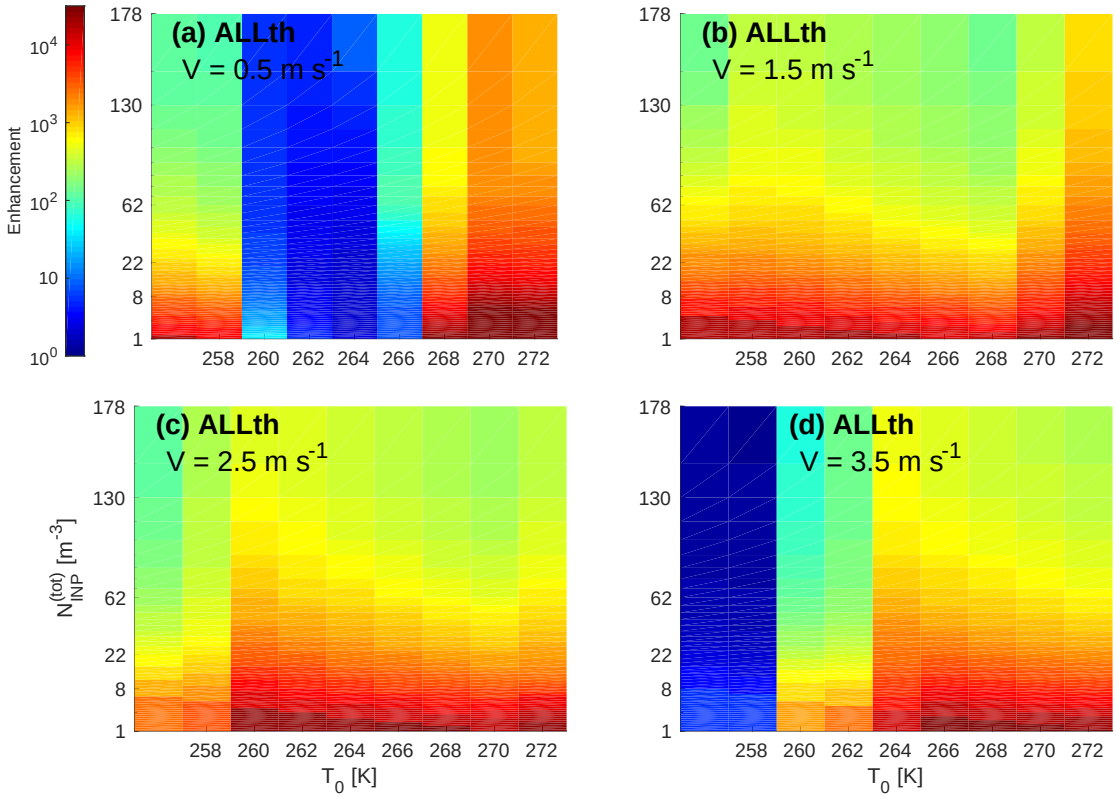

*Figure 8.8: Ice crystal number concentration enhancement, i.e., $N_{ice}(t_{end})/N_{INP}(t_{end})$, for the thermodynamics simulations at various values of $N_{INP}^{(tot)}$, the total INP number in the parcel, and T_0, the initial temperature. Red indicates a larger enhancement per INP. All panels show the enhancement when all secondary nucleation processes are active and with increasing updraft velocity V from panel **(a)** to **(b)** to **(c)** to **(d)**.*

8.4.4 Parameter perturbations

Lastly we use the insight about N_{ice} evolution and approximate enhancements from the above simulations to investigate the impact of adjustable parameters. In particular, we look at the effect of generated fragment numbers and temperature dependencies on $N_{INP}^{(lim)}$ and enhancement magnitude or timing.

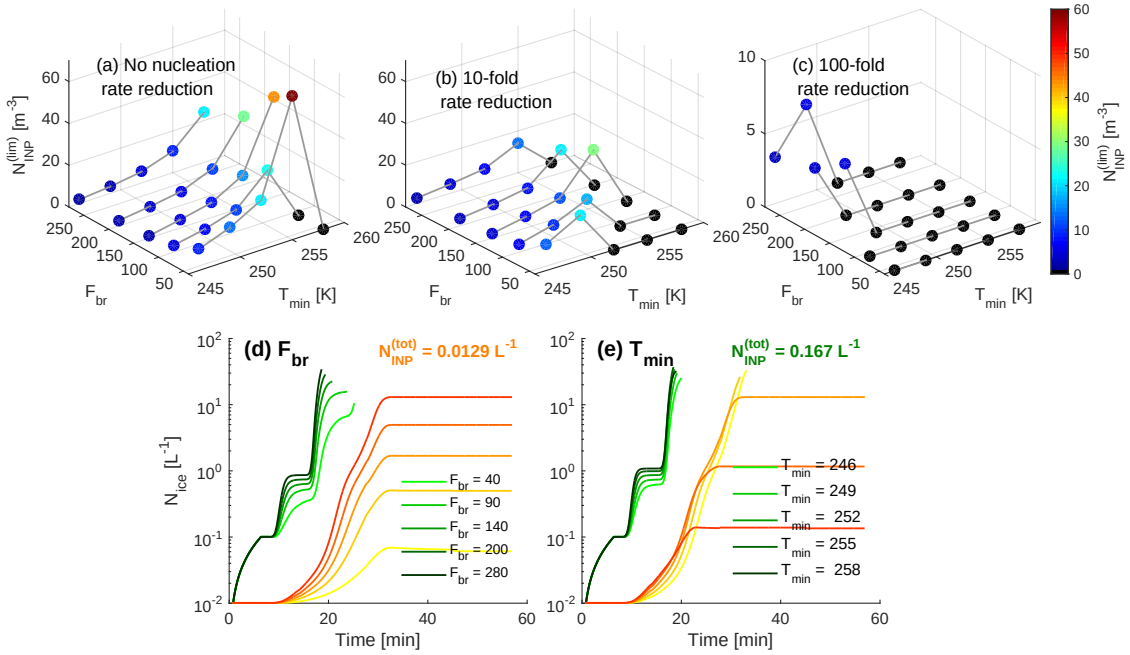

Figure 8.9: Results from the parameter perturbation simulations with breakup upon collision. The top panels show $N_{INP}^{(lim)}$ to obtain a 100-fold enhancement in N_{ice} for various values of F_{BR} and T_{min} within the breakup parameterization. Dots are also colored by $N_{INP}^{(lim)}$, where black indicates no 100-fold enhancement ever occurring. From panel ***(a)*** *to* ***(b)*** *to* ***(c)****, the nucleation rate decreases by two orders of magnitude; note that the y-axis in panel* ***(c)*** *has a smaller range than the others. The bottom panels show the temporal evolution of N_{ice} for the various values of F_{BR} and T_{min} with $N_{INP}^{(tot)}$ of 0.167 L^{-1} (green traces) and 0.012 L^{-1} (yellow traces). This coloring by $N_{INP}^{(tot)}$ is similar to that in Figure 8.4a above. These parameter perturbations are run for V of 2 m s^{-1} and T_0 of 272 K.*

The top panels of Figure 8.9 show the effect on $N_{INP}^{(lim)}$ from breakup for the default nucleation rate and one reduced by factors of 10 and 100. The conditions for which no enhancement occurs are shown in black in Figure 8.9, and the number of these points increases dramatically as the nucleation rate decreases from left to right (8 to 32 to 84%). Then as T_{min} increases, the temperature range over which breakup occurs shrinks, and $N_{INP}^{(lim)}$ increases: more ice crystals are needed initially to reach a 100-fold enhancement ultimately. As F_{BR} increases, more fragments are formed per collision, and $N_{INP}^{(lim)}$ decreases. This second effect of F_{BR} is the larger of the two. These $N_{INP}^{(lim)}$ trends for breakup occur until a sufficiently low F_{BR} or sufficiently high T_{min}, beyond which enhancement does not occur for any value of $N_{INP}^{(tot)}$ (up to 300 L^{-1}).

The bottom panels show N_{ice} evolution for various values of F_{BR} and T_{min} and for $N_{INP}^{(tot)}$

of 0.0129 L^{-1} (in yellow) and 0.167 L^{-1} (in green). The effect of both parameters is much larger when $N_{INP}^{(tot)}$ is small. Increasing F_{BR} from 40 to 280 increases N_{ice} by a factor of 200 when $N_{INP}^{(tot)}$ is 0.0129 L^{-1} and by only a factor of 3 when $N_{INP}^{(tot)}$ is 0.167 L^{-1}. Similarly, decreasing T_{min} from 258 to 246 K increases N_{ice} by a factor of 230 when $N_{INP}^{(tot)}$ is 0.0129 L^{-1} and by only a factor of 1.5 when $N_{INP}^{(tot)}$ is 0.167 L^{-1}. The parameters also mostly affect the enhancement magnitude not its timing.

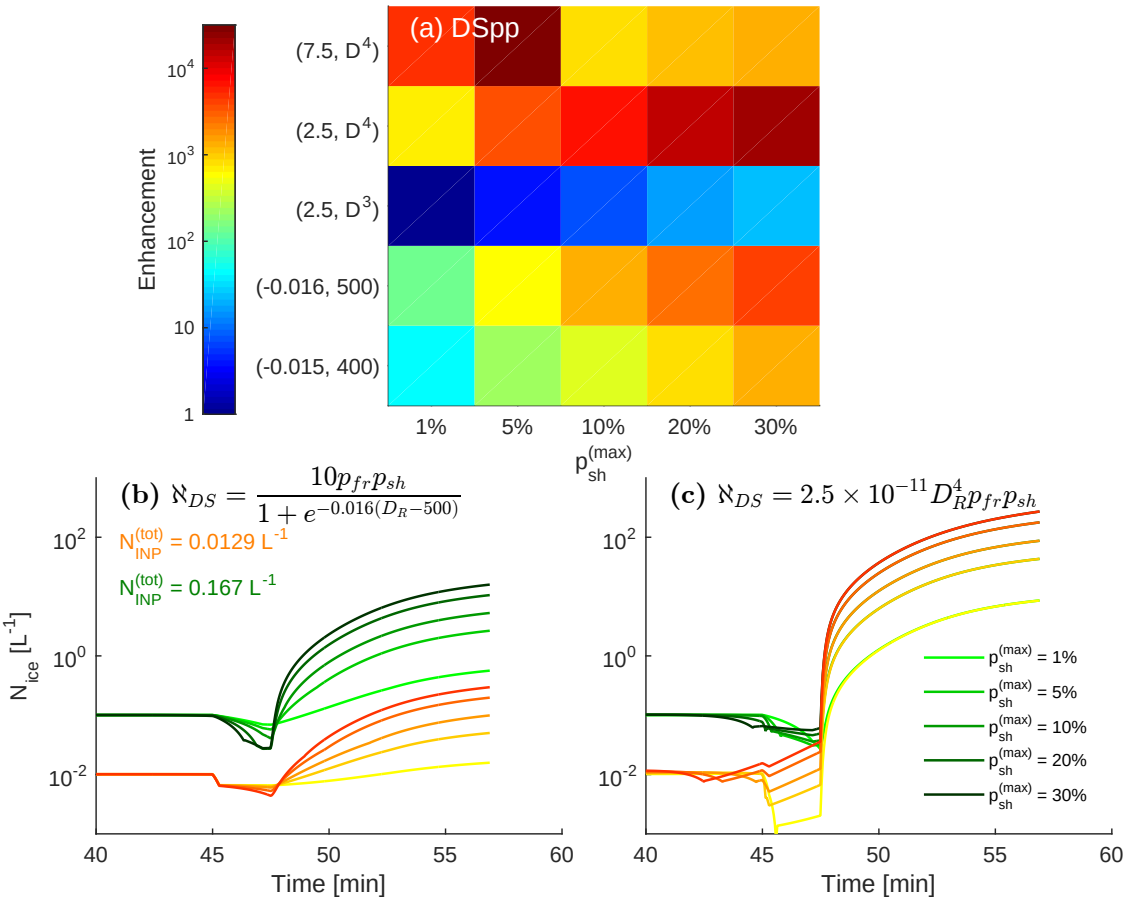

Figure 8.10: Results from the parameter perturbation simulations with droplet shattering. Panel ***(a)*** *shows how the enhancement magnitude shifts with the various values of F_{DS} and p_{max}. Panels* ***(b)*** *and* ***(c)*** *show the temporal evolution of N_{ice} for the various values of F_{DS} and p_{max} with $N_{INP}^{(tot)}$ of 0.167 L^{-1} (green traces) and 0.012 L^{-1} (yellow traces). This coloring by $N_{INP}^{(tot)}$ is similar to that in Figure 8.4b above. These parameter perturbations are run for V of 2 m s^{-1} and T_0 of 272 K.*

We next consider variations in $p_{sh}^{(max)}$ and the functional form for the fragments generated from droplet shattering. We triple the leading coefficient F_{DS} and alter the diameter

dependence from quartic to cubic within the [224] formulation. Then we use two sigmoids shown in Figure 8.3, which generate higher $\aleph_{DS}$ at small D_R and lower $\aleph_{DS}$ at large D_R relative to [224]. As above, there is no meaningful $N_{INP}^{(lim)}$ here, so we focus on the maximum enhancement from these various cases, shown in Figure 8.10.

In panel a, by far the smallest enhancements occur for a D_R^3 dependence in $\aleph_{DS}$. Independent of $p_{sh}^{(max)}$ these simulations never produce an ICNC enhancement greater than about 50. Larger enhancements occur for the D_R^4 dependence in $\aleph_{DS}$ than for a sigmoidal dependence on D_R. Interestingly for the largest leading coefficient, F_{DS} of 7.5 x 10^{-11}, higher $p_{sh}^{(max)}$ does not monotonically increase enhancement. Another kind of 'sweet spot' exists here, and too rapid initial fragment generation may actually deplete cloud liquid faster and limit ultimate ice crystal generation [242, 243, 13]. Elsewhere, increasing $p_{sh}^{(max)}$ does yield higher enhancement, up to about 2500 for the sigmoidal $\aleph_{DS}$ and an order of magnitude more for the default D_R^4 $\aleph_{DS}$.

Panels **(b)** and **(c)** show N_{ice} evolution for various values of $p_{sh}^{(max)}$ and the sigmoidal and default D_R^4 and $\aleph_{DS}$ forms respectively. The yellow traces show this evolution for $N_{INP}^{(tot)}$ of 0.0129 L^{-1} and the green for 0.167 L^{-1}, but these INP concentrations do not make a significant difference. Again it is clear that the D_R^4 dependence generates more ice crystals. And increasing $p_{sh}^{(max)}$ by a factor of 10 from 1 to 10% translates linearly to a factor 10 increase in $N_{ice}^{(max)}$.

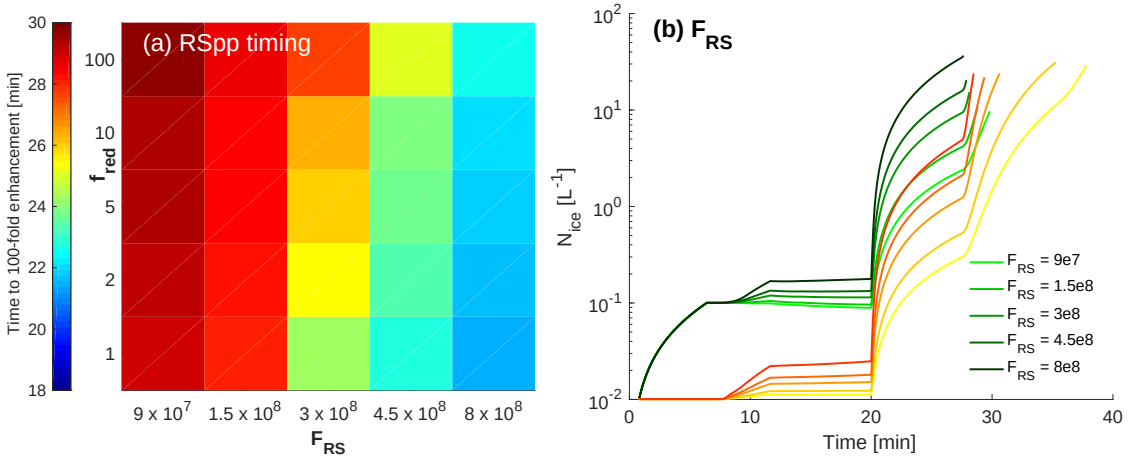

Figure 8.11: Results from the parameter perturbation simulations with rime splintering. Panel ***(a)*** *shows how time of a 100-fold enhancement shifts with the fragment number per kilogram rime F_{RS} and the nucleation reduction rate f_{red}. Panel* ***(b)*** *shows the temporal evolution of N_{ice} for various values of F_{RS} with $N_{INP}^{(tot)}$ of 0.167 L^{-1} (green traces) and 0.012 L^{-1} (yellow traces). This coloring of $N_{INP}^{(tot)}$ is as in Figure 8.4c above. These parameter perturbations are run for V of 2 m s^{-1} and T_0 of 272 K.*

Finally, Figure 8.11 shows the impact of fragment number per kilogram of rime, F_{RS}. Here we consider enhancement timing because the thermodynamic simulations show that there is no meaningful $N_{INP}^{(lim)}$ and the default ones show that the enhancement magnitude stays more or less constant. Panel **(a)** shows how the enhancement timing varies with the nucleation rate and fragment number F_{RS}. Slower nucleation rates are quantified by a reduction factor f_{red} on the y-axis. Along with lower F_{RS}, slower nucleation yields longer enhancement times, but only by about 8 minutes relative to the highest nucleation rate and F_{RS}. F_{RS} is also the more influential factor in timing, and its impact on N_{ice} evolution is shown in panel **(b)**.

8.5 Implications

Most generally, the role of INP in secondary ice production reflects how changing emissions will affect cloud phase partitioning. The low or non-existent values of $N_{INP}^{(lim)}$ calculated here indicate that perturbations in CCN concentrations are more influential on mixed-phase partitioning than those in INP concentrations, with the caveat that thermodynamic conditions are appropriate for secondary production. If the mixed-phase cloud is polluted by

more CCN, the higher droplet number will mean that fewer droplets reach a sufficient size to shatter or rime efficiently (This last factor has been called the riming indirect effect [244, 245, 30].) And in these cases, the supercooled liquid fraction remains higher, and the cloud reflects more shortwave radiation. More pollution by CCN could also yield a thermodynamic indirect effect in which latent heat is released at high altitudes and strengthens the upward movement of the cloud; Koren et al. have called this cloud invigoration [23]. Our simulations have shown that beyond a certain updraft, secondary production is no longer favored. In this way, the supercooled liquid fraction could also remain higher.

The impact of INP concentrations could be larger for deep convective clouds in which anvil spreading is caused by generation of many small crystals at cloud top [246]. If the cloud is polluted by more INP, more vigorous secondary production by breakup may occur under conditions of fast enough nucleation rate but modest enough updraft and warm enough cloud base. These limited conditions can be found in deep convective clouds, along with other regions favorable for secondary production like the "mixing regions" at the edges of rising turrets or tops of eroding ones [10]. In contrast to the riming or thermodynamic indirect effects mentioned above, an ICNC increase at the deep convective cloud top, a kind of 'anvil enhancement effect', would radiatively warm the surface.

A systematic quantification of $N_{INP}^{(lim)}$ is also relevant for the growing field of bioaerosol. Primary biological aerosol particles (PBAP) exist in the atmosphere at much lower number concentrations than dust or black carbon. But they also nucleate at warmer subzero temperatures [101, 247], and small biological residues can intermix with dust particles to boost ice nucleation activity [248]. Even when their contribution to primarily nucleated ICNC is small, they may remain influential via initiation of secondary ice production. For example, the ice active fraction of 10^{-4} for *Pseudomonas syringae* measured by [249] around -8°C could provide the 0.01 L^{-1} seed concentration from [153] for concentrations of 10^5 m^{-3}, although this is an upper bound for bioaerosol number. From our calculations, it could also provide the $N_{INP}^{(lim)}$ necessary for breakup to occur. Bioaerosol could also be sufficient to initiate rime splintering, given that this process occurs even for N_{INP} below 1 m^{-3} in our simulations. A climatically important linkage has also been hypothesized between PBAP, in-cloud ICNC, and cold phase-initiated rain and is often termed the 'bioprecipitation feed-

back' [250, 251]. The possibility of secondary production with a low $N_{INP}^{(lim)}$ means that even a few bioaerosol could trigger generation of many small ice hydrometeors from larger droplets or graupel and suppress precipitation.

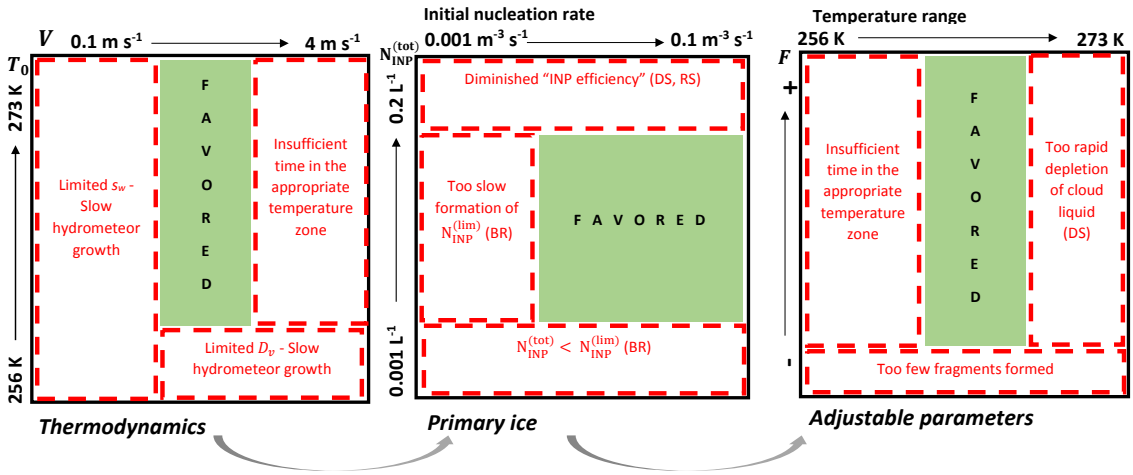

Figure 8.12: Summary of thermodynamic, primary ice, and adjustable parameter trends affecting ICNC enhancement from secondary production. F denotes the leading coefficient of a fragment number function for process X, $\aleph_X$. Regions in red indicate that secondary production may be limited, and those in green indicate that conditions are favorable. If the limitation is applicable only to one process, this is indicated in parentheses.

As a summary of our findings, we present an organizational framework for future studies of secondary production in Figure 8.12. Favorable conditions for large ICNC enhancements are shown in green, e.g., warm cloud base and intermediate updraft in the thermodynamic panel or higher nucleation rate for breakup in the primary ice panel. This classification can be used to determine where, within in-situ or remote sensing data, signatures of secondary production are likely to be found. And as more experimental studies to quantify the fragment number and temperature dependencies of these processes are done, more quantitative bounds can be established in the final adjustable parameter panel.

8.6 Chapter 8 Summary

In this chapter, three sets of simulations were run with the parcel model to consider the effect of thermodynamics and parameter perturbations on the number of primarily-nucleated ice crystals necessary to initiate secondary ice production. The findings can be summarized in

three points:

- **The evolution of N_{ice} from secondary production is determined by collision-based non-linearity and single versus two-phasedness.**

  N_{ice} increases gradually for the collision-based processes of breakup and rime splintering, whereas for non-collisional droplet shattering, N_{ice} increases significantly and suddenly, only when p_{fr} becomes large enough at cold enough temperatures. $N_{INP}^{(tot)}$ affects both the enhancement magnitude and timing for breakup. For rime splintering, $N_{INP}^{(tot)}$ affects timing to obtain a given $N_{ice}(t_{end})$, while for droplet shattering, it has almost no impact on either magnitude or timing.

- $N_{INP}^{(lim)}$ **can be as large as 0.07 L^{-1} for breakup. Rime splintering or droplet shattering enhancement is determined by a thermodynamic 'sweet spot' rather than by $N_{INP}^{(lim)}$.**

  $N_{INP}^{(lim)}$ increases for breakup as the fragment number decreases or the temperature range shrinks, particularly for $N_{INP}^{(tot)}$ of 0.01 L^{-1} or less. At faster nucleation rates, the fragment number and temperature range are also more influential: enhancement occurs for 90% of the parameter space at a default nucleation rate, and just 10% of the space at a rate 100 times slower. These trends are visualized in the 'primary ice' panel of the summary schematic (Fig. 8.12).

  For rime splintering or droplet shattering, ICNC enhancements of 10^4 are possible even for slow nucleation rates and $N_{INP}^{(tot)}$ as low as 1 m^{-3}. For these processes involving the liquid phase, an intermediate updraft for which hydrometeors grow fast enough but also spend long enough in the appropriate temperature zone is more important. The cloud base temperature must also be warm enough, i.e., greater than 260 K in our simulations.

- **When multiple secondary production processes are active, no single process dominates ICNC enhancement.**

At higher nucleation rates, low V, and warm T_0, the contribution from breakup is large. If INP are limited, V is somewhat higher, or T_0 is somewhat colder, droplet shattering should be more important. Or if temperature falls in the optimal zone of 268 to 270 and V is intermediate, the rime splintering contribution will be large. A large p_{fr} for droplet shattering, however, throws off this balance. If p_{fr} is closer to unity, non-collisional droplet shattering dominates, as it depends on liquid hydrometeors only and has less stringent temperature dependence than rime splintering.

CHAPTER 9
INTEGRATING MODELLED CLOUD PHYSICS WITH MEASUREMENTS AND HYDROCLIMATE

Going forward, the most important work to be done for cloud parameterizations is more extensive model-data intercomparison. Convectively-driven cloud fields are a highly nonlinear dynamical system (Section 1.4) and represent an especially difficult problem for model evaluation. This chapter first presents a rigorous means of performing this evaluation. Elucidating the linkages between clouds and the larger climate system poses a second challenge [51]. This outlook ends with a discussion of two possible feedbacks between cloud properties and the hydrological cycle and a general means of assessing the social impact of such feedbacks.

9.1 Multi-scale systems revisited

If clouds are understood as dynamical systems, many examples exist of their strange attractors and emergence. Arctic mixed-phase clouds may persist for up to 70 hours in spite of microscale instability due to the lower equilibrium vapor pressure of ice (Section 1.3: Bergeron process) [252], and they evolve preferentially toward either a radiatively clear or opaquely cloudy state [253]. Analogous open- and closed-cell preferential states exist for marine boundary layer clouds [254]. Convective aggregation, or self-organization, may drive transitions in these states and can affect the general circulation and hydrological cycle on large scales [22].

Given this complexity of cloud field evolution, significant current research is devoted to produce ever more sophisticated cloud microphysics and convective parameterizations. Indeed, the latter half of this dissertation presented the development of detailed secondary ice nucleation parameterizations. However, this kind of development neglects system feedbacks or emergent behavior. Then again, it remains unclear what degree of physical accuracy within a parameterization is needed to obtain acceptable predictions of climatically impor-

tant outputs [47, 255].

To guide this model development, comparisons to measurements are generally done with point metrics like the mean and standard deviation of some distribution, but recent studies indicate that disagreement at higher-order moments of these distributions can be quite influential. For example, inclusion of soil moisture affects simulated surface temperature disproportionately at very high and very low values, an effect seen only in the skewness and kurtosis of the temperature distribution [256]. Underestimation of the skewness in the vertical velocity distribution can lead to dramatic under-prediction of in-cloud maximum supersaturation and resultant cloud droplet or ice crystal number concentrations (an effect relevant to much of this work, particularly Sections 3.2, 4.4.2, and 6.2.4) [130, 257].

Instead, information theory could be used to better assess the current and requisite accuracy of subgrid-scale parameterizations. Its mathematics provide an insightful, systems-based link between a model evaluation need and an expanding satellite data resource. A plan is outlined below to quantify and visualize the accuracy of cloud schemes with discrimination information and t-distributed Stochastic Neighbor Embedding respectively.

9.2 Mathematics of information theory

In information theory, the entropy of a system describes the uncertainty associated with a particular state in that system, given only the probability distribution of states. If the possible states are denoted σ_1, σ_2,..., σ_N, then the **entropy of the system** is given by

$$H = -\sum_{i}^{N} p(\sigma_i) \ln p(\sigma_i), \tag{9.1}$$

where $p(\sigma_i)$ is the probability associated with state σ_i. System entropy is maximal when all states are equally likely. Information theory was initially created for telecommunications but has found application in fields as diverse as ecology and linguistics [258, 259]. In climate science, it has been used to estimate the predictability bounds for temperature anomalies [260] and, more recently, to rigorously quantify uncertainty and identify the most sensitive climate change direction from a stochastic test model [261]. However, information theory has never been used to quantify the information loss due to subgrid parameterizations in

climate models.

9.2.1 Kullback-Leibler divergence

The Kullback-Leibler divergence, also known as **discrimination information** or **relative entropy**, quantifies the amount of information from one probability distribution, Q, contained in a second one, P:

$$\phi(P, Q) = \int P \ln \frac{P}{Q}. \tag{9.2}$$

It can also be understood as the statistical difference between two probability distributions [262]. In the context of atmospheric modeling, the Kullback-Leibler divergence has several attractive properties. It is sensitive to higher-order moments of a distribution, not simply its mean and standard deviation. It is invariant under a change of variables, if we wanted to, for example, switch between altitudinal and pressure coordinates:

$$\phi(P, Q) = \int_{x_1}^{x_2} P(x) \ln \frac{P(x)}{Q(x)} dx = \int_{u_1}^{u_2} P(u) \ln \frac{P(u)\, du/dx}{Q(u)\, du/dx} du = \int_{u_1}^{u_2} P(u) \ln \frac{P(u)}{Q(u)} du. \tag{9.3}$$

And it is additive: for a distribution P which is the product of two independent distributions P_1 and P_2, its divergence decomposes into two separate values:

$$\phi(P||Q) = \phi(P_1||Q_1) + \phi(P_2||Q_2) \tag{9.4}$$

9.2.2 t-distributed Stochastic Neighbor Embedding

The Kullback-Leibler divergence is employed in **t-distributed Stochastic Neighbor Embedding** (t-SNE), a large dataset visualization technique [263]. t-SNE employs dimensionality reduction to illustrate the underlying structure of large datasets, like climate model output, in a two- or three-dimensional scatterplot. The multivariate Euclidean distance between data points x_i and x_j is first calculated, followed by a conditional probability that

the two are neighboring points, assuming a Gaussian distribution about x_i:

$$P(x_j|x_i) = \frac{\exp\left(-|x_i - x_j|^2/\sigma_i^2\right)}{\sum_{k\neq i}\exp\left(-|x_i - x_k|)^2/2\sigma_i^2\right)} \tag{9.5}$$

The average of $P(x_j|x_i)$ and $P(x_i|x_j)$ defines a symmetric metric, which can be understood as the similarity of points x_i and x_j and for which larger values indicate more similar points. Analogous conditional probabilities, or similarities, are calculated from a lower-dimensional equivalent to the actual, high-dimensional data:

$$Q(y_j|y_i) = \frac{(1 + |y_i - y_j|^2)^{-1}}{\sum_{k\neq i}(1 + |y_i - y_k|^2)^{-1}} \tag{9.6}$$

Then the points in low-dimensional space are arranged to minimize the Kullback-Leibler divergence between the similarity distributions in high- and low-dimensional space. The cost function C can be defined as the divergence:

$$C = \sum_i \phi(P_i, Q_i) = \sum_i \sum_j P(x_j|x_i)\log\frac{P(x_j|x_i)}{Q(y_j|y_i)}. \tag{9.7}$$

Minimizing the Kullback-Leibler divergence corresponds to retaining as much information about the high-dimensional similarity distribution in the low-dimensional equivalent. Dimensionality reduction in t-SNE is mostly constrained by similar points: the cost function penalty is highest when similar points in high-dimensional space are not kept close together in the low-dimensional equivalent. This is in contrast to a technique like principal component analysis, which attempts to explain as much variance in the dataset as possible and is thus constrained by keeping dissimilar points far apart in the low-dimensional map.

9.3 Model evaluation with discrimination information

The Kullback-Leibler divergence can be used for model evaluation, as a quantification of the amount of information lost about a cloud field during parameterization. For microphysics parameterizations, data and model output can be classified into cloud regimes on the basis of cloud top pressure and optical depth [264, 265]. For convective parameterizations,

this initial classification may take a number of forms, as discussed below. Thereafter these cloud and convective classifications can be refined with t-SNE to determine which key components, or dimensions, are most influential on the subgrid phenomena. This dimensional reduction could be particularly important to understand **convective aggregation**, the self-organization over time of many randomly rising plumes into one larger one. This kind of assessment would involve the following steps:

1. *Define a set of cloud schemes and run an ensemble of year-long simulations for each one.*

   GCM simulations will be done to ensure statistically significant sample sizes in the Kullback-Leibler divergence calculation. A set of cloud schemes can be defined, some employing the Morrison and Gettelman two-moment microphysics and Park and Bretherton shallow convection in the NCAR CAM5 [42, 266] and some employing the Morrison et al. microphysics and the cloud-resolving System for Atmospheric Modeling in the Superparameterized CAM [267, 268].

   Within a given set, the default physics or convection can be adjusted, for example by enforcing or adjusting the minimum entrainment rate, by relating updraft mass flux to different conserved surface variables [269], or by replacing microphysical substepping with semi-Lagrangian advection. The idea in these adjustments will be to consider more than the default setup because grouping certain formulations within a single scheme may amplify certain biases. The assessment will quantify how well a suite of parameterizations, taken as a whole, retains information from observations. Then for each scheme, an ensemble of 100, year-long simulations can be run to calculate probability distributions Q of a simulated cloud property like supercooled liquid fraction. These probability distributions will be calculated separately for each cloud or convective regime.

2. *Krige satellite data from the simulated year onto the temporal and spatial grid of the model and classify values by cloud regime.*

   Cloud and radiative properties, like optical thickness, liquid and ice water paths, or

shortwave top-of-atmosphere flux, will be used from the A-Train integrated CALIPSO-CloudSat-CERES-MODIS active measurements, also known as the CCCM product. These data will be interpolated onto the spatial and temporal grid of the model output and then filtered for various cloud or convective classifications. The cloud classifications will initially be defined as in previous studies, on the basis of a k-clustering analysis of cloud top pressure and cloud optical thickness histograms [264, 265].

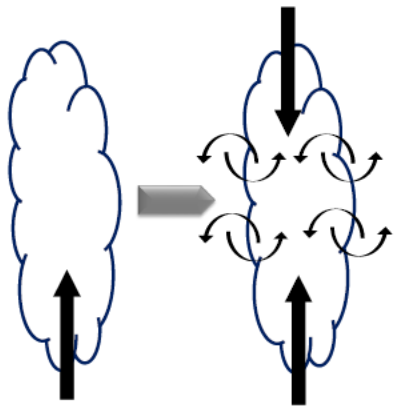

Figure 9.1: Transition from a simple updraft velocity treatment toward a more complete description of in-cloud dynamics, including downdrafts, entrainment, and detrainment.

An appropriate initial convective classification is less clear. We can begin by using the coherent structures in the atmospheric boundary layer identified within a recent study [270]. An octant analysis on output from large-eddy simulations decomposed the flow field into the updrafts, discussed extensively in Chapter 4, but also downdrafts, ascendance, and subsidence (Figure 9.1). However, convective features like stratocumulus-topped mixed layers or trade cumulus boundary layers are often classified based on radiative factors like longwave cooling or latent heat fluxes. If the first classification does not yield meaningful evaluations, we could adopt one defined by surface inhomogeneity and shortwave and longwave radiative fluxes. Finally, for each cloud or convective regime, an observed probability distribution, P, will be calculated for the property of interest.

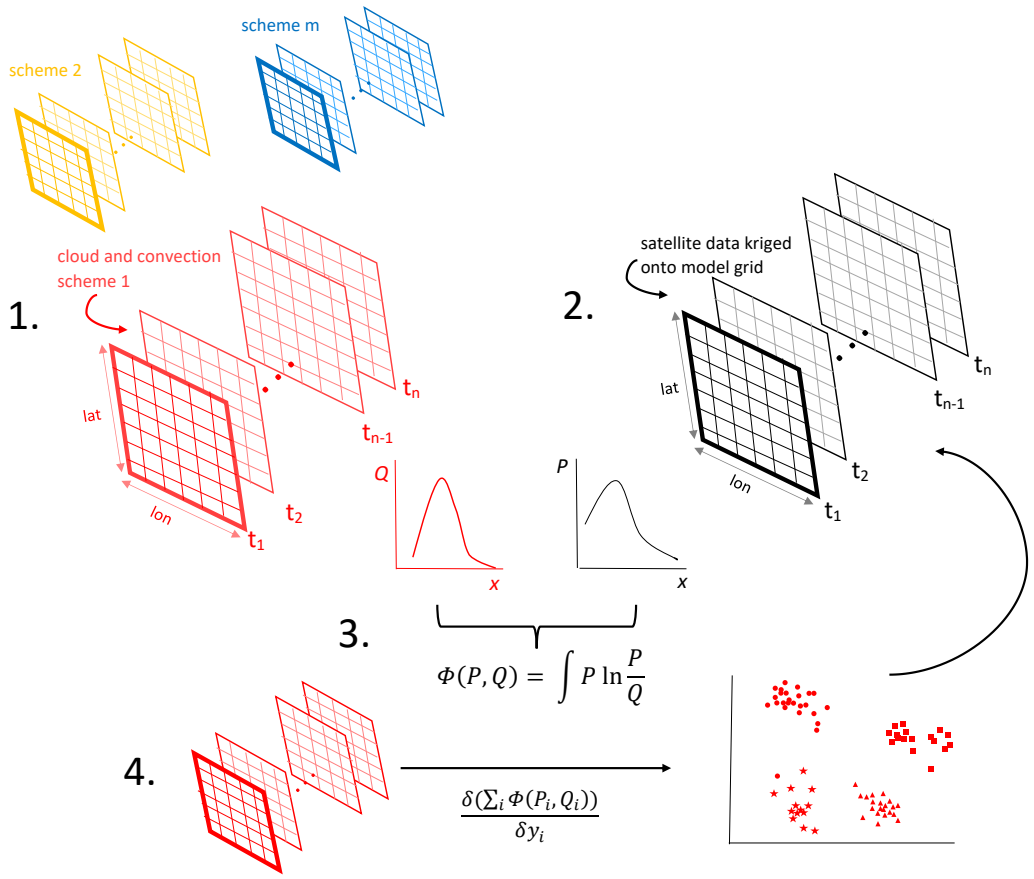

Figure 9.2: Project schematic. Steps 1 to 3 are performed in a global climate model for a single 'dimension', i.e., a particular cloud or convective classification. In step 1, we run simulations with various schemes (red, yellow, and blue grids) and obtain the simulated distribution Q. In step 2, satellite observations are kriged onto the same grid to obtain the observed distribution, P. We calculate the divergence between P and Q in step 3. Step 4 reconsiders the assumed 'dimension via t-SNE, which visualizes all model data points in a structured scatterplot. New t-SNE dimensions can be used to repeat evaluation in steps 1 to 3.

3. *Quantify the agreement between simulated and observed probability distributions of the cloud property with the Kullback-Leibler divergence.*

   The Kullback-Leibler divergence can be calculated between the simulated distribution for each scheme and the observed distribution. Those cloud schemes with a lower divergence more accurately represent the cloud field, as less information has been lost from the corresponding measurements.

4. *Visualize the simulated cloud field in a t-SNE scatterplot.*

In the final step, we can reconsider the cloud and convective classifications upon which the evaluation was based. Beginning with the scheme from steps 1 to 3 for which the data-model divergence was lowest, t-SNE can be performed on the unclassified model output from step 1. This high-dimensional model output is given by P and various lower-dimensional maps are given by Q in the Kullback-Leibler divergence-based cost function (Equation 9.7). The same is done with the satellite data. Once the divergence between the model output or data and the map is minimized, the map dimensions can be compared to the classifications assumed initially. If the two differ significantly, we can reclassify the data and model output on the basis of these new dimensions, recalculate the simulated and observed probability distributions, and reevaluate the Kullback-Leibler divergence.

For various microphysics and convective parameterizations, this process will provide an elegant way of visualizing their output structure. The insight can also be quite informative in elucidating the components that initiate and sustain convective aggregation. Although aggregation should occur in the SPCAM simulation, we will perform two final t-SNE analyses on model output from smaller-domain simulations with an idealized cloud-resolving model and the NOAA Weather Research and Forecasting Model to identify these components. Finally, if the dimensions derived from the global-scale and cloud-resolving-scale t-SNE differ, we will investigate the impact of coarse-graining various outputs.

9.4 Cloud-hydroclimate feedbacks

As discussed in Chapters 1 and 7, clouds play an important role in the hydrological cycle. Understanding how cloud properties, and in turn characteristics of the hydrological cycle, alter with climate change is of foremost societal importance. The most dramatic impact of hydrological changes will be to agriculture, as the largest consumer of water. Particularly problematic for farmers already struggling with drought is the trend mentioned earlier of 'wet gets wetter, dry gets drier [34, 35, 36]. Large-scale increases in aridity would also be quite detrimental [37, 38]. If we can identify regions especially susceptible to future

water limitations, targeted measures can be taken to make agriculture there more resilient. For example, plants with deeper root penetration, slower leaf emergence, and higher water use efficiency can be grown [271]. Crop relocation, deficit irrigation, and site-specific crop management are other strategies that can be employed on a region-by-region basis [272].

Root zone soil moisture may be the most directly relevant hydrological metric to farmers; however, all moisture fluxes – evaporation, runoff, and infiltration – must be considered for its accurate prediction. Given the high latent heat of vaporization of water, changes in the surface water budget are ultimately related to modifications of the surface energy budget. Anthropogenic greenhouse gases and aerosol emissions, along with cloud cover change, are altering this energy budget and, in turn, the hydrological cycle through cloud processes [273].

A number of factors make it difficult to translate climatic radiative changes to quantitative outcomes for the continental hydrological cycle. Many feedbacks exist, both within a single cloud and within the larger water cycle, and these may act to either mute or amplify input perturbations to the system [51, 274, 275] There is also the problem of scale, discussed at the start of Chapter 1. And finally, accurate observations are difficult to make with the necessary spatial coverage and temporal resolution for model evaluation.

Two feedbacks between cloud properties and hydroclimate could be studied initially. The first links aridity and INP concentrations. Various kinds of plant and agricultural material have recently been shown to act as INP [276, 248, 277]. Under drier conditions, more INP may be aerosolized due to desertification or as a water stress response of plants. Based upon the altitude that these particles obtain, in-cloud ICNC may increase or decrease, ultimately affecting continental precipitation rates and soil moisture.

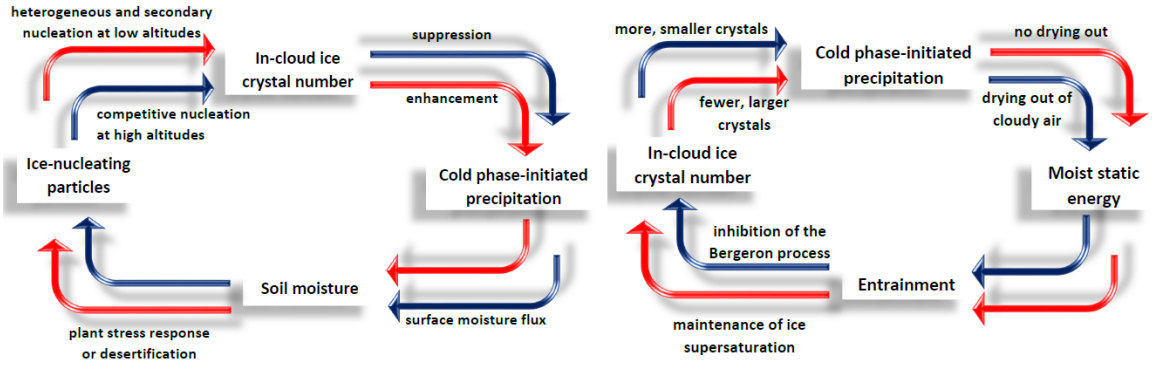

Figure 9.3: (a) Plant stress / aridity-INP feedback; (b) precipitation-cloud phase feedback. Blue arrows indicate a decrease, and red arrows indicate an increase.

The second is a self-regulating drought-cloud phase process, suggested by precipitation enhancement in the context of cirrus cloud thinning [278, 279, 280]. During drought conditions, decreased precipitation increases the atmospheric kinetic energy available for entrainment, or mixing of ambient air into the cloudy volume. At certain altitudes, this mixing subsaturates air with respect to liquid and eventually glaciates the cloud via the Bergeron mass transfer process. This cloud phase change affects precipitation efficiency. In particular, a cloud with few, large ice crystals, whose fall speeds are high, may generate more continental precipitation, mitigating drought conditions. These two feedbacks are visualized in Figure 9.3.

9.5 Feedback elucidation with satellite data

Many studies have looked at land-atmosphere feedbacks [281, 282, 283], but few integrate cloud microphysics into their analysis, as the processes above do. This gap is important, given that cloud phase determines precipitation efficiency and cloud radiative forcing. Using higher-resolution models and expanding satellite data sets to mitigate the problems of scale and observational coverage mentioned above, the following plan could be taken to fill this gap:

1. Assess feedback viability by running simulations with a range of cloud microphysical parameters and looking at the changes in altitudinal profile of cloud phase and other implicated variables, like dust number concentration or cumulative precipitation.

2. Validate or disprove the feedback based upon qualitative trends in a 'data fingerprint', defined as a sequence of the implicated variables available in satellite products. Estimate a quantitative sensitivity parameter, as a change in aridity over a change in cloud phase, from these satellite records.

3. Determine whether the validated feedback could lead to extreme water shortage in the near future by running simulations with various sensitivity parameters in the uncertainty range.

4. Pinpoint regions of agricultural vulnerability by overlaying these water shortage projections and maps of crop drought sensitivity.

9.5.1 Viability

A relevant cloud parameter in the hypothesized feedback will be chosen, e.g., ice crystal fall speeds in the second example above, and a range of its values or formulations will be defined. An ensemble of simulations will be run to analyze how a change in that parameter maps to a change in cloud phase with altitude and thereafter to other involved variables, like ice crystal number concentrations or precipitation intensity. If qualitative trends in these outputs are as expected, the feedback is deemed viable for the atmospheric conditions of that simulation. The temporal attribution metrics defined in Chapter 4 may be used to determine which cloud parameter is most influential on the phase partitioning under various conditions [130].

9.5.2 Validation

For a viable feedback, the involved variables from the viability stage will be used as the starting point to define a 'data fingerprint'. For example, in the plant stress-INP pathway above, the following products could be used to observationally reconstruct the feedback: solar-induced fluorescence from the Global Ozone Monitoring Experiment-2 [284]; gross primary production from the Water, Energy, and Carbon with Artificial Neural Networks project; MODIS aerosol optical thickness; CALIPSO aerosol extinction; and Global Precipitation Measurements. These data will be filtered, first for regions and times with the

applicable range of cloud properties, and second for collocated observations of the 'fingerprint variables'. If a statistically significant sample cannot be built up, the data fingerprint will be redefined with other satellite products to the extent possible. Thereafter, a quantitative sensitivity parameter will be estimated, i.e., the change in regional aridity over a change in the cloud property. This would be similar to the system gain λ discussed in Section 2.1. As a means of model development, this sensitivity parameter could also be calculated from the model via the adjoint technique in Chapter 2 and brought closer to these observationally-derived values.

9.5.3 Societal Impact

Finally, validated feedbacks from the first two steps will be used to predict regions of future water shortage and agricultural vulnerability. An ensemble of five-year and decadal projections can be made for a given region, with a range of perturbed cloud properties and a lower and upper bound of the sensitivity parameter from the validation step. The region will be classified as one of potential future water shortage, based upon its projected aridity index. The drought sensitivity of crop distributions from a source like the National Agriculture Statistics Service or the Socioeconomic Data and Applications Center can be quantified with a metric like the Crop Water Stress Index or Volumetric Demand-Sensitive Drought Index [285]. Then the predicted water limitation contours of objective 3 will be mapped onto contours of this drought metric to visualize agricultural susceptibility in a kind of hotspot map [286]. These maps can act as a communication tool to farmers and policymakers in the most susceptible regions.

9.6 Chapter 9 Summary

Two components will be important to advance the work presented here. First, climate and weather model evaluation is an important challenge, and new mathematical tools must be used to better address this challenge. In particular, the use of information theory in climate science can create a new conceptual paradigm: there is additional insight to be gained by considering data and model outputs outside of their physical basis and more as statistical

entities. Edwin Jaynes made a similar argument for statistical mechanics when there was a similar inability to connect "the laws of microscopic mechanics to macroscopic phenomena" [287]. His answer to this disconnect was to understand statistical mechanics as "no longer dependent on physical hypotheses, but [rather as] an example of statistical inference" [287]. The proposed work in Section 9.3 above advocates the same approach for the persistent challenge of parameterization assessment.

These mathematical and scientific efforts extend to the social domain primarily through the hydrological cycle and its effect on agriculture. As surface temperature warms, precipitation extremes become larger and ariditiy becomes more extensive. Clouds are a major component of the hydrological cycle, and if we can better elucidate their role in hydroclimate changes, we can better project drought susceptible regions. Only with this kind of scientific basis can agricultural resilience and adaptation efforts succeed in feeding a growing population under climate change.

CONCLUSIONS

A list of objectives was presented at the end of Chapter 1, and the most important conclusions of the work in Chapters 2 to 8 are outlined here.

1. Adjoint model development allows computationally efficient comparison of output ice crystal numbers in large-scale frameworks

   (a) Sulfate emissions should be better constrained to reproduce the cirrus ICNC in the tropics.

   (b) Lab data-based formulations predict more frequent and more efficient heterogeneous ice nucleation than field data-based formulations. Some process that ice nucleating particles undergo in the atmosphere seems to be missing from laboratory treatments.

2. Attribution metrics can be defined with adjoint sensitivities to pinpoint the most influential inputs for temporal variability in output ICNC.

   (a) When turbulence is parameterized in a global climate model, the vertical velocity can explain the majority of the temporal variability in output nucleated ICNC. Thresholding this velocity mutes ICNC variability.

   (b) Vertical velocity is influential in the tropics and middle latitudes because of its own large variability. Here additional measurements could constrain the vertical velocity formulation. At the highest latitudes, ICNC is simply very sensitive to any velocity fluctuations, and additional measurements will not be as useful.

3. Parcel and mesoscale model simulations show that secondary ice production can enhance ice crystal numbers by a factor of 10^3 to 10^4 in localized regions.

   (a) A balance of moderate updraft and CCN number ensures that large hydrometeors form, stay aloft, and feed into secondary ice production.

   (b) Including ice hydrometeor non-sphericity accelerates the rate of secondary ice production six-fold due to a larger collisional cross section.

(c) Breakup requires large concentrations of pre-existing graupel and a minimum INP number of about 0.01 L^{-1} to initiate. Otherwise, INP numbers do not pose a limitation to secondary ice production.

(d) Inclusion of secondary ice production may yield more accurate simulated precipitation intensities.

Prediction of atmospheric ice formation is quite difficult. In-situ measurements can only be taken locally in space and time and do not constrain simulations well, given the large spatial and temporal variability in INP numbers and updraft velocities. In the face of this difficulty, this work has advocated use of mathematical tools, both the adjoint model in Chapter 2 and information theory in Chapter 9, to gain insight from large-scale frameworks. Global scale simulations should not be the only tool in progressing toward more realistic cloud simulations. Instead, they work in tandem with more minimal frameworks, such as the parcel model developed in Chapter 5, whose output can be analyzed in a straightforward manner to understand process interactions or parametric uncertainty. Future progress will best be made on the modeling of cloud phase partitioning through a multi-scale approach that employs clever mathematics and satellite data with greater coverage.

Appendices

APPENDIX A

NOTATION

2DS	Two-Dimensional Stereo probe to measure ice crystal number concentrations
α	Cloud albedo
α_d	Deposition coefficient
β	Adjustable parameter in the sigmoidal function for the fragment number generated from shattering
$\partial N_i/\partial X$	Sensitivitiy of N_i to input X
$\Delta\epsilon$	Control action, or anthropogenic forcing, on climate in a process control context
ϵ	Cloud emissivity
η_X	Weighting for process X from 0 to 100% when process X is inactive to active
γ	Adjustable parameter in the sigmoidal function for the fragment number generated from shattering
γ_{br}	Adjustable parameter to control the decay rate of fragments generated from breakup on collision at warmer subzero temperatures
Γ	Adiabatic lapse rate
Γ_{IG}	Inherent growth factor from Chen and Lamb [210]
λ	System gain, or climate sensitivity in a process control context
$\tilde{\lambda}$	Rate parameter of the generalized gamma distribution for hydrometeor masses in SB06
λ_{eq}	Equilibrium climate sensitivity
$\bar{\lambda}$	Mean free path
λ_i	Combination of thermodynamic parameters within the heterogeneous nucleation calculations of BN09
$\Omega_{X,*}$	Baseline surface area of aerosol type X
μ	Viscosity of air
$\mu_{sub,V}$	Mean of the Gaussian updraft velocity distribution
μ_X	Geometric mean of the lognormal size distribution for aerosol type X
$(\nu+1)/\tilde{\mu}$	Shape parameter of the generalized gamma distribution for hydrometeor masses in SB06
$\aleph_X$	Fragment number generated by process X
$\phi(P,Q)$	Kullback-Leibler divergence between two proability distributions, P and Q, also called the discrimination information or the relative entropy
ρ_a	Density of air

ρ_i Density of bulk ice

ρ_w Density of liquid water

ρ_Δ Deposition density for graupel as in Chen and Lamb [210]

σ_i State i for the calculation of informational entropy

σ_X Width of the lognormal size distribution for aerosol type X

$\sigma_{sub,V}$ Width of the Gaussian updraft velocity distribution, intended to account for subgrid variability

τ_X Characteristic time for hydrometeor number in class X to grow by deposition, riming, or condensation to the next largest class or to fall out

θ_e Equivalent potential temperature

θ_X Contact angle between an INP surface of type X and ice

ξ_X Number of ice germs forming per aerosol of type X

$\xi_{x_j}^{(Y)}$ Temporal attribution of the input variable x_j for output scalar Y, i.e., how much temporal variability in Y is linked to that in x_j

$\zeta_{x_j}^{(Y)}$ Temporal attribution fraction of the input variable x_j for output scalar Y, i.e., whether the sensitivity to or variability of x_j are more influential of Y

A_{INP} Abundance of INP, defined as the ratio of available INP to the limiting number to inhibit homogeneous nucleation (N_{lim})

a_X Spheroidal major axis of hydrometeor of type X

ABN09 Adjoint of the Barahona and Nenes ice nucleation parameterization [50]

AD Automatic differentiation

AIDA Heterogeneous INP spectra derived from Aerosol Interaction and Dynamics in the Atmosphere cloud chamber data [100]

APPRAISE Aerosol Properties, PRocesses And InfluenceS on the Earth's climate programme, Clouds project

B_0 Parameter within the hydrometeor terminal velocity calculation from Mitchell and Heymsfield [199]

BC Black carbon

BN09 Barahona and Nenes ice nucleation parameterization [66]

BR Abbreviation for secondary ice production by breakup upon ice hydrometeor collision

c_p Heat capacity of ambient air

c_X Capacitance of ice hydrometeor X

c_0 Primary nucleation rate derived from the temperature dependence of the INP concentration given in DeMott et al. [123]

CALIPSO Cloud-Aerosol Lidar and Infrared Pathfinder Satellite Observations satellite within the NASA A-Train to take cloud and aerosol measurements

CAM5 Community Atmosphere Model, version 5.1

CCN Cloud condensation nuclei

CIP Cloud imaging probe

CFARR Chilbolton Facility for Atmospheric and Radio Research

CNT Classical nucleation theory

COSMO COnsortium for Small-scale MOdeling framework of the German Weather service

$\mathcal{D}_v$ Diffusion coefficient of water vapor

d_X Aerosol geometric mean diameter of type X

d_0 Rate of new droplet activation as a function of supersaturation from Twomey [196]

DEF-C Default simulations for attribution analysis with the CAM5 model

DEF-G Default simulations for attribution analysis with the GEOS-5 model

DM Dust and metallics aerosol classification

DS Abbreviation for secondary ice production by frozen droplet shattering

E_{jk} Collection efficiency between hydrometeors of type j and k

e_i Saturation vapor pressure with respect to ice

e_w Saturation vapor pressure with respect to water

e_X Nucleation efficiency of aerosol type X

EOD Equivalent optical diameter

F_{BR} Leading coefficient of the fragment number generated per collision based upon data from Takahashi et al. [15]

F_{DS} Leading coefficient of the fragment number generated per shattering droplet as in Lawson et al. [224]

F_{oc} Fraction of the black carbon surface coated in organic material

f_{red} Factor for nucleation rate reduction

F_{RS} Fragment number per kilogram of rime as in Hallett and Mossop [165]

FCDP Fast Cloud Droplet Probe to measure in-cloud hydrometeor number concentrations

FSSP Forward Scattering Spectrometeor Probe to measure ice crystal number concentrations

G_{drop} Droplet number generation function

G_{ice} Ice generation function in the parcel model

GCM Global climate model

GEOS-5 Goddard Earth Observing Model, Version 5

GOCART Goddard Chemistry Aerosol Radiation and Transport module to simulate atmospheric aerosol

H Shannon entropy (Chapter 9 only); Heaviside function (all other chapters)

H_X Threshold function that reduces INP concentrations at conditions subsaturated with respect to water and warm sub-zero temperatures

HITEMP Higher output temporal resolution for attribution analysis with the GEOS-5 model

IAT Interarrival time algorithm to filter out shattering artifacts from ICNC measurements

ICNC Ice crystal number concentration, used interchangeably with N_i

INP Ice-nucleating particle

IPCC Intergovernmental Panel on Climate Change

ISCCP International Satellite Cloud Climatology Project

IWC Ice water content of a cloud, i.e., cloud ice mass within a volume of atmospheric air

$J(s_i)$ Homogeneous nucleation rate coefficient

k_a Thermal conductivity of air

K_X Gravitational collection kernel for process X; in particular, K_{jk} is the collection kernel for collisions between hydrometeors of type j and k in COSMO

m_X Mass of hydrometeor of type X

MACPEX Mid-latitude Cirrus Properties Experiment field campaign

MAM3 Modal Aerosol Module with three modes to simulate atmospheric aerosol

MMCR Millimeter cloud radar

MODIS Moderate Resolution Imaging Spectroradiometer, an instrument aboard the NASA Terra and Aqua satellites to measure cloud properties

NH Northern Hemisphere

N^* Combination of thermodynamic parameters within the heterogeneous nucleation calculations of BN09

$N_{frag}^{(DS)}$ Fixed number of fragments generated upon droplet shattering, not dependent on droplet diameter as $\aleph_{DS}$ is

N_{het} Heterogeneously-nucleated ice crystal number

$N_{het}(s_i)$ Heterogeneous nucleation spectrum, i.e., the number of heterogeneously nucleated ice crystals for a given supersaturation with respect to ice

N_{hom} Homogeneously-nucleated ice crystal number

N_i Ice crystal number concentration, used interchangeably with ICNC

N_{ice} Total ice hydrometeor number from the parcel model, i.e., $N_i + N_g + N_G$

$N_{ice}^{(max)}$ Maximum N_{ice} formed within the parcel during a given simulation

$N_{INP}^{(lim)}$ Limiting ice nucleating particle number concentration to initiate secondary production

$N_{INP}^{(tot)}$ Total number of ice nucleating particles within a parcel available for primary nucleation, a value fixed by the user before running parcel model simulations

N_{lim} Limiting ice crystal number concentration for purely heterogeneous nucleation

N_{liq} Total liquid phase hydrometeor number, $N_d + N_r + N_R$

n_s Active site density for an ice-nucleating particle with units of per surface area

N_X Hydrometeor number in class X of the parcel model

$n_{INP,*}$ Ice-nucleating particle number from a reference activity spectrum

$n_{INP,X}$ Ice-nucleating particle number of type X

n_X Aerosol number concentration of type X; if a functionality with respect to D is given, the size distribution of aerosol number concentration of type X

NCFR Narrow cold frontal rainband

OAT "One-at-a-time" approach for sensitivity analysis

OG Original gangster

P Ambient atmospheric pressure

p Ambient partial pressure of water vapor

$p_{fr}(t, T, D)$ Temperature-, time-, and size-dependent probability that a large droplet freezes as in Bigg 1953 [233]

P_s Black carbon surface polarity

$p_{sat,i}$ Saturation vapor pressure over ice

$p_{sh}(T)$ Temperature-dependent probability that a frozen large droplet shatters with $p_{sh}^{(max)}$ being the maximum of this distribution

p_X Contribution of a microphysical process X to total N_{ice}

$\mathcal{P}_X$ Parameterized processes that are a source or sink for hydrometeors of type X

PDA08 Heterogeneous ice nucleation spectrum of Phillips et al., 2008 which accounts for aerosol composition and size [68]

PDA13 Heterogeneous ice nucleation spectrum of Phillips et al., 2013 which updates PDA08 with newer in-situ data [69]

q_i Mass mixing ratio of ice

q_{rime} Mass mixing ratio of rime

q_w Mass mixing ratio of liquid water

R Atmospheric radiation

R_a Specific gas constant for moist air

R_v Specific gas constant for water vapor

r_X Radius of hydrometeor of type X

RS Abbreviation for secondary ice production by rime splintering

$\mathcal{S}_i$ Saturation ratio with respect to ice

$\mathcal{S}_w$ Saturation ratio with respect to water

Δs_{char} Difference between ambient and threshold supersaturation for a given INP

s_{hom} Threshold supersaturation for homogeneous nucleation

s_i Supersaturation with respect to ice

$s_{i,0,X}$ Threshold supersaturation with respect to ice for aerosol type X

$s_{i,max}$ Maximum supersaturation with respect to ice obtained

$s_{i,max}^{B}$ Maximum supersaturation calculated from the bisection method in BN09

$s_{i,max}^{NR}$ Maximum supersaturation calculated after a Newton-Raphson step away from $s_{i,max}^{B}$

s_w Supersaturation with respect to liquid water in the parcel model

SB06 2-moment bulk scheme of Seifert and Beheng [41]

SCS That's me!

SD	Size distribution
SLF	Supercooled liquid fraction
SH	Southern Hemisphere
SPARTICUS	Small Particles In Cirrus field campaign
SPCAM	Superparameterized Community Atmosphere Model, a global climate model in which smaller-scale cloud resolving models are embedded in the larger framework
T	Atmospheric temperature (in or out of cloud)
T_{min}	Minimum temperature for breakup upon collision to occur
T_0	Cloud base temperature or the initial temperature of the parcel
t_{end}	Time when the simulation is terminated, either because the parcel has become water subsaturated or the temperature has reached 237 K where homogeneous nucleation can occur
TKE	Turbulent kinetic energy
TLM	Tangent linear model approach to sensitivity analysis
t-SNE	t-distributed Stochastic Neighbor Embedding
V	Updraft velocity, or vertical atmospheric motions
$V_{sub,i}$	Subgrid-scale updraft velocity for ice nucleation
$v_{t,X}$	Terminal velocity of hydrometeor type i
VIPS	Video Ice Particle Sampler

REFERENCES

[1] O. Boucher et al. "Clouds and Aerosols. In: *Climate Change 2013: The Physical Science Basis. Contribution of Working Group I to the Fifth Assessment Report of the Intergovernmental Panel on Climate Change*". In: *Cambridge University Press* (2013).

[2] M. Kormurcu et al. "Intercomparison of the cloud water phase among global climate models". In: *J. Geophys. Res.* 119 (2014), pp. 3372–3400.

[3] G. Vali. "Interpretation of freezing nucleation experiments: singular and stochastic; sites and surfaces". In: *Atmos. Chem. Phys.* 14 (2014), pp. 1711–1750.

[4] O. Hellmuth et al. *Nucleation theory and applications. Special Issues. Review Series on Selected Topics of Atmospheric Sol Formation: Volume 1.* Dubna: JINR, 2013.

[5] E. Verdurand et al. "Secondary nucleation and growth of organic crystals in industrial crystallization". In: 275.1-2 (2005), pp. 1363–1367.

[6] S. G. Agrawal and A. H. J. Paterson. "Secondary nucleation: Mechanisms and models". In: *Chem. Eng. Comm.* 202.5 (2015), pp. 698–706.

[7] S. C. Mossop. "Secondary ice particle production during rime growth: The effect of drop size distribution and rimer velocity". In: *Q. J. R. Meteorol. Soc.* 111.470 (1985), pp. 1113–1124.

[8] P. V. Hobbs and A. L. Rangno. "Ice particle concentrations in clouds". In: *J. Atmos. Sci.* 42.23 (1985), pp. 2523–2549.

[9] P. V. Hobbs and A. L. Rangno. "Rapid development of high ice particle concentrations in small polar maritime cumuliform clouds". In: *J. Atmos. Sci.* 47 (1990), pp. 2710–2722.

[10] K. V. Beard. "Ice initiation in warm-base convective clouds: An assessment of microphysical mechanisms". In: *Atm. Res.* 28.2 (1992), pp. 125–152.

[11] W. Cantrell and A. Heymsfield. "Production of ice in tropospheric clouds: A review". In: *B. Am. Meteorol. Soc.* (2005), pp. 795–807.

[12] P. J. DeMott et al. "Sea spray aerosol as a unique source of ice nucleating particles". In: *Proc. Natl. Acad. Sci.* 113 (2016), pp. 5797–5803.

[13] P.R. Field et al. "Chapter 7: Secondary ice production - current state of the science and recommendations for the future". In: *Meteor. Monogr.* (2017).

[14] L. Vardiman. “The generation of secondary ice particles in clouds by crystal-crystal collision”. In: *J. Atmos. Sci.* 35.11 (1978), pp. 2168–2180.

[15] T. Takahashi, Y. Nagao, and Y. Kushiyama. “Possible high ice particle production during graupel-graupel collisions”. In: *J. Atmos. Sci.* 52 (1995), pp. 4523–4527.

[16] N. G. Loeb et al. “Toward optimal closure of the Earth’s top-of-atmosphere radiation budget”. In: *J. Clim.* 22 (2009), pp. 748–766.

[17] J. Pinto. “Autumunal mixed-phase cloudy boundary layers in the Arctic”. In: *J. Atm. Sci.* 55 (1998), pp. 2016–2038.

[18] P. Zuidema et al. “An Arctic springtime mixed-phase boundary layer observed during SHEBA”. In: *J. Atm. Sci.* 62 (2005), pp. 160–176.

[19] M. D. Shupe, S. Matrosov, and T. Uttal. “Arctic mixed-phase cloud properties derived from surface-based sensors at SHEBA”. In: *J. Atm. Sci.* 62 (2006), pp. 160–176.

[20] K.P. Wickland et al. “Effects of permafrost melting on carbon dioxide and methane exchange of a poorly drained black spruce lowland”. In: *J. Geophys. Res.: Biogeosciences* 111 (2006), G2.

[21] J.A. Church and N.J. White. “A 20th century acceleration in global sea-level rise”. In: *GRL* 33 (2006), p. L01602.

[22] S. Bony et al. “Clouds, circulation, and climate sensitivity”. In: *Nature Geoscience* 8 (2015), pp. 261–268.

[23] I. Koren et al. “Aerosol invigoration and restructuring of Atlantic convective clouds”. In: *Geo. Res. Lett.* 32.14 (2005).

[24] P. Bartello et al. “Clouds and turbulence”. In: *B. Am. Meteorol. Soc.* (2010), pp. 1087–1089.

[25] M. B. Pinsy and A. P. Khain. “Turbulence effects on droplet growth and size distribution in clouds - A review”. In: 28.7 (1997), pp. 1177–1214.

[26] S. G. Lasher-Trapp, W. A. Cooper, and A. M. Blyth. “Broadening of droplet size distributions from entrainment and mixing in a cumulus cloud”. In: *Q. J. R. Meteorol. Soc.* 131 (2005), pp. 195–220.

[27] B. J. Devenish et al. “Droplet growth in warm turbulent clouds”. In: *Q. J. R. Meteorol. Soc.* 138 (2012), pp. 1401–1429.

[28] S. S. Lee. “Aerosols, clouds and climate”. In: *Nature* 4 (2011), pp. 826–827.

[29] D. Rosenfeld and G. Gutman. "Pollution and clouds". In: *Physics World* 14 (2001), pp. 259–283.

[30] U. Lohmann. "Anthropogenic aerosol influences on mixed-phase clouds". In: *Curr. Clim. Change Rep.* (2017).

[31] K.-M. Lau and H.-T. Wu. "Climatology and changes in tropical ocean rainfall characteristics inferred from Tropical Rainfall Measuring Mission (TRMM) data (1998-2009)". In: *J. Geophys. Res.* 116.D17111 (2011).

[32] J. Mülmenstädt, O. Sourdeval, and J. Delanoë. "Frequency of occurrencee of rain from liquid-, mixed-, and ice-phase clouds derived from A-Train satellite retrievals". In: *Geophys. Res. Lett.* 42.15 (2015), pp. 6502–6509.

[33] E. M. Fischer and R. Knutti. "Observed heavy precipitation increase confirms theory and early models". In: *Nature Clim. Change* 6 (2016), pp. 986–991.

[34] I. M. Held and B. J. Soden. "Robust responses of the hydrological cycle to global warming". In: *J. Clim.* 19 (2006), pp. 5686–5699.

[35] F. J. Wentz et al. "How much more rain will global warming bring?" In: *Science* 317 (2007), pp. 233–235.

[36] C. Chou et al. "Increase in the range between wet and dry season precipitation". In: *Nature Geoscience* 6 (2013), pp. 263–267.

[37] S. Feng and Q. Fu. "Expansion of global drylands under a warming climate". In: *Atmos. Chem. Phys.* 13 (2013), pp. 10081–10094.

[38] B. I. Cook, T. R. Ault, and J. E. Smerdon. "Unprecedented 21st century drought risk in the American Southwest and Central Plains". In: *Sci. Adv.* 1.1 (2015).

[39] T. Schneider et al. "Climate goals and computing the future of clouds". In: *Nat. Clim. Change* 7 (2017), pp. 3–5.

[40] H. Morrison et al. "Resilience of persistent Arctic mixed-phase cloud". In: *Nature Geoscience* 5 (2012), pp. 11–17.

[41] A. Seifert and K. D. Beheng. "A two-moment cloud microphysics parameterization for mixed-phase clouds. Part I: Model description". In: *Meteorol. Atmos. Phys.* 92.1–2 (2006), pp. 45–66.

[42] H. Morrison and A. Gettelman. "A new two-moment bulk stratiform cloud microphysics scheme in the Community Atmosphere Model, version 3 (CAM3), Part I: description and numerical tests". In: *J. Climate* 21 (2008), pp. 3642–3659.

[43] D. Barahona et al. “Development of two-moment cloud microphysics for liquid and ice within the NASA Goddard Earth Observing System model (GEOS-5)”. In: *Geosci. Model Devel.* 7 (2014), pp. 1733–1766.

[44] A. P. Khain et al. “Simulation of effects of atmospheric aerosols on deep turbulent convective clouds by using a spectral microphysics mixed-phase cumulus cloud model. Part I: Model description and possible applications”. In: *J. Atm. Sci.* 61 (2004), pp. 2892–2963.

[45] B. Stevens et al. “Evaluation of large-eddy simulations via observations of nocturnal marine stratocumulus”. In: *Mon. Weather Rev.* 133 (2005), pp. 1443–1462.

[46] A. M. Fridlind et al. “Ice properties of single-layer stratocumulus during the Mixed-Phase Arctic Cloud Experiment: 2. Model results”. In: *J. Geophys. Res.* 112.D24202 (2007).

[47] D. Randall et al. “Breaking the cloud parameterization deadlock”. In: *Bull. Am. Meteor. Soc.* 84 (), pp. 1547–1564.

[48] B. Stevens and A. Seifert. “Understanding macrophysical outcomes of microphysical choices in simulations of shallow cumulus convection”. In: *J. Meteorol. Soc. Jpn.* 86 (), pp. 143–162.

[49] A. D. Del Genio and J. B. Wu. “The role of entrainment in the diurnal cycle of continental convection”. In: *J. Clim.* 23 (), pp. 2722–2738.

[50] B. Sheyko et al. “Quantifying sensitivities of ice crystal number and sources of ice crystal number variability in CAM 5.1 using the adjoint of a physically based cirrus formation parameterization”. In: *J. Geophys. Res.* 120.7 (2015).

[51] G. L. Stephens. “Cloud feedbacks in the climate system: A critical review”. In: *J. Clim.* 18 (2005), pp. 237–273.

[52] F. Garcia-Menendez, Y. Hu, and M.T. Odman. “Simulating smoke transport from wildland fires with a regional-scale air quality model: Sensitivity to uncertain wind fields”. In: *J. Geoph. Res.* 118.12 (2013), pp. 6493–6504.

[53] D.V. Spracklen et al. “A global off-line model of size-resolved aerosol microphysics: I. Model development and prediction of aerosol properties”. In: *Atmos. Chem. Phys.* 5.1 (2005), pp. 179–215.

[54] A. Gettelman et al. “Climate impacts of ice nucleation”. In: *J. Geoph. Res.* 117 (2012), pp. 1–14.

[55] L.A. Lee et al. “Mapping the uncertainty in global CCN using emulation”. In: *Atmos. Chem. Phys.* 12 (2012), pp. 9739–9751.

[56] C. Zhao et al. "A sensitivity study of radiative fluxes at the top of atmosphere to cloud microphysics and aerosol parameters in the Community Atmosphere Model CAM5". In: *Atmos. Chem. Phys.* 13.8 (2013), pp. 10969–10987.

[57] R.M. Errico. "What is an adjoint model?" In: *Bull. Am. Meteorol. Soc.* (1997), pp. 2577–2591.

[58] L. Hascoët. *Automatic Differentiation by Program Transformation*. INRIA Sophia-Antipolis, TROPICS team. 2007.

[59] V.A. Karydis et al. "Adjoint sensitivity of global cloud droplet number to aerosol and dynamical parameters". In: *Atmos. Chem. Phys.* 12.19 (2012), pp. 9041–9055.

[60] R.H. Moore et al. "Droplet number prediction uncertainties from CCN: An integrated assessment using observations and a global model adjoint". In: *Atmos. Chem. Phys.* 13 (2013), pp. 4235–4251.

[61] R. Morales and A. Nenes. "Understanding the contributions of aerosol properties and parameterization discrepancies to droplet number variability in a Global Climate Model". In: *Atmos. Chem. Phys.* 13 (2013), pp. 31479–31526.

[62] V.A. Karydis et al. "Using a global aerosol model adjoint to unravel the footprint of spatially-distributed emissions on cloud droplet number and cloud albedo". In: *Atmos. Chem. Phys.* 12.19 (2012), pp. 12081–12118.

[63] S. Capps et al. "ANISORROPIA: the adjoint of the aerosol thermodynamic model ISORROPIA". In: *Atmo. Chem. Phys.* 12 (2012), pp. 527–543.

[64] D. Barahona and A. Nenes. "Parameterization of cirrus cloud formation in large-scale models: Homogeneous nucleation". In: *J. Geoph. Res.* 113 (D11, 16 2008).

[65] D. Barahona and A. Nenes. "Parameterizing the competition between homogeneous and heterogeneous freezing in cirrus cloud formation - monodisperse ice nuclei". In: *Atmos. Chem. Phys.* 9 (2009), pp. 369–381.

[66] D. Barahona and A. Nenes. "Parameterizing the competition between homogeneous and heterogeneous freezing in ice cloud formation - polydisperse ice nuclei". In: *Atmos. Chem. Phys.* 9 (2009), pp. 5933–5948.

[67] M.P. Meyers, P.J. DeMott, and R. Cotton. "New primary ice-nucleation parameterization in an explicit cloud model". In: *J. Appl. Meteorol.* 31 (1992), pp. 708–721.

[68] V.T.J. Phillips, P.J. DeMott, and C. Andronache. "An empirical parameterization of heterogeneous ice nucleation for multiple chemical species of aerosol". In: *J. Atmos. Sci.* 65 (2008), pp. 2757–2783.

[69] V.T.J. Phillips et al. "Improvements to an empirical parameterization of heterogeneous ice nucleation and its comparison with observations". In: *J. Atm. Sciences* 70 (2013), pp. 378–409.

[70] L. Hascoët and V. Pascual. "TAPENADE 2.1 user's guide". In: *INRIA Technical Report RT-0300* (2004), p. 78.

[71] M.C. Bartholomew-Biggs. "Using forward accumulation for automatic differentiation of implicitly-defined functions". In: *Comp. Opt. App.* 9 (1998), pp. 65–84.

[72] J. Skrotzki et al. "The accommodation coefficient of water molecules on ice: cirrus cloud studies at the AIDA simulation chamber". In: *Atmos. Chem. Phys.* 13.8 (2013), pp. 4451–4466.

[73] J.-C. Golaz, V.E. Larson, and W.R. Cotton. "A PDF-based model for boundary layer clouds. Part I: method and model description". In: *J. Atmos. Sci.* 59 (2002), pp. 3540–3551.

[74] Y.L. Kogan. "Large-eddy simulations of air parcels in stratocumulus clouds: time scales and spatial variability". In: *J. Atmos. Sci.* 63 (2006), pp. 952–967.

[75] H. Guo et al. "Characteristics of vertical velocity in marine stratocumulus: comparison of large eddy simulations with observations". In: *Env. Res. Letters* 3.4 (2008).

[76] R. Morales Betancourt and A. Nenes. "Characteristic updrafts for computing distribution-averaged cloud droplet number and stratocumulus cloud properties". In: *J. Geoph. Res.* 115 (2010).

[77] J.-F. Lamarque et al. "Historical (1850-2000) gridded anthropogenic and biomass burning emissions of reactive gases and aerosols: methodology and application". In: *Atmos. Chem. Phys.* 10.15 (2010), pp. 7017–7039.

[78] X. Liu et al. "Toward a minimal representation of aerosols in climate models: description and evaluation in the Community Atmosphere Model CAM5". In: *Geophys. Mod. Devel.* 5.3 (2012), pp. 709–739.

[79] T. Koop et al. "Water activity as the determinant for homogeneous ice nucleation in aqueous solutions". In: *Nature* 406 (2000), pp. 611–614.

[80] S. C. Sullivan et al. "Understanding cirrus ice crystal number variability for different heterogeneous ice nucleation spectra". In: *Atmos. Chem. Phys.* 16 (2016), pp. 2611–2629.

[81] H.R. Pruppacher and J.D. Klett. *Microphysics of clouds and precipitation, 2nd edition.* Kluwer Academic Publishers, Boston, MA, 1997.

[82] D.J. Cziczo et al. "Clarifying the dominant sources and mechanisms of cirrus cloud formation". In: *Science* 340.6138 (2013), pp. 1320–1324.

[83] R.-F. Lin et al. “Nucleation in synoptically forced cirrostratus”. In: *J. Geophys. Res.* 110.D8 (2005).

[84] A. Reinhardt and J. P. K. Doye. “Effects of surface interactions on heterogeneous ice nucleation for a monatomic water model”. In: *J. Chem. Phys.* 141.8 (2014).

[85] L. Lupi, A. Hudait, and V. Molinero. “Heterogeneous Nucleation of Ice on Carbon Surfaces”. In: *Journal of the American Chemical Society* 136.8 (2014), pp. 3156–3164.

[86] S. J. Cox et al. “Molecular simulations of heterogeneous ice nucleation. I. Controlling ice nucleation through surface hydrophilicity”. In: *J. Chem. Phys.* 142.184704 (2015).

[87] D. Barahona. “On the ice nucleation spectrum”. In: *Atmos. Chem. Phys.* 12 (2012), pp. 3733–3752.

[88] G. Kulkarni et al. “Laboratory measurements and model sensitivity studies of dust deposition ice nucleation”. In: *Atmos. Chem. Phys.* 12.16 (2012), pp. 7295–7308.

[89] B. Karcher and U. Lohmann. “A Parameterization of cirrus cloud formation: Homogeneous freezing including effects of aerosol size”. In: *J. Geophys. Res.* 107.D23 (2002).

[90] X.H. Liu and J.E. Penner. “Ice nucleation parameterization for global models”. In: *Met. Zeit.* 14.4 (2005), pp. 499–514.

[91] M. Niemand et al. “A particle-surface-area-based parameterization of immersion freezing on desert dust particles”. In: *J. Atmos. Sci.* 69 (2012), pp. 3077–3092.

[92] C. Marcolli et al. “Efficiency of immersion mode ice nucelation on surrogates of mineral dust”. In: *Atmos. Chem. Phys.* 7 (2007), pp. 5081–5091.

[93] J. Savre et al. “Parameterizing ice nucleation ability of mineral dust particles in the deposition mode: numerical investigations using large eddy simulation”. In: *AIP Proceedings* 922 (2013).

[94] Y. Wang et al. “Different contact angle distributions for heterogeneous ice nucleation in the Community Atmosphere Model version 5”. In: *Atmos. Chem. Phys.* 14 (2014), pp. 10411–10430.

[95] D. Barahona, J. Rodriguez, and A. Nenes. “Sensitivity of the global distribution of cirrus ice crystal concentration to heterogeneous freezing”. In: *J. Geoph. Res.* 115 (D23, 16 2010).

[96] N.H. Fletcher. “Heterogeneous nucleation of ice crystals”. In: *Journal of the Australian Institute of Metals* 10.1 (1965).

[97] P. J. Connolly et al. "Studies of heterogeneous freezing by three different desert dust samples". In: *Atmos. Chem. Phys.* 9.8 (2009), pp. 2805–2824.

[98] D. Niedermeier et al. "Heterogeneous freezing of droplets with immersed mineral dust particles measurements and parameterization". In: *Atmos. Chem. Phys.* 10.8 (2010), pp. 3601–3614.

[99] S.L. Broadley et al. "Immersion mode heterogeneous ice nucleation by an illite rich powder representative of atmospheric mineral dust". In: *Atmos. Chem. Phys.* 12 (2012), pp. 287–307.

[100] N. Hiranuma et al. "A comprehesive parameterization of heterogeneous ice nucleation of dust surrogate: laboratory study with hematite particles and its application to atmospheric models". In: *Atmos. Chem. Phys.* 14.5 (2014), pp. 2315–2324.

[101] C. Hoose and O. Möhler. "Heterogeneous ice nucleation on atmospheric aerosols: a review of results from laboratory experiments". In: *Atmos. Chem. Phys.* 12.5 (2012), pp. 12531–12621.

[102] S.C. Xie et al. "Sensitivity of CAM5-simulated Arctic clouds and radiation to nucleation parameterization". In: *J. Clim.* 26 (2013), pp. 5981–5999.

[103] J. A. Curry and V. I. Khvorostyanov. "Assessment of some parameterizations of heterogeneous ice nucleation in cloud and climate models". In: *Atmos. Chem. Phys.* 12.2 (2012), pp. 1151–1172.

[104] R. Morales-Betancourt et al. "Sensitivity of cirrus and mixed-phase clouds to the ice nuclei spectra in McRAS-AC: single column model simulations". In: *Atmos. Chem. Phys.* 12.22 (2012), pp. 10679–10692.

[105] H. Kalesse and P. Kollias. "Climatology of high cloud dynamics using profiling ARM Doppler Radar observations". In: *J. Clim.* 26 (2013), pp. 6340–6359.

[106] A. Muhlbauer, H. Kalesse, and P. Kollias. "Vertical velocities and turbulence in midlatitude anvil cirrus: A comparison between in situ aircraft measurements and ground-based Doppler cloud radar retrievals". In: *Geophys. Res. Lett.* 41.22 (2014), pp. 7814–7821.

[107] A. Muhlbauer et al. "Evaluation of cloud-resolving model simulations of midlatitude cirrus with ARM and A-train observations". In: *J. Geophys. Res.* 120.13 (2015), pp. 6597–6618.

[108] I. Steinke et al. "A new temperature and humidity dependent surface site density approach for deposition ice nucleation". In: *Atmos. Chem. Phys.* 14 (2014), pp. 18499–18539.

[109] J.-P. Chen, A. Hazra, and Z. Levin. "Parameterizing ice nucleation rates using contact angle and activation energy derived from laboratory data". In: *Atmos. Chem. Phys.* 8.24 (2008), pp. 7431–7449.

[110] O. Möhler et al. "Efficiency of the deposition mode ice nucleation on mineral dust particles". In: *Atmos. Chem. Phys.* 6.10 (2006), pp. 3007–3021.

[111] F. Dentener et al. "Emissions of primary aerosol and precursor gases in the years 2000 and 1750 prescribed data-sets for AeroCom". In: *Atmos. Chem. Phys.* 6.12 (2006), pp. 4321–4344.

[112] G.A. d'Almeida. "On the variability of desert aerosol radiative characteristics". In: *J. Geophys. Res.* 92.D3 (1987), pp. 3017–3026.

[113] P.R. Field et al. "Some ice nucleation characteristics of Asian and Saharan desert dust". In: *Atmos. Chem. Phys.* 6 (2006), pp. 2991–3006.

[114] K.T. Whitby. "The physical characteristics of sulfur aerosols". In: *Atm. Env.* 41 (2007), pp. 25–49.

[115] O. Popovicheva et al. "Water interaction with hydrophobic and hydrophilic soot particles". In: *Phys. Chem. Chem. Phys.* 10 (2007), pp. 2332–2344.

[116] E. J. Jensen et al. "Physical processes controlling ice concentrations in synoptically forced, midlatitude cirrus". In: *J. Geophys. Res.* 118 (2013), pp. 5348–5360.

[117] M. Krämer et al. "Ice supersaturations and cirrus cloud crystal numbers". In: *Atmos. Chem. Phys.* 9.11 (2009), pp. 3505–3522.

[118] E. J. Jensen et al. "Ice nucleation and cloud microphysical properties in tropical tropopause layer cirrus". In: *Atmos. Chem. Phys.* 10.3 (2010), pp. 1369–1384.

[119] D. Barahona and A. Nenes. "Dynamical states of low temperature cirrus". In: *Atmos. Chem. Phys.* 11.8 (2011), pp. 3757–3771.

[120] P. Spichtinger and M. Krämer. "Tropical tropopause ice clouds: a dynamic approach to the mystery of low crystal numbers". In: *Atmos. Chem. Phys.* 13.19 (2013), pp. 9801–9818.

[121] X.-J. Shi, X. Liu, and K. Zhang. "Effects of preexisting ice crystals on cirrus clouds and comparison between different ice nucleation parameterizations with the Community Atmosphere Model (CAM5)". In: *Atmos. Chem. Phys.* 15 (2015), pp. 1503–1520.

[122] P. Spichtinger and K. M. Gierens. "Modelling of cirrus clouds - Part 1b: Structuring cirrus clouds by dynamics". In: *Atmos. Chem. Phys.* 9 (2009), pp. 707–719.

[123] P. J. DeMott et al. “Predicting global atmospheric ice nuclei distributions and their impacts on climate”. In: *Proc. Nat. Acad. Sci.* (2010).

[124] B.J. Murary et al. “Ice nucleation by particles immersed in supercooled cloud droplets”. In: *Chem. Soc. Rev.* 41.19 (2012), pp. 6519–6554.

[125] X. Liu et al. “Sensitivity studies of dust ice nuclei effect on cirrus clouds with the Community Atmosphere Model CAM5”. In: *Atmos. Chem. Phys.* 12.24 (2012), pp. 12061–12079.

[126] B. Zuberi et al. “Heterogeneous nucleation of ice in ammonium sulfate-water particles with mineral dust immersions”. In: *Geophys. Res. Letters* 29.10 (2002).

[127] K. A. Köhler et al. “Cloud condensation nuclei and ice nucleation activity of hydrophobic and hydrophilic soot particles”. In: *Phys. Chem. Chem. Phys.* 11.36 (2009), pp. 7906–7920.

[128] I. Crawford et al. “Studies of propane flame soot acting as heterogeneous ice nuclei in conjunction with single particle soot photometer measurements”. In: *Atmos. Chem. Phys.* 11.18 (2011), pp. 9549–9561.

[129] P.J. DeMott et al. “Ice formation by black carbon particles”. In: *Geophys. Res. Letters* 26 (1999), pp. 2429–2432.

[130] S. C. Sullivan et al. “Role of updraft velocity in temporal variability of global cloud hydrometeor number”. In: *Proc. Nat. Acad. Sci.* 113.21 (2016), 57915796.

[131] T. Chen, W. B. Rossow, and Y. Zhang. “Radiative effects of cloud-type variations”. In: *J. Clim.* 13.1 (2000), pp. 264–286.

[132] Y.-S. Choi et al. “Space observations of cold-cloud phase change”. In: *Proc. Nat. Acad. Sci.* 107.25 (2010), pp. 11211–11216.

[133] Y.-S. Choi et al. “Influence of cloud phase composition on climate feedbacks”. In: *J. Geophys. Res. - Atm.* 119.7 (2013), pp. 3687–3700.

[134] M. Salzmann et al. “Two-moment bulk stratiform cloud microphysics in the GFDL AM3 GCM: description, evaluation, and sensitivity tests”. In: *Atmos. Chem. Phys.* 10.16 (2010), pp. 8037–8064.

[135] R. L. Miller et al. “CMIP5 historical simulations (1850-2012) with GISS ModelE2”. In: *J. Adv. Mod. Earth Sys.* 6 (2014), pp. 441–447.

[136] A. Gettelman et al. “Advanced two-moment bulk microphysics for global models. Part II: Global model solutions and aerosol-cloud interactions”. In: *J. Clim.* 28 (2015), pp. 1288–1307.

[137] J. E. Penner et al. "Model intercomparison of indirect aerosol effects". In: *Atmos. Chem. Phys.* 6.11 (2006), pp. 3391–3405.

[138] S. J. Ghan et al. "Droplet nucleation: Physically-based parameterizations and comparative evaluation". In: *J. Adv. Mod. Earth Sys.* 3.4 (2011), pp. 1942–2466.

[139] A. McComiskey and G. Feingold. "The scale problem in quantifying aerosol indirect effects". In: *Atmos. Chem. Phys.* 12 (2012), pp. 1031–1049.

[140] R. Morales-Betancourt and A. Nenes. "Understanding the contributions of aerosol properties and parameterization discrepancies to droplet number variability in a global climate model". In: *Atmos. Chem. Phys.* 14.9 (2014), pp. 4809–4826.

[141] Y. C. Sud et al. "Performance of McRAS-AC in the GEOS-5 AGCM: aerosol-cloud-microphysics, precipitation, cloud radiative effects, and circulation". In: *Geosci. Model Dev.* 6 (2013), pp. 57–79.

[142] D. Lee et al. "Modeling the influences of aerosols on pre-monsoon circulation and rainfall over Southeast Asia". In: *Atmos. Chem. Phys.* 14 (2014), pp. 6853–6866.

[143] M. Chin et al. "Atmospheric sulfur cycle simulated in the global model GOCART: Comparison with field observations and regional budgets". In: *J. Geophys. Res. - Atm.* 105.D20 (2000), pp. 24689–24712.

[144] P. Ginoux et al. "Sources and distributions of dust aerosols simulated with the GOCART model". In: *J. Geophys. Res.* 106.D17 (2001), pp. 20255–20273.

[145] R.B. Neale et al. "Description of the NCAR Community Atmosphere Model (CAM 5.0)". In: *NCAR Technical Note* (2012).

[146] P. Reutter et al. "Aerosol- and updraft-limited regimes of cloud droplet formation: influence of particle number, size, and hygroscopicity on the activation of cloud condensation nuclei (CCN)". In: *Atmos. Chem. Phys.* 9 (2009), pp. 7067–7080.

[147] M. Simmel et al. "Ice phase in altocumulus clouds over Leipzig: remote sensing observations and detailed modeling". In: *Atmos. Chem. Phys.* 15 (2015), pp. 10453–10470.

[148] J. Schmidt et al. "Strong aerosol-cloud interaction in altocumulus during updraft periods: lidar observations over central Europe". In: *Atmos. Chem. Phys.* 15 (2015), pp. 10687–10700.

[149] S. C. Sullivan, C. Hoose, and A. Nenes. "Investigating the contribution of secondary ice production to in-cloud ice crystal numbers". In: *J. Geophys. Res.* (2017).

[150] S. C. Mossop and J. Hallett. "Ice crystal concentration in cumulus clouds - influence of drop spectrum". In: *Science* 186.4164 (1974), pp. 632–634.

[151] A. L. Rangno and P. V. Hobbs. “Ice particle concentrations and precipitation development in small polar maritime cumuliform clouds”. In: *Q. J. R. Meteorol. Soc.* 117.497 (1991), pp. 207–241.

[152] A. L. Rangno and P. V. Hobbs. “Ice particles in stratiform clouds in the Arctic and possible mechanisms for the production of high ice concentrations”. In: *J. Geophys. Res.* 106 (D14 2001), pp. 15065–15075.

[153] I. Crawford et al. “Ice formation and development in aged, wintertime cumulus over the UK: observations and modelling”. In: *Atmos. Chem. Phys.* 12 (2012), pp. 4963–4985.

[154] D. Baumgardner et al. “Cloud ice properties: In-situ measurement challenges”. In: *Meteorol. Mono.* (2017).

[155] S. Lance. “Coincidence errors in a cloud droplet probe and a cloud and aerosol spectrometeor and the improved performance of a modified CDP”. In: *J. Atmos. Tech.* 29 (2012), pp. 1532–1541.

[156] A. J. Heymsfield. “On measurements of small ice particles in clouds”. In: *Geophys. Res. Lett.* 34.L23812 ().

[157] G. M. McFarquhar et al. “Importance of small ice crystals to cirrus properties: Observations from Tropical Warm Pool International Cloud Experiment (TWP-ICE)”. In: *Geophys. Res. Lett.* 34 (2007).

[158] B. Baker et al. “The effects of precipitation on cloud droplet measurements devices”. In: *J. Atm. Ocean. Tech.* 7 (2009), pp. 1404–1409.

[159] A. V. Korolev et al. “Quantification of the effects of shattering on airborne ice particle measurements”. In: *J. Atm. Ocean. Tech.* 30 (), pp. 2527–2553.

[160] A. V. Korolev et al. “Improved airborne hot-wire measurements of ice water content in clouds”. In: *J. Atm. Ocean. Tech.* 30 (), pp. 2121–2131.

[161] P. R. Field et al. “Ice particle interarrival times measured with a fast FSSP”. In: *J. Atm. Ocean. Tech.* 20 (2003), pp. 249–261.

[162] P. R. Field, A. J. Heymsfield, and A. Bansemer. “Shattering and particle interarrival times measured by optical array probes in ice clouds”. In: *J. Atm. Ocean. Tech.* 23 (2006), pp. 1357–1371.

[163] A. V. Korolev and P. R. Field. “Assessment of the performance of the inter-arrival time algorithm to identiy ice shattering artifacts in cloud particle probe measurements”. In: *Atm. Meas. Tech.* 8 (2015), pp. 761–777.

[164] A. V. Korolev, E. Emery, and K. Creelman. "Modification and tests of particle probe tips to mitigate effects of ice shattering". In: *J. Atm. Ocean. Tech.* 30 (2013), pp. 690–708.

[165] J. Hallett and S. C. Mossop. "Production of secondary ice particles during the riming process". In: *Nature* 249 (1974), pp. 26–28.

[166] D. J. Griggs and T. W. Choularton. "Freezing modes of riming droplets with application to ice splinter production". In: *Q. J. Roy. Meteor. Soc.* 109 (1983), pp. 243–253.

[167] B. J. Mason. "The rapid glaciation of slightly supercooled cumulus clouds". In: *Q. J. R. Meteorol. Soc.* 122 (1996), pp. 357–365.

[168] S. C. Mossop. "The influence of drop size distribution on the production of secondary ice particles during graupel growth". In: *Q. J. R. Met. Soc.* 104 (1978), pp. 323–330.

[169] J. Crosier et al. "Microphysical properties of cold frontal rainbands". In: *Q. J. Roy. Meteorol. Soc.* 140 (2014), pp. 1257–1268.

[170] A. Heymsfield and P. Willis. "Cloud conditions favoring secondary ice particle production in tropical maritime convection". In: 71 (2014), pp. 4500–4526.

[171] S. Lasher-Trapp et al. "A multisensor investigation of rime splintering in tropical maritime cumuli". In: *J. Atm. Sci.* 73 (2016), pp. 2547–2564.

[172] A. M. Blyth and J. Latham. "A multi-thermal model of cumulus glaciation via the Hallett-Mossop process". In: *Q. J. R. Meterol. Soc.* 123 (1997), pp. 1185–198.

[173] J. R. Cardwell et al. "Use of an explicit model of the microphysics of precipitating stratiform cloud to test a bulk microphysics scheme". In: *Q. J. R. Meteorol. Soc.* 128 (580 2002), pp. 573–592.

[174] M. Ovtchinnikov and Y.L. Kogan. "An investigation of ice production mechanisms in small cumuliform clouds using a 3D model with explicit microphysics. Part I: Model description". In: *J. Atm. Sci.* 57 (2000), pp. 2989–3003.

[175] V. T. J. Phillips et al. "The glaciation of a cumulus cloud over New Mexico". In: *Q. J. R. Meteorol. Soc.* 127 (2001), pp. 1513–1534.

[176] P.D. Clark et al. "Numerical modelling of mixed-phase frontal clouds observed during the CWVC project". In: *Q. J. R. Meteorol. Soc.* 131 (2005), pp. 1677–1693.

[177] V. T. J. Phillips, L. J. Donner, and S. T. Garner. "Nucleation processes in deep convection simulated by a cloud-system-resolving model with double-moment bulk microphysics". In: *J. Atmos. Sci.* 64 (2007), pp. 738–761.

[178] T. Storelvmo, J. E. Kristjánsson, and U. Lohmann. "Aerosol influence on mixed-phase clouds in CAM-Oslo". In: *J. Atm. Sci.* 65 (2008), pp. 3214–3230.

[179] R. F. Chisnell and J. Latham. "Ice particle multiplication in cumulus clouds". In: *Q. J. R. Meterol. Soc.* 102.431 (1976), pp. 133–156.

[180] A. L. Rangno and P. V. Hobbs. "Ice particle concentrations and precipitation development in small continental cumuliform clouds". In: *Q. J. R. Meteorol. Soc.* 120.517 (1994), pp. 573–601.

[181] S. C. Mossop, J. L. Brownscombe, and G. J. Collins. "The production of secondary ice particles during riming". In: *Q. J. R. Meteorol. Soc.* 100.425 (1974), pp. 427–436.

[182] M. Bader et al. "The production of sub-micron ice fragments by water droplets freezing in free fall or on accretion upon an ice surface". In: *Q. J. R. Met. Soc.* 100 (1974), pp. 420–426.

[183] P. V. Hobbs and A. L. Rangno. "Reply to "Comments by Alan M. Blyth and John Latham on 'Cumulus glaction papers by P.V. Hobbs and A.L. Rangno"". In: *Q. J. R. Meteorol. Soc.* 124 (1998), pp. 1009–1011.

[184] T. Leisner et al. "Secondary ice processes upon heterogeneous freezing of cloud droplets". In: 14th Conf. on Cloud Physics and Atmospheric Radiation, Amer. Meteor. Soc. Boston, MA, 2014.

[185] G. Lloyd et al. "The origins of ice crystals measured in mixed phase clouds at High-Alpine site Jungfraujoch". In: *Atmos. Chem. Phys.* 15 (2015), pp. 18181–18224.

[186] P. V. Hobbs and J. Farber. "Fragmentation of ice particles in clouds". In: *J. Rech. Atmos.* 6 (1972), pp. 245–258.

[187] J.-I. Yano and V. T. J. Phillips. "Ice-ice collisions: an ice multiplication process in atmospheric clouds". In: *J. Atmos. Sci.* 68 (2011), pp. 322–333.

[188] C. L. Hosler and R. E. Hallgren. "The aggregation of small ice crystals". In: *Discuss. Faraday Soc.* 30 (1960), pp. 200–207.

[189] P. J. Connolly, C. Emersic, and P. R. Field. "A laboratory investigation into the aggregation efficiency of small ice crystals". In: *Atmos. Chem. Phys.* 12 (2012), pp. 2055–2076.

[190] C. L. Hosler, D. C. Jensen, and L. Goldshlak. "On the aggregation of ice crystals to form snow". In: *J. Meteor.* 14 (1957), pp. 415–420.

[191] P. V. Hobbs. "The aggregation of ice particles in clouds and fogs at low temperatures". In: *J. Atmos. Sci.* 22 (1965), pp. 296–300.

[192] V. T. J. Phillips et al. “A parameterization of sticking efficiency for collisions of snow and graupel with ice crystals: Theory and comparison with observations”. In: *J. Atmos. Sci.* 72.12 (2015), pp. 4885–4902.

[193] K. C. Young. “The role of contact nucleation in ice phase initiation in clouds”. In: *J. Atmos. Sci.* 31 (1974), pp. 768–776.

[194] P. Roberts and J. Hallett. “A laboratory study of the ice nucleating properties of some mineral particulates”. In: (1967), pp. 25–34.

[195] D. A. Knopf and T. Koop. “Heterogeneous nucleation of ice on surrogates of mineral dust”. In: *J. Geophys. Res.* 111.D12201 (2006).

[196] S. Twomey. “The nuclei of natural cloud formation part II: The supersaturation in natural clouds and the variation of cloud droplet concentration”. In: *Geofisica pura e applicata* 43.1 (1959), pp. 243–249.

[197] P. Bogacki and L. F. Shampine. “A 3(2) pair of Runge-Kutta formulas”. In: *Appl. Math. Letters* 2 (1989), pp. 321–325.

[198] A. A. Jensen and J. Y. Harrington. “Modeling ice crystal aspect ratio evolution during riming: a single-particle growth model”. In: *J. Atmos. Sci.* 72 (2015), pp. 2569–2590.

[199] D. L. Mitchell and A. J. Heymsfield. “Refinements in the treatment of ice particle terminal velocities, highlighting aggregates”. In: *J. Atmos. Sci.* 62 (2005), pp. 1637–1644.

[200] B. S. Ferrier. “A double-moment multiple-phase four-class bulk ice scheme. Part I: Description”. In: *J. Atmos. Sci.* 51.2 (1994), pp. 249–280.

[201] A. Ono. “The shape and riming properties of ice crystals in natural clouds”. In: *J. Atmos. Sci.* 26 (1968), pp. 138–147.

[202] J. D. Klett and M. H. Davis. “Theoretical collision efficiencies of cloud droplets at small Reynolds numbers”. In: *J. Atm. Sci.* (1973), pp. 107–117.

[203] D. Zhang et al. “Ice concentration retrieval in stratiform mixed-phase clouds using cloud radar reflectivity measurements and 1D ice growth model simulations”. In: *J. Atmos. Sci.* 71 (2014), pp. 3613–3635.

[204] R. F. Reinking. “Formation of graupel”. In: *J. Appl. Meteorol.* 14 (1975), pp. 745–754.

[205] D. A. Hegg, L. F. Radke, and P. V. Hobbs. “Measurements of Aitken nuclei and cloud condensation nuclei in the marine atmosphere and their relation to the DMS-cloud-climate hypothesis”. In: *J. Geophys. Res. - Atm.* 97.D7 (1992), pp. 7659–7660.

[206] A. Korolev and P. R. Field. "The effect of dynamics on mixed-phase clouds: Theoretical considerations". In: *J. Atm. Sci.* 65 (2007), pp. 66–86.

[207] J. Bühl et al. "Combined vertical-velocity observations with Doppler lidar, cloud radar and wind profiler". In: *Atmos. Meas. Tech.* 8 (2015), pp. 3527–3536.

[208] A. V. Korolev and I. P. Mazin. "Supersaturation of water vapor in clouds". In: *J. Atm. Sci.* 60 (2003), pp. 2957–2974.

[209] J. E. McDonald. "USe of the electrostatic analogy in studies of ice crystal growth". In: *Z. Angew. Math. Phys.* 14 (1963), pp. 610–620.

[210] J.-P. Chen and D. Lamb. "The theoretical basis for the parameterization of ice crystal habits: growth by vapor deposition". In: *J. Atm. Sci.* 51.9 (1994), pp. 1206–1221.

[211] H. H. Rosenbrock. "Some general impliciat processes for the numerical solution of differential equations". In: *The Comp. Jour.* 5.4 (1963), pp. 329–330.

[212] R. R. Rogers and M. K. Yau. *A short course in cloud physics. Second edition.* Elsevier Science, Burlington, MA, 1979.

[213] D. M. Murphy and T. Koop. "Review of the vapor pressures of ice and supercooled water for atmospheric applications". In: *Q. J. R. Meteorol. Soc.* 131 (2005), pp. 1539–1565.

[214] W. G. Kannuluik and E. H. Carman. "Temperature dependence of the thermal conductivity of air". In: *Aust. Jour. Sci. Res.* 3 (1951), pp. 305–309.

[215] J. H. Seinfeld and S. Pandis. *Atmospheric chemistry and physics, 2nd edition.* John Wiley & Sons, Inc., 2006.

[216] K. J. Sulia and J. Y. Harrington. "Ice aspect ratio influences on mixed-phase clouds: Impacts on phase partitioning in parcel models". In: *J. Geophys. Res.* 116.D21309 (2011).

[217] J. W. Taylor et al. "Observations of cloud microphysics and ice formation during COPE". In: *Atmos. Chem. Phys.* 16.2 (2016).

[218] R. L. Harris-Hobbs and W. A. Cooper. "Field evidence supporting quantitative predictions of secondary ice production rates". In: *J. Atmos. Sci.* 44 (1987), pp. 1071–1082.

[219] S. C. Mossop. "Production of secondary ice particles during the growth of graupel by riming". In: *Q. J. Roy. Meteor. Soc.* 102 (1976), pp. 45–57.

[220] J. Zikmunda and G. Vali. "Fall patterns and fall velocities of rimed ice crystals". In: *J. Atm. Sci.* 29 (1972), pp. 1334–1347.

[221] H.-R. Cho, J. V. Iribarne, and W. G. Richards. "On the orientation of ice crystals in a cumulonimbus cloud". In: *J. Atmos. Sci.* 38 (1981), pp. 1111–1114.

[222] A. Korolev and G. Isaac. "Phase transformation of mixed-phase clouds". In: *Q. J. R. Meteorol. Soc.* 129 (2003), pp. 19–38.

[223] I. Sednev, S. Menon, and G. McFarquhar. "Simulating mixed-phase Arctic stratus clouds: sensitivity to ice initiation mechanisms". In: *Atmos. Chem. Phys.* 9 (2009), pp. 4747–4773.

[224] R. P. Lawson, S. Woods, and H. Morrison. "The microphysics of ice and precipitation development in tropical cumulus clouds". In: *J. Atm. Sci.* 72 (2015), pp. 2429–2445.

[225] A. Khain, D. Rosenfeld, and A. Pokrovsky. "Aerosol impact on the dynamics and microphysics of deep convective clouds". In: *Q. J. R. Meteorol. Soc.* 131 (2005), pp. 2639–2663.

[226] P. J. Connolly et al. "Cloud-resolving simulations of intense tropical *Hector* thunderstorms: Implications for aerosol-cloud interactions". In: *Q. J. Meteorol. Soc.* 132 (2006), pp. 3079–3106.

[227] C. Dearden et al. "Exploring the diabatic role of ice microphysical processes in two North Atlantic summer cyclones". In: *Mon. Wea. Rev.* 144 (2016), pp. 1249–1272.

[228] K. A. Browning. "Conceptual models of precipitation systems". In: *Weather and Forecasting* 1 (1986), pp. 23–41.

[229] J. D. Locatelli, J. E. Martin, and P. V. Hobbs. "Development and propagation of precipitation cores on cold fronts". In: *Atmos. Res.* 38 (1995), pp. 177–206.

[230] D. P. Jorgensen et al. "Variations associated with cores and gaps of a pacific narrow cold frontal rainband". In: *Mon. Weather Rev.* 131 (2003), pp. 2705–2729.

[231] M. Baldauf et al. "Operational convective-scale numerical weather prediction with the COSMO model: Description and sensitivities". In: *Mon. Weather Rev.* 139 (2011), pp. 3887–3905.

[232] G. Doms and M. Baldauf. *A description of the nonhydrostatic regional COSMO-Model. Part II: Physical parameterization.* Tech. rep. 2015.

[233] E. K. Bigg. "The formation of atmospheric ice crystals by the freezing of droplets". In: 79.342 (1953), pp. 510–519.

[234] S. C. Sullivan et al. "Initation of secondary ice nucleation in clouds". In: *Atmos. Chem. Phys. Disc.* (2017).

[235] D. C. Rogers et al. "Measurements of ice nucleating aerosols during SUCCESS". In: *Geophys. Res. Lett.* 25.9 (1998), pp. 1383–1386.

[236] T. H. Chubb et al. “In situ observations of supercooled liquid clouds over the Southern Ocean during the HIAPER Pole-to-Pole Observation campaigns”. In: *Geophys. Res. Lett.* 40 (2013), pp. 5280–5285.

[237] P. J. DeMott et al. “Sea spray aerosol as a unique source of ice nucleating particles”. In: *Proc. Nat. Acad. Sci.* 113.21 (2015), pp. 5797–5803.

[238] L. A. Ladino et al. “On the role of ice-nucleating aerosol in the formation of ice particles in tropical mesoscale convective systems”. In: *Geophys. Res. Lett.* 44.3 (), pp. 1574–1582.

[239] B. J. Mason and J. Maybank. “The fragmentation and electrification of freezing water drops”. In: *Q. J. Roy. Met. Soc.* 86.368 (1960), pp. 176–185.

[240] Y. Huang et al. “Factors controlling secondary ice production in cumulus clouds”. In: *Q. J. Roy. Met. Soc.* (2017).

[241] M. Paukert, C. Hoose, and M. Simmel. “Redistribution of ice nuclei between cloud and rain droplets: Parameterization and application to deep convective clouds”. In: *J. Adv. Mod. Earth Sys.* 9.1 (2017), pp. 514–535.

[242] K. D. Beheng. “Microphysical properties of glaciating cumulus clouds: Comparison of measurements with a numerical simulation”. In: *Q. J. Roy. Meteor. Soc.* 113 (1987), pp. 1377–1382.

[243] P. J. Connolly, A. J. Heymsfield, and T. W. Choularton. “Modelling the influence of rimer surface temperature on the glaciation of intense thunderstorms: The rime-splinter mechanism of ice multiplication”. In: *Q. J. R. Meteorol. Soc.* 132 (2006), pp. 3059–3077.

[244] D. R. Borys et al. “Mountaintop and radar measurements of anthropogenic aerosol effects on snow growth and snowfall rate”. In: *Geophys. Res. Lett.* 30.10 (2003).

[245] S. Lance et al. “Cloud condensation nuclei as a modulator of ice processes in Arctic mixed-phase clouds”. In: *Atmos. Chem. Phys.* 11.15 (2011), pp. 8003–8015.

[246] J. Fan et al. “Microphysical effects determine macrophysical response for aerosol impacts on deep convective clouds”. In: *Proc. Nat. Acad. Sci.* 110.48 (2013), E4581–4590.

[247] J. Fröhlich-Nowoisky et al. “Bioaerosols in the Earth system: Climate, health, and ecosystem interactions”. In: *Atm. Res.* 182 (2016), pp. 346–376.

[248] D. O’Sullivan et al. “The relevance of nanoscale biological fragments for ice nucleation in clouds”. In: *Sci. Rep.* 5.8082 (2015).

[249] O. Möhler et al. “Heterogeneous ice nucleation activity of bacteria: new laboratory experiments at simulated cloud conditions”. In: *Biogeosciences* 5 (2008), pp. 1425–1435.

[250] J. A. Huffman et al. “High concentrations of biological aerosol particles and ice nuclei during and after rain”. In: *Atmos. Chem. Phys.* 13 (2013), pp. 6151–6164.

[251] C. E. Morris et al. “Bioprecipitation: a feedback cycle linking Earth history, ecosystem dynamics and land use through biological ice nucleators in the atmosphere”. In: *Global Change Bio.* 20 (2014), pp. 341–351.

[252] M. D. Shupe. “Clouds at Arctic atmospheric observatories. Part II: Thermodynamic phase characteristics”. In: *J. Appl. Meteorol. Clim.* 50 (2011), pp. 645–661.

[253] B. Stevens et al. “Pockets of open cells and drizzle in marine stratocumulus”. In: *Bull. Amer. Meteorol. Soc.* 1 (2005), pp. 51–57.

[254] G. Feingold et al. “Precipitation-generated oscillations in open cellular cloud fields”. In: *Nature* 466 (2010), pp. 849–852.

[255] A. M. L. Ekman. “Do sophisticated parameterizations of aerosol-cloud interactions in CMIP5 models improve the representation of recent observed temperature trends?” In: *J. Geophys. Res.* 119.2 (2014), pp. 817–832.

[256] A. Berg et al. “Impact of soil moisture-atmosphere interactions on surface temperature distribution”. In: *J. Clim.* 27 (2013), pp. 7976–7993.

[257] L. J. Donner et al. “Are atmospheric updrafts a key to unlocking climate forcing and sensitivity?” In: *Atmos. Chem. Phys.* 16 (2016), pp. 12983–12992.

[258] R. E. Ulanowicz. “Information theory in ecology”. In: *Comp. Chem.* 25.4 (2001), pp. 393–399.

[259] “Formal grammar and information theory: together again?” In: *Phil. Trans. R. Soc.* 358.1769 (2000), pp. 1239–1253.

[260] L.-Y. Leung and G. R. North. “Information theory and climate prediction”. In: *J. Clim.* 3 (2000), pp. 5–14.

[261] A. J. Majda and B. Gershgorin. “Quantifying uncertainty in climate change science through empirical information theory”. In: *Proc. Nat. Acad. Sci.* 107.34 (2010), pp. 14958–14963.

[262] S. Kullback and R. A. Leibler. “On information and sufficiency”. In: *Ann. Math. Statist.* 22.1 (1951), pp. 79–86.

[263] L. van der Maaten and G. E. Hinton. “Visualizing high-dimensional data using t-SNE”. In: *J. Mach. Learn. Res.* 9 (2008), pp. 2579–2605.

[264] G. Tselioudis et al. “Global weather states and their properties from passive and active satellite cloud retrievals”. In: *J. Clim.* 26 (2013), pp. 7734–7746.

[265] L. Oreopoulos et al. “An examination of the nature of global MODIS cloud regimes”. In: *J. Geophys. Res.* 119 (2014), pp. 8362–8383.

[266] S. Park and C. S. Bretherton. “The University of Washington shallow convection and moist turbulence scheme”. In: *J. Clim.* 22.12 (2009), pp. 3449–3469.

[267] M. F. Khairoutdinov and D. A. Randall. “A cloud resolving model as a cloud parameterization in the NCAR Community Climate System Model: Preliminary results”. In: *Geophys. Res. Lett.* 28.18 (2001), pp. 3617–3620.

[268] H. Morrison, J. A. Curry, and V. I. Khvorostyanov. “A new double-moment microphysics parameterization for application in cloud and climate models. Part I: Description”. In: *J. Atm. Sci.* 62.6 (2005), pp. 1665–1677.

[269] P. Gentine et al. “A probabilistic bulk model of coupled mixed layer and convection. Part II: Shallow convection case”. In: *J. Atm. Sci.* 70 (2013), pp. 1557–1576.

[270] S.-B. Park et al. “Coherent structures in the boundary and cloud layers: Role of updrafts, subsiding shells, and environmental subsidence”. In: *J. Atm. Sci.* 73 (2016), pp. 1789–1814.

[271] J. R. Porter and M. A. Semenov. “Crop responses to climatic variation”. In: *Philos. Trans. R. Soc. Lond. B. Biol. Sci.* 360.1463 (2005), pp. 2021–2035.

[272] R. G. Evans and E. J. Sadler. “Methods and technologies to improve efficiency of water use”. In: *Water Resour. Res.* 44.W00E04 (2008).

[273] S. Manabe and R. F. Strickler. “Thermal equilibrium of the atmosphere with a convective adjustment”. In: *J. Clim.* 7 (1964), pp. 361–385.

[274] B. Stevens and G. Feingold. “Untangling aerosol effects on clouds and precipitation in a buffered system”. In: *Nature* 461 (2009), pp. 607–613.

[275] J. H. Seinfled et al. “Improving our fundamental understanding of the role of aerosol-cloud interactions in the climate system”. In: *Proc. Nat. Acad. Sci.* 113.21 (2016), pp. 5781–5790.

[276] B. Pummer et al. “Suspendable macromolecules are responsible for ice nucleation activity of birch and conifer pollen”. In: *Atmos. Chem. Phys.* 12 (2012), pp. 2541–2550.

[277] Y. Tobo et al. “Organic matter matters for ice nuclei of agricultural soil origin”. In: *Atmos. Chem. Phys.* 14 (2014), pp. 8521–8531.

[278] J. A. Crook et al. “A comparison of temperature and precipitation responses to different Earth radiation management geoengineering schemes”. In: *J. Geophys. Res.* 120 (2015), pp. 9352–9373.

[279] J. Kristj'ansson, H. Muri, and H. Schmidt. “The hydrological cycle response to cirrus cloud thinning”. In: *Geophys. Res. Lett.* 42.24 (2015), pp. 10807–10815.

[280] L. S. Jackson, J. A. Crook, and P.M. Forster. “An intensified hydrological cycle in the simulation of geoengineering by cirrus cloud thinning using ice crystal fall speed changes”. In: *J. Geophys. Res.* 121 (2016), pp. 6822–6840.

[281] E. A. B. Eltahair. “A soil moisture rainfall feedback mechanism”. In: *Water Resour. Res.* 34.4 (1998), pp. 765–776.

[282] S. I. Seneviratne et al. “Land-atmosphere coupling and climate change in Europe”. In: *Nature* 443 (2006), pp. 205–209.

[283] A. Berg et al. “Land-atmosphere feedbacks amplify aridity increase over land under global warming”. In: *Nature Climate Change* 6 (2016), pp. 869–874.

[284] Y. Sun et al. “Drought onset mechanisms revealed by satellite solar-induced chlorophyll fluorescence: Insights from two contrasting extreme events”. In: *J. Geophys. Res.* 120 (2015), pp. 2427–2440.

[285] E. Etienne et al. “Development of a demand sensitive drought index and its application for agriculture over the coterminous United States”. In: *J. Hydrol.* 534 (2016), pp. 219–229.

[286] A. de Sherbinin. “Climate change hotspots mapping: what have we learned?” In: *Clim. Change* 123 (2014), pp. 23–37.

[287] E. T. Jaynes. “Information theory and statistical mechanics”. In: *Phys. Rev.* 106.4 (1957), pp. 620–630.

The only people for me are the mad ones, the ones who are mad to live, mad to talk, mad to be saved, desirous of everything at the same time, the ones who never yawn or say a commonplace thing, but burn, burn, burn like fabulous yellow roman candles exploding like spiders across the stars.

J. Kerouac